University of California
Santa Barbara

The influence of (de)intercalation mechanics on the electrochemical performance of NASICON structured Na-ion cathodes

A dissertation submitted in partial satisfaction
of the requirements for the degree

Doctor of Philosophy
in
Materials

by

Eliovardo A. Gonzalez-Correa

Committee in charge:

Professor Raphaële Clément, Chair
Professor Ram Seshadri
Professor Michael Chabinyc
Professor Javier Read de Alaniz

June 2024

The Dissertation of Eliovardo A. Gonzalez-Correa is approved.

Professor Ram Seshadri

Professor Michael Chabinyc

Professor Javier Read de Alaniz

Professor Raphaële Clément, Committee Chair

February 2024

The influence of (de)intercalation mechanics on the electrochemical performance of NASICON structured Na-ion cathodes

by

Eliovardo A. Gonzalez-Correa

Para mi padre que me enseño resiliencia y,
para mi madre que me enseño la importancia de paciencia.

Acknowledgements

First and foremost I would like to thank Dr. Raphaële Clément, whose exceptional guidance has been the cornerstone of this work. Her ability to go above and beyond what is expected from an advisor is a quality that has, and will, continue to impact future students in the years to come.

A special acknowledgement goes to a dear friend who I have coined "The NMR Guru," Dr. Raynald Giovine. You can set a price on textbooks but sitting next to an expert for hours on end who challenges your understanding to make you develop intuition for the subject matter at hand is invaluable.

To members of my committee, Dr. Ram Seshadri and Dr. Michael Chabynic, thank you for being a resource and a mentor throughout this journey. Dr. Javier Read de Alaniz and Dr. Arica Lubin, your support with the Bridge to Doctorate fellowship has helped several underrepresented minorities, myself included, feel welcomed in academia. For that, we will forever be grateful.

To Dr. Brent Minchew, thank you for being the role model I didn't know I needed. It isn't often that combat veterans pop up in academia but seeing an individual such as yourself and the success you've accomplished gave me a sense that we do belong and that we have something to contribute long after we've taken off our service uniforms and traded them in for lab coats.

To my brothers, Juan and Osvaldo, thank you for keeping me grounded on this journey and always reminding me that our futures aren't limited by where we come from. A special thanks to all the members of the Clément group who have been a pillar of support as we all continue on this journey. Lastly, but just as important, are the members of the MRL staff, specifically Dr. Amanda Strom, Dr. Rachel Behrens, and Jaya Nolt for their commitment to student excellence. hyperref

Curriculum Vitæ

Eliovardo A. Gonzalez-Correa

Education

2024	Ph.D. in Materials, University of California, Santa Barbara. Emphasis: *Functional & Quantum Materials* Advisor: Raphaële Clément
2018	B.S. in Applied Physics, California State University, San Bernardino Minor: Applied Mathematics

Publications

1. **E. Gonzalez-Correa**, T. Li, F. Zhou, A. Zohar, H.A. Evans, V. Wu, R. J. Clément, "Impact of phase transtions during electrochemical cycling of Al subsituted $Na_3V_{2\text{-}y}Al_y(PO_4)_3$, Na-ion cathodes", *In preparation.*
2. **E. Gonzalez-Correa**, K. Kumar, S. Ghosh, M. Mazumder, S. K. Pati, R. J. Clément, P. Senguttuvan, "High voltage cycling degradation mechanisms of Mg subsituted $Na_{3+y}V_{2\text{-}y}Mg_y(PO_4)_3$ Na-ion cathodes" *Submitted.*
3. E. Sebti, H. A. Evans, H. Chen, P. M. Richardson, K. M. White, K. P. Koirala, Y. Xu, **E. Gonzalez-Correa**, C. Wang, C. Brown, A. K. Cheetham, P. Canepa, R. J. Clément, "Stacking Faults Assist in Lithium-Ion Conduction in a Halide-Based Superionic Conductor", *J. Am. Chem. Soc.*, **144**, (2022), 5795-5811. DOI: 10.1021/jacs.1c11335
4. S. Ghosh, N. Barman, **E. Gonzalez - Correa**, M. Mazumder, A. Zaveri, R. Giovine, A. Manche, S. K. Pati, R. J. Clément, P. Senguttuvan, "Elucidating the Impact of Mg Substitution on the properties of NASICON $Na_{3+y}V_{2\text{-}y}Mg_y(PO_4)_3$ Cathodes", *Adv. Funct. Mater*, **31**, (2021), 2105463. DOI: 10.1002/adfm.202105463
5. E. E. Foley, A. Wong, R. C. Vincent, A. Manche, A. Zaveri, **E. Gonzalez-Correa**, G. Menard, R. J. Clément, "Probing reaction processes and reversibility in Earth-abundant Na_3FeF_6 for Na-ion batteries", *Phys. Chem. Chem. Phys.*, **23**, (2021), 20052-20064. DOI: 10.1039/D1CP02763H
6. R. Xiao, Y. Hou, Y. Fu, X. Peng, Q. Wang, **E. Gonzalez-Correa**, S. Jin, D. Yu, "Photocurrent Mapping in Single-Crystal Methylammonium Lead Iodide Perovskite Nanostructures", *Nano Lett.*, **16**, (2016), 7710-7717. DOI: 10.1021/acs.nanolett.6b03782

Abstract

The influence of (de)intercalation mechanics on the electrochemical performance of NASICON structured Na-ion cathodes

by

Eliovardo A. Gonzalez-Correa

Sodium-ion batteries (SIBs) are attractive alternatives for electrochemical energy storage due to sodium's natural abundance and cost-effectiveness when compared to their lithium counterparts. Among the various Na-ion cathode classes, sodium superionic conductor (NASICON) structured $Na_3V_2(PO_4)_3$ (NVP) has emerged as a promising candidate for SIB applications owing to its high structural stability, 3−D Na^+ diffusion network, and high operating voltage of 3.4 V vs. Na^+/Na^0. Although promising, the impact of temperature dependent Na^+/ vacancy ordering transitions, potential cation migration, and influence of phase separation upon Na (de)intercalation on Na^+ diffusion is still poorly understood.

Here, we focus on the effects of isovalent (Al^{3+}) and aliovalent (Mg^{2+}) substitution for V into the NVP framework and investigate a series of $Na_{3+y}V_{2-y}Mg_y(PO_4)_3$ (Mg-NVP) (y = 0−1.0) and $Na_3V_{2-y}Al_y(PO_4)_3$ (Al-NVP) (y = 0, 0.5) cathodes to better understand the impact of V by substitution on the Na (de)intercalation mechanics by complementing short and long range characterization techniques such as synchrotron X-ray diffraction, ^{23}Na, ^{31}P, ^{51}V solid-state NMR, and scanning electron microscopy (SEM) with first principles calculations to unravel the complex electrochemical cycling behavior of these materials. We demonstrate the vastly different effect of each dopant on electrochemical performance with an emphasis on (de)intercalation mechanics and causes of structural degradation during high voltage cycling.

In the case of Mg-NVP, Na extraction and reinsertion results in a two-phase reaction mechanism when $y < 0.5$ and transitions to a solid-solution mechanism above $y = 0.5$, when cycled over a potential window of $3.8-2.75$ V. Conversely, when Al^{3+} is introduced into the NVP framework, it exacerbates the formation of an intermediary $Na_{2.24}V_{1.5}Al_{0.5}(PO_4)_3$ phase leading to successive biphasic reactions during Na (de)intercalation, in stark contrast to the solid-solution mechanism that emerges at higher Mg concentrations. It is found that the formation of the intermediary phase in Al-NVP helps reduce the propensity for particle cracking during long term cycling and lowers overpotentials associated with Na extraction during electrochemical cycling. Thus, we have highlighted the significant role of transition metal dopants to modify the reaction mechanisms associated with Na (de)intercalation in NASICON structured $Na_3V_2(PO_4)_3$.

Contents

Chapter 1

Introduction

1.1 How batteries could help us

The technological revolution, particularly the Industrial Revolution that began in the 18th century was significantly fueled by the widespread adaptation and use of fossil fuels such as coal, oil, and natural gas to power machinery, transportation, and energy systems that have transformed various aspects of modern society. While these technological advancements have improved our quality of life to an extent, it is crucial to find avenues to mitigate the environmental and sustainability concerns that this rapid growth has raised. The burning of fossil fuels releases greenhouse gases contributing to climate change at an alarming rate such that according to a recent review by Jacobson et al.[1], preventing global warming from rising above 1.5°C will require at least an 80% conversion to zero emission energy by 2030 and 100% by 2050, predominantly powered via the increased use of renewable energy.

Although renewable energy sources such as wind and solar provide an alternative to fossil fuels, their energy production is not constant and readily available as required for the stability of an energy grid. A grid capable of storing the intermittent energy

produced from renewable sources is needed for their implementation and success. To this regard, rechargeable Na-ion (and Li-ion) battery integration will play a critical role in the successful implementation of renewable energy sources.

The need for efficient and large-scale energy storage systems to successfully utilize intermittent energy sources, such as wind and solar, is a pressing issue. Li-ion technology has proven itself in its ability to power our portable electronic devices and in the realm of electric vehicle propulsion but, many experts advise that once the Li-ion technology reaches maturity, the sustainability of lithium resources will be questionable given its non-uniform geographical distribution and uncertain supply chain. LIBs also suffer from questionable ethics in regards to the sourcing of Co (and Li) used predominantly in LIBs along with high cost and unsustainable practices [2, 3]. As a result, Na-ion based technology has emerged as a potential alternative to Li-ion batteries.

This dissertation explores the advancement of cathode (positive electrode) materials for Na-ion batteries, focusing specifically on Natrium Superionic Conductor (NASICON) structured materials. The general formula for the materials covered here is $Na_xMM'(PO_4)_3$ where M and M′ are transition metal species. Enhancing these cathode materials necessitates a comprehensive exploration of how their composition, structure, and properties interrelate. We elaborate on the experimental and theoretical approaches used in this dissertation to probe the influence of transition metal dopants on the Na (de)intercalation properties compounds.

1.2 Rechargeable Batteries

All state of the art batteries are comprised of three components: the cathode, the anode, and the electrolyte (ionically conducting Na (or Li) salt in an inorganic solvent) used to convert chemical energy into electrical energy reversibly and efficiently. Most

commercial batteries operate via intercalation reactions upon (dis)charge often referred to as a"rocking-chair" cell [4, 5] as shown in Figure 1.1. When the battery is charged, Na^+ ions migrate from the cathode (positive electrode) towards the anode (negative electrode) coupled with an oxidation reaction occurring at the cathode and a reduction reaction occurring at the anode, typically referred to as redox reactions. For example, at the cathode the following oxidation reaction occurs:

$$M \rightarrow M^{n+} + ne^- \tag{1.1}$$

where M is the metal species and n is the number of electrons oxidized. Conversely, at the anode the following reduction reaction occurs in the opposite direction, namely:

$$M^{n+} + ne^- \rightarrow M \tag{1.2}$$

In order to achieve these redox reactions, the cathode and the anode must be capable of both electronic and ionic conduction. The electrolyte on the other hand must be electronically insulating but, ionically conductive. A separator is often used to prevent the circuit from shorting by physically isolating contact between the cathode and the anode. The electronically insulating electrolyte layer is necessary so that the electrons are forced to travel through an external circuit allowing us to power our devices or for other useful work. The insulating electrolyte layer also prevents a short circuit of the battery, where electrical current flows through an unintended path (here the electrolyte layer) with little or no resistance between the cathode and anode. In the context of batteries, a short circuit may be potentially dangerous because it can lead to rapid discharge of the battery generating excessive heat causing the battery to fail. This thermal runaway condition may cause battery materials to ignite and catch fire [6]. In an ideal system, there would not be any reactions taking place between the electrolyte and electrodes,

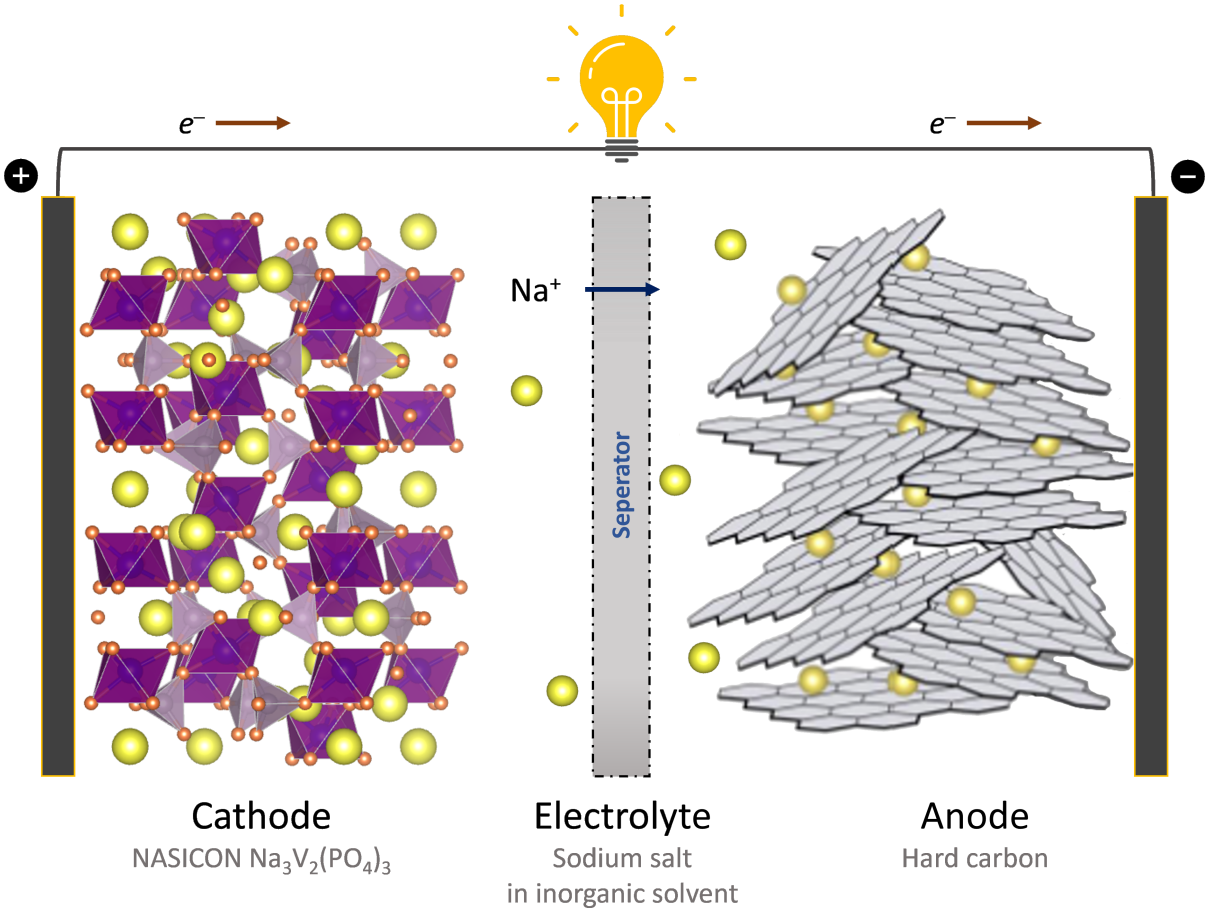

Figure 1.1: Schematic of Na-ion battery during charge. The electrochemical cell is composed of a intercalation cathode material (NASICON pictured here) and a hard carbon anode in a liquid electrolyte. Upon charge, Na^+ ions (yellow circles) are intercalated into the cathode from the anode. The reverse process occurs on discharge.

unfortunately this is not the case and a solid-electrolyte interface (SEI) will inevitably to form when batteries are (dis)charged at the location of contact between electrode and electrolyte. In the ideal case, the SEI would be ionically conducting but, electronically insulating, and prevent further side reactions from occurring. However, in practice the SEI is sometimes electronically conducting leading to continued electrolyte degradation through redox process (Eq. 1.1 and 1.2) during electrochemical cycling [7].

1.2.1 Na^+ vs. Li^+ for Batteries

The pursuit of sodium-ion batteries (SIBs) as an alternative for lithium-ion batteries (LIBs) holds immense promise to address challenges associated with cost and sustainability. SIBs operate similarly to LIBs, but have the added benefit that sodium is abundant and widely available. Unlike lithium, which faces supply constraints and environmental concerns, sodium is far more abundant in the Earth's crust offering a more sustainable source for battery technologies as shown in Table 1.1.

Characteristic	Na	Li
ratio of reserves	1000	1
price of carbonates [US $ per ton]	150	5000
atomic weight [g/mol]	23	6.9
ionic volume [Å]	4.44	1.84
theoretical capacity (mAh/g)	1165	3829
voltage (V) vs SHE	−2.714	−3.045
melting point (° C)	98	182
coordination preference	octahedral, prismatic	octahedral, tetrahedral
distribution	everywhere	70% in South America

Table 1.1: Comparison of Na and Li properties [8] SHE: standard hydrogen electrode

Although sodium is promising from a cost and abundance perspective, it is not totally superior to lithium. Firstly, the standard operating potential of Na metal is 0.331 V greater than Li metal [8] which will result in lower operating potentials (covered in section 1.2.2) for SIBs when compared to their LIB counterparts. Regardless of these drawbacks, SIBs still show promise due to their cost-effectiveness in large-scale grid energy storage adaptation. A critical component of the transition to renewable energy sources will be the ability of providing power stability to the grid. The development of cost-effective and efficient SIBs have the potential make grid energy storage feasible on a global scale. While LIBs have proven its utility in portable power and electric vehicles, the scalability for grid applications will face challenges related to resource availability, making SIBs a suitable avenue to approach this problem. Further research into the development of SIBs

will contribute to the global transition to more sustainable means of powering our society.

1.2.2 Key Performance Metrics

This dissertation will mention a wide-range of performance metrics related to battery materials that are outlined below. To begin, the battery capacity, denoted Q, is described by the following equation:

$$Q = I * t \tag{1.3}$$

Where I is the applied current in amps (A) or milliamps (mA) and t is time in hours. Equation 1.3 encapsulates the concept that the capacity of a battery is directly proportional to the amount of electric charge that it can deliver over a given period of time. The specific capacity of a battery is then the ratio of the battery capacity to its mass given in units of mAh/g.

Building on Equation 1.3, another key metric when evaluating the performance of a battery is its energy density (Wh/kg). The gravimetric energy density (i.e., the energy density per unit mass of the electrode material) is the product of the cell potential (V or E^0_{cell}) and the specific capacity of the cell (Q) in units of mAh/g or C/g.

$$E = Q * V \tag{1.4}$$

The cell potential is defined as the potential difference between the cathode and the anode, namely:

$$\Delta G^0_{cell} = \Delta G^0_{cathode} - \Delta G^0_{anode} = -nFE^0_{cell} \tag{1.5}$$

where

$$E^0_{cell} = E^0_{cathode} + E^0_{anode} \tag{1.6}$$

Here ΔG^0_{cell} is the Gibbs Free Energy of the cell, F represents Faraday's constant, and n is the number of electrons that are shuttled from the anode to the cathode. The potential difference (or voltage), E^0_{cell}, is the difference in the electronic energy levels of the cathode and anode. Changes in the potential difference is directly related to the thermodynamic changes taking place at the cathode and anode.

The power density of a battery is an important metric for certain high power applications, including electric vehicles, trucks, seacraft, aircraft, and drones. Power density is the rate at which energy can be delivered per unit of volume or weight. On the other hand, low power applications may benefit from prioritizing battery capacity over high power density. The power density is the rate at which this power is delivered:

$$P = \frac{\partial E}{\partial t} = \frac{\partial Q}{\partial t} * V = I * V \tag{1.7}$$

The applied current is typically defined in terms of a "C-rate." The meaning of this C-rate refers to amount of time for which current is applied to fully (dis)charge the cell. For example, at a current rate of 1C enough current would be applied such that the cell is fully (dis)charged in one hour. A C-rate of C/40 would require 40 hours to fully (dis)charge the sample and a rate of 40C would require only 1.5 minutes. A batteries cycle life is directly related to the capacity retention over various cycles. In industry, batteries capable of thousands of (dis)charged cycles is typically desired and maintain more than 80% of its initial capacity. It is widely acknowledged in the field of battery technology that once a battery reaches 80% of its initial capacity, it is considered spent.

The overall energy efficiency of a cell is given as the product of Coulombic efficiency (CE) and must be greater than 99.99% for a cell to be able to sustain the thousands of cycles and still maintain more than 80% of its initial capacity as desired for industrial applications. The CE of a battery is given by the ratio of actual charge delivered during

discharge to the charge delivered during the charging process and is given as a percentage by the following equation:

$$\mathrm{CE} = \frac{\text{Total charge discharged}}{\text{Total charge charged}} \times 100\% \tag{1.8}$$

Drops in Coulombic efficiency may imply a few things including including, but not limited to, electrolyte decomposition at high voltage and undesired side reactions at the SEI that occur during (dis)charge. These side reactions consume energy without contributing to the sought after electrochemical reactions and thus serve to lower the Coulombic efficiency.

Another term used throughout this dissertation is voltage hysteresis and refers to a phenomenon in which the voltage of a battery varies during the charge and discharge process observed at the same state of charge (SOC). This may be influenced by different reaction kinetics depending on whether the battery is charging or discharging. It may also be influenced by irreversible side reactions and losses that indicate some of the chemical energy is lost during electrochemical cycling further leading to battery inefficiency. Minimizing voltage hysteresis to optimize battery efficiency and performance is crucial for rechargeable batteries. Details of electrochemical cycling techniques will be outlined in section 2.5 of Chapter 2 covering the methods employed throughout this dissertation.

1.3 NASICON Structured Cathodes for Batteries

Much of the commercial success of Li-ion batteries has resulted from the discovery of layered transition metal (TM) oxides as high voltage intercalation-type cathodes, starting with lithium cobalt oxide ($LiCoO_2$) [5], and currently dominated by lithium nickel manganese cobalt oxides (NMC) [9, 10]. This success has driven much of the research

into their sodium analogues over the past 15 years, namely Na_xMO_2 (M = redox active transition metal) containing edge sharing MO_6 coordination polyhedra that form two-dimensional layers. In these compounds, the Na^+ ions reside in octahedral or prismatic sites in the interlayer space, depending on the layer stacking. While Na extraction from and reinsertion into the interlayer space is an effective charge storage strategy, such compounds are prone to phase transitions during Na (de)intercalation, resulting from glides of the MO_6 layers and a change in the Na coordination. Such transitions are typically only partially reversible, leading to gradual structural degradation during cycling, and capacity fade [11]. These limitations have motivated investigations of alternative structures and chemistry's for Na intercalation compounds, polyanionic cathodes being an obvious choice due to their robust framework and the ability to tune the Na (de)intercalation potential and ion transport properties by modulating the polyanion chemistry [12, 13].

Other important classes of Na-ion cathodes include Prussian Blues and Prussian Whites. While these materials have found applications in various fields, the focus here will be on their energy storage applications. The discovery of Prussian Blue has been attributed to the accidental mixing of pot ash and animal blood [14]. The structure of Prussian Blue is characterized by a cubic lattice framework capable of incorporating various ions including sodium and is given by the chemical formula $Fe_4[Fe(CN)_6]_3$. Prussian White, on the other hand, is less commonly mentioned but is a counterpart of Prussian Blue where Fe^{3+} is reduced to Fe^{2+} leading to a color change from blue to nearly colorless. The transformation is reversible which makes these compounds useful for their redox reactions and applications requiring ion exchange. Their open framework allows for facile Na^+ insertion and extraction, a key underpinning of SIB operation. However, they also face several challenges related to low electronic conductivity and sensitivity to moisture in the case of Prussian Whites [15]. Additionally, another key factor affecting the electrochemical performance of Prussian Blue analogues is the presence of crystal

water in the structure arising from aqueous synthesis environments linked to structural defects [16, 17, 18].

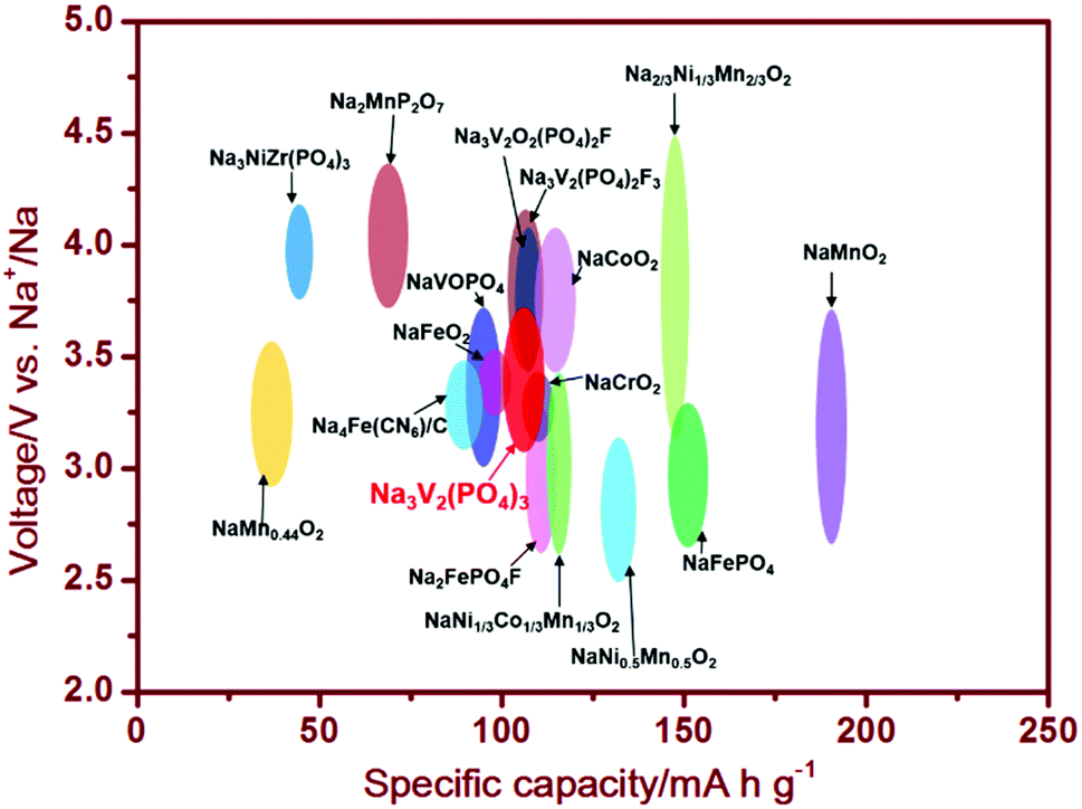

Figure 1.2: Typical cathodic materials for SIBs (specific capacity versus voltage). Adapted from Zhang et al.[19] with permission from the Royal Society of Chemistry

In the mid-1970's, Hong and Goodenough *et al.* reported on a new type of polyanionic Na-ion conductors, $Na_{1+x}Zr_2P_{3-x}Si_xO_{12}$ $(0 \leq x \leq 3)$. Unlike layered materials, such as β-alumina $(Na_2O{\cdot}11Al_2O_3)$[20, 21] discovered a decade earlier, and layered Na_xMO_2 oxides, which provide 2-dimensional Na-ion conduction pathways, the open framework structure of $Na_{1+x}Zr_2P_{3-x}Si_xO_{12}$ $(0 \leq x \leq 3)$ enables Na-ion conduction in 3-dimensions. Their high ionic conductivites [22, 23] has earned them the denomination of NASICON (Natrium Super Ionic Conductor)[24, 25], and makes them suitable candidates for use as solid electrolytes. More broadly, NASICON-type compounds can be described as $Na_{3+x}M_{2-x}M'_x(XO_4)_3$ (M,M' = metal species, X = P, Si). Depending on the choice

of transition metal, these materials may be suitable Na-ion solid electrolytes, cathodes, or anodes providing an avenue for an all NASICON structured solid-state battery [26, 27]. The high symmetry NASICON structure can be described in the rhombohedral $R\bar{3}c$ space group, and comprises two partially occupied sodium crystallographic sites namely, Na(1) (6-coordinate, Wyckoff position 6b) and Na(2) (8-coordinate, Wyckoff position 18e). So-called 'lantern units' composed of two corner sharing VO_6 octahedra connected via 3 corner sharing PO_4 tetrahdra are stacked along the *c*-direction, as shown in Figure 1.3. Specifically, $Na_3V_2(PO_4)_3$ (NVP) has received significant interest from the research community as a potential SIB cathode material for its open NASICON framework where Na ions may diffuse relatively fast (and reversibly) through interstitial sites with minimal structural degradation [28]. NVP, however, does suffer from relatively low electronic conductivity [29] and much of the research thrust has been focused on increasing this to fully access the theoretical capacity of this material. To this end, many endeavours have been used to increase charge carrier transport kinetics in NVP such as incorporating conductive carbon [30, 31] and downsizing of particles to improve surface electrical conductivity.

1.3.1 $Na_3V_2(PO_4)_3$

The $Na_3V_2(PO_4)_3$ (NVP) NASICON cathode has garnered particular interest over the past decade thanks to its good structural stability, compositional flexibility in terms of potential dopants on the V sites, and fast Na-ion diffusion [32, 22, 33]. Additionally, the presence of V allows to access multiple oxidation states (i.e. $V^{3+}/V^{4+}/V^{5+}$) enabling large amounts of Na to be extracted and reinserted during charge and discharge, and increasing specific capacity and energy density.

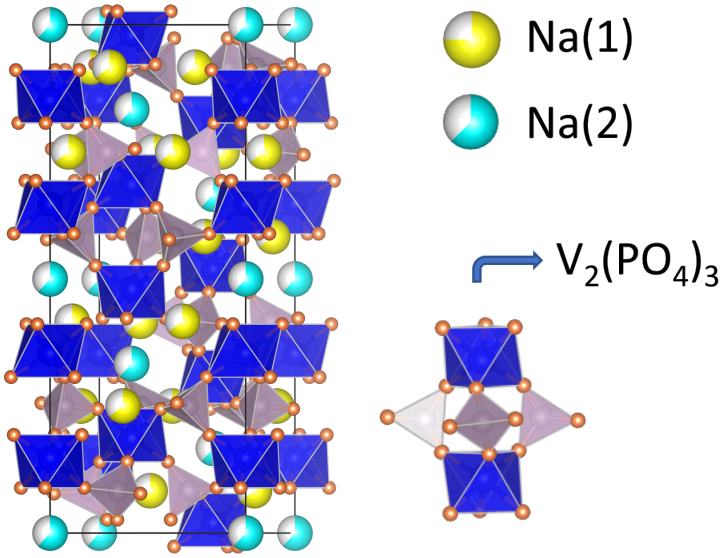

Figure 1.3: Crystal structure of the rhombohedral R$\bar{3}$c NASICON space group. $V_2(PO_4)_3$ "lantern" units are depicted at the bottom right.

1.3.2 Temperature-dependent phase transitions in $Na_3V_2(PO_4)_3$

The crystal structure of $Na_3V_2(PO_4)_3$ was originally reported by Delmas et al. in 1978 [35], who used the standard rhombohedral R$\bar{3}$c unit cell. For nearly 40 years, the scientific community agreed upon this crystal structure until in 2015 when Masquelier and Chotard et al. discovered sodium-ordered form of NVP [34] near room temperature, as evidenced by differential scanning calorimetry (DSC) shown in Figure 1.4.

The work by Chotard et al. uncovered the existence of four distinct polymorphs of NVP across a temperature spectrum from -30 to 225 ° C. Central to the findings is the identification of a sodium-vacancy ordered monoclinic (C2/c) form of NVP near room temperature. Further, upon heating NVP undergoes multiple reversible phase transitions, namely: $\alpha \Leftrightarrow \beta$ at 25.8 °C, $\beta \Leftrightarrow \beta'$ at 118.6 °C, and $\beta' \Leftrightarrow \gamma$ at 177.2 °C as shown in Figure 1.4. These transitions exhibit distinctive thermal behaviors, with the $\beta \Leftrightarrow \beta'$ showing weak and broad thermal peaks indicative of a complex phase transition mechanism. In the low temperature $\alpha-$NVP phase, a distinct occupancy pattern emerges at

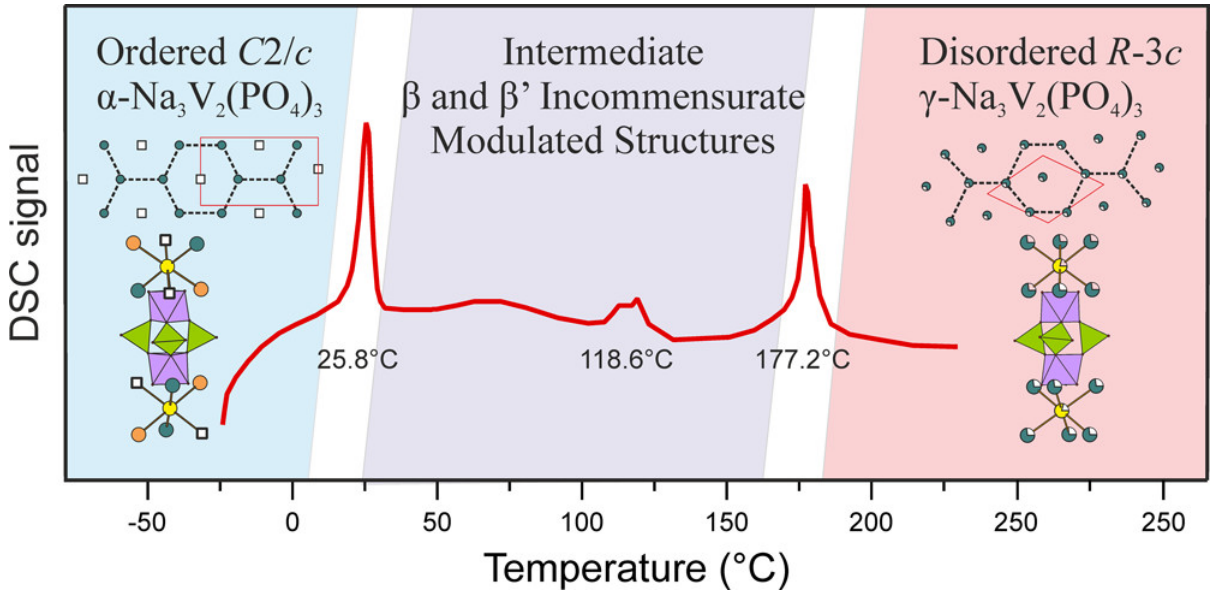

Figure 1.4: DSC measurement of NVP from −30 to 225° C upon heating. Adapted from Chotard et al.[34] with permission from the American Chemical Society

the Na(1) and Na(2) sites, which split into Na(1a), Na(1b), Na(2a), Na(2b), and Na(2c) sites. Na−vacancy ordering slows down Na−ion transport [36] which makes the stabilization of the high temperature, Na−disordered R$\bar{3}$c structure desirable. However, most studies to date still report NVP−derived cathode structures in the R$\bar{3}$c space group, with few efforts to further characterize potential Na−vacancy ordering. Overall, a better understanding of how doping/substitutions on the V site impacts temperature−dependent phase transitions in NVP is crucial for the implementation, design, and optimization of all-climate Na-ion batteries.

1.3.3 Formation of intermediary phases in $Na_3V_2(PO_4)_3$ during electrochemical cycling

The exploration of intermediate phases during electrochemical cycling represents a pivotal area of research in the advancement of battery materials, particularly for the

development of high-performance sodium-ion batteries. These intermediate phases play an important role in the kinetics of ion (de)intercalation, structural reversibility and, by extension, the overall electrochemical performance of battery systems. The conventional understanding of the (de)intercalation mechanism of NVP posits a two-phase reaction mechanism between the $Na_3V_2(PO_4)_3$ –$NaV_2(PO_4)_3$ compositional end-members. However, it was recently reported (2022) by Park et al. [37] that an intermediate phase, $Na_2V_2(PO_4)_3$ emerges during non-equilibrium cycling conditions.

The existence of this $Na_2V_2(PO_4)_3$ phase was conclusively demonstrated by employing operando synchrotron X-ray diffraction (XRD) and corroborated by density functional theory (DFT) calculations. A complete isolation of the $Na_2V_2(PO_4)_3$ phase was not achieved electrochemically and always coexisted with either the $Na_3V_2(PO_4)_3$ phase or the desodiated $NaV_2(PO_4)_3$ phase. The researchers proposed multiple possible crystal structures for the intermediate phase with $P2_1/c$ as the most likely. The discovery is signficant as this intermediate phase is believed to reduce the lattice mismatch between the compositional endmembers, $Na_3V_2(PO_4)_3$ and $NaV_2(PO_4)_3$, facilitating faster and potentially more reversible phase transitions.

The work by Park and Chotard [37] has shown that the rate at which Na is extracted/ reinserted into the NVP framework affects the Na (de)intercalation mechanism, however, there may be other ways to do so, much like those explored in Chapters 3, 4, and 5. For example, substitution of V in $Na_3V_2(PO_4)_3$ by another redox-active or redox-inactive species and/ or modulation of the crystal structure may also modify the Na (de)intercalation mechanism. The contents of this dissertation serve as a study to the effect phase transitions in electrode materials during electrochemical cycling.

1.4 Aims & Outline of this Dissertation

The studies presented in this dissertation investigate the impact of V substitution by Mg^{2+} (aliovalent substitution) and Al^{3+} (isovalent substitution) on the mechanism and kinetics of Na (de)intercalation, structural stability, and therefore the achievable capacity, rate performance and cycle life of NVP-type cathode materials. The overarching goal of this work is to better understand the complex structure-(electrochemical) property relationships in NVP-type cathodes, to further inform their design for next-generation Na-ion batteries.

Firstly, the experimental and computational methods employed to characterize the materials of interest to this work are described in Chapter 2. In Chapters 3 and 4, we investigate a series Mg-substituted $Na_3V_2(PO_4)_3$ cathodes. This family of cathodes is of particular interest as aliovalent Mg^{2+} substitution on the V site, results in an increased Na content and opens the door to V^{4+}/V^{5+} redox. The use of an electrochemically-inactive substituent further enables to isolate the impact of V redox processes on Na (de)intercalation and structural processes during extended cycling. In Chapter 3, we investigate the impact of Mg substitution on the Na(de)intercalation mechanism, evolving from two-phase to solid solution-type, the electrochemical reversibility, and Na^+ diffusion kinetics in $Na_{3+y}V_{2-y}Mg_y(PO_4)_3$ (y = 0.0, 0.25, 0.5, 0.75, and 1.0) cycled over the 3.8−2.4 V vs. Na^+/Na^0 window. In Chapter 4, we focus on the redox and structural (degradation) processes taking place in $Na_{3+y}V_{2-y}Mg_y(PO_4)_3$ (y = 0.0, 0.5, and 1.0) when these cathodes are cycled over a wider voltage window (4.2−2.4 V).

Chapter 5 focuses on isovalent Al^{3+} substitution on the V site, through a comparison of $Na_3V_{2-y}Al_y(PO_4)_3$ (y = 0.0 and 0.5) compounds. In particular, the formation of a stable Na/vacancy ordered structure at an intermediate stage of charge, leading to two consecutive two-phase reactions during electrochemical cycling for the Al-substituted

compound, is investigated.

1.5 Permissions and Attributions

1. Figure 1.2 in Chapter 1 has been adapted from the work of Zhang et al. [19] with permission from the Royal Society of Chemistry (Great Britain), National Center for Nanoscience and Technology. Order license ID: 1440098-1
   https://doi.org/10.1039/C8NR09391A

2. Figure 1.4 in Chapter 1 has been adapted from Chotard et al. [34] with permission from the American Chemical Society. Copyright (2015)
   https://doi.org/10.1021/acs.chemmater.5b02092

3. The contents of Chapters 3 and 4 is the result of a collaboration with the research group of Prof. Premkumar Senguttuvan of the New Chemistry Unit, International Centre for Materials Science and School of Advanced Materials Jawaharlal Nehru Centre for Advanced Scientific Research in Jakkur, Bangalore, India. This is also in collaboration with Prof. Swapan K. Pati of the Theoretical Science Unit also at the Jawaharlal Nehru Centre for Advanced Scientific Research. This work has previously appeared in the journal of Advanced Functional Materials, reference [32] and is reproduced with the permission of the Wiley Online Library: https://doi.org/10.1002/adfm.202105463

Chapter 2

Methods

2.1 Diffraction

2.1.1 Principles

Diffraction, a phenomenon rooted in wave optics, plays a pivotal role in understanding the behavior of light when encountering obstacles. When a beam of light encounters an obstacle, it scatters, and the waves interfere with each other, creating an intricate pattern known as an interference pattern. This phenomenon is not confined to light waves and has broad applications, extending to various fields of study, including the characterization of proteins and the exploration of the long-range, periodic structure of quantum materials.

In the context of this dissertation, the focus lies on powder X-ray diffraction (XRD), a powerful technique for probing the structure of crystalline materials. In powder XRD, a beam of X-rays is directed towards a powdered sample, and the resulting diffraction pattern provides critical information about the arrangement of atoms within the material. The interaction of X-rays with the material is influenced by its electron density, and materials with higher electron densities exhibit more pronounced diffraction features.

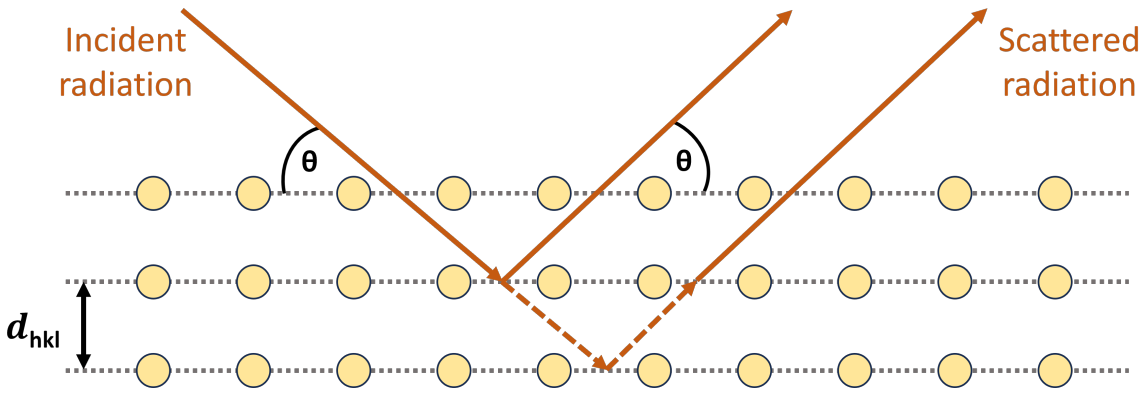

Figure 2.1: Schematic of Bragg diffraction law. The path length difference between scattered beams is depicted with a dotted line.

For materials containing "lighter" elements like sodium (Na), the utilization of higher energy synchrotron X-ray sources becomes essential to achieve the required resolution for detailed structural analysis.

Crystalline materials are characterized by their smallest repeating unit cell which can be translated in all directions to construct the overall crystal structure. This unit cell includes a motif, a set of atoms centered at each lattice point, reproducing the atomic arrangement within the lattice when extended across space[38]. The periodic arrangement of the lattice results in families of parallel planes of atoms, each characterized by Miller indices (hkl), which play a pivotal role in the diffraction process.

The distance between a set of (hkl) planes is denoted as d_{hkl}. When a monochromatic X-ray beam interacts with a crystalline material at an incidence angle θ, the X-rays scatter from these planes. However, only constructive interference results in a measurable signal intensity. Constructive interference occurs when the path length difference between beams scattered off parallel planes equals an integer number (n) of wavelengths (λ)[38]. Bragg's Law precisely defines this condition, establishing a fundamental relationship between the incidence angle, the wavelength of the X-rays, and the lattice spacing as shown in Figure 2.1. It is given by,

$$n\lambda = 2d_{hkl} \sin\theta \tag{2.1}$$

The diffraction pattern, obtained by measuring the intensity of scattered X-rays at different angles, reflects the crystallographic information encoded within the material. Peaks in the diffraction pattern correspond to specific planes in the crystal lattice that satisfy the constructive interference condition. Analyzing these peaks enables researchers to deduce the crystal structure of the material, providing insights into its composition, symmetry, and other structural features. The meticulous application of diffraction techniques, particularly powder XRD, enhances our ability to unravel the structural details of crystalline materials across diverse scientific domains.

In this work, powder samples are prepared by loading and flattening into the sample well of a zero-diffraction Si plate which does not add any additional constructive interference peaks to the diffraction pattern. Additional sources of incident radiation are also used including neutrons instead of x-rays. In the case of neutrons, they do not scatter off the electron cloud, instead they scatter directly off the nuclear cross-section which varies from atom to atom[38].

2.1.2 Refinements

Having established the usefulness of XRD to unravel the structural characteristics of a material, the next step involves extracting useful information from the diffraction pattern. To extract quantitative information contained in a diffraction pattern, the data must be fit to an appropriate model. The calculated pattern from a model structure may deviate from the observed pattern with respect to peak locations, peak intensities, and defects present in the sample [39]. XRD data is commonly fit using two methods. First, a purely structural model known as a Pawley refinement [40]. Secondly, a chemical

and structural model known as a Rietveld refinement [41] is also used that accounts for the identity constituent atoms present in the material along with their occupancies and thermal parameters.

Pawley refinements are useful to obtain information regarding the lattice parameters and space group of the crystal structure, and does not require much prior knowledge. For example, no information is provided regarding the chemical species present in the material allowing peak intensities to be arbitrarily fit to the data to provide the best theoretical fit. The algorithm implemented in Pawley fits uses mathematical optimization techniques to systematically adjust the parameters of the crystal structure until the calculated diffraction pattern closely matches that of the experimental data. Its utility lies in the ability to obtain proper peak shape parameters, that are largely influenced by crystallite distribution, that may be fixed in a Rietveld refinement where the precise chemical species present in the material are accounted for.

On the other hand, a Rietveld refinement is a more comprehensive approach that simultaneously refines the crystal structure parameters and other instrumental parameters such as sample displacement and background. Unlike a Pawley refinement, a Rietveld refinement requires an initial crystal structure model. The theoretical underpinnings of this type of refinement lies in the convolution of the ideal crystal structure with the instrumental and sample related parameters. The refinement process applies a least-squares minimization algorithm that iteratively refines parameters until a convergence criterion that minimizes the difference between the observed and calculated pattern is met. In the work presented in Chapters 3, 4, and 5, both Pawley and Rietveld refinements were used extensively for the interpretation of the observed data.

2.2 Nuclear Magnetic Resonance

Nuclear magnetic resonance (NMR) is a powerful analytical technique that has revolutionized the field of molecular spectroscopy. It is widely used in various scientific disciplines including physics, chemistry, materials science, medical imaging, and biochemistry to name a few. NMR provides detailed insights into the local environments of specific elements within a material such as those investigated in this dissertation namely, ^{23}Na, ^{51}V, ^{31}P, and ^{27}Al. This experimental technique shines light on the dynamic, structural, and chemical properties of molecules making it an indispensable tool for the scientific community.

At its essence, NMR operates by exploiting a phenomenon known as Zeeman splitting, a consequence of the interaction between nuclear magnetic moments and an external magnetic field. A schematic of the Zeeman interaction is shown in Figure 2.2. This interaction arises from the fact that nuclei posses an intrinsic quantum spin number I. This quantum spin number can be further split into $2(I + \frac{1}{2})$ magnetic spin states ($m_i = -I, ..., +I,$, integer steps)[42]. In the absence of an external magnetic field, these nuclear magnetic spins are randomly aligned but when placed under an applied external magnetic field, these magnetic spin states undergo Zeeman splitting giving an energy difference of:

$$\Delta E = \hbar \gamma_I B_0 = \hbar \omega_0 \tag{2.2}$$

where $\hbar$ is the reduced Planck's constant, γ_I is the gyromagnetic ratio of the nucleus, and B_0 is the strength of the applied magnetic field strength. The gyromagnetic ratio is a fundamental property of the nucleus that characterizes the strength of the magnetic moment associated with the particles intrinsic spin. Note that the product of the gyromagnetic ratio and applied field is known as the Larmor frequency (ω_0). The Larmor frequency

refers to the precessional frequency of a magnetic moment in a magnetic field. Figure 2.2 provides a schematic for Zeeman splitting in the case a spin $\frac{1}{2}$ (non-quadrupolar) nucleus. By irradiating a nuclei with a radiofrequency (RF) pulses in NMR at the Larmor frequency, it is possible to induce transitions between different energy states of the magnetic moments allowing for the measurement of spectroscopic information. It serves as a key parameter in the design and interpretation of NMR experiments covered in this dissertation.

The chemical shift (δ) is a crucial, dimensionless, quantity that expresses the difference in resonant frequency of a nucleus in a sample relative to a reference standard for which the chemical shift is well defined (and often as 0 ppm). This chemical shift is calculated as follows:

$$\delta = \frac{(\omega - \omega_{ref})}{\omega_{ref}} * 10^6 \tag{2.3}$$

where ω_{ref} is the angular freqency of the reference compound. This chemical shift interaction stems from the shielding of the applied magnetic field by the electrons around the nucleus. The total Hamiltonian representing NMR interactions can be written as:

$$\hat{H} = \hat{H}_{ext} + \hat{H}_{int} \tag{2.4}$$

$$\hat{H}_{ext} = \hat{H}_0 + \hat{H}_1 \tag{2.5}$$

here, $\hat{H}_0$ is the Zeeman term and $\hat{H}_1$ describes the resulting interaction with the RF field. The internal contribution contains terms for the sum of the contributions stemming from chemical shift interactions ($\hat{H}_{CS}$), scalar couplings between two nuclei ($\hat{H}_{SC}$), dipolar interactions ($\hat{H}_D$, covered in section 2.2.2), hyperfine interactions ($\hat{H}_{hyp}$, see 2.2.2), and quadrupolar interactions ($\hat{H}_Q$, see 2.2.3) given as:

Nucleus	Spin (I)	Quadrupole Moment, Q (b)	Gyromagnetic Ratio (γ_l)	Natural Abundance (%)
^{23}Na	3/2	0.104	7.080	100
^{51}V	7/2	−0.043	7.049	99.8
27Al	5/2	0.147	6.976	100
^{31}P	1/2	—	10.839	100

Table 2.1: NMR properties of the nuclei investigated in this dissertation[43]. Note: The electric quadrupole moment is given in units of the barn (1 barn = 10^{-28} m^2)

$$\hat{H}_{int} = \hat{H}_{CS} + \hat{H}_{SC} + \hat{H}_D + \hat{H}_{hyp} + \hat{H}_Q \tag{2.6}$$

The key NMR properties of the nuclei probed in this work are summarized in Table 2.1. The dominant interactions covered in this work consist primarily of hyperfine and quadrupolar interactions of the ^{23}Na, ^{51}V, ^{31}P.

2.2.1 Magic Angle Spinning for Solid-State NMR

Magic angle spinning (MAS), the controlled spinning of solids at kHz frequencies at the "magic angle" of 54.74°, is a technique utilized in solid-state NMR (ssNMR) spectroscopy to address challenges faced during the study of crystalline materials [44]. While liquid NMR excels in the analysis of liquid samples, the investigation of solid samples present unique challenges associated with the lack of molecular mobility and inherent anisotropy present in crystalline materials. In liquid state NMR, the rapid Brownian motion of the molecules results in an effective time-averaging of the anisotropic interactions that is not achieved in crystalline or solid samples making MAS unnecessary for liquid samples. In a MAS experiment for crystalline materials, rotation of the sample at the magic angle eliminates some of the anisotropic interactions leading to more interpretable NMR spectra. Interactions averaged out by MAS include chemical shift anisotropy (CSA), dipolar couplings between nuclear spins, and to a certain extent

quadrupolar interactions.

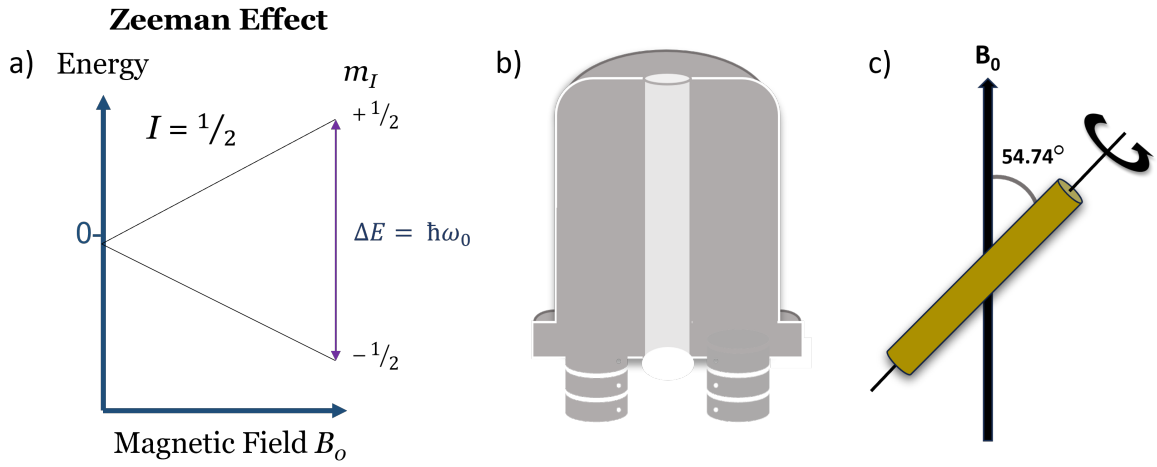

Figure 2.2: a) Schematic of the Zeeman splitting for a spin 1/2 nucleus. b)NMR magnet schematic and c) depiction of the magic angle with respect to the external magnetic field B_0.

To enhance the extraction of meaningful information from ssNMR spectra, especially when dealing with anisotropic interactions, the MAS technique is commonly employed. Anisotropic interactions in ssNMR often exhibit an orientation dependence described by the mathematical expression $3cos^2\theta - 1$ where θ represents the orientation of the nucleus in relation to the applied magnetic field. The principle behind MAS is that under sufficiently fast spinning conditions ($\approx$ 3 - 4 times the magnitude of the anisotropic interaction)[45], a sharp resonance at the isotropic chemical shift is observed. This rapid spinning averages out the orientation dependence of the anisotropic interaction(s). At slow (relative to the size of the anisotropic interaction) MAS speeds, the NMR signal appears broad with the anisotropic effects more pronounced and broken up into spinning sidebands separated by the MAS frequency. Due to the paramagnetic and quadrupolar nature of the compounds studied in this work (with anisotropic interaction strenghts on the order of tens of MHz), all spectra were acquired under fast MAS, with spinning speeds ranging from 20 to 50

kHz.

2.2.2 Paramagnetic Interactions

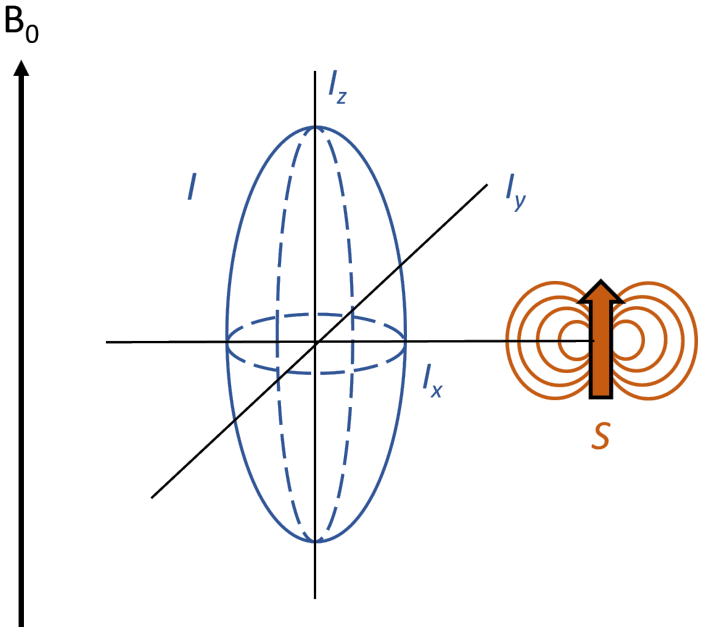

Figure 2.3: Representation of the hyperfine (paramagnetic) interaction.

To understand hyperfine (paramagnetic) interactions one must first understand the nature of dipolar coupling. Dipolar coupling refers to the magnetic interaction between nuclear magnetic moments (usually spins) associated with a nearby nuclei in a sample and arises from magnetic dipole-dipole interactions. In paramagnetic systems where unpaired electrons are present, much like the vanadium containing compounds studied in this work, the local magnetic field experienced by a nuclei is influenced by the electronic spin distribution. Electrode materials comprising of open-shell transition metal (TM) species feature strong hyperfine (i.e. paramagnetic) interactions between unpaired TM electrons and the nuclei under observation resulting in a broadened NMR spectra, an example is shown in Figure 2.3. Paramagnetic couplings between the nucleus and sur-

rounding TM species comprise through-space electron-nuclear dipolar interactions and through-bond Fermi contact interactions. The electron-nuclear dipolar coupling strength depends on the spatial proximity between the two spins and the orientation of the vector relating those relative to the external magnetic field. It can be described by the following Hamiltonian:

$$H_{e-n} = \langle \mu_e \rangle \cdot \mathbf{D_{e-n}} \cdot \mu_{\mathbf{N}} \tag{2.7}$$

where $\mathbf{D_{e-n}}$ is the dipolar coupling tensor, μ_N is the magnetic moment of the nucleus of interest, and $\langle \mu_e \rangle$ is the time averaged magnetic moment of the electron. In the case where the magnetic moment of the electron is isotropic, the coupling results in changes of the lineshape of the NMR spectra seen as broadening and asymmetry but does not lead to any shift of the resonant frequency. However, coupling to an anisotropic magnetic moment leads to an isotropic 'pseudocontact' shift and line broadening.

Fermi contact interactions, named after the Italian physicist Enrico Fermi, between the nucleus of interest and neighboring TMs are additive and the total Fermi contact shift (δ_{FC}) may be calculated as follows [46]:

$$\delta_{FC} = \frac{10^6 \mu_0 \mu_B \mu_N g_e g_N}{3\hbar\omega_0} \Phi \mid \psi^{\alpha-\beta}(R_N) \mid^2 \tag{2.8}$$

where μ_N is the nuclear magneton, g_N the nuclear g-factor, and $\mid \psi^{\alpha-\beta}(R_N) \mid^2 = \rho(r=0)$ the unpaired electron spin density at the nuclear position. It should be noted that $\psi^{\alpha-\beta}(R_N)$ is the output of CRYSTAL calculations with all spins ferromagnetically aligned, covered in detail in the following sections 2.3.1 and 2.3.2. The factor Φ scales the computed shifts to a value consistent with the magnetic state of the system at the temperature at which the corresponding to NMR experiments were performed. The Fermi contact shift is also defined as:

$$\delta_{FC} = -\sum_i \frac{A_i}{\omega_0 \hbar} \langle S_z \rangle \tag{2.9}$$

$$\langle S_z \rangle = -\frac{B_0}{\mu_0 g N_A \mu_B} \chi_M \tag{2.10}$$

Where A_i is the isotropic hyperfine coupling constant, ω_0 is the Larmor frequency. $\langle S_z \rangle$ is the time-averaged value of the z-component of the electron spin and is proportional to the external magnetic field strength, B_0. Other parameters include the magnetic susceptibility χ_M, the permeability of free space μ_0, the Bohr magneton μ_B, the electron g-factor (assumed equal to 2), and Avogadro's number N_A[47]

Alternatively, δ_{FC} is proportional to the electron spin density at the position of the nucleus, and each paramagnetic center in the vicinity of the nucleus of interest (roughly 5 Å) transfers a finite amount of unpaired electron spin density to its s orbital via a spin density transfer pathway denoted P_i and bridging O $2p$ orbitals. For example, P_i pathways for a Na local environment in the NASICON structure is shown in Figure 2.4.

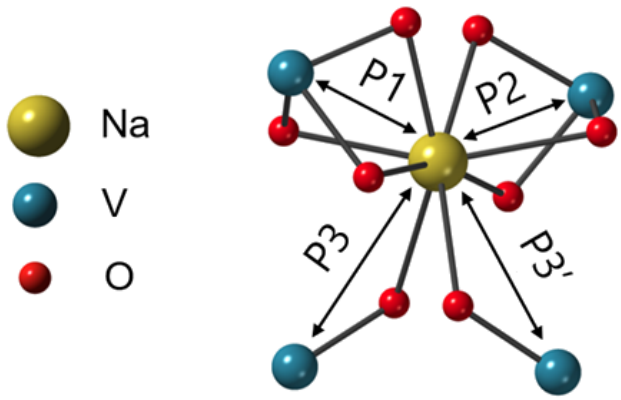

Figure 2.4: Example of spin density transfer pathways P1, P2, P3 and P3' from the d orbitals of neighboring TM species to the central Na s orbital and bridging O $2p$ orbitals. The P_i pathways differ in the TM-Na distance and the TM-O-Na bond angle.

The total Fermi contact shift is obtained from the sum of all individual TM-O-Na bond

pathway shift contributions (P_i)[48, 49, 50].

$$\delta_{FC} = \sum_i P_i \tag{2.11}$$

The extent of spin transfer along each bond pathway (i.e. P_i) depends on the degree of orbital overlap along the bond pathway between the paramagnetic center and the nucleus of interest. For 3d TM-containing compounds, much like the ones covered in this dissertation, the pseudocontact shift is much smaller than the Fermi contact shift and may be neglected. In this case the overall isotropic shift $\delta_{iso} \approx \delta_{FC}$

2.2.3 Quadrupolar Interaction

Another important interaction for the compounds studied here is the quadrupolar interaction. In NMR, nuclei with a non-zero nuclear quadrupole moment present in nuclei with spin quantum numbers $I \geq \frac{3}{2}$ experience a complex interaction due to the non-spherical charge distribution at the position of the nucleus which, much like the paramagnetic interaction, serves to broaden and split NMR spectral lines providing useful information regarding molecular environments and dynamics. The Hamiltonian for the quadrupolar component is given as:

$$\hat{H} = \frac{eQ}{2I(2I-1)\hbar}\hat{I} \cdot \mathbf{V} \cdot \hat{I} \tag{2.12}$$

where e is the electron charge, Q is the nuclear quadrupole moment, $\hat{I}$ is the nuclear spin angular momentum operator, and V is the second-rank EFG tensor which describes the nuclear charge distribution and local electronic structure. In isotropic liquid samples, quadrupolar interactions are significantly reduced compared to solid-state NMR (ssnMR) owing to fast molecular motion. Molecules undergo rapid isotropic motion leading to fast

reorientation and this rapid motion averages the spatial variation of the EFG experienced by quadrupolar nuclei to zero. In solid samples, the environments experienced by these nuclei can have anisotropic EFGs that contribute significantly to the quadrupolar interaction. This EFG tensor is specified by two terms: eq, the magnitude of the EFG tensor and η_Q, the asymmetry parameter given by:

$$eq = V_{zz} \tag{2.13}$$

$$\eta_Q = \frac{V_{xx} - V_{yy}}{V_{zz}} \tag{2.14}$$

Here, V_{ii} represent the principal components of the EFG tensor with $\mid V_{zz} \mid \geq \mid V_{xx} \mid \geq \mid V_{yy} \mid$. The quadrupolar coupling constant C_Q is a parameter that characterizes the strength of the quadrupolar interaction and is given by:

$$C_Q = \frac{e^2qQ}{\hbar} = \frac{eQ}{\hbar}V_{zz} \tag{2.15}$$

where the units of C_Q are typically expressed in hertz (Hz), kilohertz (kHz), and if strong enough in megahertz (MHz) representing the frequency associated with the quadrupolar interaction. C_Q influences the splitting and broadening of spectral lines for nuclei with a non-zero quadrupole moment and the magnitude determines the extent of these effects. Understanding the quadrupolar coupling constant is crucial for interpreting quadrupolar effects in NMR spectra of solid samples. In this work, ^{23}Na ($I = 3/2$), and ^{51}V ($I = 7/2$) are the nuclei investigated via solid-state NMR with all exhibiting strong quadrupolar interactions. The second−order quadrupolar shift, in ppm is given by:

$$\delta_Q = -\frac{1 \times 10^6}{20}\frac{3}{\nu_0}\left(\frac{3C_Q}{2I(2I-1)}\right)^2\left(\frac{1+\frac{\eta_Q^2}{3}}{\nu_0}\right) \tag{2.16}$$

where $\nu_0 = \frac{\omega_0}{2\pi}$. Considering ^{23}Na ($I = 3/2$) as an example, the Zeeman states without the quadrupolar interaction would be fourfold degenerate corresponding to $m_l = -3/2, -1/2, 1/2, 3/2$. The presence of the quadrupolar interaction lifts this degeneracy leading to a splitting of these states into sublevels as shown in Figure 2.5.

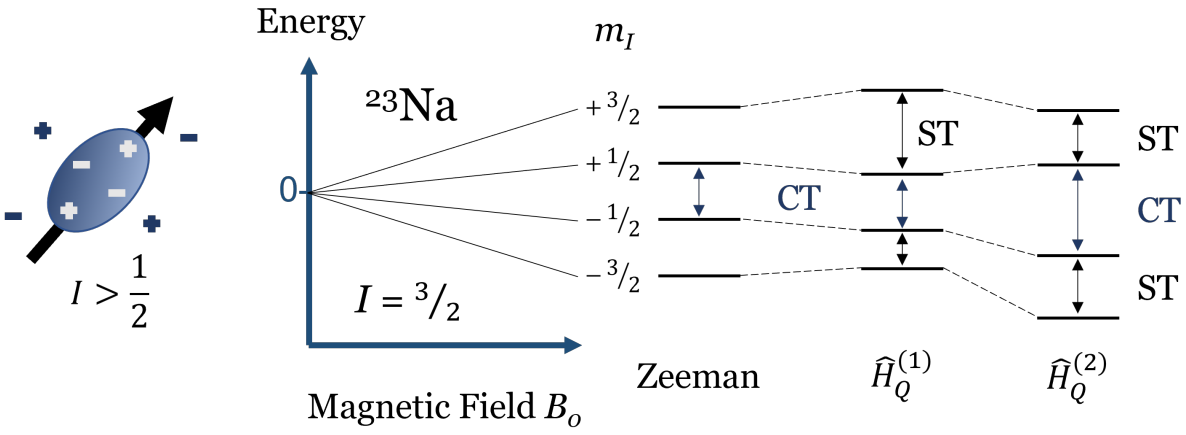

Figure 2.5: Zeeman splitting and quadrupolar effects in a $I = 3/2$ nucleus (^{23}Na in this case)

These sublevels can be broken down into its first and second order contributions and consist of the central transition (CT) ($m_l = 1/2 \leftrightarrow 1/2$), which is unaffected to the first order, and satellite transitions (ST) which are affected, the full Hamiltonian may be represented as:

$$\hat{H}_Q^{full} = \hat{H}_Q^{(1)} + \hat{H}_Q^{(2)} + \cdots + \hat{H}_Q^{(i)} \tag{2.17}$$

If cases where the quadrupolar interaction is weak (i.e. $\leq 10\%$ of Zeeman splitting) only the first order transition may be considered and the ST's may be partially averaged by MAS [42]. On the other hand, the second-order contribution is inversely proportional to the magnetic field strength and may be minimized by acquiring NMR data at higher magnetic fields. Finally, seeing as the broadening resulting from the paramagnetic in-

teraction is lessened at lower magnetic field strengths and the quadrupolar interaction is lessened at higher magnetic fields, for samples that contain both quadrupolar and paramagnetic species (like those covered in this work) requires an optimization of which magnetic field to choose and multiple may be investigated before choosing the magnetic field that gives the best spectral resolution. The experimentally observed shift (δ_{obs}) is then the sum of the field independent isotropic shift ($\delta_{iso} \approx \delta_{FC}$) and the field dependant quadrupolar induced shift (δ_Q) given as:

$$\delta_{obs} = \delta_{iso} + \delta_Q \tag{2.18}$$

The second-order quadrupolar shift (δ_Q), while generally smaller than the isotropic shift (δ_{iso}), is not always negligible and needs to be accounted for when interpreting NMR spectra.

2.2.4 NMR Experiments

The paramagnetic and quadrupolar interactions present in the materials covered in Chapters 3, 4, and 5, makes the analysis of NMR data non-trivial. Although the quadrupolar interaction may induce large shifts, it is the hyperfine interaction that typically dominates. For example, in Chapter 3, this paramagnetic interaction leads to chemical shifts on the order of thousands of ppm. The experimental techniques used to address this issue will be discussed here. It should be noted that typical quadrupolar NMR experiments (e.g. multiple-quantum MAS or MQMAS) were not performed as they require longer RF pulsing times and would make detection of the fast relaxing paramagnetic NMR signals unattainable.

Two fundamental pulse sequences widely employed in NMR experiments are the zero-go (ZG) and the Hahn-Echo pulse sequences. Both pulse sequences have been used

extensively in this dissertation and will be outlined below.

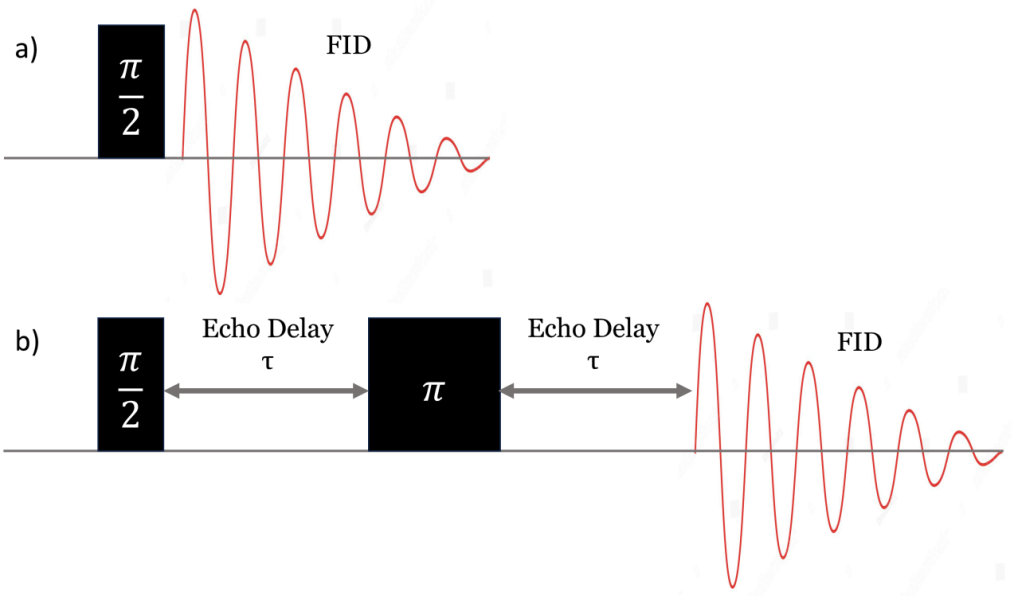

Figure 2.6: a) Pulse sequence for zero-go (ZG) pulse acquisition NMR experiment and b) the pulse sequence for a Hahn-echo NMR measurement.

Zero-Go Pulse Sequence

In the context of solid-state NMR, the ZG pulse sequence is considered on of the most basic ssNMR experiments and serves as a foundation for which other pulse sequences build off of by incorporating additional pulses, gradients, delays, or variations in pulse timings. The ZG pulse sequence starts with the establishment of initial magnetization within the sample, this is achieved when the sample contained in a rotor is placed in the magnetic field (B_0) created by the NMR magnet which aligns nuclear spins along the direction of B_0. A 90° RF pulse is applied perpendicular to the direction of B_0 creating transverse magnetization. After the 90° pulse, the nuclear spins precess around B_0 field at their characteristic Larmor frequencies creating a time-domain NMR signal known as the Free Induction Decay (FID) (Figure 2.6) that contains information regarding nuclear spin interactions present within the sample.

Due to hardware limitations, the FID cannot be recorded immediately following the transverse magnetization pulse. The delay between pulse and acquisition before data may be recorded is known as "dead time." To obtain meaningful ssNMR information, the time-domain FID must be Fourier transformed into the frequency domain. The Fourier transformed FID is what is seen in a typical NMR spectrum and represents the frequency distribution of nuclear spins in the sample. Fourier transformation of the FID is displayed as a plot of signal intensity (amplitude) versus chemical shift (frequency). Peaks in an NMR spectrum correspond to different resonating nuclei and their positions (i.e. chemical shifts) where intensities convey information regarding site populations and specific local environments of the nuclei under investigation within the sample.

To maximize the resolution (i.e. signal-to-noise ratio) of the Fourier transformed NMR spectrum, multiple scans are typically used with each scan corresponding to one pulse and the measurement of the resulting FID. A given NMR experiment begins with the optimization of the pulse length. This is achieved by monitoring a given spin's nutation curve and is done by incrementally increasing the signal intensity as a function of pulse length. An example nutation curve is given in Figure 2.7, it is a sinusoidal curve that details signal intensity as a function of pulse length [51]. For spin 1/2 nuclei ($C_Q = 0$), the optimal 90° RF pulse is determined by finding the pulse length which gives the largest amplitude. However, quadrupolar nuclei in high C_Q environments may have much faster nutation frequencies [51]. As a result, exciting multiple quadrupolar nuclei within a sample uniformly may require shorter pulse lengths on the order of 30-45°.

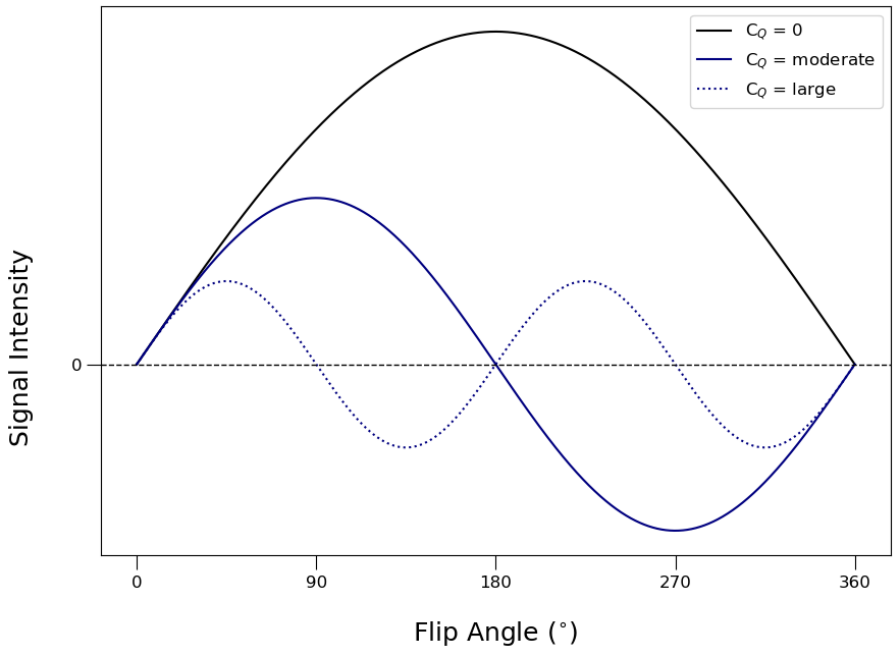

Figure 2.7: Nutation curve for spins in environments with varying quadrupolar coupling constant magnitudes.

Hahn-Echo Pulse Sequence

The Hahn-echo (spin-echo) pulse sequence originally developed by the physicist Erwin Hahn in the 1950's expands on the ZG pulse sequence where the initial 90° RF pulse is followed by a waiting time, τ, during which the magnetization is allowed evolve. Similar to the ZG pulse, after the 90° RF pulse, the nuclear spins precess about B_0 at their characteristic Larmor frequency creating an FID. As shown in Figure 2.6b, after the waiting time (τ), a 180° RF pulse is applied which inverts the direction of the rotating magnetization vector in the transverse plane followed by another identical τ delay that allows the magnetization to be refocused before the FID is recorded. The additional 180° RF pulse allows for the reduction of magnetic field inhomogeneities on the NMR spectrum. The τ delays must be rotor-synchronized (i.e. at an integer multiple of the MAS period) in order to retain information regarding anisotropic interactions [42]. The Hahn-echo pulse sequence is valuable for measuring T_2 relaxation times, which represent

the time it takes for the transverse magnetization to decay due to interactions between neighboring nuclear spins (spin-spin relaxation). T_1 relaxation times, on the other hand, are typically measured using other pulse sequences such as the inversion recovery or saturation recovery sequences. T_2 relaxation measurements will be discussed in the following section but none of the work in this dissertation utilized inversion recovery experiments and will not be outlined here. For information regarding T_1 relaxation techniques the reader is referred to the following references [52, 53].

2.2.5 Transverse T_2 Relaxation

Upon application of the transverse 90° RF pulse, random fluctuations of the local electric and magnetic field experienced by the nuclei under investigation leads to variations in the immediate precession frequency of their spins and the subsequent loss of coherence, known as spin dephasing within the xy plane. This phenomenon is referred to as relaxation which contributes to a gradual decline in the intensity of the NMR signal over time. The extent of spin dephasing in the xy plane may be quantified using the transverse relaxation time (T_2) using the Hahn-echo (spin-echo) experiment discussed in the previous section.

The overall relaxation time is denoted by T_2' and is particularly short in samples containing paramagnetic centers. The τ delay following the 180° RF pulse in a Hahn-echo sequence leads to an inevitable loss in signal and must be accounted for in order to extract quantitative information from the NMR spectrum. This may be achieved by scaling the NMR signal intensity by a relaxation factor given by the following expression:

$$f = exp(\frac{-T}{T_2'}) \tag{2.19}$$

where T is the total relaxation time between the excitation RF pulse and the start of the

FID recording. The use of the scaling factor is especially important for multi-component mixtures where different species may have significantly different T_2 values, leading to differential relaxation rates and potentially misleading intensity ratios if not correctly accounted for. For the compounds investigated in Chapters 3, 4, and 5, both the paramagnetic and quadrupolar interactions serve to shorten the T_2 relaxation. Understanding and accounting for these effects enables accurate quantitative NMR analyses.

2.3 Computational Methods

First principles calculations form the cornerstone of modern quantum mechanical simulations providing an invaluable tool for understanding the ground state structure and magnetic properties of a material. Due to the reduced spectral resolution and possible signal overlap caused by paramagnetic and quadrupolar broadening, first principles calculations of NMR parameters are often necessary to interpret experimental data. This dissertation utilizes first principles calculations performed by collaborators to predict NMR parameters and magnetic couplings as implemented in the CRYSTAl17 software package. The theoretical background of these first principles calculations will be briefly reviewed, however, since these calculations were performed by collaborators the methodology will not be described thoroughly. Rather, the focus will be on the analysis of computational outputs.

2.3.1 CRYSTAL17 Calculations of Paramagnetic NMR Parameters

CRYSTAL17 is a widely-used computational package for ab initio quantum mechanical calculations of the properties of crystalline materials. It provides a powerful suite

of tools for modeling the electronic structure and properties of periodic systems, including crystals, surfaces, and polymers. Developed by the group of Prof. Roberto Dovesi at the University of Torino, CRYSTAL17 offers a comprehensive set of methods based on density functional theory (DFT), Hartree-Fock theory, and hybrid functionals. Its capabilities include geometry optimization, vibrational analysis, electronic structure calculations, and the prediction of a wide range of physical properties, such as energies, forces, and spectroscopic data. CRYSTAL17 is known for its accuracy, efficiency, and versatility, making it an indispensable tool for researchers in materials science, chemistry, and related fields. Here, CRYSTAL17 is used to predict ^{23}Na and ^{31}P ssNMR paramaters in Chapter 3.

Spin-unrestricted hybrid density functional theory (DFT) / Hartree Fock (HF) calculations were performed using the CRYSTAL17 all-electron linear combination of atomic orbital code [46, 54] to determine ^{23}Na and ^{31}P NMR parameters in $\alpha-Na_3V_2(PO_4)_3$ ($\alpha-$NVP) structure discussed in Chapter 3. Two spin-polarized exchange-correlation functionals based upon the B3LYP form [55, 56, 57, 58], and with Fock exchange weights of F_0 = 20 % (H20) and 35 % (H35) were chosen for their good performance for the electronic structure and band gaps of transition metal compounds [59, 60] (H20), and for their accurate description of the magnetic properties of related compounds [61, 62, 63] (H35). Besides, previous studies have shown that the hyperfine shifts calculated with the H20 and the H35 functionals on similar compounds are in good agreement with experiment [48, 64, 65]. All-electron atom-centered basis sets comprising fixed contractions of Gaussian primitive functions were employed throughout. Two types of basis sets were used: a smaller basis set (BSI) was employed for structural optimizations, and a larger basis set (BS-II) was used for computing ^{23}Na and ^{31}P NMR parameters which require an accurate description of the occupation of core-like electronic states. For BS-I, individual atomic sets are of the form (15s7p)/[1s3sp] for Na, (20s12p4d)/[1s4sp2d] for V,

(14s6p1d)/[1s3sp1d] for O, and (16s8p1d)/[1s3sp1d] for P where the values in parentheses denote the number of Gaussian primitives and the values in square brackets the contraction scheme. All BS–I sets were obtained from the CRYSTAL online repository and were unmodified from their previous use in a broad range of compounds [46]. For BS-II, modified IGLO-III (10s6p2d)/[6s5p2d] and (11s7p3d)/[7s6p3d] sets were adopted for O and P, respectively, a flexible and extended TZDP-derived (11s7p)/[7s3p] set was used for Na, and an Ahlrichs DZP-derived [66] (13s9p5d)/[7s5p3d] was adopted for V. The O and P BS–II sets are consistent with those used in a recent study on lithium transition metal phosphates [65]. NMR parameters were computed on the fully optimized (atomic positions and cell parameters) $\alpha-$NVP structure proposed by Chotard et al [34].

All first principles structural optimizations were carried out in the ferromagnetic (FM) state, after removal of all symmetry constraints (within the P1 space group) and using the H20 and H35 hybrid functionals. The 240 atom cell proposed by Chotard et al.[34] was used throughout. Structural optimizations were pursued using the quasiNewton algorithm with RMS convergence tolerances of 10^{-7} , 0.0003, and 0.0012 au for total energy, root-mean-square (rms) force, and rms displacement, respectively. Tolerances for maximum force and displacement components were set to 1.5 times the respective rms values. Sufficient convergence in total energies and spin densities was obtained by application of integral series truncation thresholds of 10^{-7} , 10^{-7} , 10^{-7} , 10^{-7} , and 10^{-14} for Coulomb overlap and penetration, exchange overlap, and g- and n-series exchange penetration, respectively, as defined in the CRYSTAL17 documentation [46]. The final total energies and spin and charge distributions were obtained in the absence of any spin and eigenvalue constraints. NMR parameters were obtained on ferromagnetically aligned supercells, and on supercells in which one V spin was flipped, using BS-II sets and a method identical to that described in Middlemiss et al.'s work [64]. Anisotropic Monkhorst-Pack reciprocal space meshes [67] with shrinking factors 6 9 3 were used

for both H20 and H35 calculations. The lattice parameters for the $\alpha-$NVP structures relaxed using the H20 and H35 functionals are compared to the experimental (EXP) unit cell parameters [34] Appendix B of Chapter 3.

2.3.2 Comparing first principles (CRYSTAL17) and experimental NMR parameters

The computed hyperfine (paramagnetic) NMR properties are obtained at 0 K for NVP supercells containing ferromagnetically-aligned open-shell V^{3+} ions. To compare CRYSTAL17 calculation results with experimental data acquired at room temperature, the computed shifts must be subsequently scaled to a value consistent with the paramagnetic state of the system at the temperature of the NMR experiments, using a magnetic scaling factor of the form:

$$\Phi(T_{exp}) = \frac{\langle M(T_{exp})\rangle}{M_{sat}} \tag{2.20}$$

where M_{sat} is the saturated (ferromagnetic) V^{3+} magnetic moment at 0 K, and $\langle M(T_{exp})\rangle$ the bulk average magnetic moment measured at the sample experimental temperature, T_{exp}. Here, T_{exp} is set to 310 K to account for frictional heating caused by fast (30 kHz) sample rotation during NMR data acquisition. The magnetic scaling factor in eq. (2.20) can be evaluated from the experimental magnetic properties of the material:

$$\Phi(T) = \frac{B_0\mu_{eff}^2}{3k_b g_e \mu_B S(T-\Theta)} \tag{2.21}$$

where B_0 is the external magnetic field, μ_{eff} is the effective magnetic moment per V site, k_b is Boltzmann's constant, g_e is the free electron g-value, μ_B is the Bohr magneton, S is the formal spin of V^{3+} (d^2, $S = 1$), and Θ is the Weiss constant. A derivation of eq.

(2.21), starting from the Brillouin function in the low field, high temperature limit, can be found in a previous study by Kim et al [48]. Eq. (2.21) uses the 'spin-only' expression for the magnetic moment and is only strictly valid when the orbital angular momentum is quenched [68]. Yet, for systems where spin orbit coupling effects are negligible, such as NVP, the spin-only expression is a good approximation to the true magnetic behavior of the system. The experimental inverse magnetic susceptibility vs. temperature curve obtained for NVP is shown in Appendix B (Figure 3.10). From these data, an effective magnetic moment per V site $\mu_{eff} = 3.77\mu_B$ and a Weiss temperature $\Theta = -54.75$ K are obtained. A bulk magnetic scaling factor $\Phi = 0.030755$, is obtained for T = 310 K and $B_0 = 7.05$ T. This value was used to scale the computed ^{23}Na and ^{31}P NMR parameters listed in Chapter 3 of this dissertation.

2.4 Magnetometry

Sodium-ion cathode materials typically contain redox-active paramagnetic centers necessary for the normal operation of a battery. During cycling, these paramagnetic centers undergo oxidation state changes which may affect the materials properties, including its magnetic response. In this regard, magnetometry is a versatile experimental technique employed to measure and characterize the magnetic properties of a given material. This technique encompasses various methods for studying magnetization including a materials magnetic susceptibility (χ). This technique is utilized in Chapter 3 of this dissertation to characterize the paramagnetic behavior of $Na_{3+y}V_{2-y}Mg_y(PO_4)_3$ cathodes in order to scale the computed NMR parameters discussed in Section 2.3.2 to the experimentally relevant room temperature parameters. A basic introduction to the theoretical background of magnetometry will be provided in this section.

The magnetic susceptibility of a material is a fundamental property that quantifies

the response of a material to an applied magnetic field, which, in turn provides insights into its magnetic behavior. It is defined as the ratio of the magnetization (M) induced in a material to the applied magnetic field (H), expressed mathematically as:

$$\chi = \frac{M}{H} \tag{2.22}$$

this dimensionless quantity reflects the materials ability to become magnetized in response to an external magnetic field. The magnetic susceptibility is a key parameter in understanding the interaction between magnetic moments and the applied field, much like in NMR experiments.

In the context of paramagnetic materials, the magnetic susceptibility (χ) is often described by the Curie law:

$$\chi = \frac{C}{T} \tag{2.23}$$

where C is the Curie constant and T is the absolute temperature. The Curie law indicates the propensity of paramagnetic materials to align their magnetic moments in response to thermal excitation. The Curie-Weiss law is an extension of the Curie law that introduces a temperature-dependant parameter, the Weiss constant (Θ), which accounts for long-range interactions among magnetic moments. It should also be noted that paramagnetic systems exhibit a diamagnetic response (χ_{dia}) to an applied field. Although relatively small in paramagnetic systems, this diamagnetic contribution to the magnetic susceptibility should still be included in the analysis. The relationship for the magnetic susceptibility then becomes,

$$\chi = \frac{C}{T - \Theta} + \chi_{dia} \tag{2.24}$$

Here, the Weiss constant Θ characterizes the critical temperature above which thermal disorder dominates resulting in a reduction of magnetic alignment. Values of the Weiss constant corresponds to a ferromagnetic material when $\Theta > 0$ and antiferromagnetic when $\Theta < 0$. To obtain the values of the Curie and Weiss constants, a plot of $\frac{1}{\chi - \chi_{dia}} vs. T$ may be fit with the slope corresponding to $1/C$ and the intercept representing $-\Theta/C$. Both of these parameters will be required to determine the effective magnetic moment (μ_{eff}) of paramagnetic materials.

The effective magnetic moment (μ_{eff}) describes the overall magnetic behavior arising from the alignment of individual magnetic moments within the material and is related to the Weiss and Curie constants through the expression,

$$\mu_{eff} = \sqrt{C(T - \Theta)} \tag{2.25}$$

Considering the total angular monentum of the electrons transition metal ions with partially filled d or f orbitals, the effective magnetic moment may also be represented as:

$$\mu_{eff} = \sqrt{8C} \tag{2.26}$$

this value may then be compared to the spin-only magnetic moment (μ_{SO}) given as:

$$\mu_{SO} = 2\sqrt{S(S+1)} \tag{2.27}$$

where S is the spin quantum number. This equation is only valid when spin-orbit coupling is small. In Chapter 3 of this work, magnetic susceptibility data was taken at a set field against temperature in both zero-field cooled (ZFC) and field-cooled (FC) manner. ZFC corresponds to cooling the sample to approximately 2K in the absence of a magnetic field and FC is the same process with the exception that it cools in the presence of a magnetic

field.

2.5 Electrochemical Cycling

In a galvanostatic cycling experiment the battery is subjected to a constant electrical current between set upper and lower cutoff voltage limits [69]. For Na-ion batteries upper cutoff voltage limits are set to to reduce side reactions arising from electrolyte decomposition that may occur at higher voltages [70]. This controlled current induces charge-discharge reactions within the material and various performance metrics can be characterized including: cyclic stability, capacity retention, rate capability, and insight into potential degradation mechanisms. The data from a galvanostatic cycling experiment may be analyzed further via differential capacity analysis to enhance our understanding of the electrochemical processes and underlying mechanisms taking place during (dis)charge of the battery. This is done by taking the derivative of the capacity with respect to voltage (dQ/dV). In the context of this dissertation, plots of dQ/dV vs. voltage show peaks or changes in the curve corresponding to different electrochemical processes. These changes in dQ/dV may indicate transitions between different phases during electrochemical cycling on charge or discharge as discussed in detail in Chapter 5.

Another electrochemical cycling technique used extensively in this work is the Galvanostatic Intermittent Titration Technique (GITT). The experiment begins with the application of a constant current pulse to the electrode for a predetermined amount of time causing a change in the electrode potential. After the current pulse, the system is allowed to relax, and the potential change is recorded until it stabilizes at equilibrium. This process is repeated throughout the charge−discharge cycle and provides valuable insight into diffusion kinetics, overpotentials associated with Na insertion/ extraction, and has been used to investigate the interface mobility of phase-transformation electrodes in

the two-phase region [71].

Chapter 3

Impact of aliovalent Mg substitution on the properties of NASICON $Na_{3+y}V_{2-y}Mg_y(PO_4)_3$ cathodes

Vanadium multiredox-based NASICON-$Na_zV_{2-y}M_y(PO_4)_3$ ($3 \leq z \leq 4$; M = Al^{3+}, Cr^{3+}, and Mn^{2+}) cathodes are particularly attractive for Na-ion battery applications due to their high Na insertion voltage (> 3.5 V vs. Na^+/Na^0), reversible storage capacity ($\approx$ 150 mAh/g), and rate performance. However, their practical application is hindered by rapid capacity fade due to bulk structural rearrangements at high potentials involving complex redox and local structural changes. To decouple these factors, a series of Mg^{2+}-substituted $Na_{3+y}V_{2-y}Mg_y(PO_4)_3$ ($0 \leq y \leq 1$) cathodes is studied for which the only redox-active species is vanadium. While X-ray diffraction (XRD) confirms the formation of solid solutions between the y = 0 and 1 end members, X-ray absorption spectroscopy and solid-state nuclear magnetic resonance reveal a complex evolution of the local structure upon progressive Mg^{2+} substitution for V^{3+}. Concurrently, the intercalation voltage rises from 3.35 to 3.45 V, due to increasingly more ionic V−O bonds, and the sodium

(de)intercalation mechanism transitions from a two-phase for y $\leq$ 0.5 to a solid solution process for y $\geq$ 0.5, as confirmed by in operando XRD, while Na-ion diffusion kinetics follow a nonlinear trend across the compositional series. In this work structural and electrochemical characterization was performed in collaboration with the group of Premkumar Senguttuvan. The theoretical VASP calculations performed by the group of Swapan K. Pati and Crystal calculations werer performed by Clément group members Aryan Zaveri and Alexis Manche.

3.1 Introduction

Over the past decade, a large number of Na-ion electrode and electrolyte materials have been discovered, in part thanks to the materials design knowledge gained from earlier investigations of Li-based systems and the similar properties of Li and Na alkali metals. However, the exploration of suitable Na-ion cathodes with high energy density, good rate performance, and long cycle life remains critical. To this end, NA SuperIonic CONductor (NASICON) type phosphate cathodes are particularly appealing because of their high insertion voltages and good sodium diffusivity, as well as excellent structural and thermal stabilities [72].

Earlier studies on $Na_3M_2(PO_4)_3$ (M = Ti, V, Cr, and Fe) [73, 74, 75, 76] have reported a maximum reversible exchange of two moles of Na per formula unit (pfu), corresponding to a one-electron redox process per transition metal center, leading to moderate charge storage capacities of $\approx$ 100–120 mAh/g. One obvious avenue to improve the capacity of NASICON phosphate cathodes is to introduce multielectron redox centers to enable the exchange of a larger number of sodium ions in the framework. From this viewpoint, the $Na_3V_2(PO_4)_3$ (NVP) cathode has received a lot of attention as V^{3+} can, in theory, undergo a two-electron redox process to form V^{5+} on charge, yet only $V^{4+}/^{3+}$ redox has

been realized experimentally[77]. This limitation has motivated several studies of iso- and alio-valent cationic substitutions into NVP to realize multielectron $V^{5+}/V^{4+}/V^{3+}$ redox reactions [78, 79, 80, 81, 82, 83, 84]. This strategy has proven successful for iso-valently substituted cathodes, such as $Na_3V_{1.5}Al_{0.5}(PO_4)_3$ and $Na_3VCr(PO_4)_3$, which exhibit two-step voltage profiles at 3.4 and 4.0 V corresponding to the redox activity of the V^{4+}/V^{3+} and V^{5+}/V^{4+} couples, respectively. Although the high intercalation voltage of the V^{5+}/V^{4+} couple leads to improvements in energy density compared to unsubstituted NVP, their intercalation capacities are similar to that of NVP (i.e., two moles of Na-ions exchanged pfu). Alternatively, aliovalent Mn^{2+} substitution into the NVP framework results in the formation of a fully sodiated NASICON $Na_4VMn(PO_4)_3$ cathode [85]. When cycled between 3.75 and 2.5 V versus Na^+/Na^0, this material exhibits two voltage plateaus at 3.4 (V^{5+}/V^{3+}) and 3.6 V (Mn^{3+}/Mn^{2+}) versus Na^+/Na^0, but is again limited to two moles of reversible Na-ion exchange pfu. Upon extending the charge voltage window to 4.2 V versus Na^+/Na^0, an additional one mole of sodium ions can be removed, raising the total charge capacity of the $Na_4VMn(PO_4)_3$ cathode to 150 mAh/g [33]. This additional capacity has been attributed to the redox activities of the V^{5+}/V^{4+} and Mn^{4+}/Mn^{3+} couples. Unfortunately, on subsequent discharge, only 1.5 moles of Na^+ ions are reinserted into the structure. Operando X-ray diffraction (XRD) studies have attributed this capacity loss to an irreversible structural transformation of the NASICON framework at high voltage, triggered by the removal of Na^+ ions from Na(1) sites and possible vanadium cation migration into them [86, 87]. Further, the $Na_4VMn(PO_4)_3$ cathode displays rapid capacity fade upon cycling. Structural and capacity degradation upon high voltage cycling has also been observed in Mn-rich $Na_{3+y}V_{2-y}Mn_y(PO_4)_3$ cathodes [88, 89]. However, it is not yet clear what role concomitant local structural and electronic processes occurring at higher voltages play in the above mentioned issues. Specifically, the interplay between the removal of Na^+ ions from Na(1) and Na(2)

sites and the oxidation of V^{4+} to V^{5+} as well as $Mn^{3+}$to Mn^{4+} and associated changes to $(V/Mn)O_6$ local environments makes it difficult to separate individual contributions to the observed electrode degradation phenomena. Therefore, it is necessary to decouple structural and electronic processes to better understand the links between structure/composition and electrochemical properties. In the present work, we have designed a series of Mg^{2+}-substituted NASICON cathodes with compositions $Na_{3+y}V_{2-y}Mg_y(PO_4)_3$ akin to previously studied Mn^{2+}-substituted NVP compounds [88, 89]. The electrochemical inactivity of Mg^{2+} entails that V redox centers are solely responsible for Na^+ exchange in the $Na_{3+y}V_{2-y}Mg_y(PO_4)_3$ cathodes, which enables us to follow structural and electrochemical (de)sodiation processes during charge–discharge more clearly than in the structurally and compositionally similar V^{3+}/Mn^{2+} system. Specifically, this study allows us to evaluate the impact of metal mixing on the V site on the Na (de)intercalation mechanism, on the electrochemical reversibility, and on Na^+ diffusion kinetics, without the complications of multimetal redox processes on charge and discharge. We find that the progressive replacement of V^{3+} by Mg^{2+} in these Na-ion intercalation hosts provides a convenient handle for tuning their average intercalation voltage, voltage hysteresis, and Na (de)intercalation mechanism.

3.2 Results and Discussion

3.2.1 Structural characterization & first-principles characterization

NASICON $Na_{3+y}V_{2-y}Mg_y(PO_4)_3$ (y= 0, 0.25, 0.5, 0.75, and 1) cathodes were prepared via a sol–gel assisted high temperature method (see the Experimental Section). Particle morphology of the as-prepared cathodes was studied using scanning electron

microscopy (SEM) (Figure 3.8). The micrographs indicate the formation of micron-sized secondary particles composed of nanoscale primary particles, while CHN elemental analysis reveals the presence of 3–5 wt% carbon in the NASICON samples (Table 3.3 in Appendix A).

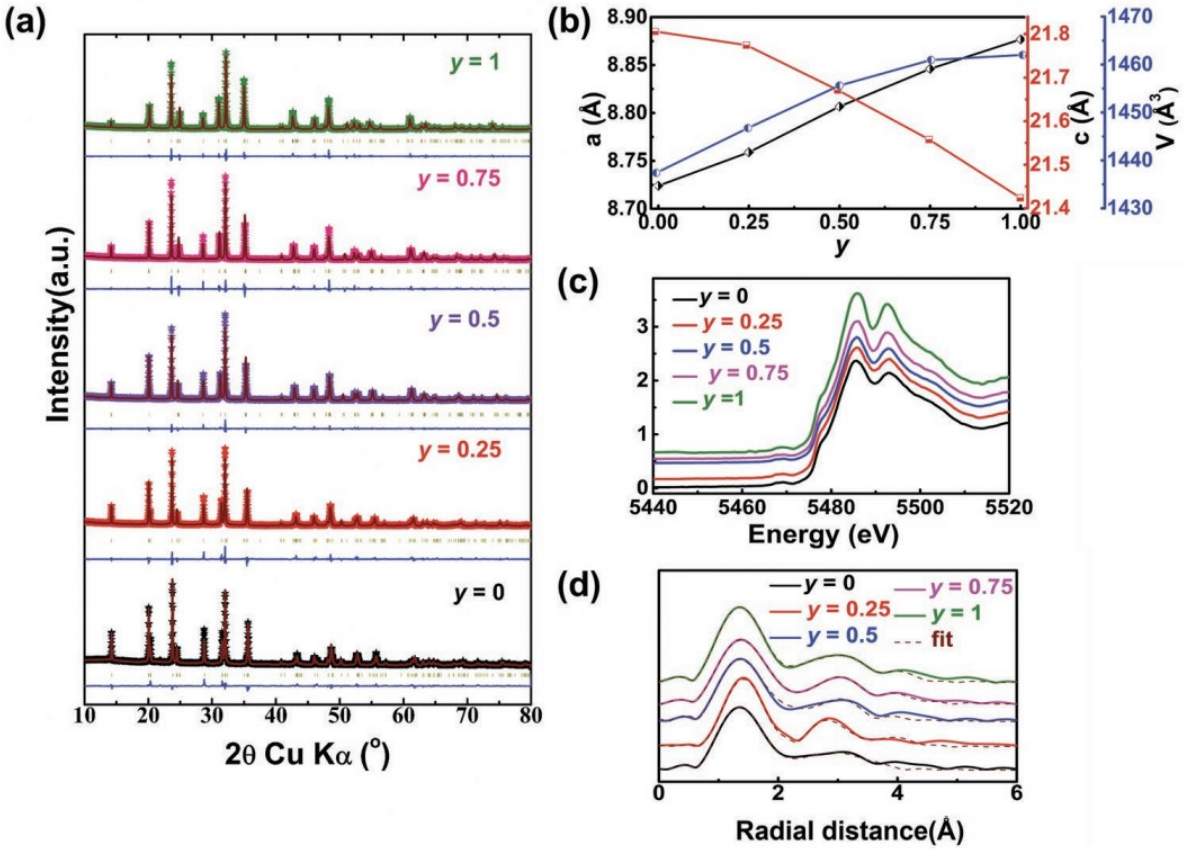

Figure 3.1: a) Rietveld analysis of powder XRD patterns collected on $Na_{3+y}V_{2-y}Mg_y(PO_4)_3$ samples. b) Variations in the unit cell parameters and volumes as a function of y. c) Normalized absorption spectra and d) FT-EXAFS at the V K-edge of the $Na_{3+y}V_{2-y}Mg_y(PO_4)_3$ cathodes.

XRD measurements were conducted to study the solubility of Mg^{2+} cations in the NVP framework (Figure 3.1a). All Bragg peaks observed for the $Na_{3+y}V_{2-y}Mg_y(PO_4)_3$ cathode samples can be fully indexed using a rhombohedral $R\bar{3}c$ space group, with no evidence of crystalline impurities. It is also worth noting that Inoishi et al.,[79] highlighted the

solubility limit of Mg^{2+} in the NVP lattice as y = 0.5, however, their sample preparation involved a high temperature annealing (800 °C) step that could lead to phase decomposition. To gain insights into long-range structural changes upon Mg^{2+} substitution, Rietveld refinements of the lab XRD data were carried out, and the results are displayed in Figures 3.1b, with structural parameters summarized in Table 3.4 in Appendix A. Although NVP undergoes a series of phase transitions upon cooling from the R$\bar{3}$c form to a monoclinic C2/c structure near room temperature due to Na^+-ion/vacancy ordering [34], herein its XRD pattern is refined using the rhombohedral R$\bar{3}$c setting for the sake of comparison across the compositional series, and because the use of a C2/c structural model does not improve the refinement significantly. As the concentration of Mg^{2+} (y) increases from 0 to 1 in the NVP framework, we notice anisotropic changes to the lattice parameters along with an expansion of the unit cell volume (Δa/a = +1.75, Δc/c = −1.75, and ΔV/V = +1.71). The decrease in the c lattice parameter with increasing y (from y = 0.25 to y = 1) can be related to the progressive filling of Na(1) sites, which minimizes the electrostatic repulsion between oxygen layers perpendicular to the c-axis of the NASICON structure. The larger ionic radius of Mg^{2+} (0.72 Å), as compared to V^{3+} (0.64 Å), and the increase in Na(2) site population, are responsible for the increase in a-parameter. Further, BVS calculations reveal minor changes to the average (V/Mg)O_6 and Na(1)−O bond lengths, and reduced (V/Mg)O_6 and Na(1)O_6 octahedral distortions upon increased Mg^{2+}substitution (Table 3.4 in Appendix A), which is also confirmed by X-ray absorption spectroscopy (XAS) results presented in the next section. When comparing these structural changes to those reported in our recent study of Mn^{2+} substitution into the NVP lattice [88], we notice that (V/Mg)O_6 octahedra in $Na_{3+y}V_{2-y}Mg_y(PO_4)_3$ are less distorted (Δ= 2–3 × 10^{-4}) than (V/Mn)O_6 octahedra in $Na_{3+y}V_{2-y}Mn_y(PO_4)_3$ (Δ= 5–7 × 10^{-4}), which is presumably due to the different ionic sizes and bonding characteristics of Mg^{2+} and Mn^{2+}.

First principles calculations were carried out to confirm the phase stability and to evaluate the most favorable V/Mg ordering for the various $Na_{3+y}V_{2-y}Mg_y(PO_4)_3$ compositions of interest. For this, the formation energies of the solid solutions were computed using the following formula: $\Delta E_f = E_i - (\gamma - 3) \times E_{[Na_4VMg(PO_4)_3]} - (4 - \gamma) \times E_{[Na_3V_2(PO_4)_3]}$, where E_i is the total energy of the $Na_{3+y}V_{2-y}Mg_y(PO_4)_3$ composition under consideration, and $E_{[Na_4VMg(PO_4)_3]}$ and $E_{[Na_3V_2(PO_4)_3]}$ are the total energies of the end member phases. Starting from $Na_4VMg(PO_4)_3$ with a fully occupied Na sublattice, other compositions in the series were generated by removing Na-ions and adjusting the V^{3+}/Mg^{2+} ratio to maintain charge neutrality and achieve the targeted stoichiometries. Using the Supercell code, multiple V/Mg orderings were generated for each stoichiometry (see details in Table 3.1 in Appendix A). A convex hull plot was constructed using the formation energies of all of the converged $Na_{3+y}V_{2-y}Mg_y(PO_4)_3$ configurations and is shown in Figure 3.9a in Appendix A. The optimized lattice parameters for the most stable configurations are summarized in Table 3.5 in Appendix A, and their evolution resembles our XRD results. We note here that no particular V and Mg ordering is observed for the lowest energy structures of $Na_{3+y}V_{2-y}Mg_y(PO_4)_3$, in good agreement with our experimental XRD results. We observe three types of local environments for Na(1) in the NASICON skeleton, namely, MgO_6—Na(1)O_6—MgO_6, VO_6—Na(1)O_6—MgO_6, and VO_6—Na(1)O_6—VO_6, wherein Na(1)O_6 polyhedra face share with MgO_6/VO_6 octahedra. In the case of Na(2)O_8 polyhedra, these are found to be face sharing in MgO_6—Na(2)—MgO_6, VO_6—Na(2)—MgO_6, and VO_6—Na(2)—VO_6, and corner sharing in MgO_6—Na(2)—MgO_6 subunits. The calculations reveal that changing the local V/Mg ratio around Na species influences the energies of the configurations significantly, and thus plays a role in the preferred occupation of Na(1) and Na(2) sites across the $Na_{3+y}V_{2-y}Mg_y(PO_4)_3$ compositional series. In the lowest energy structures, both Na(1) and Na(2) prefer to occupy Mg-rich environments rather than mixed V/Mg and

V-rich environments. The most stable configurations for the y = 0, 0.25, 0.5, 0.75, and 1 phases have a Na(1):Na(2) occupation ratio of 0.66:0.77, 0.75:0.83, 0.83:0.89, 0.91:0.94, and 0.94:0.99, respectively, and are considered hereafter.

To understand how Mg^{2+} substitution influences Na^+ ion mobility in the NASICON framework, Na^+ diffusion barriers (E_a) and bottleneck sizes (T1) obtained for the series of $Na_{3+y}V_{2-y}Mg_y(PO_4)_3$ compositions are plotted in Figure 3.9b in Appendix A. The bottleneck area (T1) corresponds to the area of an isosceles triangle located in between Na(1) and Na(2) sites. T1 values obtained from first principles calculations at each Mg^{2+} substitution agree fairly well with those obtained from Rietveld analysis. While a drop in T1 is observed at low substitution levels ($y \leq 0.25$), this is followed by a steady increase in T1 upon further Mg^{2+} substitution. Activation energies were obtained from CI-NEB calculations for sodium-ion hops between Na(1) to Na(2) sites through the T1 area. While E_a and T1 may naively be expected to be inversely related to one another, the trend in E_a is more complex upon increasing the Mg^{2+} content. Indeed, E_a increases from $\approx$ 0.15 eV at y= 0 to $\approx$ 0.38 eV at y= 0.25, and stabilizes at about 0.25 eV for y= 0.5 and 0.75 compositions, before increasing again to 0.5 eV in the fully sodiated compound (y= 1). This complex evolution is likely the result of the interplay between changes to the T1 bottle neck area and to Na site occupation on Mg^{2+} substitution.

XAS experiments were performed on as-synthesized $Na_{3+y}V_{2-y}Mg_y(PO_4)_3$ ($0 \leq y \leq 1$) samples to investigate potential changes in the vanadium oxidation state, as well as local structure changes across the series. Normalized V K-edge absorption spectra are shown in Figure 3.1c. Irrespective of the amount of Mg^{2+} substituted into the NVP framework, the position of the absorption edge is similar in all XAS spectra, confirming that the average V oxidation state is +3 in all samples. Magnitude plots of the Fourier-transformed extended X-ray absorption fine structure (FT-EXAFS) at the V K-edge, along with theoretical fits and extrapolated bond distances, are shown in Figure 3.1d

and Table 3.6 in the Appendix, respectively. We note that the FT-EXAFS data are not phase corrected and peak positions do not reflect actual bond lengths. The first peak located at $\approx$ 1.6 Å corresponds to scattering from V−O pairs, while the next two peaks at $\approx$ 2.8–3.2 Å are associated with V−P and V−Na outer shell correlations. Fits of the EXAFS spectra indicate a slight increase in the average V−O bond length on Mg^{2+} substitution, presumably due to reduced overlap between the V 3d orbitals and O 2p orbitals and enhanced bond ionicity. In contrast, the fits do not show any clear correlation between the evolution of the V–Na(1), V–P, and V–Na(2) distances and the Mg^{2+}substitution level, yet significant changes are observed at each Δy= 0.25 step increase in Mg content. This may be explained by the concurrent increase in the total Na content and variations in the relative occupation of Na(1) and Na(2) sites upon Mg^{2+} substitution, resulting in a unique local structure for each composition.

3.2.2 ^{23}Na and ^{31}P solid-state NMR

^{23}Na and ^{31}P solid-state NMR experiments were conducted to obtain further insights into local structure changes across the $Na_{3+y}V_{2-y}Mg_y(PO_4)_3$ series. The presence of open-shell V^{3+} species in these compounds results in strong hyperfine (or paramagnetic) interactions between unpaired electron spins nominally present in the V 3d orbitals and the ^{23}Na/^{31}P nuclear spins under study. These strong interactions result in significant NMR line broadening and potential signal overlap, complicating the assignment of the spectral features to specific local environments in the material. Furthermore, the isotropic chemical shift (δ_{iso}) is dominated by the Fermi contact shift resulting from delocalization of unpaired electron spin density from the V 3d orbitals to the ^{23}Na (or ^{31}P) s orbitals via bridging O 2p orbitals. For an I= 3/2 quadrupolar nucleus such as ^{23}Na, the interaction between the nuclear quadrupole moment and the electric field gradient (EFG) present

at the nucleus leads to a further broadening of the spectrum and to a shift of the ^{23}Na resonant frequency due to second-order effects (denoted as δ_Q). The observed chemical shift (δ_{obs}) is then the sum of the isotropic Fermi contact shift and of the second-order quadrupolar shift: $\delta_{obs}=\delta_{iso}+\delta_Q$. In contrast, ^{31}P is a spin-$\frac{1}{2}$ nucleus with no quadrupole moment and $\delta_{obs}=\delta_{iso}$. The assignment of the complex paramagnetic NMR spectra of the $Na_{3+y}V_{2-y}Mg_y(PO_4)_3$systems is assisted here by first principles hybrid DFT/Hartree Fock (HF) calculations of ^{23}Na and ^{31}P NMR parameters on the room temperature monoclinic (C2/c space group) and Na-ordered form of $Na_3V_2(PO_4)_3$ (α-$Na_3V_2(PO_4)_3$) identified by Chotard et al[34].

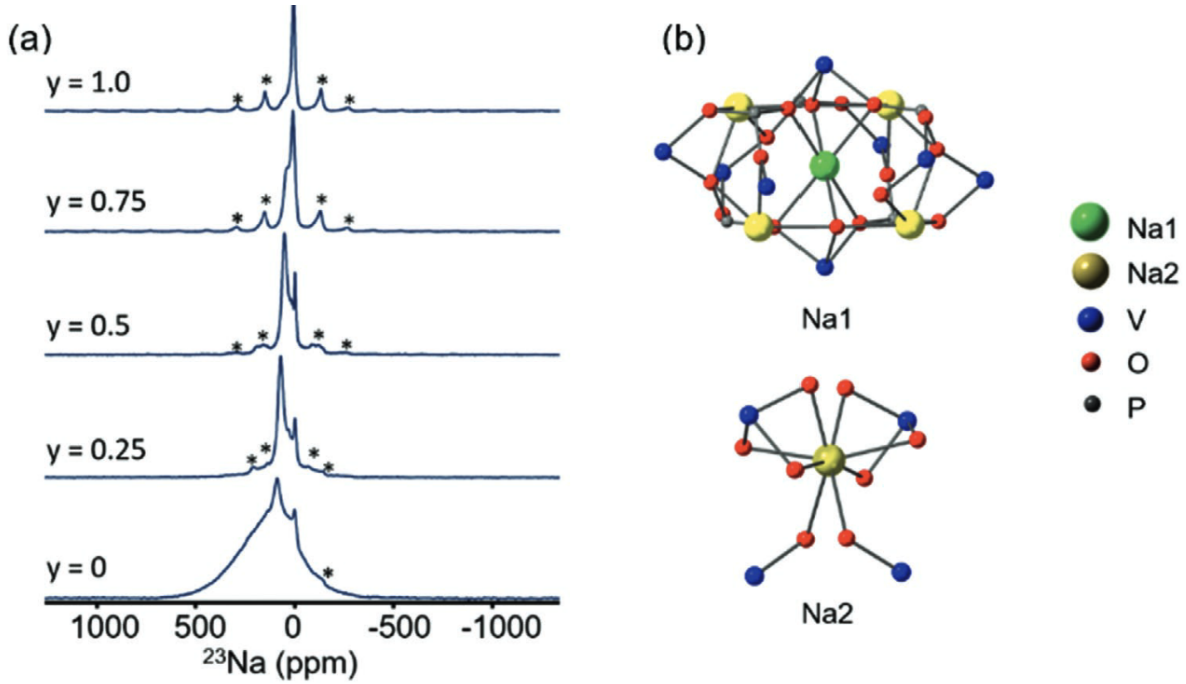

Figure 3.2: a) ^{23}Na solid-state NMR spectra obtained on the as-synthesized $Na_{3+y}V_{2-y}Mg_y(PO_4)_3$ at 18.8 T using a spin echo pulse sequence. b) Local environments Na(1) (surrounded by 8 V atoms) and Na(2) (surrounded by 4 V atoms) in the $Na_3V_2(PO_4)_3$ structure. Asterisks indicate spinning sidebands coming from the fast rotation of the sample during acquisition.

^{23}Na spin echo NMR spectra obtained at 18.8 T are shown in Figure 3.2a. As expected

from the reduced hyperfine interactions upon progressive replacement of paramagnetic V^{3+} by diamagnetic Mg^{2+}, a decrease in signal broadening is observed as y increases[90]. A shift of the average ^{23}Na resonant frequency toward 0 ppm is also observed on increasing the Mg^{2+} content, again, as expected from the reduced paramagnetism. To facilitate the interpretation of the high-field ^{23}Na NMR data, additional spectra were collected at 7.05 T. Fits of the 7.05 and 18.8 T NMR data are shown in Figure 3.11 in Appendix A. The observed chemical shifts (δ_{obs}) and relative integrated intensities of the various ^{23}Na resonances determined from fits of the NMR data are recorded in Table 3.7 in Appendix A.

For the y= 0 composition, the two ^{23}Na resonances observed at δ_{obs}= 134 ppm and δ_{obs}= 55 ppm at 7.05 T (Figure 3.11a, Appendix A) can be attributed to Na^+ species in the NASICON structure, while the low intensity resonance near 0 ppm is attributed to (a) diamagnetic sodium phosphate and pyrophosphate impurity(ies)[91]. ^{23}Na NMR parameters computed on the room temperature α-$Na_3V_2(PO_4)_3$[34] structure, where Na(1) sites split into Na(1a) and Na(1b) sites, and Na(2) sites split into Na(2a), Na(2b), and Na(2c) sites, are summarized in Table 3.8 in Appendix A. A comparison of the observed (Table 3.7, Appendix A) and ab initio predicted (Table 3.8, Appendix A) ^{23}Na chemical shifts indicates that the 134 and 55 ppm resonances are average signals due to fast Na^+ exchange on the NMR timescale between subsets of Na(1) and Na(2) environments in the α-NVP structure, rather than signals arising from the Na(1) and Na(2) crystallographic sites in the average rhombohedral R$\bar{3}$c structural model. The NMR timescale denotes the ability of NMR to distinguish between different environments that are in chemical exchange and depends on the frequency separation ($\Delta\nu$, in Hz) between signals corresponding to the various environments in exchange. The presence of two distinct signals in the y = 0 spectrum indicates that room temperature Na-ion exchange between all Na sites in the NASICON structure is not sufficiently fast to result in a single average ^{23}Na

resonance, but it is fast enough to average out signals with similar resonant frequencies. We attribute the 134 ppm resonance to an average signal arising from Na nuclei in Na(1a), Na(1b), and Na(2c) sites in the structure and associated with high (more positive) resonant frequencies. We further assign the 55 ppm resonance to an average signal due to Na nuclei in Na(2a), Na(2b) sites in the structure and associated with low (more negative) resonant frequencies. Moreover, the intensity ratio of the 134 and 55 ppm signals of 1.21:1 is in much better agreement with partial averaging over Na(1a), Na(1b), and Na(2c) sites on the one hand, and over Na(2a) and Na(2b) sites on the other hand (predicted 1.25:1 intensity ratio obtained from Na site multiplicities in the α-NVP structure), than over all Na(1) and all Na(2) sites (predicted 1:2 intensity ratio), as shown in Table 3.9 (Appendix A). Based on the frequency difference (in Hz) between the 134 and 55 ppm resonances in the low field (7.05 T) data, we estimate the exchange rate of Na^+ species between the high- and low-frequency resonances to be less than ≈ 12 kHz (i.e., the rate of exchange needed for these two ^{23}Na resonances to coalesce at the experimental temperature).

For the Mg-substituted samples, the assignment of the ^{23}Na NMR resonances (Figure 3.11, Appendix A) to specific sites in the NASICON structure is not straightforward. Assuming that Mg randomly substitutes on V sites, a large number of Na local environments are expected with varying numbers of Mg^{2+} species in the first metal coordination shell around Na(1) and Na(2) depicted in Figure 3.2b, resulting in a distribution of chemical shifts. For example, in the y= 0.5 sample, a total of 35 distinct Na(1) environments and 6 distinct Na(2) environments are expected. However, only two to three ^{23}Na resonances are observed in the NMR spectra collected on these phases (see Figure 3.11, Appendix A), suggesting that fast chemical exchange between subsets of Na(1) and Na(2) sites in these compounds results in ^{23}Na NMR signal averaging. Additionally, while we assign the sharp ^{23}Na resonance near 0 ppm in the y= 0.25 and 0.5 samples to diamagnetic sodium

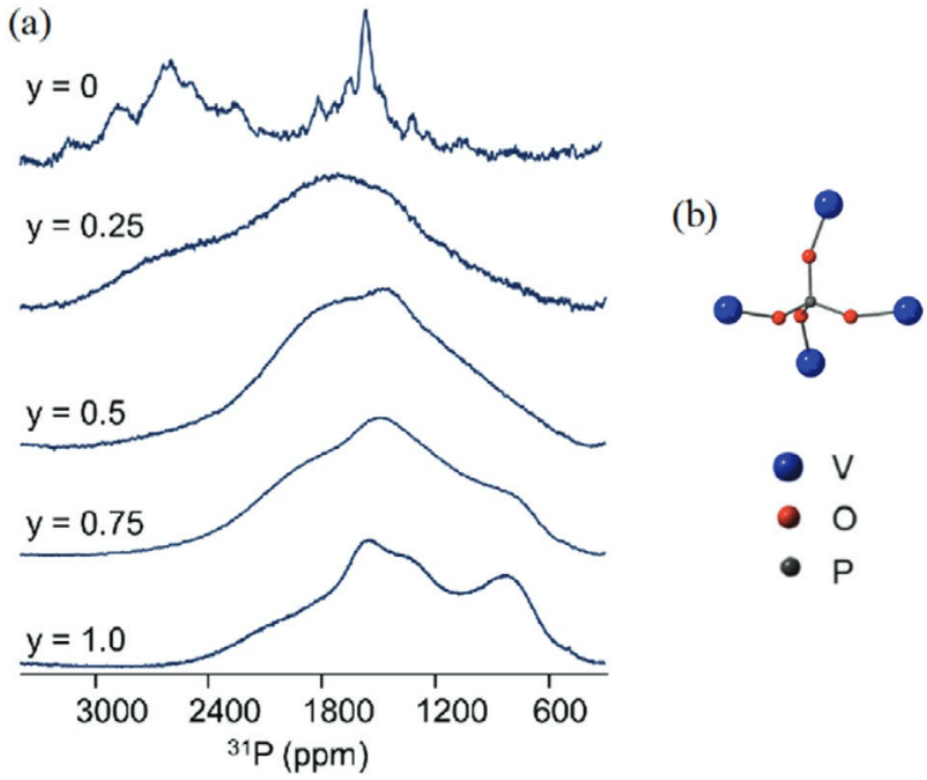

Figure 3.3: a) Enlargements of the paramagnetic region of ^{31}P NMR spectra obtained on pristine $Na_{3+y}V_{2-y}Mg_y(PO_4)_3$ cathode samples at 7.05 T and at a spinning speed of 30 kHz. b) Example P local environment in $Na_3V_2(PO_4)_3$

phosphate/pyrophosphate impurity(ies), the broader resonances in this frequency range in the y= 0.75 and 1 samples likely have contributions from Na sites in the paramagnetic NASICON cathode primarily surrounded by diamagnetic Mg^{2+} species.

^{31}P solid-state NMR experiments were conducted to monitor the evolution of the P local environments across the $Na_{3+y}V_{2-y}Mg_y(PO_4)_3$ series (Figure3.3a). Spectral regions featuring paramagnetic ^{31}P NMR signals arising from the NASICON cathodes are shown in Figure 3.3a, and an example P local environment in NVP is provided in Figure 3.3b. As shown in Figure 3.3a, ^{31}P spectra collected on $Na_{3+y}V_{2-y}Mg_y(PO_4)_3$ pristine compounds are significantly broadened and feature multiple overlapping signals spanning a chemical shift range on the order of thousands of ppm. As the Mg dopant concentration is in-

creased from y = 0.25 to y = 1, the reduced hyperfine interactions result in a decrease of the ^{31}P NMR signal broadening and concomitant shift of the resonant frequencies toward 0 ppm. For the y = 0 compound, we see multiple ^{31}P resonances suggesting the presence of multiple local ^{31}P environments in the material. This result is inconsistent with the rhombohedral (R$\bar{3}$c) model of $Na_3V_2(PO_4)_3$[34], which contains a single P environment, and confirms the presence of a monoclinic structural distortion due to Na^+-ion/vacancy ordering close to room temperature [34]. The α-NVP structure comprises a total of five ^{31}P environments (PA, PB, PC, PD, and PE) that differ slightly in terms of P−O/O−V bond lengths and P−O−V bond angles (see Table 3.10, Appendix A). The remarkable ^{31}P chemical shift range in the y= 0 spectrum, and the fact that all ^{31}P environments are similarly coordinated to four paramagnetic V^{3+} ions, as shown in Figure 3.3b, highlights the high sensitivity of ^{31}P shifts to even minor changes in the P local coordination. Although significant spectral overlap precludes a full assignment of the ^{31}P resonances, first principles calculations of ^{31}P NMR properties suggest that the PC and PE environments are responsible for the signals seen below 2000 ppm, and that resonances above 2000 ppm can be attributed to PA, PB, and PD environments (see Table 3.11, Appendix A).

Although paramagnetic interactions are reduced on Mg^{2+}substitution into the $Na_{3+y}V_{2-y}Mg_y(PO_4)_3$, the y = 0.25 spectrum is broader than the y = 0 spectrum. The broader line shape can be accounted for by the presence of a broad distribution of chemical shifts reflecting a distribution of P local environments as Mg partially substitutes on the V sites. As the Mg concentration is increased beyond y= 0.25, the paramagnetic broadening is decreased but the distribution of ^{31}P environments is still present. Assuming a random substitution of V by Mg, we expect 16 distinct P environments in the rhombohedral (R$\bar{3}$c) Mg-substituted compounds; the probability of finding each of these 16 P sites depends on the exact Mg:V ratio. The presence of a large number of broad and overlapping signals makes the assignment of the ^{31}P spectra nontrivial, as shown in Figure 3.12 (Appendix

A) for the y = 0.5 spectrum. The full ^{31}P NMR spectra (from −2000 to 4000 ppm) collected on all samples are shown in Figure 3.4, and exhibit additional resonances near 0 ppm attributed to diamagnetic phosphate/pyrophosphate impurities[92, 93], and/or to ^{31}P sites in the NASICON structure surrounded by four diamagnetic Mg^{2+} ions. For instance, assuming a statistical distribution of V and Mg species in the y= 1 composition, the probability of finding a ^{31}P nucleus surrounded only by 4 Mg is 6.25%.

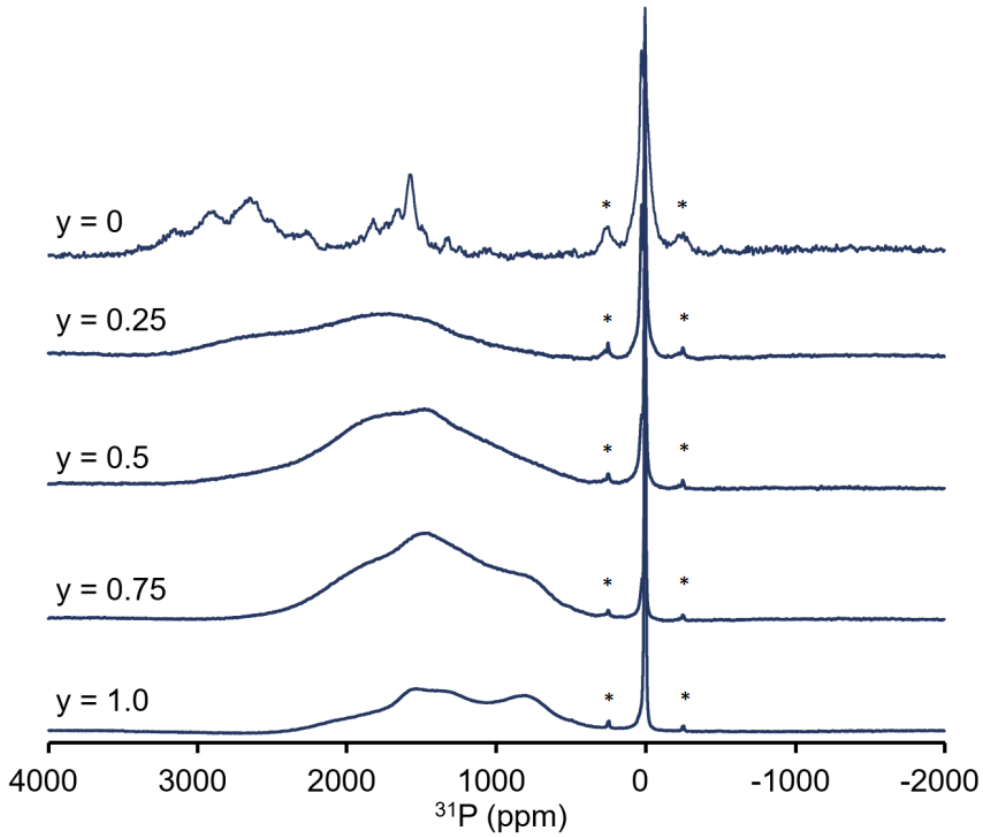

Figure 3.4: Full ^{31}P NMR spectra obtained on the series of pristine $Na_{3+y}V_{2-y}Mg_y(PO_4)_3$ cathode samples at 7.05 T and a spinning speed of 30 kHz. While resonances due to ^{31}P nuclei in the paramagnetic NASICON cathode appear above 200 ppm, signals near 0 ppm (along with one spinning sideband on either side denoted with an asterisk) correspond to diamagnetic impurities, likely including Na_2HPO_4.

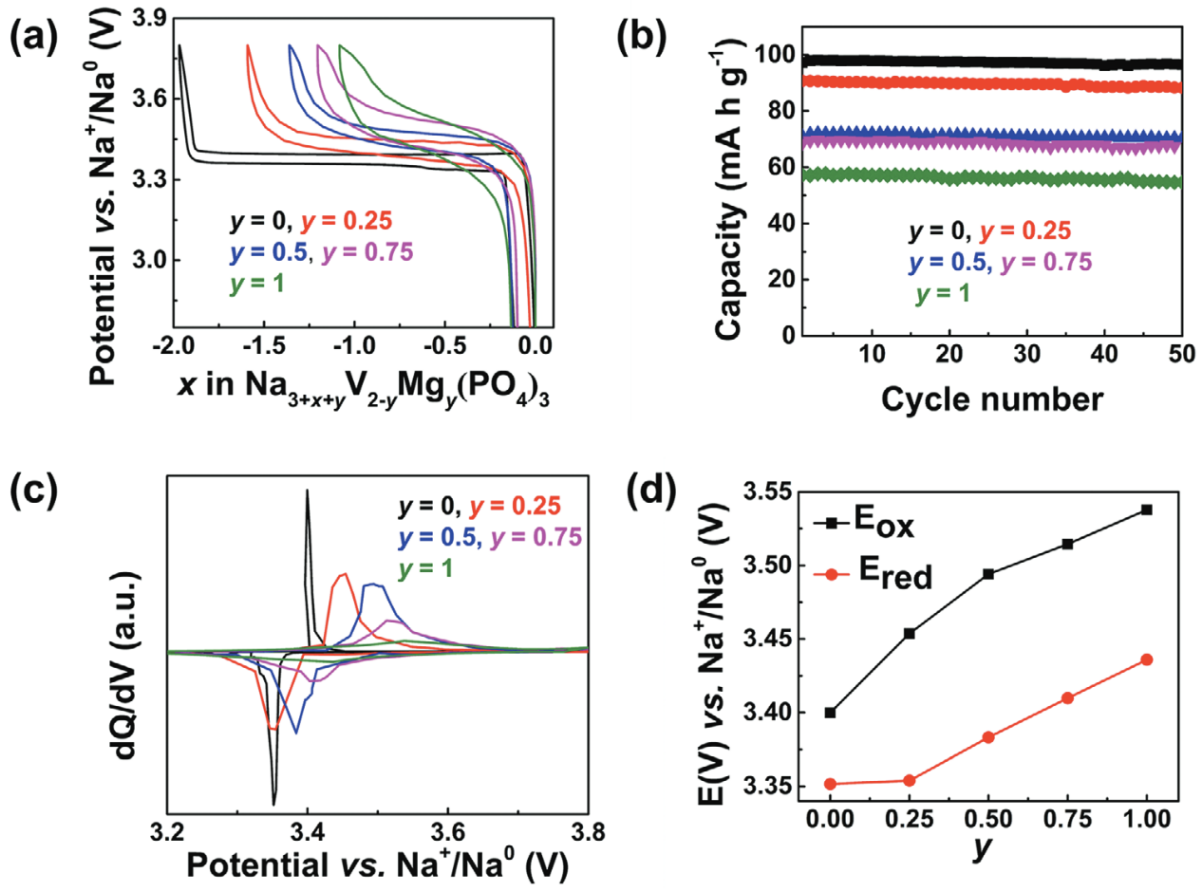

Figure 3.5: Voltage versus composition (x), b) cycling performance, c)dQ/dV profiles, and d) evolution of oxidation/reduction voltages (deduced from dQ/dV plots) of the $Na_{3+y}V_{2-y}Mg_y(PO_4)_3$ cathodes.

3.2.3 Electrochemical performance

Having established how Mg^{2+} substitution for V^{3+} in $Na_{3+y}V_{2-y}Mg_y(PO_4)_3$ cathodes affects their (local) crystal structure and Na^+ ion diffusion properties, we move on to study their Na (de)intercalation properties through galvanostatic cycling at a C/10 rate in the voltage window of 3.8–2.75 V versus Na^+/Na^0. The voltage composition (x) profiles of the $Na_{3+y}V_{2-y}Mg_y(PO_4)_3$ cathodes from their second cycle are given in Figure 3.5a, and their cycling stability evaluated at C/10 rate, is shown in Figure 3.5b. Remarkably, all of the NASICON cathodes retain almost 99% of their initial discharge capacities

at the end of 50th cycle. The $Na_3V_2(PO_4)_3$ cathode exhibits a flat charge/discharge profile with an average voltage of $\approx$ 3.45 V versus Na^+/Na^0, corresponding to the reversible exchange of 1.9 moles of Na pfu[94, 77]. The large voltage plateau indicates that Na (de)intercalation proceeds via a two-phase reaction between the $Na_3V_2(PO_4)_3$ and $NaV_2(PO_4)_3$ end member compositions. Compared to NVP, several changes in the electrochemical properties are observed as y increases: the amount of reversible Na exchange decreases (to 1.7, 1.43, 1.13, and 1.0 moles pfu for y= 0.25, 0.5, 0.75, and 1, respectively), the slope of the voltage-composition profiles increases, and the average intercalation voltage increases.

The decrease in the amount of cyclable Na (i.e., the charge storage capacity) with increasing y is related to the replacement of redox active V^{3+} by electrochemically inactive Mg^{2+} cations. The evolution of the average sodium (de)intercalation voltage and mechanism is best characterized via dQ/dV plots, as shown in Figure 3.54c,d. Changes to the average (de)intercalation potential (Figure 3.5d), from $\approx$ 3.38 V at y = 0 to $\approx$ 3.49 V at y = 1, can be attributed to variations in the V$-$O bonding character across the $Na_{3+y}V_{2-y}Mg_y(PO_4)_3$ series. Specifically, substitution of more electropositive Mg^{2+} ions for V^{3+} ions in the structure is expected to increase the ionicity of V$-$O bonds, thus raising the (de)intercalation voltage of the V^{4+}/V^{3+} redox couple. To confirm this, we computed the projected density of states (pDOS) for all members of the $Na_{3+y}V_{2-y}Mg_y(PO_4)_3$ series (Figure 3.13a, Appendix A). We find that, while the valence states are majorly comprised by O 2p and Mg 2s orbitals, the V 3d orbitals dominate the higher energy conduction band states. The density of both V 3d and O 2p orbitals that are located near and below the Fermi level, respectively, decreases with increasing concentration of dopant Mg atoms, indicating a weakening of the hybridization between V and O orbitals due to the more polarizing nature of Mg^{2+}. This leads to a gradual reduction in the V$-$O bond covalency and to a lowering of the V$-$O antibonding states,

which in turn increases the V^{4+}/V^{3+}redox voltage. The pDOS results are confirmed by Bader charge analysis, which indicates an increase in the ionicity of V−O bonds and higher Bader charges on the V cations with increasing Mg content[95] (Figure 3.13b, Appendix A). The redox peaks in the dQ/dV plots in Figure 3.5c also become broader as y increases from 0 to 1, indicating a change in the Na (de)intercalation process upon Mg^{2+} substitution.

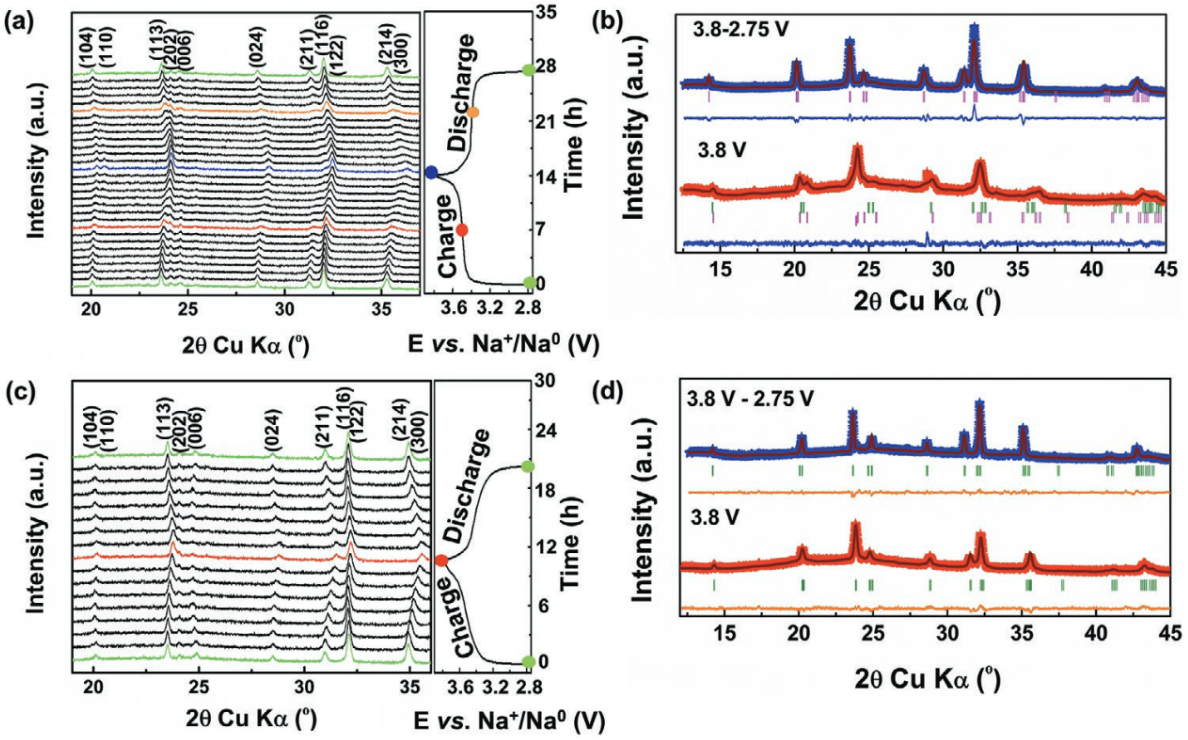

Figure 3.6: a,c) Operando XRD and b,d) ex situ pattern refinements of $y = 0.5$ and $y = 1.0$ cathodes

To understand how Mg^{2+} substitution affects the Na (de)intercalation mechanism of the NVP cathode, we performed in operando XRD studies on the y = 0.5 and 1 cathodes (Figure 3.6). Previous in operando XRD studies on the unsubstituted NVP cathode have revealed a complete two-phase transformation mechanism between the $Na_3V_2(PO_4)_3$ and $NaV_2(PO_4)_3$ end-members, accompanied by the oxidation of V^{3+} to V^{4+}[96]. During

the initial charge process, the XRD peaks of the $Na_{3.5}V_{1.5}Mg_{0.5}(PO_4)_3$ cathode progressively shift toward higher 2θ angles until 0.5 Na pfu has been extracted to form an intermediate $Na_3V_{1.5}Mg_{0.5}(PO_4)_3$, indicating a solid solution mechanism over this compositional range (Figure 3.6a). As the cathode is charged further, the XRD peaks of the $Na_3V_{1.5}Mg_{0.5}(PO_4)_3$ phase diminish while a new set of XRD peaks appears and grows at $2\theta = 20.65^\circ$ and 24.11°, confirming a first-order phase transformation in this range. The XRD pattern collected at the end of charge (3.8 V) can be fitted with two NASICON phases (Figure 3.6b) and their corresponding lattice parameters are displayed in Table 3.12 (Appendix A). The overall cell volume change between the Na-rich and Na-poor phases is estimated as 6.2%, which is significantly lower compared to the NVP cathode ($\Delta V/V = 8.1\%$). It is worth mentioning here that the presence of unextracted Na-ions in the Mg-substituted phases increases their volume and reduces the volume mismatch between Na-rich and Na-poor phases, resulting in enhanced structural integrity during cycling. Upon subsequent discharge, all of the processes observed on charge are reversed, and the XRD pattern collected at the end of the first cycle matches that of the pristine $Na_{3.5}V_{1.5}Mg_{0.5}(PO_4)_3$cathode perfectly, thus confirming full reversibility of the Na (de)intercalation mechanism. In contrast, the fully sodiated $Na_4VMg(PO_4)_3$ cathode exhibits a solid solution mechanism over the entire Na (de)intercalation range (Figure 3.6c). Its XRD peaks shift toward higher and lower 2θ values during the charge and discharge process, respectively. The desodiated $Na_3VMg(PO_4)_3$ phase observed at 3.8 V shows anisotropic lattice parameter changes (i.e., a decrease and an increase in the a and c lattice parameter, respectively) (see Figure 3.6d and Table 3.12, Appendix A). Importantly, we find that the occupancy of Na(1) and Na(2) sites decreases to 0.867 and 0.688, respectively, implying simultaneous Na extraction from both Na sites. This observation is in contrast with the desodiation processes of $Na_3V_2(PO_4)_3$ and $Na_4VMn(PO_4)_3$[85, 97] cathodes wherein Na-ions from Na(1) site are not involved in the desodiation process until 3.8

V. Thus, it is clear that Mg-substitution affects the preference of sodium ion extraction from Na(1) and Na(2) sites, which could be due to the differences in site energies among the various local environments ((V/Mg)O_6-(Na(1)O_6/Na(2)O_8)-(V/Mg)O_6) as described in the earlier section. Detailed theoretical calculations are underway to decipher about it. Overall, the in operando XRD results prove that the Na (de)intercalation mechanism of Mg-substituted $Na_{3+y}V_{2-y}Mg_y(PO_4)_3$ cathodes progressively changes from a two-phase process to a solid solution process as the Mg content increases in the NVP lattice. Similar behavior has also been noticed in the case of $Na_{3+y}V_{2-y}Mn_y(PO_4)_3$ cathodes[98].

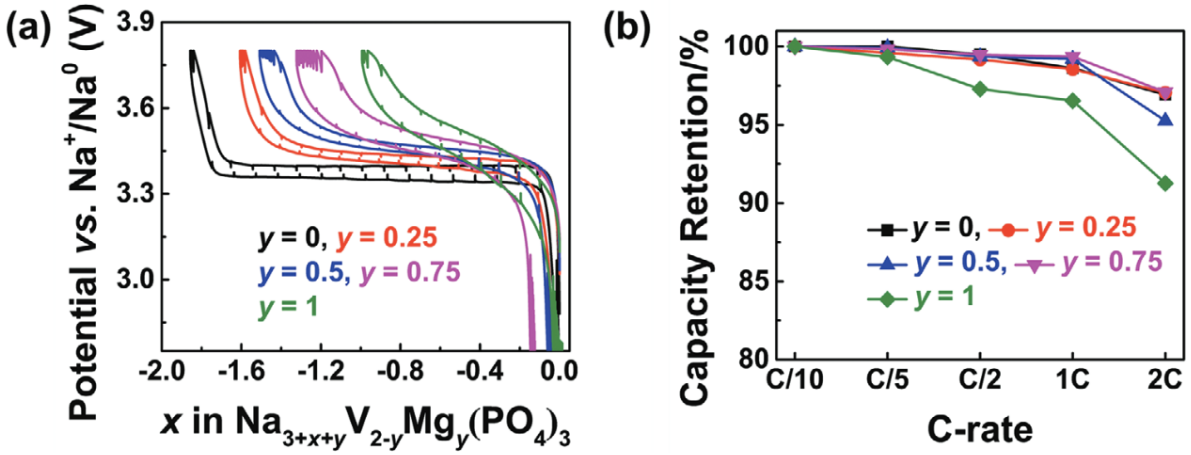

Figure 3.7: a) GITT and b) rate capability profiles of the $Na_{3+y}V_{2-y}Mn_y(PO_4)_3$ cathodes.

To understand the origin of the increased voltage polarization at higher Mg^{2+} substitution levels, galvanostatic intermittent titration technique (GITT) experiments were performed (Figure 3.7a and enlargements in Figure 3.14, Appendix A). We also recall here the theoretical calculation results presented earlier to correlate the Mg-substitution to the kinetic behaviors of the $Na_{3+y}V_{2-y}Mg_y(PO_4)_3$ cathodes. Although we cannot establish a direct correlation between the bottleneck sizes and the Na diffusion barrier (E_a), the latter increases for all of the Mg-substituted cathodes as compared to the NVP.

Therefore, we expect an increase in the voltage hysteresis upon Mg substitution. However, we find that the charge–discharge voltage hysteresis initially decreases from y = 0 to y = 0.25 and 0.5, followed by an increase for the y = 0.75 and 1 compounds. The voltage-composition profiles obtained from GITT and galvanostatic cycling experiments are compared in Figure 3.15 (Appendix A). For the y = 0.25 and 0.5 compositions, polarization is drastically reduced or completely vanishes when the voltage is allowed to relax to its equilibrium value (as in the GITT measurement), which is not the case for the y = 0.75 and 1 cathodes. The lowest polarization observed for y = 0.5 cathode can be attributed to reduced lattice mismatch between the Na-rich and Na-poor end members of the two-phase reaction, as demonstrated by the in operando XRD results. Such a phenomenon has been observed in, e.g., related Li(Fe/Mn)PO4 cathodes[99, 100, 101]. The impact of Mg-substitution on the Na (de)intercalation mechanism and kinetics is reflected in the rate performance of the $Na_{3+y}V_{2-y}Mg_y(PO_4)_3$, shown in Figure 3.7b. The y= 0.25, 0.5, and 0.75 cathodes deliver similar capacities as the y = 0 cathode at 1 C and 2 C rates, in contrast, the capacity of the y = 1 end member declines significantly at these high C-rates. These results highlight that two-phase Na (de)intercalation phenomena is not deleterious for high-rate performance and in fact lower voltage hysteresis can be achieved at intermediate Mg^{2+} substitution levels.

3.3 Conclusions

In this work, the impact of Mg^{2+} substitution on the structural and electrochemical Na (de)intercalation properties of $Na_{3+y}V_{2-y}Mg_y(PO_4)_3$ cathodes was investigated. Our combined XRD, XAS, NMR, and first principles results revealed a complex evolution of the (local) structure upon progressive replacement of V^{3+} by Mg^{2+}, along with the addition of Na ions into Na(1)/Na(2) sites, resulting in nonlinear changes in the Na^+ diffusion

properties across the compositional series. When cycled in the voltage window of 3.8–2.75 V, significant differences in the voltage-capacity profiles of the $Na_{3+y}V_{2-y}Mg_y(PO_4)_3$ cathodes were observed, including discrepancies in the average intercalation voltage, in the shape of the voltage curves and in their polarization. The increased Na insertion voltage on Mg substitution was attributed to a more ionic V–O bond, as determined from pDOS and Bader charge analyses. A transition from a two-phase for $y \leq 0.5$ to a solid solution process on Na (de)intercalation for $y \geq 0.5$ was confirmed through in operando XRD measurements. The lowest polarization value obtained for the $y = 0.5$ cathode was ascribed to minimizing lattice mismatch between the Na-rich and Na-poor end members of the two-phase reaction. Further experimental and theoretical studies are in progress to understand the high voltage behavior of the $Na_{3+y}V_{2-y}Mg_y(PO_4)_3$ cathodes. Overall, the present work underlines the importance of tuning functionalities of cathodes and understanding their structure–property relationship upon cationic substitution to achieve high energy density NASICON cathodes.

3.4 Experimental Section

3.4.1 Synthesis

NASICON-$Na_{3+y}V_{2-y}Mg_y(PO_4)_3$ samples were synthesized using sol–gel method. Initially V_2O_5 (99.6%, Sigma) was reduced using citric acid (99.5%, Sigma) in water following addition of stoichiometric amount of NaH_2PO_4 (99%, Sigma), Na_2CO_3 (99.5%, Sigma), and Mg-acetate (99%, Sigma) and the solution was subsequently heated at 100 °C to obtain powder mixture. The recovered powders were grinded using a mortar and pestle followed by annealing at 350 °C for 10 h and 700 °C for 12 h in N_2 atmosphere with an intermittent grinding.

3.4.2 Material characterization

Powder XRD patterns of the $Na_{3+y}V_{2-y}Mg_y(PO_4)_3$ samples were collected on a Bruker D8 diffractometer using Cu-Kα source in the 2θ region of 10°–100°. Rietveld analyses were performed to refine all the powder patterns using the FullProf program[102]. The as-synthesized phosphate cathode materials were examined by scanning electron microscope (Jeiss Ultra-55 SEM instrument) to get the microstructures. Carbon, hydrogen, and nitrogen (CHN) analysis was conducted on a Perkin–Elmer EA 2400 instrument.

XAS studies of the as-synthesized NASICON compounds and the electrodes with different state-of-charge were performed at the PETRA-III (P65 beamline, operating at 100 mA and 7.0 GeV) of Deutsches Elektronen-Synchrotron (DESY). The NASICON samples were mixed with boron nitride and pressed into pellets (13 mm diameter, thickness 0.5–0.9 mm). For data collection purpose, the electrodes at different charge states and the pellets were sealed in Kapton tape. The edge energy of 5349 eV was chosen for vanadium at the inflection point with the energy resolution of 1 eV. Each measurement was calibrated to the absorption energy of V metal plate reference. A double crystal monochromator consistent of parallel Si (1 1 1) crystals was used for the measurement in transmission mode. Three consecutive ionization detectors, filled with gas mixtures of (first) 1250 mbar N_2, 750 mbar He; (second) 250 mbar Ar, 1000 mbar N_2, 750 mbar He; (third) 1000 mbar N_2, 300 mbar He, 700 mbar Ar, are at a path length of 30 cm. AutoBK algorithm[103] as implemented in Athena and a graphical front-end for the IFFEFIT software package[104] were used for the normalization of data and removal of background.

In Operando: XRD measurements were conducted using the same BRUKER D8 diffractometer with Cu-Kα source in an in situ cell fitted with Be window. The cell was cycled at a C/10 rate in the voltage window of 3.8–2.75 V.

3.4.3 Solid-state NMR

Room temperature ^{23}Na and ^{31}P solid-state NMR spectra were collected on $Na_{3+y}V_{2-y}Mg_y(PO_4)_3$ powder samples using a 7.05 T (300 MHz for ^{1}H) Bruker superwide bore NMR spectrometer equipped with an Avance III console and operating at Larmor frequencies of 79.39 and 121.5 MHz, respectively. Additional ^{23}Na solid-state NMR experiments were performed at 18.8 T (800 MHz for ^{1}H) on a Bruker standard bore NMR spectrometer equipped with an Avance III console and operating at a Larmor frequency of 211.65 MHz. All NMR spectra were obtained under magic angle spinning (MAS) at a rate of 30 kHz using a 2.5 mm double resonance HX probe. The ^{23}Na spectra were referenced against a 1 m NaCl solution ($\delta(^{23}\text{Na}) = 0$ ppm), and the ^{31}P spectra against a 1 m H_3PO_4 solution ($\delta(^{31}\text{P}) = 0$ ppm). Line shape analysis was carried out within the Bruker TopSpin software using the SOLA line shape simulation package. ^{23}Na and ^{31}P NMR spectra were recorded using a rotor-synchronized spin echo ($90°-\tau_r-180°-\tau_r-$acq). Low field (7.05 T) ^{23}Na spin echo was obtained using a 90° RF pulse of 0.8 μs and a 180° pulse of 1.6 μs at 300 W, with a recycle delay of 100 ms and averaged over 16 384 transients. High field (18.8 T) ^{23}Na NMR data were obtained using a 90° RF pulse of 0.97 μs and a 180° pulse of 1.94 μs at 200 W, with a recycle delay of 100 ms and averaged over 4096 transients. Low field (7.05 T) ^{31}P spin echo spectra were obtained using a 90° RF pulse of 1.1 μs and a 180° pulse of 2.2 μs at 250 W, with a recycle delay of 100 ms. Further details on the analysis of the NMR results are provided in Appendix A.

3.4.4 Magnetometry

The field-cooled (FC) and zero field-cooled (ZFC) DC magnetic susceptibility of $Na_3V_2(PO_4)_3$ was recorded on a commercial magnetic property measurement system (MPMS) over a 2–350 K temperature range. Measurements were performed under an

external field of 1000 Oe.

3.4.5 Electrochemical characterization

All electrochemical tests of the $Na_{3+y}V_{2-y}Mg_y(PO_4)_3$ cathodes were performed in two-electrode Swagelok cells. The cathode materials were mixed with carbon (C45 TIMCAL) and polyvinylidene fluoride (PVDF) binder in a weight ratio of 70:22:8 in N-methyl-2-pyrrolidone solvent. The slurry was coated on aluminum foil and dried under vacuum at 90 °C overnight. Thereafter, electrodes were punched into 10 mm diameter disks and the mass loading of active materials was found to be approximately 2.0 mg cm^{-2}. Sodium (Sigma, > 99%) metal was used as the counter electrode and 1 M $NaClO_4$ in ethylene carbonate/propylene carbonate/dimethyl carbonates (in a weight ratio of 4.5:4.5:0.1) with 3 wt% fluoroethylene carbonate was used as the electrolyte. The cells were assembled in an Ar-filled glovebox ($O_2 < 0.1$ ppm, $H_2O < 0.1$ ppm) and evaluated in a battery cycler (BT-lab, Biologic) over the voltage range 3.8–2.75 V versus Na^+/Na^0 at different C-rates. For GITT experiments, a current equivalent to a C/10 rate was applied for 1 hour followed by a 4-hour relaxation. Prior to the GITT experiments, the cells were cycled at C/10 for three cycles.

3.4.6 First principles calculations

Theoretical VASP Calculations: First principles density functional theory (DFT) calculations were performed using the projector augmented plane wave [105] formalism as implemented in Vienna ab initio Simulation Package [106, 107, 108]. The Perdew−Burke −Ernzerhorf [109] functional under the generalized gradient approximation was used to treat exchange and correlation effects. A Hubbard U correction term (UV = 3.25 eV) was employed to treat electronic correlation in transition metal 3d orbitals, with the effective

on-site exchange interaction parameter J fixed to 1 eV. A kinetic energy cutoff of 520 eV was used for PW expansion. The Brillouin Zone integration was performed using a $2\times2\times1$ Monkhorst−Pack grid. All systems were optimized using the conjugate-gradient algorithm with a convergence criterion of 10^{-4} eV on energy and 10^{-4} eV Å^{-1} for residual forces. Crystal symmetry was preserved for all configurations.

A $2 \times 1 \times 6$ supercell (with 252 atoms) was generated in order to achieve target compositions across the $Na_{3+y}V_{2-y}Mg_y(PO_4)_3$ series, and study local environments and possible Na^+ occupancies. The Supercell[110] code was utilized to generate multiple configurations with a stochastic distribution of V^{3+} and Mg^{2+} for the entire series. Na^+/vacancy configurations with the lowest computed electronic energy were retained for further calculations. These configurations were then geometry optimized, with an energy convergence criterion of 10^{-4} eV Å^{-1} for residual forces on the atoms, and the lowest energy ordering was determined (for more details, see Appendix A).

Bader charge analysis was performed using a code developed by Henkelman et al[111]., to determine the evolution of atomic charges and V−O bonding across the compositional series.

The climbing-image nudged elastic band (CI-NEB)[112] method was utilized to determine activation barriers for Na ion hopping. For single ion hops, a path was interpolated from a filled Na site to the nearest vacant Na site.

Theoretical Calculations—Crystal Calculations: Hybrid DFT/Hartree Fock (HF) calculations were performed in the spin-unrestricted approach to determine ^{23}Na and ^{31}P NMR parameters in monoclinic α-$Na_3V_2(PO_4)_3$, the Na-ordered form of $Na_3V_2(PO_4)_3$ (C2/c space group) determined by Chotard et al[34]., to be stable below $\approx$ 25.8 °C using single-crystal XRD. NMR calculations were carried out on ab initio optimized structures, with full optimization of the atomic positions and cell parameters. The CRYSTAL17 all-electron linear combination of atomic orbital code was used[113, 114], and two spin-

polarized exchange-correlation functionals based on the B3LYP form[115, 56, 57, 58] were applied, with Fock exchange weights of F0 = 20% (B3LYP or H20) and 35% (H35). Full details of the hybrid DFT calculations, including basis sets, numerical parameters, and the procedure for scaling the computed NMR parameters to compare with experimental results were outlined in Chapter 2.

3.5 Appendix A

3.5.1 Additional Details on Structural Enumeration and DFT Calculations

Before proceeding with electronic structure calculations, we generated all possible configurations of the $Na_{3+y}V_{2-y}Mg_y(PO_4)_3$ series using the Supercell code to identify the most stable arrangement of V/Mg species and most favorable distribution of Na amongst Na(1) and Na(2) lattice sites.

Firstly, the crystal structure of $Na_4VMg(PO_4)_3$ obtained from Rietveld analysis was used in a 2x1x3 conventional cell (containing 6 formula units) configuration to generate multiple random orderings of V/Mg and Na(1/)Na(2). Because Supercell uses the special quasirandom structures (SQS) approximation, this procedure generated 924 random prototypical disordered structures. We identified 100 symmetrically-unique structures by visual inspection using the VESTA software package. Structures with minor differences were disregarded to keep computational costs tractable. The lowest energy configuration was identified after geometry optimization of these symmetrically-unique structures. Thereafter, we replicated the $Na_4VMg(PO_4)_3$ conventional cell twice along the c axis, generating a 2x1x6 supercell in the process. This large supercell (12 formula units) allowed for intermediate compositions within the $Na_{3+y}V_{2-y}Mg_y(PO_4)_3$ series to be generated

by removing stoichiometric amounts of Na(1) and Na(2), while changing the V/Mg ratio. A similar procedure as the one employed for $Na_4VMg(PO_4)_3$ was followed to obtain symmetrically-unique optimized structures for all of the compositions of interest. The number of structures generated by the Supercell code and the number of symmetrically-unique structures used as a starting point for DFT calculations are listed in Table 3.1, Appendix C. The ground state V/Mg and Na1/Na2 configuration for each Na3+yV2-yMgy(PO4)3 composition corresponds to the structure with the lowest formation energy after structural relaxation, as shown with the convex hull in Figure 3.9 in Appendix C.

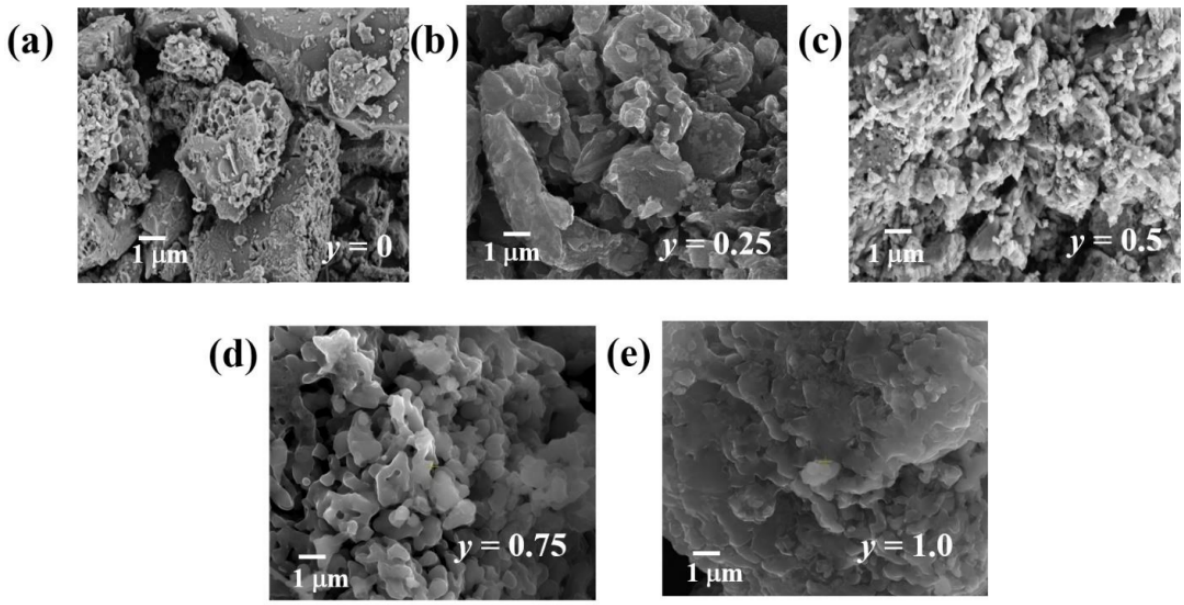

Figure 3.8: SEM images of NASICON $Na_{3+y}V_{2-y}Mg_y(PO_4)_3$ cathodes

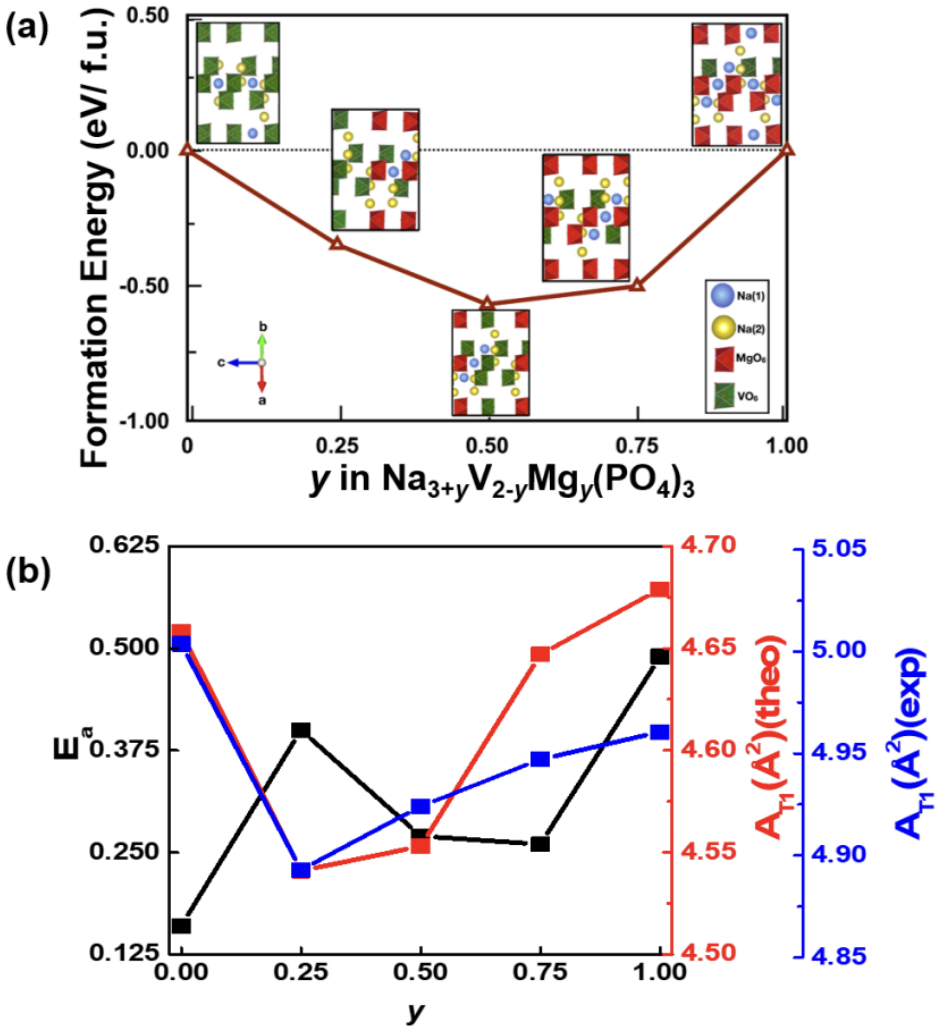

Figure 3.9: (a) Formation energies of the ground state $Na_{3+y}V_{2-y}Mg_y(PO_4)_3$ NASICON configurations as a function of y. The ground state structures are provided as insets. (b) Na^+ ion diffusion barriers (E_a) and diffusion bottleneck sizes (T1) computed for the ground state V/Mg and Na(1)/Na(2) orderings are plotted as a function of y in $Na_{3+y}V_{2-y}Mg_y(PO_4)_3$.

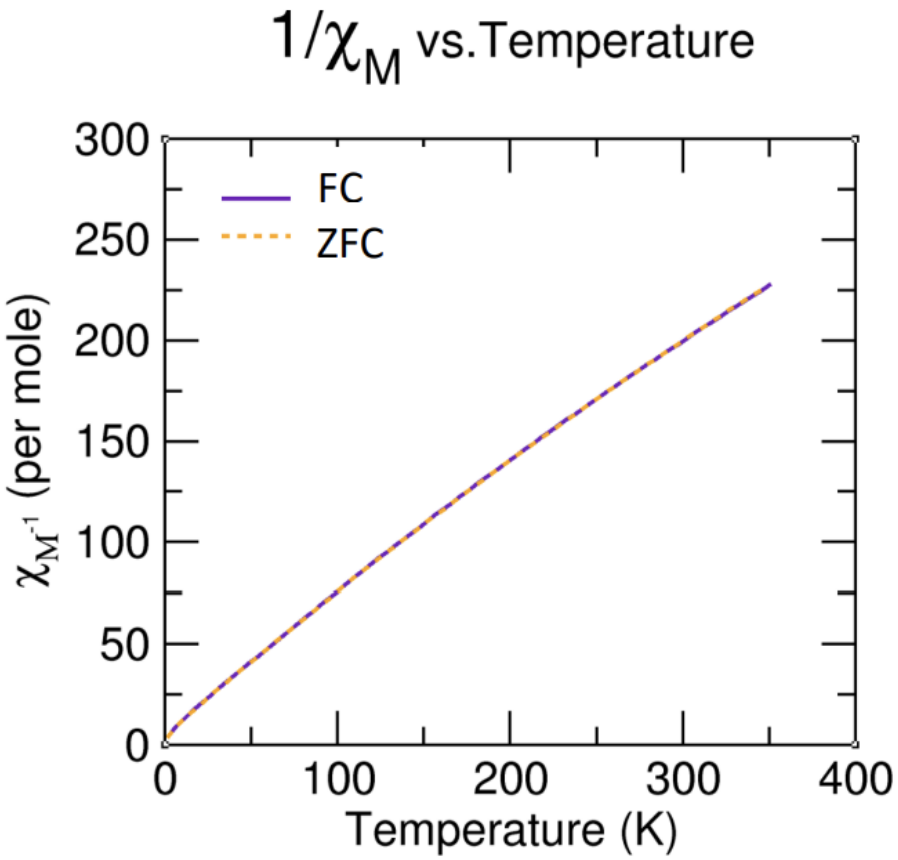

Figure 3.10: Experimental inverse magnetic susceptibility vs. temperature curve obtained from field cooled (FC) and zero field cooled (ZFC) magnetometry measurements on the $y = 0$ cathode over the 2-350 K temperature range at a magnetic field strength of 1000 Oe.

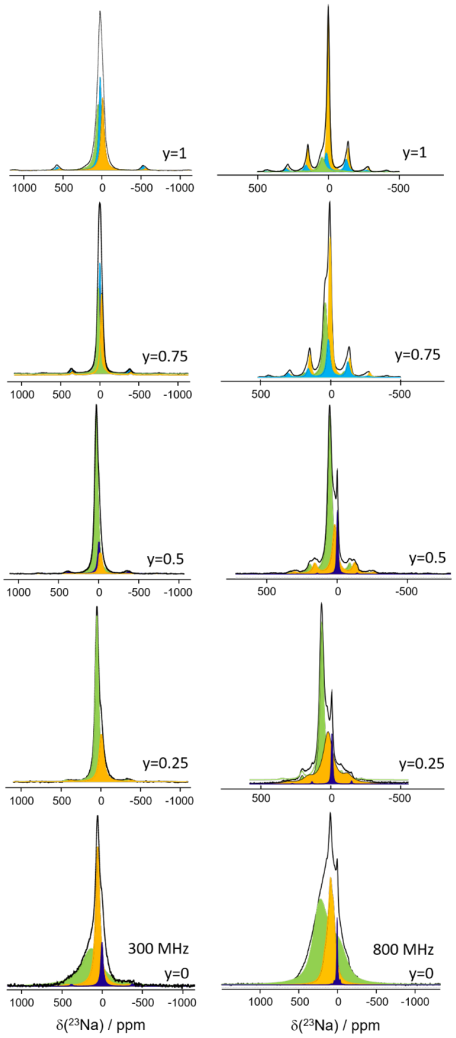

Figure 3.11: ^{23}Na NMR data collected on Mg-substituted $Na_{3+y}V_{2-y}Mg_y(PO_4)_3$ powder samples at (a) 7.05 T (300 MHz for 1H) and (b) 18.8 T (800 MHz for 1H). The yellow, green, light blue and dark blue signals in each spectrum correspond to the minimal set of ^{23}Na resonances that provide a satisfactory fit of the experimental data using a QUAD + CSA model. NMR parameters obtained from these fits are listed in Table 3.7. The dark blue signal at ca. 0 ppm in the data collected on y = 0, 0.25, and 0.5 samples is attributed to a diamagnetic impurity phase. This impurity phase is no longer clearly observed in spectra obtained on samples with a higher Mg content. Resonances near 0 ppm in these spectra may instead be due to ^{23}Na nuclei predominantly surrounded by diamagnetic Mg^{2+} species in the paramagnetic NASICON phase, which is also be consistent with their greater linewidth compared to that of the dark blue signals in y = 0, 0.25 and 0.5 samples.

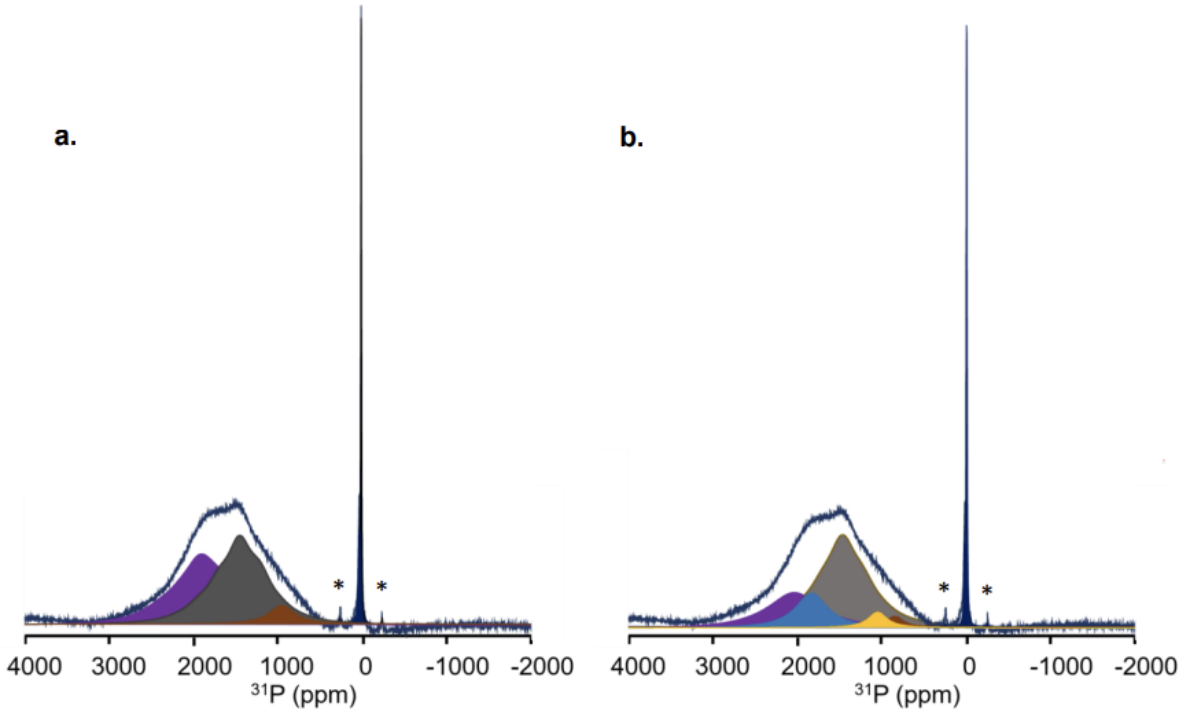

Figure 3.12: Example fits of the ^{31}P NMR data collected on the y = 0.5 pristine cathode: (a) using 3 environments and (b) using 5 environments. Both fits describe the observed lineshape equally well and highlight the ambiguity in fitting and assigning the spectra.

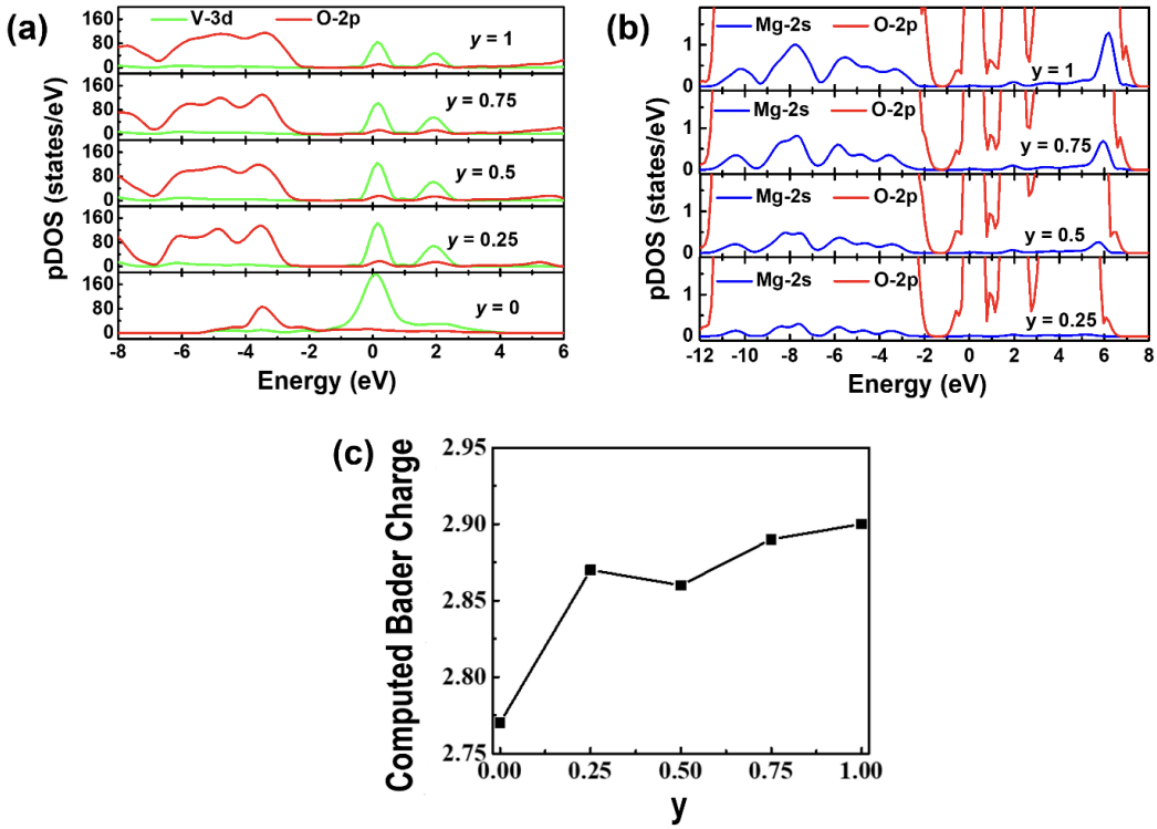

Figure 3.13: Calculated (a) and (b) pDOS and (c) Bader charges on vanadium in the $Na_{3+y}V_{2-y}Mg_y(PO_4)_3$ cathodes as a function of y

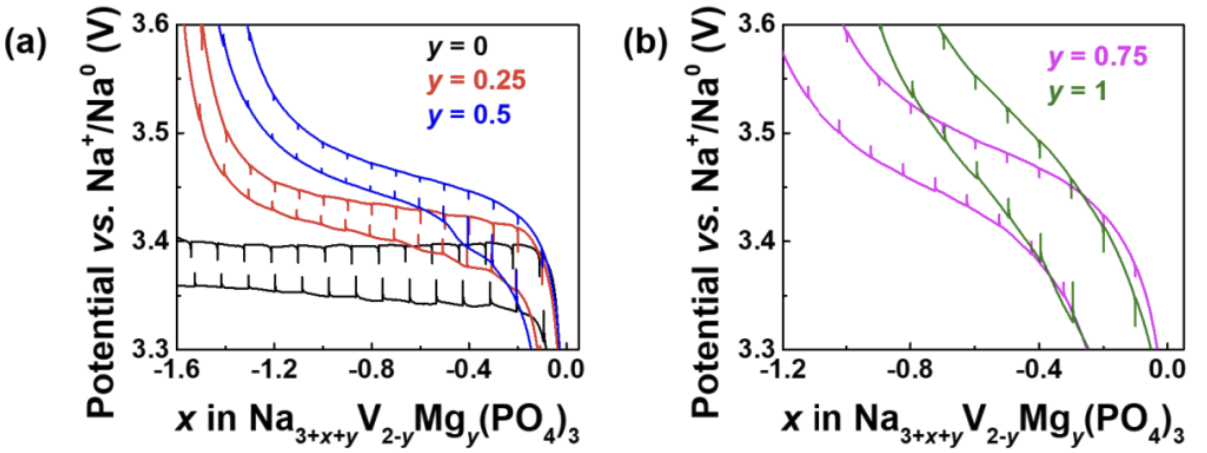

Figure 3.14: Enlarged views of the GITT profiles of the $Na_{3+y}V_{2-y}Mg_y(PO_4)_3$ cathodes

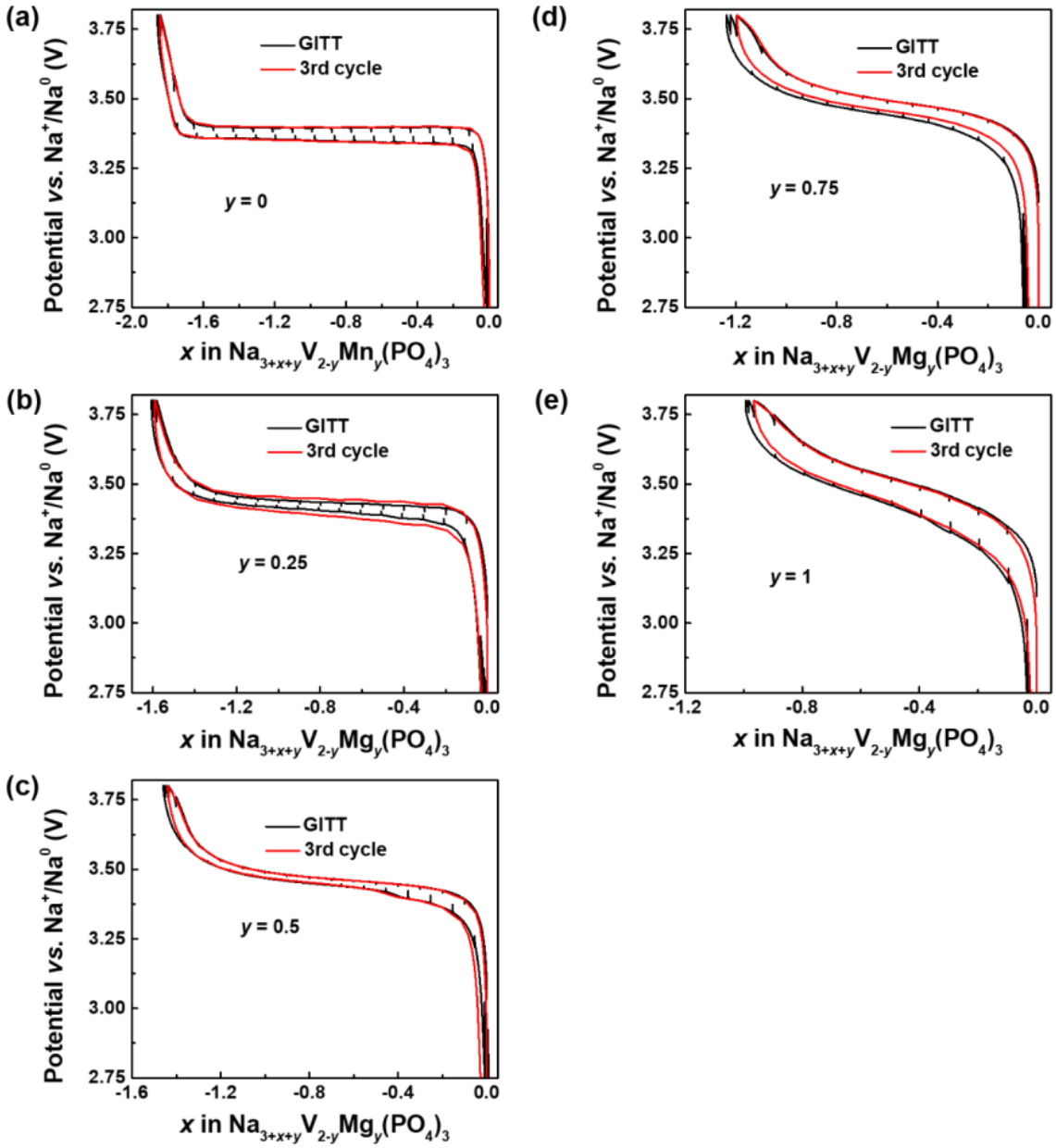

Figure 3.15: Comparison of voltage vs. composition profiles of $Na_{3+y}V_{2-y}Mg_y(PO_4)_3$ cathodes obtained from galvanostatic cycling (C/10 rate) and GITT protocols

$Na_{3+y}V_{2-y}Mg_y(PO_4)_3$	No. Of configurations generated from Supercell code	No. of symmetrically unique structures considered for DFT calculations
$y = 1$	924	100
$y = 0.75$	8910	800
$y = 0.50$	23,760	1200
$y = 0.25$	11,016	600
$y = 0$	1244	400

Table 3.1: Number of structural configurations generated using Supercell code and symmetrically unique structures considered for DFT calculations.

Structure	*a* / Å	*b* / Å	*c* / Å	α / °	β / °	γ / °
EXP	15.124	8.729	21.614	90.0	90.2	90.0
OPT H20	15.232	8.790	21.577	90.0	90.1	90.0
OPT H35	15.176	8.756	21.494	90.0	90.1	90.0

Table 3.2: Unit cell parameters obtained by Chotaed et al. [34] for the experimental α-$Na_3V_2(PO_4)_3$ structure, and for the structures optimized using H20 and H35 functionals in this work.

$Na_{3+y}V_{2-y}Mg_y(PO_4)_3$	Carbon content (%)
$y = 0$	3.25
$y = 0.25$	4.97
$y = 0.5$	4.51
$y = 0.75$	5.13
$y = 1$	4.07

Table 3.3: CHN elemental analysis of $Na_{3+y}V_{2-y}Mg_y(PO_4)_3$ samples

	$y = 0$	$y = 0.25$	$y = 0.5$	$y = 0.75$	$y = 1$
Lattice parameters (Å)	a = 8.724(1) c =21.806(6)	a = 8.759 (17) c = 21.775 (7)	a = 8.807 (33) c = 21.671 (12)	a = 8.846(17) c = 21.558 (7)	a = 8.877 (15) c = 21.424 (6)
Na(1) occupancy	0.790	0.722	0.757	0.913	1
Na(2) occupancy	0.713	0.767	0.848	0.899	0.964
V–O average bond length (Å)	2.054(1) × 6	2.038(2) × 6	2.042(5) × 6	2.045(3) × 6	2.046 (5) × 6
Na(1)–O average bond length (Å)	2.431(1)× 6	2.424(1)× 6	2.423(1)× 6	2.420(1)× 6	2.415(1)× 6
Na(2)–O average bond length (Å)	2.433(1)× 2 2.443(1)× 2 2.886(1)× 2 2.613(1)× 2	2.418(2)× 2 2.471(2)× 2 2.879(1)× 2 2.609(1)× 2	2.431(1)× 2 2.485(1)× 2 2.889(0)× 2 2.601(1)× 2	2.443(1)× 2 2.492(1)× 2 2.901(1)× 2 2.591(1)× 2	2.451(1)× 2 2.502(1)× 2 2.904(0)× 2 2.579(1)× 2
Reliability factors	R_{wp} = 3.9% Chi^2 = 3.47	R_{wp} = 3.62% Chi^2 = 3.54	R_{wp} = 2.98% Chi^2 = 2.75	R_{wp} = 3.43% Chi^2 = 2.71	R_{wp} = 3.70% Chi^2 = 2.62

Table 3.4: Lattice parameters and bond distances obtained from the Rietveld analysis of the powder XRD patterns of $Na_{3+y}V_{2-y}Mg_y(PO_4)_3$ samples.

$Na_{3+y}V_{2-y}Mg_y(PO_4)_3$	a (Å)	c (Å)	V-O (Å)	Na(1)-O (Å)	Na(2)-O (Å)
$y = 0$	8.865	42.96	2.00	2.405	2.53, 2.58, 2.90, 2.92
$y = 0.25$	8.868	42.930	2.01	2.400	2.51, 2.58, 2.91, 2.93
$y = 0.5$	8.872	42.888	2.04	2.39	2.45, 2.48, 2.55, 2.92
$y = 0.75$	8.871	42.904	2.06	2.40	2.48, 2.50, 2.55, 2.91
$y = 1$	8.883	42.784	2.07	2.38	2.45, 2.51, 2.93, 2.91

Table 3.5: Lattice parameters and bond distances obtained from DFT calculations of the $Na_{3+y}V_{2-y}Mg_y(PO_4)_3$ samples on ($1x1x2$ supercells)

$Na_{3+y}V_{2-y}Mg_y(PO_4)_3$	Co-ordination shell	Distances between atoms (r±Δr) (Å)	S_0^2	$\sigma^2(Å^2)$
y = 0	**V-O×3**	1.992 +0.071	0.76	0.00904
	V-O×3	1.926+0.096		0.00860
	V-P×6	3.399-0.069		0.03806
	V-Na(1)×3	3.137+0.019		0.01339
	V-Na(2)×3	3.845-0.013		0.01905
y = 0.25	**V-O×3**	2.003 -0.013	0.82	0.00764
	V-O×3	1.947+ 0.018		0.00468
	V-P×6	3.148+ 0.011		0.04588
	V-Na(1)×3	3.409+ 0.058		0.00511
	V-Na(2)×3	3.846+0.058		0.00979
y = 0.5	**V-O×3**	2.000 +0.019	0.87	0.00088
	V-O×3	1.961+0.043		0.00272
	V-P×6	3.411+ 0.012		0.00091
	V-Na(1)×3	3.151+ 0.087		0.01054
	V-Na(2)×3	3.856-0.038		0.00409
y = 0.75	**V-O×3**	2.003 -0.011	0.89	0.00168
	V-O×3	1.990+0.023		0.00184
	V-P×6	3.413+ 0.017		0.001191
	V-Na(1)×3	3.156+ 0.019		0.00072
	V-Na(2)×3	3.857+ 0.082		0.00478
y = 1	**V-O×3**	2.024+ 0.069	0.83	0.00389
	V-O×3	2.009+0.0167		0.00618
	V-P×6	3.444+ 0.023		0.00050
	V-Na(1)×3	3.189+ 0.0919		0.00982
	V-Na(2)×3	3.891- 0.0355		0.0297

Table 3.6: EXAFS parameters obtained from the fitting of $Na_{3+y}V_{2-y}Mg_y(PO_4)_3$ samples.

(a)

7.05 T	δ_{obs} (1) (ppm)	δ_{obs} (2) (ppm)	δ_{obs} (3) (ppm)	Rel. Integrated Ratios (S1 : S2 :S3)
$y = 0$	134	55	0	6.8 : 5.6 : 1.0
$y = 0.25$	44	-14	0	34.7 : 11.7 : 1.0
$y = 0.5$	26	-8	0	7.8 : 1.4 : 1.0
$y = 0.75$	23	4	-17	1.0 : 1.3 : 1.1
$y = 1$	10	-9	-30	1.2 : 1.1 : 1.0

(b)

18.8 T	δ_{obs} (1) (ppm)	δ_{obs} (2) (ppm)	δ_{obs} (3) (ppm)	Rel. Integrated Ratios (S1 : S2 :S3)
$y = 0$	182	86	-1	Significant signal overlap prevents accurate estimation of relative integrated intensities
$y = 0.25$	71	24	-3	9.3 : 9.0 : 1.0
$y = 0.5$	51	20	-3	8.1 : 4.3 : 1.0
$y = 0.75$	43	19	7	1.5 : 1.0 : 2.1
$y = 1.0$	48	17	4	1.0 : 1.8 : 5.1

Table 3.7: Observed chemical shifts and relative integrated intensities of the various ^{23}Na resonances determined from fits of the NMR data collected on $Na_{3+y}V_{2-y}Mg_y(PO_4)_3$ (y = 0, 0.25, 0.5, 0.75, and 1.0) powder samples at (a) 7.05 T and (b) 18.8 T using a QUAD + CSA model.

Significant differences are observed between the chemical shifts and relative intensities of the ^{23}Na resonances at 7.05 T and 18.8 T. These discrepancies could be due to:

1. differential motional averaging of the ^{23}Na NMR signals arising from Na(1)- and Na(2)-type local environments at 7.05 and 18.8 T. Indeed, signal averaging results from chemical exchange between various Na sites in the NASICON structure at a higher rate than the frequency separation between NMR resonances ($\Delta\nu$, in Hz) corresponding to the sites in exchange. $\Delta\nu$ (in Hz) scales with the magnetic field strength and signals that may be averaged out at 7.05 T could appear as distinct peaks at 18.8 T. That is, the NMR timescale is 2.67x faster at 18.8 T compared to 7.05 T;

2. the second-order quadrupolar shift, introducing a field-dependance to the observed chemical shift ($\delta_{obs} = \delta_{iso} + \delta_Q$) of Na nuclei in Na(1) and Na(2) sites in the NASICON structure. This field-dependance in turn impacts the propensity for resonances corresponding to various Na environments in the samples to average out at 7.05 T vs. 18.8 T;

3. differences in NMR signal relaxation times at 7.05 T and at 18.8 T, which has an effect on the relative intensities of the observed resonances.

4. the difficulty of fitting overlapping NMR signals, and errors associated with these fits.

Environment	Parameter	OPT H20	OPT H35
Na(1a) (x4)	δ_{iso}/ppm	297	195
	$\Delta\delta$/ppm	1609	1607
	η	0.1	0.1
	C_Q/MHz	-3.50	-3.32
	η_Q	0.1	0.0
	δ_Q/ppm	-49	-44
	$\delta_{iso} + \delta_Q$/ppm	248	152
Na(1b) (x8)	δ_{iso}/ppm	422	306
	$\Delta\delta$/ppm	1444	1450
	η	0.0	0.0
	C_Q/MHz	-4.28	-4.15
	η_Q	0.1	0.1
	δ_Q/ppm	-73	-69
	$\delta_{iso} + \delta_Q$/ppm	349	237
Na(2a) (x8)	δ_{iso}/ppm	88	-7
	$\Delta\delta$/ppm	1202	1209
	η	0.7	0.7
	C_Q/MHz	-3.73	-3.64
	η_Q	0.2	0.2
	δ_Q/ppm	-56	-54
	$\delta_{iso} + \delta_Q$/ppm	32	-60
Na(2b) (x8)	δ_{iso}/ppm	78	-24
	$\Delta\delta$/ppm	1040	1061
	η	1.0	0.9
	C_Q/MHz	-3.10	-3.05
	η_Q	0.4	0.3
	δ_Q/ppm	-40	-38
	$\delta_{iso} + \delta_Q$/ppm	39	-62
Na(2c) (x8)	δ_{iso}/ppm	231	108
	$\Delta\delta$/ppm	1249	1251
	η	0.6	0.6
	C_Q/MHz	-4.20	-4.10
	η_Q	0.1	0.1
	δ_Q/ppm	-70	-67
	$\delta_{iso} + \delta_Q$/ppm	161	41

Table 3.8: First principles ^{23}Na NMR parameters computed for α-$Na_3V_2(PO_4)_3$ using the CRYSTAL17 code. NMR shifts are computed using two hybrid correlation-exchange functionals (H20 and H35), as it has been found that shifts computed using the H20 (H35) functional provide an upper (lower) bound to the experimentally-observed chemical shift.[64] The computed NMR properties have been scaled using a magnetic scaling factor $\Phi = 0.030755$, and are comparable to room temperature ^{23}Na NMR data obtained at a 7.05 T external magnetic field. There are five Na local environments in α-NVP, denoted Na(1a), Na(1b), Na(1c), Na(2a), and Na(2b) with multiplicities specified in parenthesis in the table below. δ_{iso} is the isotropic Fermi contact shift, $\Delta\delta$ and η are the electron-nuclear dipolar anisotropy and asymmetry parameters, respectively, C_Q is the quadrupolar coupling constant, η_Q is the quadrupolar asymmetry, δ_Q is the second-order quadrupolar shift, and $\delta_{obs} = \delta_{iso} + \delta_Q$ is the observed chemical shift.

OPT HYB20	**ppm**	**Intensity**
If average over Na(1) sites	316	1
If average over Na(2) sites	77	2
If average over Na(1a), Na(1b), Na(2c) sites	254	5
If average over Na(2a), Na(2b) sites	35	4
OPT HYB35	ppm	Intensity
If average over Na(1) sites	209	1
If average over Na(2) sites	-27	2
If average over Na(1a), Na(1b), Na(2c) sites	142	5
If average over Na(2a), Na(2b) sites	-61	4

Table 3.9: Analysis of the computed ^{23}Na NMR parameters for the assignment of the average resonances observed experimentally at 7.05 T.

If we average over the resonances for Na(1a), Na(1b), Na(2c) sites, and over the Na(2a) and Na(2b) sites from Table 3.7, we can account for the experimentally observed resonances at 134 and 55 ppm in the low-field (7.05 T) NMR data with a relative integrated intensity ratio equal to 1.21. This value of the relative integrated intensity ratio is close to the 1.25 ratio obtained from the multiplicity of the Na sites in the unit cell.

Interaction	Geometry	PA	PB	PC	PD	PE
1st	d(P – V) / Å	3.394 Å,	3.358 Å,	3.423 Å,	3.364 Å,	3.317 Å,
	P – O – V / °	136.45°	139.87°	139.88°	141.74°	138.46°
2nd	d(P – V) / Å	3.360 Å,	3.358 Å,	3.438 Å,	3.464 Å,	3.435 Å,
	P – O – V / °	139.73°	139.75°	146.69°	159.85°	162.32°
3rd	d(P – V) / Å	3.410 Å,	3.462 Å,	3.424 Å,	3.403 Å,	3.445 Å,
	P – O – V / °	148.77°	152.25°	157.40°	143.91°	140.32°
4th	d(P – V) / Å	3.448 Å,	3.463 Å,	3.370 Å,	3.420 Å,	3.440 Å,
	P – O – V / °	155.64°	152.53°	148.11°	146.53°	148.90°

Table 3.10: P-O-V bond pathway geometries for PA, PB, PC, PD, and PE in α-NVP. These are given for H20 optimized (OPT) structure obtained from CRYSTAL17 calculations

Parameter	H20	H35	Average
$\Delta\delta_{iso,EC}$/ppm	618	370	494
$\Delta\delta_{iso,AC}$/ppm	1068	919	994
$\Delta\delta_{iso,BC}$/ppm	1392	1350	1371
$\Delta\delta_{iso,DC}$/ppm	1701	1453	1577

Table 3.11: Predicted chemical shift differences between ^{31}P NMR signals associated with crystallographically-distinct P sites in the α-NVP structure (PA, PB, PC, PD, and PE), and computed using the H20 and H35 functionals as implemented in the CRYSTL17 code. ^{31}P chemical shift differences, rather than absolute ^{31}P chemical shifts, are considered here since our previous work[65] has shown tha the former is more reliable than the latter. Computed NMR shifts have been scaled using a magnetic scaling factor $\Phi = 0.030755$, and are comparable to room temperature ^{31}P NMR data obtained at a 7.05 T external magnetic field. The chemical shift of a ^{31}P nucleus in a PC-type environment in α-NVP is used as a reference for the calculations of chemical shift differences, as it has the lowest absolute chemical shift. For example, the chemical shift difference between ^{31}P nuclei in PA and PC environments is denoted $\Delta\delta_{iso,AC}$

$Na_{3.5}V_{1.5}Mg_{0.5}(PO_4)_3$ (S.G.: $R\bar{3}c$)							
	a (Å)	**c (Å)**	**V (Å^3)**	**Na(1) occupancy**	**Na(2) occupancy**	**R_{wp}**	**Chi^2**
Pristine	8.807(11)	21.672(5)	1455.6(3)	0.758(7)	0.848(2)	2.6%	2.12
Charged 3.8 V	8.528(13)	21.634(4)	1362.5(4)	0.742(3)	0.688(12)	3.02%	1.88
	8.620(2)	21.389(6)	1376.4(6)	0.702(17)	0.824(7)	2.33%	
Discharged 2.75 V	8.777(6)	21.672(2)	1446.0(2)	0.751(14)	0.839(6)	3.17%	3.92

$Na_4VMg(PO_4)_3$ (S.G.: $R\bar{3}c$)							
	a (Å)	**c (Å)**	**V (Å^3)**	**Na(1) occupancy**	**Na(2) occupancy**	**R_{wp}**	**Chi^2**
Pristine	8.851(11)	21.487(3)	1457.9(3)	0.981(8)	0.977(3)	2.19%	2.95
Charged 3.8 V	8.739(10)	21.563(3)	1426.2(3)	0.867(14)	0.688(3)	2.79%	2.49
Discharged 2.75 V	8.852(5)	21.454(14)	1456.00(15)	0.967(9)	0.953(4)	3.61%	4.26

Table 3.12: Refined cell parameters and unit cell volumes of ex-situ $Na_{3+y}V_{2-y}Mg_y(PO_4)_3$ (y = 0.5 and 1.0) cathodes

Chapter 4

High voltage behavior of NASICON $\mathbf{Na_{3+y}V_{2-y}Mg_y(PO_4)_3}$ cathodes

This chapter builds on the work covered in Chapter 3 to investigate the $Na_{3+y}V_{2-y}Mg_y(PO_4)_3$ compositional series when cycled at high voltage (4.2−2.75 V). Through ex situ ^{23}Na, ^{31}P, and ^{51}V ssNMR analysis along with first principles calculations, we elucidate the mechanisms responsible for structural degradation during electrochemical cycling. After the 1st cycle, there is a clear change in the voltage−capacity profiles hinting at bulk structural rearrangement at high voltage further supported by ex situ ^{23}Na, ^{51}V, and ^{31}P ssNMR. In a previous study, bulk structural degradation has been attributed to V cation migration [87], however, here we propose that the mechanism underlying structural degradation is Mg cation migration into the Na(2) sites of the NVP framework as evidenced by first principles calculations performed in collaboration with Madhulika Mazumder of the Swapan K. Pati group. Synthesis and electrochemical characterization was performed in collaboration with the group of Premkumar Senguttuvan at the School of Advanced Materials, Jawaharlal Nehru Centre for Advanced Scientific Research, Jakkur, Bangalore, Karnataka, 560064 India.

4.1 Introduction

While Li-ion batteries have dominated the energy storage market for several decades, Na-ion batteries have garnered attention as potential alternatives owing to the greater abundance and lower cost of Na precursors when compared to their Li counterparts, and the ability to use Al current collectors at the anode. The development of high voltage and high capacity Na-ion cathodes is the key for the successful realization of high energy density sodium-ion batteries (NIBs)[116, 117]. Much of the focus has been on Na-ion layered oxide electrodes, but these compounds suffer from lower intercalation voltages, rapid capacity decay due to multiple structural transformations during cycling and air/moisture instability issues[11]. On the contrary, polyanionic cathodes offer higher intercalation voltages, and enhanced structural, chemical and thermal stabilities[118].

NASICON-type transition metal phosphates have received significant attention as NIB cathodes due to their long cycle lifetimes and high rate performance[72]. Given their chemical composition of $Na_xMM'(PO_4)_3$, different combinations of transition metals with varying oxidation states can be substituted on the M and M' sites and modulate the Na stoichiometry within the range $0 \leq x \leq 4$ [119]. Among the compositions explored so far, vanadium- and manganese-based NASICON cathodes are attractive due to their multielectron reactions based on the $V^{5+}/V^{4+}/V^{3+}$ and $Mn^{4+}/Mn^{3+}/Mn^{2+}$ redox couples[120]. Goodenough et al. were the first to explore the fully sodiated NASICON-$Na_4VMn(PO_4)_3$ cathode, which demonstrates a two-step voltage-capacity profile with a reversible capacity of $\approx$ 100 mAh/g (i.e., equivalent to the exchange of 2 Na per formula unit over the $3.8-2.75$ V window[85]. In later studies, the cycling window was extended to $4.2-2.75$ V so that a greater amount of sodium ions could be exchanged, thereby increasing the material's capacity[33, 86]. However, $Na_4VMn(PO_4)_3$ undergoes an irreversible structural transformation above 4.0 V, leading to fast capacity

decay. Similar structural transformations have been observed for other Mn-rich NASICON cathodes[88, 98]. Although synchrotron X-ray diffraction (XRD) and X-ray absorption (XAS) studies have attributed the structural collapse to the extraction of Na ions from the Na(1) site during high voltage charging, the exact nature of the local structural changes responsible for performance degradation remains unclear. To better comprehend the evolution of the local structure during high voltage cycling, we have designed a series of NASICON-$Na_{3+y}V_{2-y}Mg_y(PO_4)_3$ cathodes that are structurally analogous to the V/Mn-based NASICON series. Unlike in $Na_4VMn(PO_4)_3$, Na (de)intercalation from $Na_{3+y}V_{2-y}Mg_y(PO_4)_3$ solely relies on vanadium redox since Mg is electrochemically inactive. As the Mg content is increased, the reversible capacity decreases and the Na (de)intercalation mechanism evolves from a two-phase reaction to a solid solution-like mechanism over the 3.8−2.75 V range as shown in Chapter 3[32]. Building upon the work presented in Chapter 3, the present chapter focuses on the high voltage behavior of NASICON-type $Na_{3+y}V_{2-y}Mg_y(PO_4)_3$ (y = 0, 0.25, 0.5, 0.75, and 1.0) cathodes during cycling over a larger voltage window of 4.2−2.75 V. Here, the Mg-substituted cathodes also show poor capacity retention/ rapid capacity degradation during high voltage cycling in stark contrast to the good capacity retention observed via solid-state NMR and X-ray diffraction in the 3.8−2.75 V cycling window covered in Chapter 3. Previous reports on a similar Cr substituted $Na_3VCr(PO_4)_3$ have attributed the structural degradation to V cation migration into Na(1) sites during deep desodiation [87] at high voltage, however, here ^{51}V ssNMR does not suggest that this occurs in the magnesium doped analogue. Rather, first principles calculations suggest that the mechanism of structural degradation during high voltage cycling for $Na_4VMg(PO_4)_3$ is driven by Mg migration into the Na(2) sites, as opposed to the V migration into Na(1) sites seen in the $Na_3VCr(PO_4)_3$ system. Furthermore, using long-range and local structure probes, the structural degradation processe(s) may also stem from the distortion of VO_6 octahedra in $Na_{3+y}V_{2-y}Mn_y(PO_4)_3$,

triggered by the removal of Na from the Na(1) site.

4.2 Results and Discussion

4.2.1 Structural and electrochemical characterization upon high voltage cycling

NASICON $Na_{3+y}V_{2-y}Mg_y(PO_4)_3$ cathodes (y = 0, 0.25, 0.5, 0.75, and 1) were synthesized using a sol-gel assisted solid-state route outlined in Chapter 3 and in our previous work[32]. All of the Bragg peaks of the XRD patterns collected on the pristine cathode samples could be indexed to the rhombohedral $R\bar{3}c$ space group. In Chapter 3, the electrochemical Na (de)intercalation properties of this series of cathodes was investigated over the 3.8−2.75 V voltage window, where the V^{4+}/V^{3+} redox couple is activated. Gradual susbtitution of redox-inactive Mg for V was shown to reduce the reversible capacity, while also leading to a Na (de)intercalation mechanism evolving from a two-phase process to a solid solution-like process. More importantly, the NASICON was generally found to be very stable upon cycling over this voltage range.

The Na (de)intercalation properties of the same series of cathodes was herein explored over a wider voltage window of 4.2−2.75 V vs. Na^+/Na^0. The voltage profiles obtained for $Na_{3+y}V_{2-y}Mg_y(PO_4)_3$ cathodes (y = 0, 0.25, 0.5, 0.75, and 1) at a rate of C/10 are shown in Figure 4.1a, no additional redox feature is observed for the unsubstituted (i.e. $Na_3V_2(PO_4)_3$) cathode compared to cycling over the narrower voltage window (3.8−2.75 V). On the other hand, the first charge voltage profiles of the Mg-substituted cathodes exhibit an additional voltage feature at ≈ 3.9 V vs. Na^+/Na^0, attributed to V^{4+}/V^{5+} redox based on prior studies of related, V-based NASICON cathodes [121, 122, 123, 124, 83]. The initial charge capacity of the y = 0.25, 0.5, 0.75 and 1 cathodes reaches

102.5, 116.3, 108.3 and 104.3 mAh/g, corresponding to the extraction 1.74, 1.97, 1.83 and 1.76 Na per formula unit, respectively. Interestingly, on subsequent discharge, the Mg-substituted cathodes display S-shaped voltage profiles indicative of a solid solution reaction mechanism. These changes can be better visualized in the differential capacity (dQ/dV vs. V) curves shown in Figure 4.1b. The dQ/dV profiles of the Mg-substituted cathodes contain two oxidation peaks at $\approx 3.4-3.6$ and 3.9 V vs. Na^+/Na^0 on charge, corresponding to V^{3+} to V^{4+} and V^{4+} to V^{5+} oxidation, respectively. However, the discharge dQ/dV profiles exhibit a broad voltage feature at $3.4-3.5$ V vs. Na^+/Na^0, ascribed to mixed $V^{5+}/V^{4+}/V^{3+}$ redox [121, 125]. From the 2nd cycle onwards, the Mg-substituted cathodes display S-shaped charge-discharge voltage profiles (Figure 4.1c). The cycling stability of the $Na_{3+y}V_{2-y}Mg_y(PO_4)_3$ cathodes was assessed at a rate of C/10 over the $4.2-2.75$ V vs. Na^+/Na^0 window. After 30 cycles, the y = 0.25, 0.5, 0.75 and 1 cathodes deliver discharge capacities of 76, 70, 54 and 42 mAh/g, respectively (Figure 4.1d), corresponding to a capacity retention of 74.1, 60.2, 50.1, and 40.3 %.

These changes in the electrochemical features of the $Na_{3+y}V_{2-y}Mg_y(PO_4)_3$ cathodes indicate a possible structural transformation during high voltage cycling. To investigate this possibility, we performed in-situ XRD measurements on the y = 0.5 and 1.0 cathodes over the 4.2–2.75 V voltage window at a C/10 rate, with XRD patterns collected during the first charge-discharge cycle shown in Figure 4.2. It is evident that, during the first charge process, the y = 0.5 cathode displays an initial solid solution mechanism followed by a two-phase transformation up to 3.8 V vs. Na^+/Na^0. At higher potentials, desodiation proceeds via another solid solution process up to 4.2 V vs. Na^+/Na^0, resulting in two rhombohedral NASICON phases between 3.8 and 4.2 V. On subsequent discharge to 2.75 V, corresponding to Na reinsertion into the NASICON structure, the y = 0.5 cathode exhibits a complete solid solution behavior.

In the case of the y = 1.0 cathode, two solid solution domains are observed over the

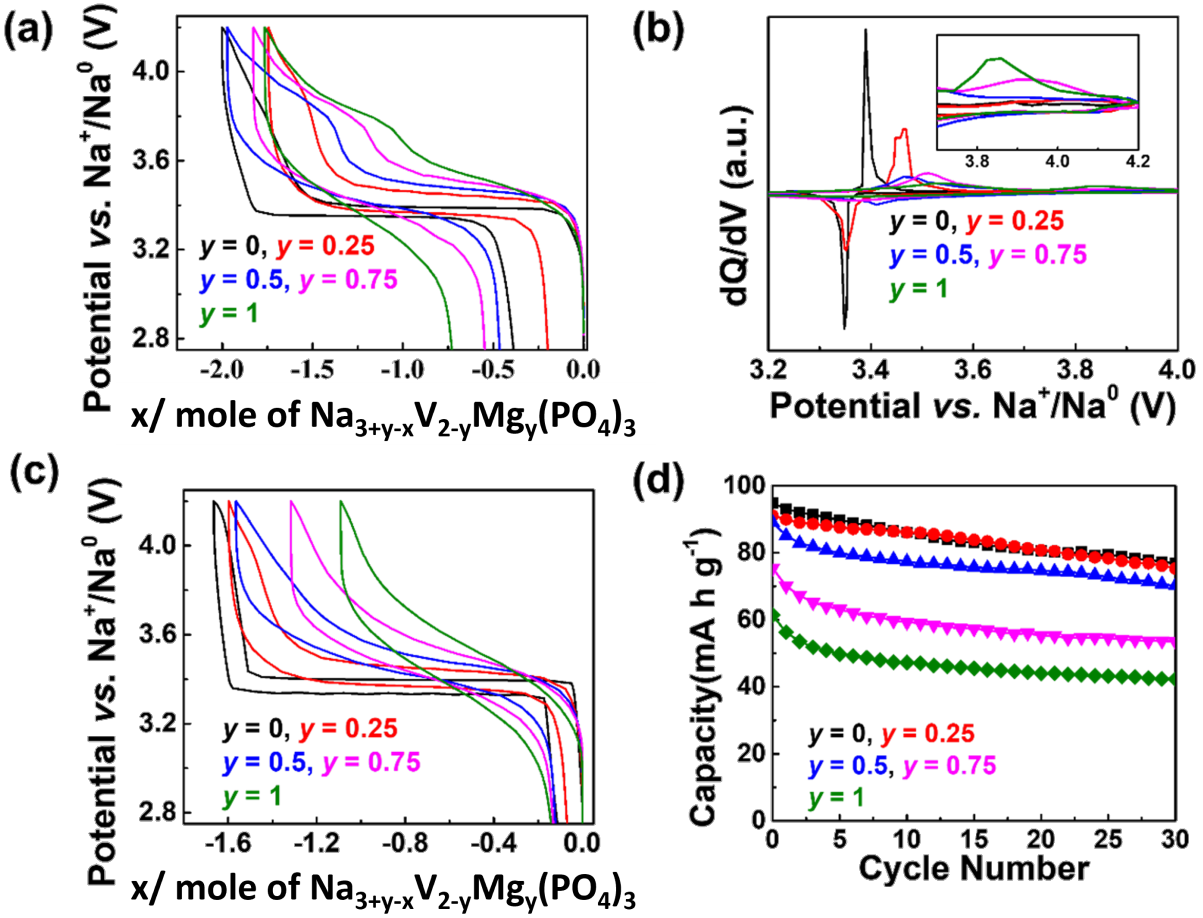

Figure 4.1: a) First cycle voltage vs. composition (x). b) Differential capacity (dQ/dV vs. V) profiles. c) Second cycle vs. composition (x). d) Cycling performance of the $Na_{3+y}V_{2-y}Mg_y(PO_4)_3$ cathodes.

compositional ranges "$Na_4VMg(PO_4)_3$-$Na_3VMg(PO_4)_3$" (OCV-3.8 V) and "$Na_3VMg(PO_4)_3$–$Na_{2.25}VMg(PO_4)_3$ " as charging continues up to 4.2 V. The subsequent discharge process proceeds via a complete solid solution, similar to the y = 0.5 compound. Notably, the XRD patterns collected on the y = 0.5 and 1 cathode samples after the first charge-discharge cycle do not coincide with those obtained on the pristine electrodes, implying bulk structural transformation as has been reported for other V-based NASICON cathodes [118, 86, 88]. To better understand the structural evolution of the y = 0.5

and 1 cathodes during high voltage cycling, ex-situ synchrotron XRD (SXRD) patterns were collected at different states of charge (SOCs) (Figure 4.3). Rietveld analysis of the XRD patterns and the corresponding crystallographic parameters are displayed in Table 4.2. Both cathodes retain a rhombohedral R$\bar{3}$c structure upon cycling over a restricted voltage window of 3.8−2.75 V (Figure 4.8, Appendix B), in agreement with our previous report[32].

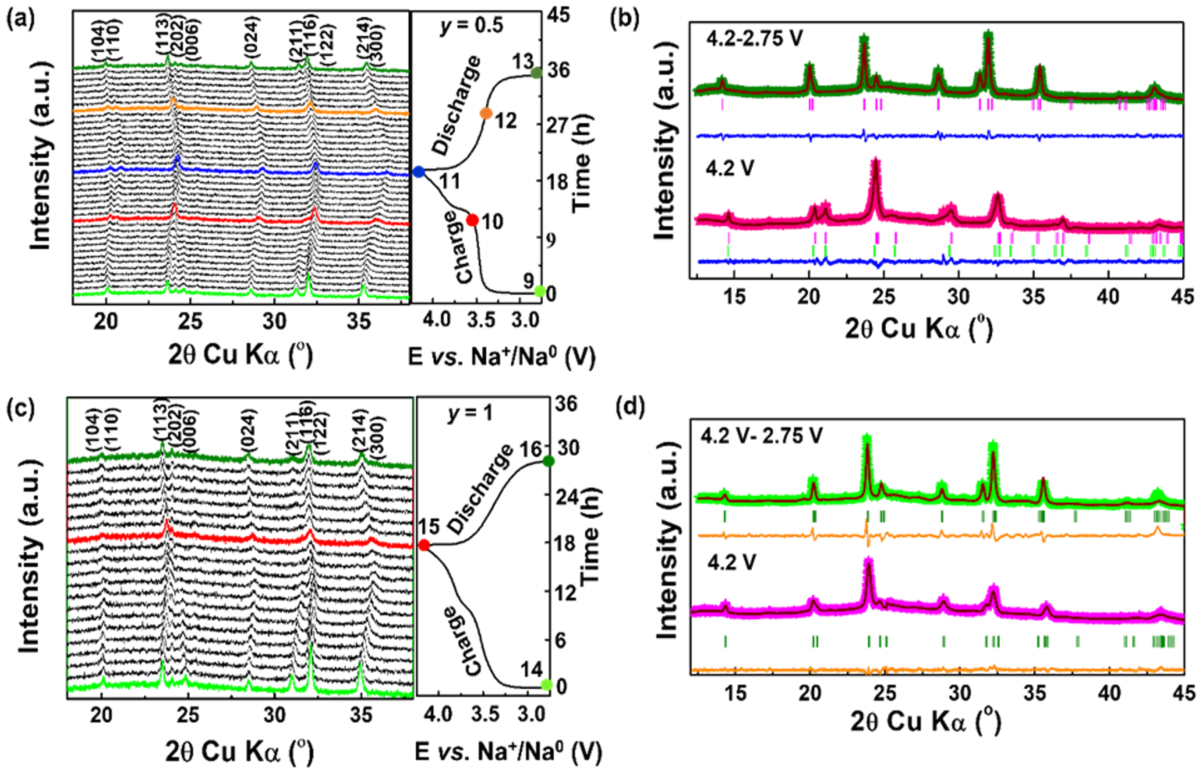

Figure 4.2: In situ (a,c) and ex situ pattern refinements (b,d) of the y = 0.5 and 1.0 cathodes collected over the 4.2 - 2.75 V vs Na^+/Na^0 voltage range.

In the case of y = 0.5 cathode, Rietveld refinements indicate the presence of two NASICON-type phases (space group: R$\bar{3}$c) at 3.8 V (Figure 4.3a) and at 4.2 V (Figure 4.3b), which agrees well with the in-situ XRD results. The cathode harvested at 4.2 V shows anisotropic lattice parameter changes induced by the removal of Na from Na(1)

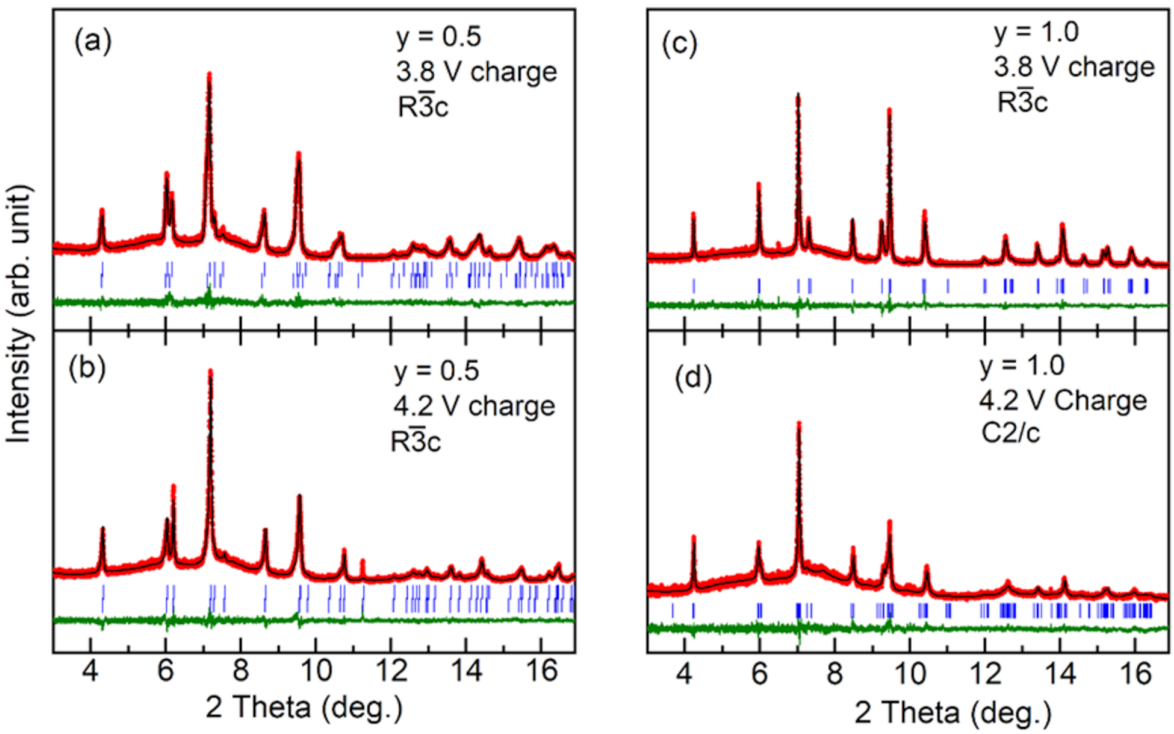

Figure 4.3: Rietveld refinements of synchrotron XRD patterns collected on the (a,b) y = 0.5 and (c,d) y = 1.0 cathodes at different states of charge.

sites (Table 4.2, Appendix B). The y = 0.5 cathode harvested at the end of discharge after charge to 4.2 V (Figure 4.2b) shows significant lattice parameter changes compared to the pristine cathode structure. When it comes to the y = 1 cathode, the XRD patterns obtained at 3.8 and 4.2 V indicate the presence of a single NASICON phase (Figures 4.3c and 4.3d). While the pattern at 3.8 V charge can be indexed using the R$\bar{3}$c space group, a refinement of the pattern obtained at 4.2 V charge using the same space group was unsuccessful, indicating a change in crystal symmetry as more Na is extracted from the structure. To identify the crystal symmetry of the 4.2 V cathode sample, we performed a subgroup analysis using ISODISTORT (Figure 4.9, Appendix B) [126, 127]. There are five isotropy subgroups (R$\bar{3}$c, R$\bar{3}$, R32, C2/c and P$\bar{3}$c1) in the

R$\bar{3}$c space group. Among them, a refinement of the data using the C2/c space group led to the best fit (Figure 4.10, Appendix B). The chemical formulae for the y = 1 samples on charge to 3.8 V and 4.2 V, obtained from the Rietveld refinements, are $Na_{2.91}$VMg(PO4)3 and $Na_{2.45}$VMg(PO4)3, respectively. Hence, an additional 0.46 moles of Na is removed between 3.8 to 4.2 V, reducing the symmetry of the cathode from rhombohedral R$\bar{3}$c to monoclinic C2/c. Notably, the symmetry of the cathode is unchanged (i.e., C2/c) and the Na sites are not completely refilled upon subsequent discharge from 4.2 to 2.75 V (Figure 4.8, Appendix B), corroborating the irreversibility observed with electrochemical testing and in-situ XRD.

4.2.2 ^{23}Na solid-state NMR

Whilst in-situ and ex-situ XRD analyses reveal changes to the bulk structure of the y = 0.5 and 1 cathodes, local structure probes provide additional insights into the processes triggering the structural collapse observed during high voltage cycling. To this end, we performed ^{23}Na, ^{31}P and ^{51}V solid-state NMR (ssNMR) experiments on ex situ $Na_{3+y}V_{2-y}Mg_y(PO_4)_3$ (y = 0.5, 1.0) cathode samples to monitor changes in the Na, P, and V local environments, respectively, during cycling.

Focusing first on ^{23}Na ssNMR, similar to what was done in Chapter 3 given the quadrupolar and paramagnetic nature of Mg-NVP, here we also report the observed shift $\delta_{obs} = \delta_{iso} + \delta_Q$, where δ_{iso} is the paramagnetic shift contribution and δ_Q is the second-order quadrupolar shift contribution. All ^{23}Na ssNMR parameters obtained from fits of the ex-situ data for the $y = 0.5$ and $y = 1.0$ cathodes are listed in Tables 4.8 and 4.9 in Appendix B. The ^{23}Na ssNMR spectrum collected at 7.05 T and at 30 kHz magic angle spinning (MAS) on the pristine $y = 0.5$ cathode consists of at least three overlapping signals with observed shifts (δ_{obs}) of 27, 0, and −23 ppm (Figure 4.4a). The relatively

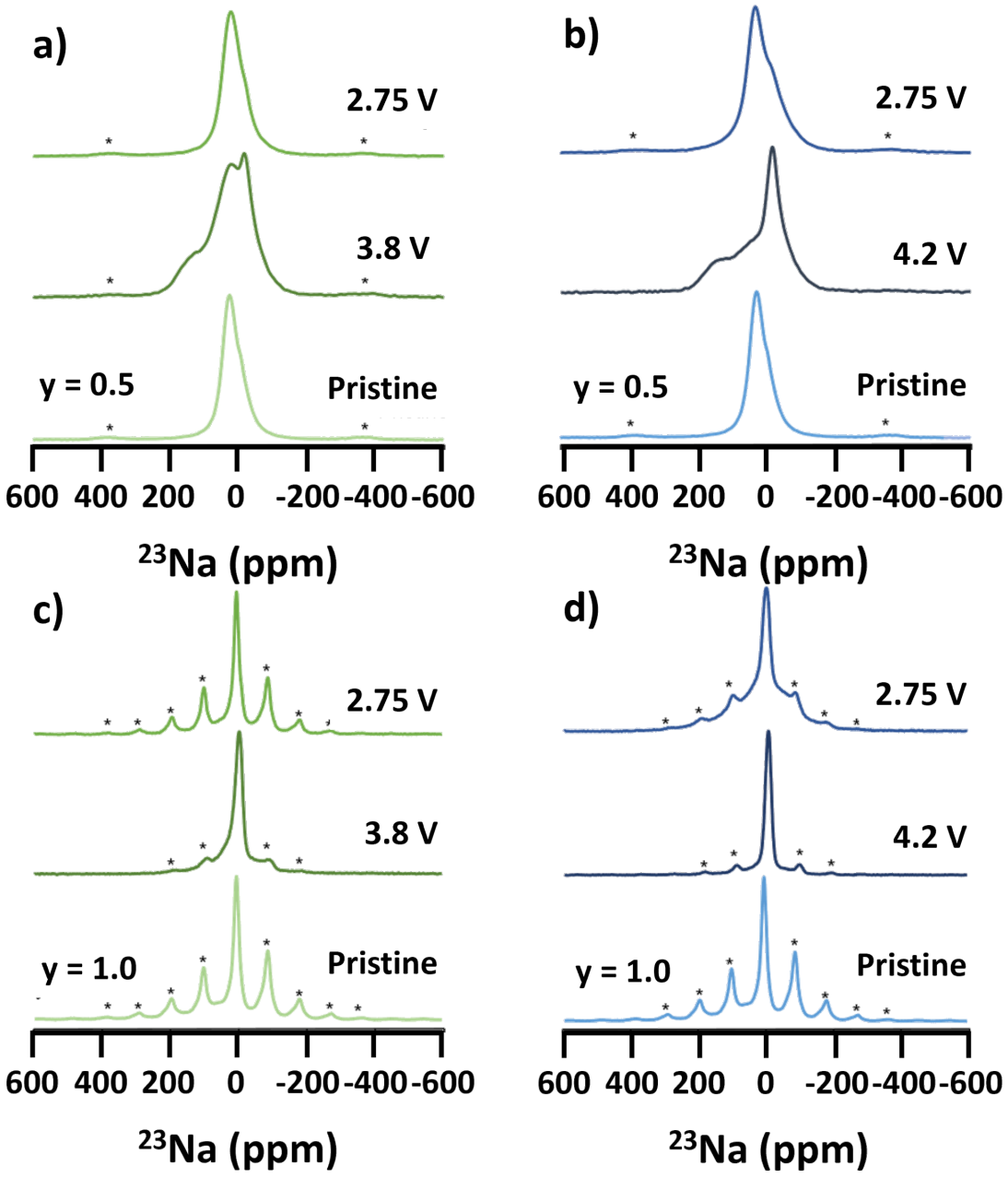

Figure 4.4: ^{23}Na spin echo ssNMR spectra collected on a) the pristine and ex situ y = 0.5 cathode samples cycled over the 3.8−2.75 V range at 7.05 T; b) the pristine and ex situ y = 0.5 cathode samples cycled over the 4.2−2.75 V range at 7.05 T; c) the pristine and ex situ y = 1.0 cathode samples cycled over the 3.8−2.75 V range at 18.8 T; d) the pristine and ex situ y = 1.0 cathode samples also cycled over the 4.2−2.75 V range at 18.8 T. Asterisks indicate spinning sidebands resulting from fast rotation of the sample during acquisition (30 kHz MAS for the y = 0.5 cathode and 20 kHz MAS for the y = 1.0 cathode.)

sharp and low intensity component centered at 0 ppm is attributed to residual NaH_2PO_4 precursor, while the more intense and broader components centered at 27 and −23 ppm are attributed to Na in the paramagnetic $Na_{3.5}V_{1.5}Mg_{0.5}(PO_4)_3$ cathode. We note that a direct assignment of these two resonances to the two crystallographic Na sites (Na(1) and Na(2)) in the average $R\bar{3}c$ structure is complicated by the large number of local Na environments resulting from possible V/Mg ordering and fast Na chemical exchange between those different environments leading to partial NMR signal averaging. Upon charging the cathode to 3.8 V, three resonances are visible at $\delta_{\text{obs}} = 137, 27$, and −15 ppm. The broad signals at 27 and 137 ppm are assigned to the new $Na_{1.5}V_{1.5}Mg_{0.5}(PO_4)_3$ phase formed during the two-phase reaction observed electrochemically and via XRD. The resonance at −15 ppm increases in intensity and sharpens compared to the pristine spectrum (see Table 4.8, Appendix B), suggesting the formation of Na-containing diamagnetic phases due to, e.g., decomposition of the carbonate solvent to form Na_2CO_3 (with an expected ^{23}Na shift close to −15 ppm) [128], or of the FEC additive to form NaF [129, 130]. A small amount of the pristine $Na_{3.5}V_{1.5}Mg_{0.5}(PO_4)_3$ phase is likely still present in the 3.8 V charged sample (which is consistent with the two-phase reaction observed by XRD up to 3.8 V), contributing to the ^{23}Na NMR signals at 27 ppm and −15 ppm. Subsequent discharge to 2.75 V leads to almost complete recovery of the pristine $Na_{3.5}V_{1.5}Mg_{0.5}(PO_4)_3$ local structure, as revealed by the very similar lineshapes of the pristine and discharged ^{23}Na NMR spectra (Figure 4.4a). The spectrum obtained on discharge is slightly broader than the pristine spectrum, presumably due to increased site disorder on the Na sublattice and/or local structure distortions upon Na reinsertion.

The y = 0.5 cathode was also charged to a higher voltage cutoff of 4.2 V, and the corresponding ^{23}Na ssNMR spectrum exhibits at least four overlapping resonances at δ_{obs} = −64, −18, 48, and 137 ppm, as shown in Figure 4.4b, indicating a greater range of Na local environments in the charged cathode. The dominant signal in this spectrum is

centered at −18 ppm (see Table 4.8, Appendix B), which is consistent with Na in mostly diamagnetic (V^{4+}-rich) environments in the cathode. The ^{23}Na NMR spectrum obtained on a sample charged to 4.2 V and subsequently discharged to 2.75 V is a lot broader than the pristine spectrum, as shown in Figure 4.4b. This implies that the local structure of the cathode is poorly reversible when cycled over the 4.2−2.75 V voltage window, in contrast to the good structural reversibility observed over the 3.8−2.75 V voltage range and in good agreement with the electrochemical and XRD results presented earlier.

For the y = 1.0 ex-situ cathode samples, the ^{23}Na ssNMR spectra were acquired at a higher magnetic field of 18.8 T and 20 kHz MAS due to the limited spectral resolution at the lower field of 7.05 T. Three overlapping resonances at δ_{obs} = 5, 23, and 59 ppm are observed in the spectrum obtained on the pristine cathode, as shown in Figure 4.4c and Table 4.9 in Appendix B. The broad 23 and 59 ppm resonances are assigned to Na environments in the paramagnetic cathode, and the sharp resonance at 5 ppm is attributed to a diamagnetic impurity. Similar to the y = 0.5 cathode, the two resonances attributed to Na in the bulk cathode structure cannot be straightforwardly related to the two crystallographic Na sites in the average R$\bar{3}$c structure. Upon charge to 3.8 V, at least three relatively sharp and overlapping ^{23}Na resonances are observed at δ_{obs} = −2, 33, and −71 ppm, and the resonances associated with the pristine y = 1.0 phase are no longer present, consistent with a solid solution-type (de)intercalation mechanism over the entire potential range. The intense signal at −2 ppm (see Table 4.9, Appendix B) likely comprises some contribution from Na nuclei in diamagnetic electrolyte decomposition products, and some contribution from Na nuclei in diamagnetic V^{4+} and Mg^{2+} rich environments in the bulk cathode. The presence of V^{4+} at 3.8 V could arise from disproportionation of the V^{4+} ions into V^{3+} and V^{5+} in the bulk cathode, as has been reported for related systems such as $Na_{3+y}V_{2-y}Mn_y(PO_4)_2F_3$ [131], and will be discussed further in the ^{51}V ssNMR section. The spectrum obtained on a cathode sample sub-

sequently discharged to 2.75 V is similar to the one obtained on the pristine cathode, albeit slightly broadened, implying a mostly reversible charge−discharge process over the 3.8−2.75 V window. When the upper cutoff voltage is increased to 4.2 V, the ^{23}Na spectrum consists of four resonances (Figure 4.4d and Table 4.9 in Appendix B). The relatively sharp signal at −7 ppm is attributed to a diamagnetic electrolyte decomposition product, and the three signals at $\delta_{obs} = -14$, −67, and 48 ppm are assigned to Na environments in the bulk cathode. When the cathode is subsequently discharged to 2.75 V, the resulting ^{23}Na ssNMR spectrum is a lot broader than the one collected on the pristine sample, indicating poor reversibility of the y = 1.0 cathode material over this wider voltage window, in line with the electrochemical and diffraction data.

4.2.3 ^{31}P solid-state NMR

Complementary ^{31}P ssNMR experiments conducted on y = 0.5 and y = 1.0 ex situ cathode samples largely corroborate the ^{23}Na ssNMR results. ^{31}P nuclei are sensitive NMR probes of the local structure of materials, with a high gyromagnetic ratio and a wide chemical shift range. However, the attribution of ^{31}P NMR signals to specific local environments in cathode materials is complicated by the presence of very large paramagnetic ^{31}P chemical shifts, and broad and overlapping resonances resulting from strong hyperfine (paramagnetic) interactions between ^{31}P nuclei and unpaired d electron spins from neighboring V^{3+} and V^{4+} species (V^{5+} is d^0 and therefore diamagnetic).

In the ^{31}P ssNMR spectrum collected on the pristine y = 0.5 cathode (see Figure 4.5a), a broad paramagnetic signal centered at 1850 ppm is observed. This broad resonance is composed of multiple overlapping signals corresponding to the many phosphorous local environments present in the cathode. Two additional ^{31}P resonances are observed at ≈ 3 and between 25 and 30 ppm (see inset in Figure 4.5a). The sharp resonance at

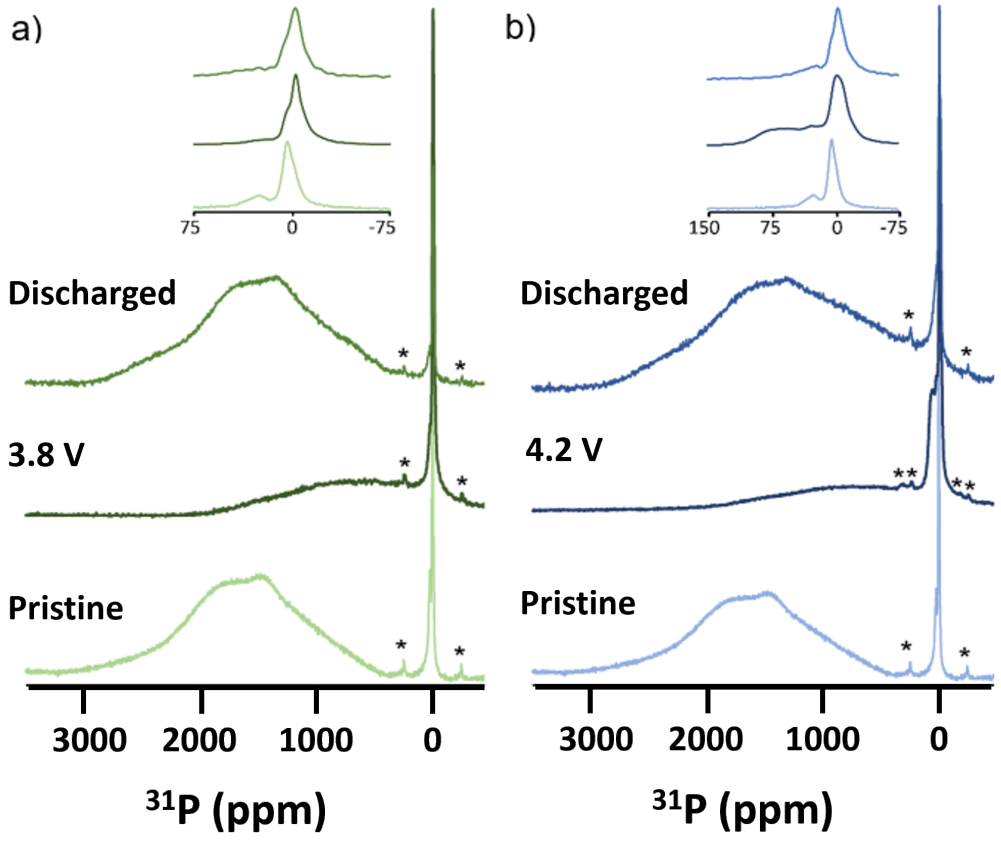

Figure 4.5: ^{31}P spin echo ssNMR spectra collected on various y = 0.5 ex situ cathode samples at 7.05 T: a) pristine cathode and ex situ spectra obtained on charge to 3.8 V and subsequent discharge to 2.75 V and b) the pristine cathode and ex situ spectra obtained on charge to 4.2 V and subsequent discharge to 2.75 V. Magnified views of the diamagnetic regions of the ssNMR spectra are shown in the insets.

$\approx$ 3 ppm is assigned to (a) diamagnetic phosphate impurity phase(s) (possibly $VOPO_4$, NaH_2PO_4, $\alpha_{II}-VOPO_4$, $\beta-VOPO_4$) formed during synthesis[132]. We tentatively assign the broader and weaker resonance at $\approx$ 26 ppm to a paramagnetic $VOH_yPO_4 \bullet zH_2O$ phase that cannot be observed by ^{51}V ssNMR [133]. Upon charge to 3.8 V, the intensity of the broad paramagnetic ^{31}P signal is reduced and the magnitude of its chemical shift decreases as a result of the weaker paramagnetic interactions as V^{3+} is oxidized to V^{4+}. The shifts and relative intensities of the signals in the -20 to 50 ppm region of the ^{31}P spectrum also evolve upon cycling, presumably due to electrochemical decomposition of

some of the impurity phases present in the pristine cathode. Upon subsequent discharge to 2.75 V, the pristine ^{31}P ssNMR spectrum is largely recovered, providing further evidence for the good structural reversibility of the y = 0.5 cathode when cycled over this potential range. The impurity signal near 26 ppm is no longer present in the discharged cathode, suggesting that the corresponding phase has decomposed or dissolved into the electrolyte during the first charge-discharge cycle.

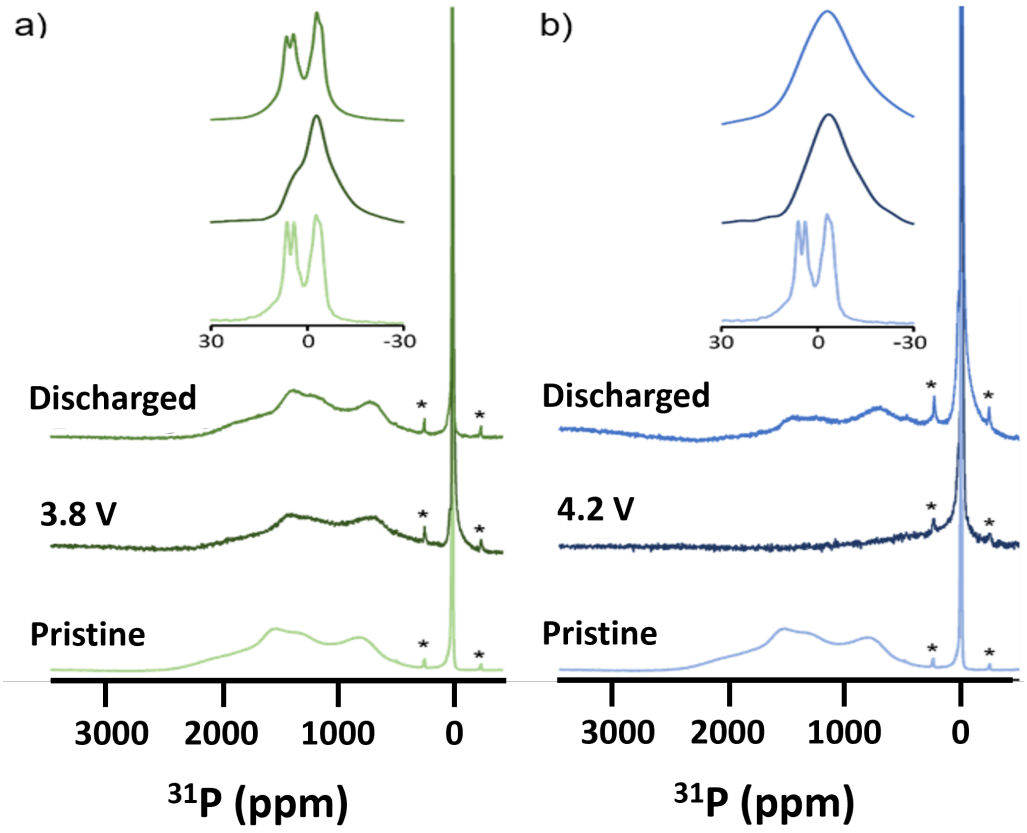

Figure 4.6: ^{31}P spin echo ssNMR spectra collected on various y = 1.0 ex situ cathode samples at 7.05 T: a) pristine cathode and ex situ spectra obtained on charge to 3.8 V and subsequent discharge to 2.75 V and b) the pristine cathode and ex situ spectra obtained on charge to 4.2 V and subsequent discharge to 2.75 V. Magnified views of the diamagnetic regions of the ssNMR spectra are shown in the insets.

When the y = 0.5 cathode sample is charged to 4.2 V (Figure 4.5b), the intensity of the ^{31}P signal arising from the cathode is tremendously reduced, and several new

resonances appear in the 150 to −50 ppm range, notably a broad signal near 61 ppm. Upon subsequent discharge to 2.75 V, the initial ^{31}P cathode signal is only partially recovered and exhibits a lower average chemical shift and a broader lineshape than in the pristine state, clearly indicating structural irreversibilities upon high voltage cycling.

Although ^{31}P resonances are better resolved in the spectrum collected on the y = 1.0 pristine cathode sample than in the one obtained on the y = 0.5 cathode, as expected from the more dilute paramagnetic V species in $Na_4VMg(PO_4)_3$, multiple phosphorous local environments are present in the bulk of the cathode and result in overlapping signals in the 500 to 2500 ppm range. Additionally, six sharp resonances are observed at 6, 4, 2, −1, −3, and −4 ppm (inset of Figure 4.6a) and are ascribed to diamagnetic phosphate impurities, potentially including various polymorphs of $VOPO_4$ formed during synthesis [132, 133]. This assignment is consistent with the ^{51}V ssNMR signal at δ_{obs} = −724 ppm (Figure 4.7). Similar to the y = 0.5 sample, the NASICON structure is very stable upon cycling over the low voltage range, and the paramagnetic region of the ^{31}P ssNMR spectrum barely changes upon charge to 3.8 V and subsequent discharge to 2.75 V (see Figure 4.6a). The diamagnetic impurity peaks broaden at the top of charge but are largely recovered on subsequent discharge. When the y = 1.0 cathode is then charged to 4.2 V (see Figure 4.6b), the broad paramagnetic ^{31}P signal almost fully disappears and is replaced by a broad resonance near 0 ppm that is composed of multiple overlapping signals. The ^{31}P cathode signal intensity increases again upon subsequent discharge to 2.75 V (Figure 4.6b), but the chemical shifts and line shapes of the various ^{31}P signals observed for the discharged sample differ from those observed for the pristine cathode, indicating poor structural reversibility over this wider potential window.

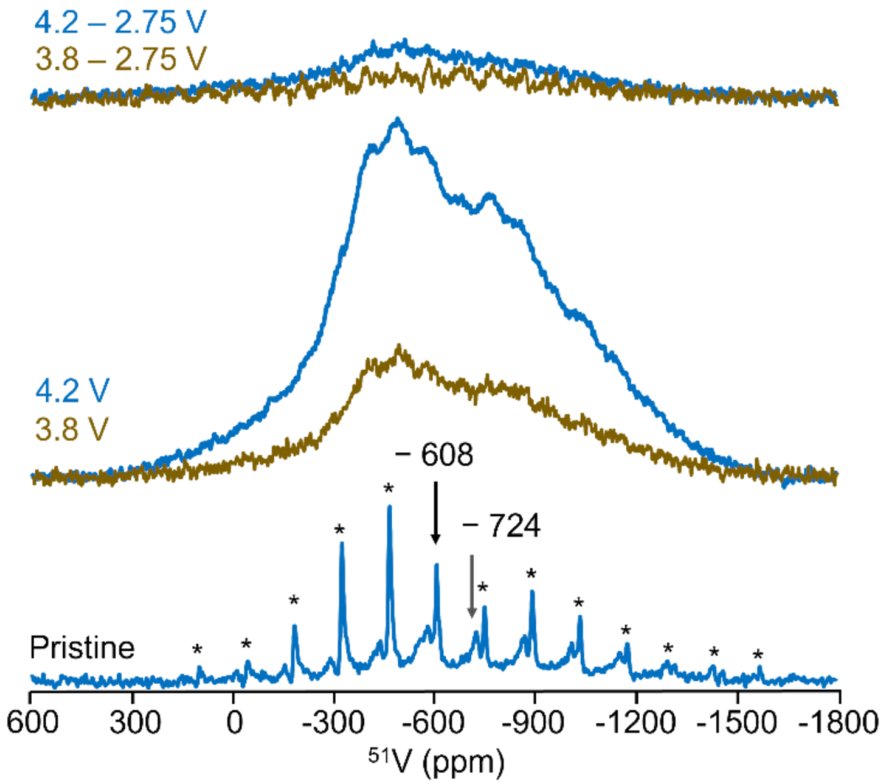

Figure 4.7: ^{51}V spin echo ssNMR spectra obtained on the as synthesized, 4.2 V charged, 3.8 V charged, and 2.75 V discharged y = 1.0 cathode sample at 18.8 T. For the pristine spectrum, asterisks indicate spinning sidebands resulting from fast rotation of the sample during data acquisition, and arrows indicate the center frequency of the two ^{51}V signals. The spectra are scaled according to the number of scans used for signal averaging and the number of moles of cathode sample in the NMR rotor

4.2.4 ^{51}V solid-state NMR

^{51}V ssNMR spectra were collected on y = 1.0 cathode samples to gain further insights into the local structure changes around V species and to monitor changes in the V oxidation state during cycling. The results are shown in Figures 4.7. When using ^{51}V as an NMR probe, only diamagnetic V^{4+} species (with no localized unpaired d electron spins) are typically observed [134]. Based on Rietveld analysis of the XRD data obtained on the pristine and ex situ cathode samples presented in Chapter 3 and in our previous work [32], the stoichiometry of the y = 1 cathode evolves from $Na_{3.89}VMg(PO_4)_3$ initially,

to $Na_{2.91}VMg(PO_4)_3$ and $Na_{2.45}VMg(PO_4)_3$ upon charge to 3.8 and 4.2 V, respectively, resulting in an average V oxidation state evolving from +3.11 to +4.09 and +4.55 at those different states of charge. In the pristine y = 1 cathode, all V cations are paramagnetic, mostly in the V^{3+} oxidation state, and not observable by NMR. However, two ^{51}V ssNMR signals are observed in the spectrum collected on the pristine cathode sample, which are centered at $\delta_{obs} = -608$ ppm and $\delta_{obs} = -724$ ppm and ascribed to residual V_2O_5 precursor [135] and $VOPO_4$ formed during the synthesis [132], respectively. The latter assignment is supported by the sharp signal near 0 ppm in the ^{31}P ssNMR spectrum collected on the same sample and shown in Figure 4.6 [133]. The significant increase in the ^{51}V NMR signal intensity upon charge to 4.2 V (Figure 4.7) is consistent with the oxidation of a significant fraction of V species to V^{5+}. The much broader ^{51}V NMR signal observed at the top of charge, as compared to those observed in the pristine state, results from the strong paramagnetic interactions between residual V^{3+}/V^{4+} species and the V^{5+} nuclei under observation in the bulk cathode. Notably, there is no sign of diamagnetic V_2O_5 and $VOPO_4$ impurity phases at 4.2 V, presumably due to dissolution of those phases in the carbonate electrolyte, as has been reported for V_2O_5[136], or due to electrochemical decomposition. Interestingly, when the upper cutoff voltage is limited to 3.8 V, a broad ^{51}V NMR signal similar to the one present upon charge to 4.2 V is also observed (Figure 4.7), but lower in intensity, suggesting the presence of similar V^{5+} environments in the two charged samples. This result is unexpected given that the overwhelming majority of V species in the 3.8 V charged sample are expected to be in the paramagnetic V^{4+} state, suggesting (at least partial) V^{4+} disproportionation into V^{3+} and V^{5+} at this charge state. On discharge to 2.75 V following charge to 4.2 or 3.8 V, a broad, low intensity ^{51}V resonance is observed in contrast to the sharp signals observed in the pristine sample. This result indicates that the diamagnetic impurity phases present in the pristine cathode sample are no longer present on discharge, and that the Na content

in the discharged cathode is lower than that in the pristine state, resulting in a small amount of V^{5+} species in the material. The intensity of the ^{51}V NMR signal on discharge to 2.75 V after charging to 4.2 V is more intense than when the cathode was only charged to 3.8 V, suggesting a greater amount of irreversibility and of residual V^{5+} in the former sample, in good agreement with the rest of the characterization data presented here. It is important to note, however, that the ^{51}V NMR results presented here do not suggest V migration during high voltage cycling, as has been reported for $Na_3VCr(PO_4)_3$ [137], since the NMR signals observed on first charge to 3.8 V, 4.2 V, and subsequent discharge to 2.75 V all exhibit very similar lineshapes. In contrast, V migration is expected to result in drastic changes in both the paramagnetic and quadrupolar interactions, which would manifest as changes in the lineshape and resonant frequency.

4.2.5 (De)sodiation behavior from first principles calculations

Having established the insights provided by ^{23}Na, ^{31}P, and ^{51}V ssNMR on the local structure during electrochemical cycling of the Mg-NVP cathodes, we turn our attention to understanding the (de)sodiation behavior of this material from a first principles perspective. The lowest energy V^{3+}/Mg^{2+} configuration for each of the $Na_{3+y}V_{2-y}Mg_y(PO_4)_3$ ($0 \leq y \leq 1$) compositions of interest was established, as shown with the convex hull in Figure 4.13 as shown in Appendix B. This analysis indicated that the distribution of V^{3+}/Mg^{2+} cations has a significant impact on the formation energy. Due to significant differences in ionic radii (0.72 Å for Mg^{2+} and 0.64 Å for V^{3+}, respectively, in a 6-coordinate site, Mg^{2+} substitution on the V^{3+} lattice disrupts the local bonding environments, and results in a shortening of the Na(1)-O and Na(2)-O bonds. To understand how Mg substitution and V^{3+}/Mg^{2+} ordering affect the local structure and formation energy of the $y = 0.5$ and 1 compounds, the VO_6 octahedral distortion index was computed

for both stable and unstable configurations, and plotted as a function of formation energy (Figure 4.14, Appendix B). For y = 0.5, as expected, the octahedral crystal field stabilization energy of V^{3+} leads to a strong correlation between the extent of VO_6 distortion and the formation energy of the configuration, whereby structures with more distorted VO_6 octahedra lie higher above the hull. For y = 1, VO_6 octahedral distortions are not much smaller, resulting in little change in the formation energies of the various orderings.

To gain further insight into the desodiation behavior of the Mg-substituted cathodes, convex hulls were computed as a function of Na content for the y = 0.5 and 1 (using the lowest V/Mg orderings determined previously (Figure 4.13, Appendix B), and are shown in Figure 4.15 located in Appendix B. The convex hulls shed light on the energetics of intermediate compositions and stable Na/vacancy orderings during electrochemical cycling. In good agreement with experimental findings, those results indicate a solid solution behavior for both the y = 0.5 and y = 1 compounds, as indicated by the fact that all intermediate compositions considered here lie on the hull.

The evolution of lattice parameters upon desodiation was investigated from the lowest energy structures obtained from the convex hull analysis (Figure 4.15, Appendix B). Regarding the y = 1.0 system, we considered two phases at 3.8V and 4.2V with the compositions, $Na_3VMg(PO_4)_3$ and $Na_{2.25}VMg(PO_4)_3$, respectively, obtained from inspection of the electrochemical profile in Figure 4.1a. The computed structures were found to evolve anisotropically upon Na removal, i.e. there is a reduction in the relaxed 'a' parameter from 8.955 Å to 8.910 Å at 3.8 V and 8.888 Å at 4.2V and increase in the 'c' parameter from 21.392 Å to 21.505 Å at 3.8V and 21.451 Å at 4.2V. For the y = 0.5 phase, the compositions considered were $Na_{2.25}VMg(PO_4)_3$ at 3.8V and $Na_2VMg(PO_4)_3$ at 4.2V respectively. The relaxed lattice parameter 'a' was found to increase from 8.872 Å to 8.896 Å at 3.8V, and then decrease to 8.886 Å at 4.2V, and 'c' was found to increase from 21.444 Å to 21.712 Å at 3.8V and 21.796 Å at 4.2V. The lowest energy structure

for the charged states had Na occupancy and lattice parameters are tabulated below.

Composition	Voltage (V)	a (Å)	c (Å)	Na(1) occ.	Na(2) occ.
y = 0.5	0	8.872	21.444	0.83	0.89
y = 0.5	3.8	8.896	21.712	0.75	0.80
y = 0.5	4.2	8.886	21.796	0.41	0.36
y = 1.0	0	8.955	21.392	0.94	0.99
y = 1.0	3.8	8.910	21.505	0.83	0.72
y = 1.0	4.2	8.88	21.451	0.75	0.50

Table 4.1: Evolution of DFT computational lattice parameters and Na occupancy during desodiation.

The XRD and NMR data indicate irreversible long-range and local structural changes occurring upon charge to 4.2 V. One potential rationale for the irreversibility of the $Na_{3+y}V_{2-y}Mg_y(PO_4)_3$ cycling behavior at high voltage was believed to be potential V migration but is not supported by the ^{51}V NMR data presented here. However, it is possible that the irreversibility observed during high voltage cycling is due Mg migration that has been observed in other layered oxide cathodes [138] and/ or VO_6 octahedral distortions.

Here, the possibility of Mg migration into vacant Na(1) or Na(2) sites at high states of charge was investigated using bond valence sum (BVS) and CI-NEB calculations. These were performed on the ground state y = 0.5 structure corresponding to the 4.2 V charged composition (i.e $Na_2V_{1.5}Mg_{0.5}(PO_4)_3$) obtained from visual inspection of the electrochemical profile in Figure 4.1a. Probable positions of Mg^{2+} in the lattice were identified from the bond valence energy landscapes shown in Figure 4.16 in Appendix B. A continuous migration path was observed, that connected regular Mg positions in the NASICON cathode to vacant Na(2) sites. Hence, the activation barrier for a Mg^{2+} ion hop from an initial MgO_6 octahedral site to the nearest Na(2) site was computed and found equal to 0.27 eV using the climbing image nudged elastic band (CI-NEB) method. The low energy barrier hints to possible Mg migration in the lattice in the

Composition	Voltage	S.G.	a (Å)	b (Å)	c (Å)	β (⁰)	Na1	Na2	Na3
For y = 0.5 cathode									
$Na_2V_{1.5}Mg_{0.5}(PO_4)_3$ (Phase 01: 66.2(3) %)	3.8 V	R$\bar{3}$c	8.522(4)	8.522(4)	21.579(4)	120	0.839(1)	0.389(6)	-
$Na_2V_{1.5}Mg_{0.5}(PO_4)_3$ (Phase 02: 35.7(3) %)		R$\bar{3}$c	8.611(4)	8.611(4)	21.4125(8)	120	0.804(2)	0.399(6)	-
$Na_{3.43}V_{1.5}Mg_{0.5}(PO_4)_3$	3.8 -2.75 V	R$\bar{3}$c	8.7888(5)	8.7888(5)	21.678(4)	120	0.92(2)	0.836(1)	
$Na_{1.5}V_{1.5}Mg_{0.5}(PO_4)_3$ (Phase 01: 53.3(4) %)	4.2 V	R$\bar{3}$c	8.4649(2)	8.4649(2)	21.611(1)	120	0.913(1)	0.196(1)	-
$Na_{1.49}V_{1.5}Mg_{0.5}(PO_4)_3$ (Phase 02: 46.7(5) %)		R$\bar{3}$c	8.479(2)	8.479(2)	21.695(9)	120	0.53(2)	0.322(7)	-
$Na_{3.02}V_{1.5}Mg_{0.5}(PO_4)_3$	4.2 -2.75 V	R$\bar{3}$c	8.7648(3)	8.7648(3)	21.743(4)	120	0.901(1)	0.707(7)	-
For y = 1.0 cathode									
$Na_{2.91}VMg(PO_4)_3$	3.8 V	R$\bar{3}$c	8.7566(1)	8.7566(1)	21.576(4)	120	0.907(1)	0.668(3)	-
$Na_{3.91}VMg(PO_4)_3$	3.8 -2.75 V	R$\bar{3}$c	8.8650(1)	8.8650(1)	21.4125(8)	120	1.0	0.97(4)	-
$Na_{2.27}VMg(PO_4)_3$	4.2 V	C2/c	15.389(2)	8.7028(6)	8.7950(4)	125.909(6)	0.62(8)	0.63(1)	0.51(6)
$Na_{3.28}VMg(PO_4)_3$	4.2 – 2.75 V	C2/c	15.181(1)	8.8678(2)	8.7738(2)	124.846(4)	0.90(3)	0.84(5)	0.77(4)

Table 4.2: Lattice parameters and Na-ion occupancies obtained from Rietveld refinement of the y = 0.5 and 1.0 cathode samples

highly desodiated state. In contrast, Mg^{2+} migration to Na(1) sites was found to be unfavorable.

4.3 Conclusions

We conducted a comprehensive investigation of the high voltage degradation processes in the $Na_{3+y}V_{2-y}Mg_y(PO_4)_3$ (y = 0.5 and 1) NASICON cathode materials using bulk and local structural probes alongside electrochemical testing and first principles calculations. Our results indicate significant degradation of the crystal structure during the first charge-discharge process when cycling over a wide potential window of 4.2

V−2.75 V. Structural degradation is primarily driven by removal of Na from the Na(1) sites of the R$\bar{3}$c structure for the y = 0.5 sample, as shown by the significant lattice parameter changes in the ex situ diffraction data. Upon cycling the y = 1.0 cathode to 4.2 V, an irreversible change in crystal symmetry from rhombohedral R$\bar{3}$c to monoclinic C2/c prevents complete reinsertion of Na-ions on discharge leading to significant capacity loss. Ex situ ^{23}Na and ^{31}P solid-state NMR results indicate that, while the local structure is reversible upon cycling over the 3.8 to 2.75 V window, it irreversibly disorders upon increasing the upper cutoff voltage to 4.2 V. Notably, ^{51}V NMR did not indicate V migration during high voltage cycling. However, our DFT calculations do suggest potential Mg^{2+} migration into the Na(2) sites during cycling potentially leading to structural degradation. The combination of these experimental and computational techniques provides a detailed understanding of the degradation processes in NASICON structured materials and highlights the importance of deconvoluting complex degradation mechanisms to understand performance limiting factors.

4.4 Methods

4.4.1 Synthesis and as prepared materials characterization

The synthesis of NASICON-$Na_{3+y}V_{2-y}Mg_y(PO_4)_3$ materials was performed via a sol-gel assisted solid-state method, outlined in our previous work[32]. Powder X-ray diffraction (XRD) patterns were collected at Bruker D8 diffractometer using Cu-Kα source (λ = 1.5406 Å) in the 2θ region of 10-100°. The recorded XRD patterns were used to refine the crystal structure using the Rietveld method. Rietveld refinements were carried out using the FullProf suite[139]. The microstructures of the as-synthesized NASICON samples were examined with a scanning electron microscope (Jeiss Ultra-55 SEM instru-

ment). X-ray absorption spectroscopy (XAS) measurements were performed on the at V K-edge (5464 eV) of $Na_{3+y}V_{2-y}Mg_y(PO_4)_3$ cathodes in a transmission mode at Beamline 8 (BL8), Synchrotron Light Research Institute (SLRI), Thailand, using Ge (220) double crystal monochromator with storage ring running at 1.2 GeV and beam current of 80-150 mA. The as-synthesized NASICON samples used for this experiment were mixed with boron nitride and pressed into pellets (13 mm diameter, thickness 0.5-0.9 mm). The NASICON electrodes harvested from electrochemical cells were packed inside Kapton tape to avoid air exposure. X-ray absorption near edge structure (XANES) and extended X-ray absorption fine structure (EXAFS) spectra were divided into three regions with the following relative energy ranges and energy step: -200 to -20 eV (5 eV step), -20 to 80 eV (0.3 eV step) and 80 eV to 15k (0.05k step). The dwell time of each step was 1 second and three scans were collected from each sample. The normalization of XANES spectra, including the pre-edge and post-edge background subtraction, was done using the ATHENA program[104]. The EXAFS spectra were converted by Fourier transform from k space to real space using a k3 – weighting factor and without phase correction. All spectra were normalized using the ATHENA program while EXAFS spectra were modeled using Artimis[104]

4.4.2 Electrochemical characterization

All electrochemical tests of the NASICON cathode materials were performed in half cells using a Swagelok configuration. Cathode active materials were mixed with carbon (C45 TIMCAL) and polyvinylidene fluoride (PVDF) binder in a weight ratio of 70:22:8 in N-Methyl-2-pyrrolidone solvent. The slurry was coated onto aluminum foil and dried under vacuum at 90 °C for overnight. Thereafter, electrodes were punched into 10 mm diameter discs and the mass loading of active materials was found to be 2.0-3.0 mg/cm^2.

Sodium metal (Sigma, > 99%) was used as the counter electrode, and 1 M $NaClO_4$ in EC/PC/DMC (in a weight ratio of 4.5:4.5:0.1) with 3 wt% FEC additive was used as the electrolyte. The cells were assembled in an Ar-filled glove box (O_2 < 0.1 ppm, H_2O < 0.1 ppm) and evaluated in a battery cycler (BT-lab, Biologic) over the voltage range 4.2–2.75 V vs. Na^+/Na^0 at different C-rates. For ex-situ analysis, electrodes were cycled in powder form from a 7:3 weight mixture with carbon in large Swagelok cells. The electrode materials were harvested from the Swagelok cells at different states of charge, washed, and then dried inside the glove box.

4.4.3 Ex-situ and in-situ XRD analysis

Ex-situ samples were packed in Kapton capillaries for synchrotron XRD analysis. In-situ XRD measurements were conducted using a Bruker D8 diffractometer equipped with a Cu-Kα source (λ = 1.5406 Å) in an in-situ electrochemical cell fitted with a Be window. The cell was cycled at a C/10 rate over different voltage windows. Each pattern was recorded in the 2θ range of 10 to 60° with exposure time of one hour. Selected in-situ XRD patterns were refined using Le-Bail method to obtain cell parameters.

4.4.4 NMR characterization

Room temperature solid-state NMR (ssNMR) spectra were collected on as-synthesized and ex-situ $Na_{3+y}V_{2-y}Mg_y(PO_4)_3$ (y = 0.5, 1.0) samples at the top of charge and bottom of discharge, when cycled over the voltage windows of 3.8−2.75 V and 4.2−2.75 V vs Na^+/Na^0. The spectra were acquired at 18.8 T (800 MHz for ^1H) using a standard bore magnet, or at 7.05 T (300 MHz for ^1H) using a superwide bore magnet, with both spectrometers equipped with a Bruker Avance III console. The y = 0.5 ^{23}Na spectra were obtained at 7.05 T, at a Larmor frequency of 79.39 MHz, using a 2.5 mm double-resonance

HX probe and a magic angle spinning (MAS) rate of 30 kHz. The y = 1.0 ^{23}Na spectra were obtained at 18.8 T to improve spectral resolution, at a Larmor frequency of 211.65 MHz, using a 2.5 mm double-resonance HX probe and at a MAS rate of 20 kHz. ^{51}V ssNMR spectra were also collected at 18.8 T at a Larmor frequency of 210.46 MHz and using a 2.5 mm double-resonance HX probe. The ^{23}Na spectra were referenced against a 1 M NaCl solution ($\delta(^{23}Na) = 0$ ppm) and the ^{51}V spectra were referenced against solid V_2O_5 ($\delta(^{51}V)$ = -610 ppm) [135]. Line shape analysis was carried out within the Bruker TopSpin software using the SOLA lineshape simulation package. ^{23}Na and ^{51}V spectra were obtained using a rotor-synchronized spin-echo sequence ($90^\circ - \tau_r - 180^\circ - \tau_r -$ acq). The y = 1.0 ^{23}Na spectra used a 90° radiofrequency (RF) pulse of 0.73 μs and a 180° RF pulse of 1.46 μs at 300 W, with a recycle delay of 100 ms. The y = 0.5 ^{23}Na spectra used a 90° RF pulse of 1.16 μs and a 180° RF pulse of 2.32 μs at 100 W, with a recycle delay of 50 ms. The ^{51}V spectra used a 90° RF pulse of 1.2 μs and a 180° pulse of 2.4 μs at 400 W, with a recycle delay of 50 ms. ^{31}P solid-state NMR experiments were conducted at 7.05 T and at a Larmor frequency of 121.49 MHz, using a MAS rate of 30 kHz and a 2.5 mm double resonance HX probe. ^{31}P spectra were recorded with a rotor-synchronized spin-echo sequence ($90^\circ - \tau_r - 180^\circ - \tau_r -$ acq), a 90° RF pulse of 1.1 μs, a 180° pulse of 2.2 μs at 250 W, and a recycle delay of 100 ms. ^{31}P spectra were referenced against a 1 M H_3PO_4 solution ($\delta(^{31}P) = 0$ ppm).

4.4.5 Computational methods

The crystal structure of the $Na_4VMg(PO_4)_3$ (y = 1) cathode obtained from Rietveld analysis was used to build a 1x1x2 supercell containing 12 formula units of $Na_4VMg(PO_4)_3$. A large supercell was constructed to ensure that the Na^+, V^{3+} and Mg^{2+} stoichiometries were comparable to those targeted experimentally. V^{3+}/Mg^{2+}

cation orderings were enumerated using the Supercell code following the Special Quasirandom Structure (SQS) approach[140, 141]. Symmetrically distinct structures were then optimized via DFT calculations to identify the lowest energy geometries for every composition. First principles calculations were carried out using the VASP 5.4.1[142, 143, 144] software package and the Projector Augmented Wave (PAW) approach[145] as implemented in VASP. The Generalized Gradient Approximation (GGA) Perdew-Burke-Ernzerhorf (PBE[146]) functional, and a Hubbard U correction term of U = 3.25 eV, were employed to treat electronic correlation effects in the Vanadium 3d orbitals, with the effective on-site exchange interaction parameter J fixed to 1 eV. A kinetic energy cutoff of 520 eV was used for plane wave expansions. Brillouin Zone integration was performed over a 2x2x3 Monkhorst-Pack grid for geometry optimization. All systems were optimized using the conjugate-gradient algorithm[147] with a convergence criterion of 10-4 eV $Å^{-1}$ on forces. Bond Valence Sum (BVS) analysis was carried out using PyAbstantia to generate BVEL (Bond Valence Energy Landscape) maps that determine likely positions of Mg^{2+} in the lattice and probe possible migration pathways. Following BVS analysis, the Climbing Image Nudged Elastic Band (CI-NEB)[148] method was used to compute activation barriers associated with cation migration within the NASICON framework. Crystal structures and BVS maps were visualized in VESTA[149]

4.5 Appendix B

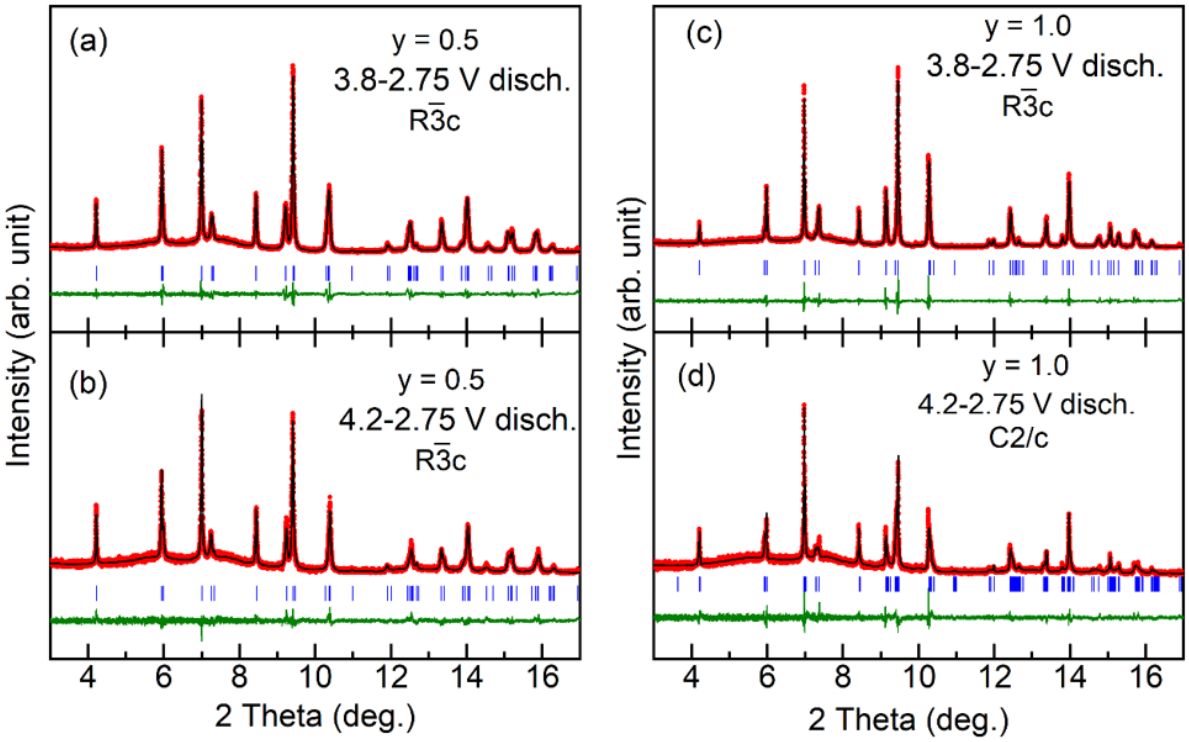

Figure 4.8: Rietveld refinement of synchrotron XRD patterns collected on the (a,b) y = 0.5 and (c,d) y = 1.0 cathodes at different states of charge.

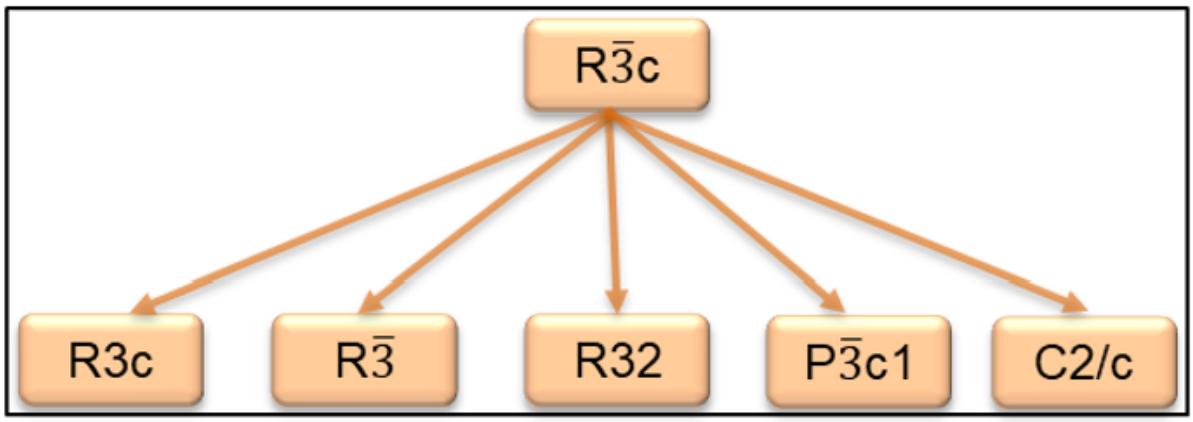

Figure 4.9: Isotropy subgroup tree of R$\bar{3}$c space group

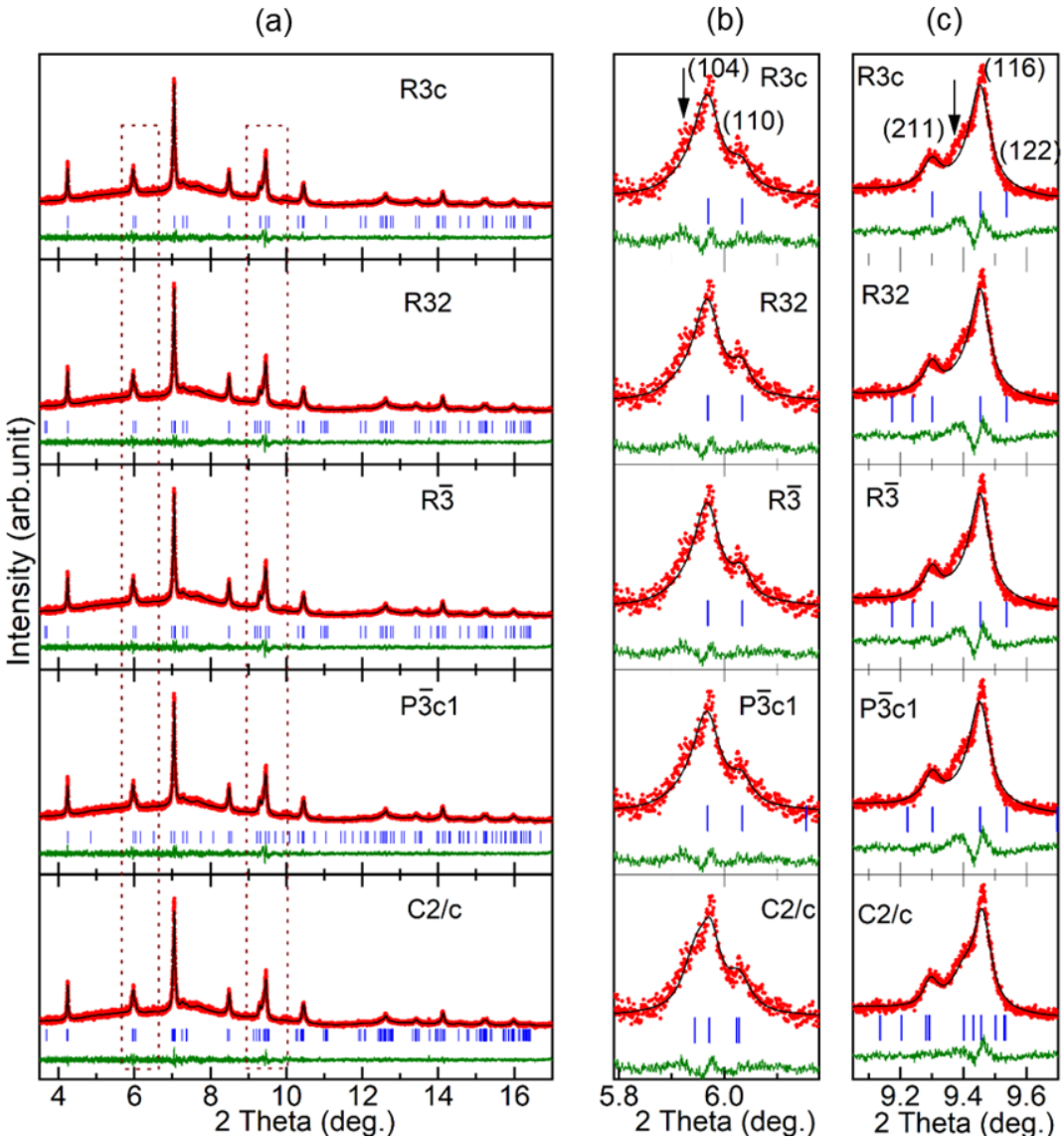

Figure 4.10: Comparison of synchrotron XRD patterns of y = 1.0 cathode collected at 4.2 V using isotropy subgroups of the R$\bar{3}$c spacegroup.

For the 4.2 V charge sample, the reflections at $2\theta = 5.92°$ and 9.37° (denoted by arrow) could not be indexed with the R$\bar{3}$c model. The best fit profiles for the 4.2 V sample was obtained using the C2/c space group.

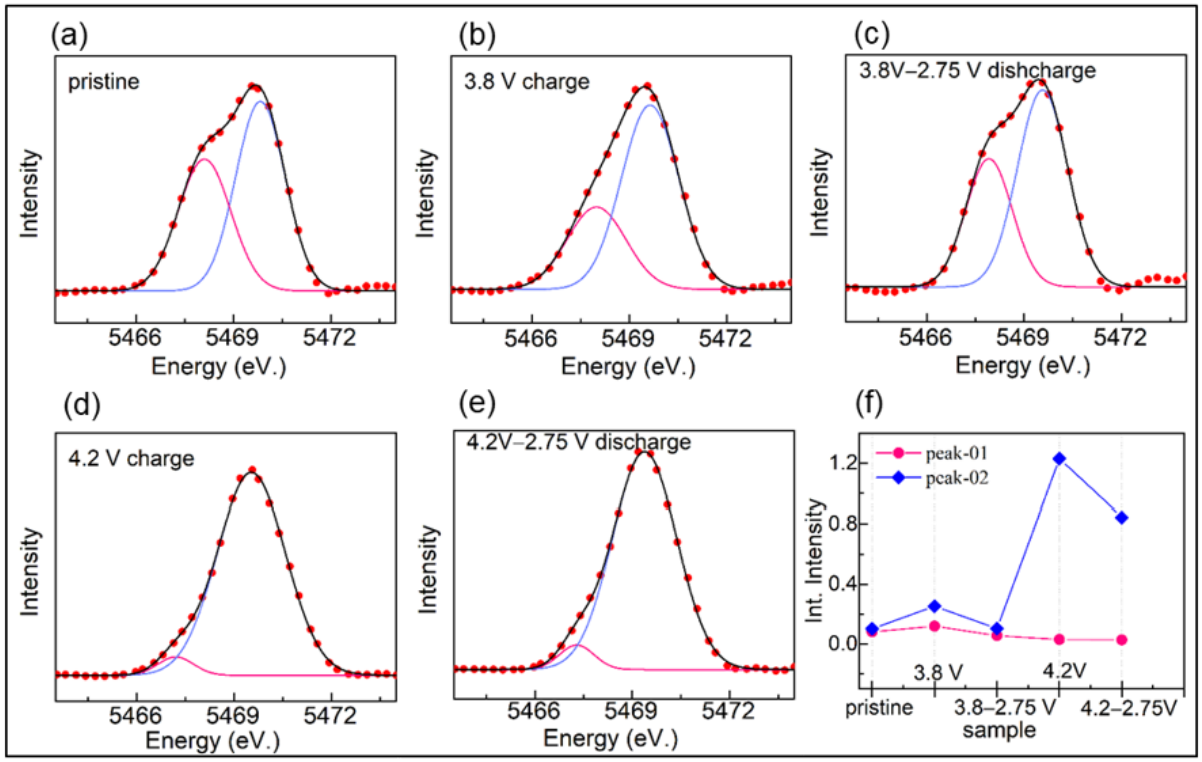

Figure 4.11: (a-e) Deconvoluted profiles of the pre-edges of XANES spectra collected on y = 1.0 cathodes at V K-edge and f) the variation of the integrated intensity of the pre-edge peak.

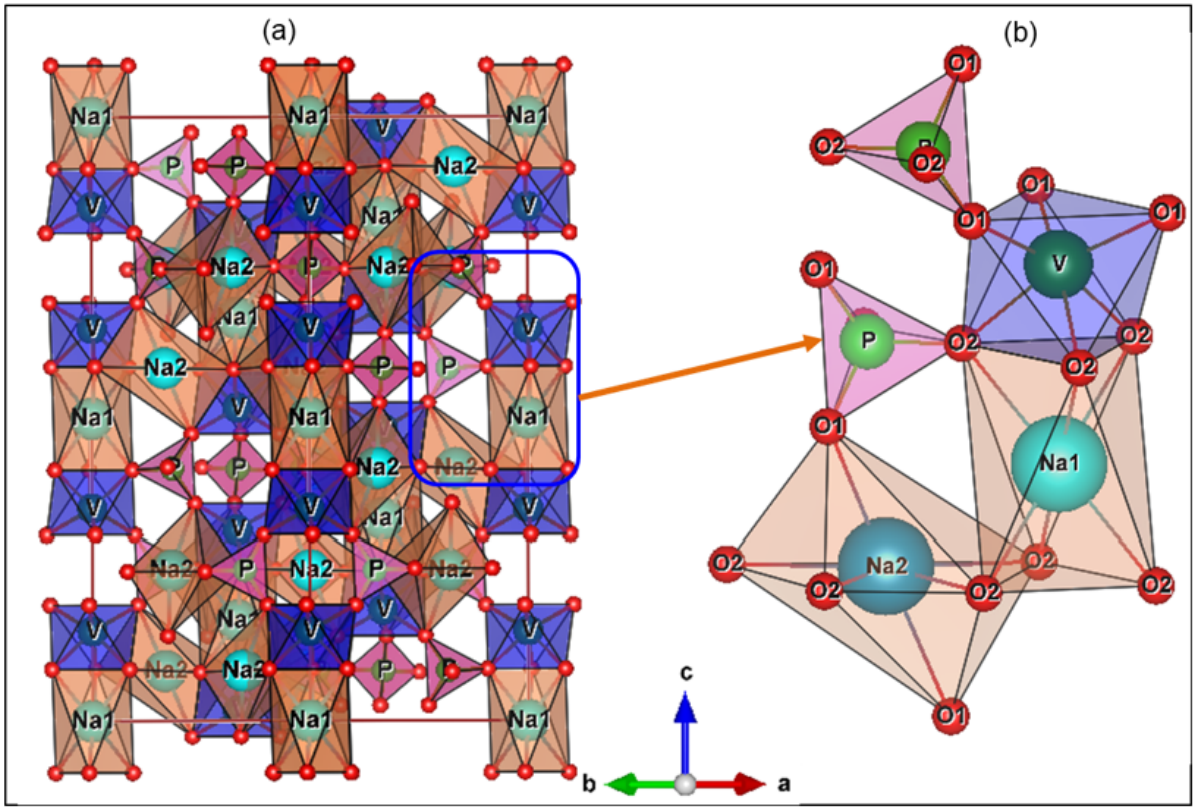

Figure 4.12: a) Unit cell of $Na_4VMg(PO_4)_3$ and b) local environments of V^{3+} within the unit cell.

First principles calculations

DFT calculations were carried out to assess the energetics of V^{3+}/Mg^{2+} orderings across the $Na_{3+y}V_{2-y}Mg_y(PO_4)_3$ series. Starting from the experimentally refined CIF for the end member y = 1 phase, the Supercell [140] code was used to generate SQS's (special quasirandom structures). This approach generated 924 disordered structures, each corresponding to a different V^{3+}/Mg^{2+} ordering. 100 symmetrically-unique structures were isolated by visual inspection using VESTA. Structures with minor differences were disregarded to keep computational costs tractable. The lowest energy configuration was identified after geometry optimization of these symmetrically-unique structures.

The convex hull built from the structures described above is shown in Figure 4.13 in Appendix B and provides insight into the thermodynamic stability (at 0 K) of the various V^{3+}/Mg^{2+} orderings in the compositional space spanning from y = 0 to 1. The hull was constructed by plotting the formation energies of $Na_{3+y}V_{2-y}Mg_y(PO_4)_3$ as a function of Mg content y, using the formula: $\Delta E_f = E_i - (y) \times E_{[Na_4VMg(PO_4)_3]} - (1 - y) \times E_{[Na_3V_2(PO_4)_3]}$, where E_i is the total energy of the $Na_{3+y}V_{2-y}Mg_y(PO_4)_3$ composition under consideration, and $E_{[Na_4VMg(PO_4)_3]}$ and $E_{[Na_3V_2(PO_4)_3]}$ are the total energies of the end member phases.

For the y = 0.5 and 1.0 structures, the average VO_6 octahedral distortion index was derived from the V−O bond lengths using Baur's formula [150] $\Delta = \frac{1}{6}\sum_{i=1}^{6}\left(\frac{d_i - \bar{d_{mean}}}{\bar{d_{mean}}}\right)^2$, where d_i is the $V - O_i$ distance and d_{mean} is the average $V - O$ distance. The formation energy of y = 0.5 and 1.0 orderings is plotted as a function of this distortion index in Figure 4.14 (Appendix B). For the y = 0.50 composition (Figure 4.14a), larger VO_6 octahedral distortions are clearly correlated with higher formation energies. For the y = 1 composition (Figure 4.14b), however, a narrower distribution of VO_6 octahedral distortions is observed (see large y axis scale), also resulting in a very narrow spread in the formation energies. An increase in the average V−O bond lengths is observed upon

Mg substitution (Figure 4.15), presumably due to the increased ionicity of the V−O bonds with increasing Mg^{2+} substitution.

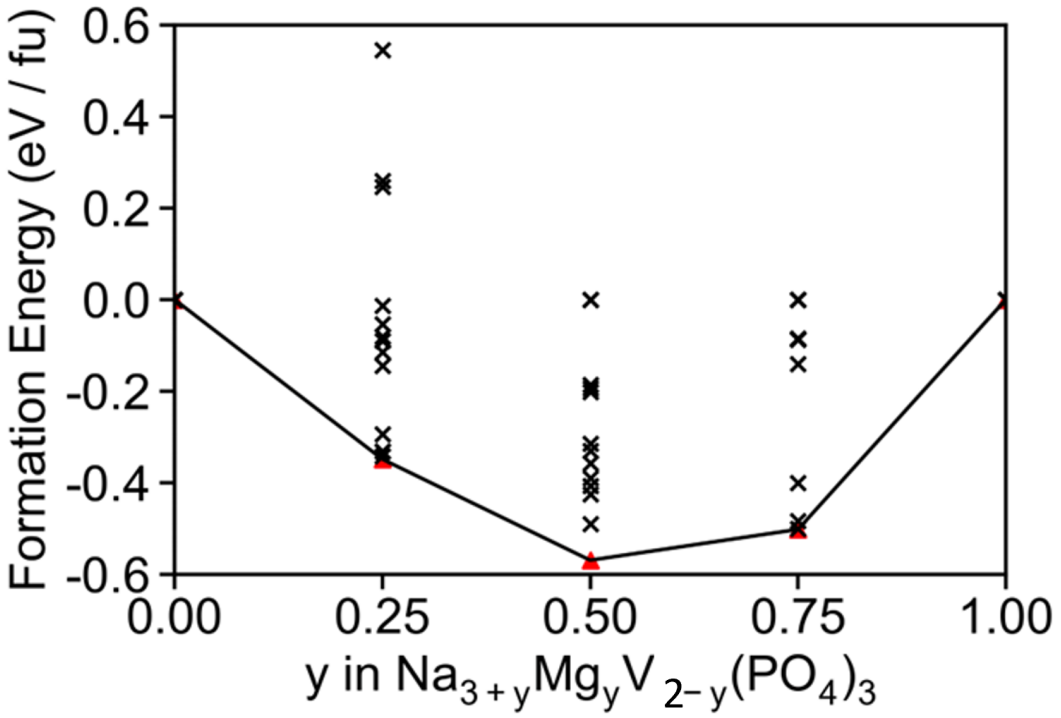

Figure 4.13: Convex hull obtained by varying the Mg content across the $Na_{3+y}V_{2-y}Mn_y(PO_4)_3$, series, and showing the ground state V^{3+}/Mg^{2+} orderings on the hull (red triangles), and unstable orderings (black crosses) above the hull.

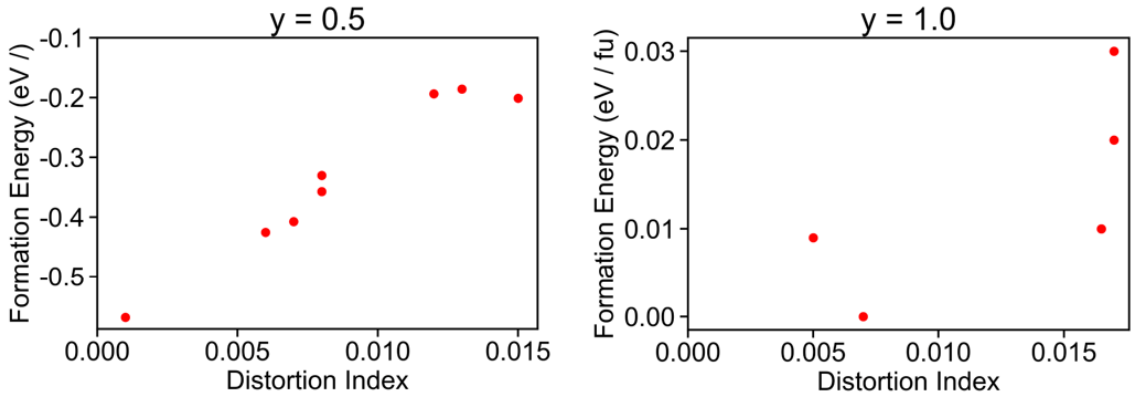

Figure 4.14: Formation energies of $Na_{3+y}V_{2-y}Mn_y(PO_4)_3$ (a) y = 0.5, and (b) y = 1.0 orderings plotted as a function of the average VO_6 octahedral distortion index.

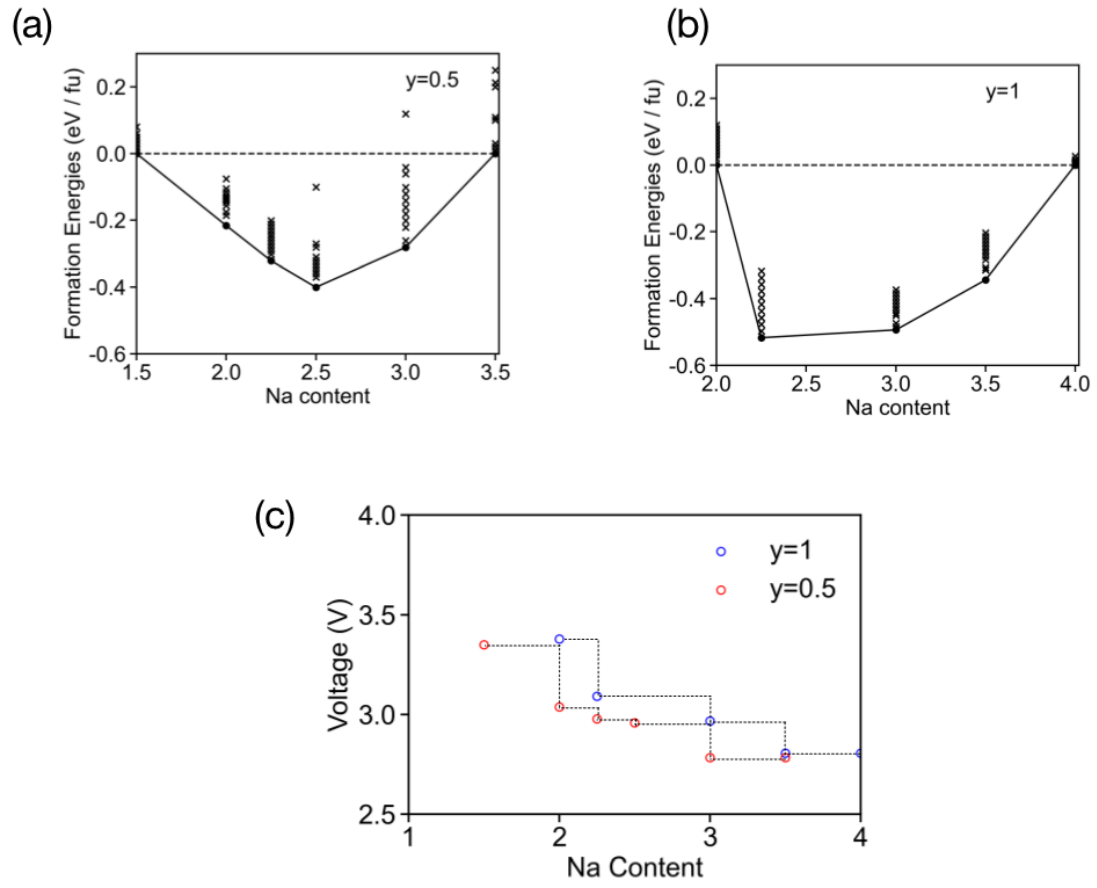

Figure 4.15: Convex hulls obtained on desodiation of $Na_{3+y}V_{2-y}Mn_y(PO_4)_3$ cathodes with a) y = 0.50, b) y = 1, and c) computed voltage profiles.

To compute the energies of the charged states, Na(1) and Na(2) sites were first enumerated in the discharged ground state structures for the y = 1 and y = 0.5 compositions. Na ions were then extracted from both sites to generate multiple orderings whose formation energies were calculated using the equations:

y = 1.0

$$E_f = E_x - [(4-x)/2 \times E_{Na_3VMg(PO_4)_3}] - [(x-2)/2 \times E_{Na_4VMg(PO_4)_3}](2 < x < 4) \quad (4.1)$$

y = 0.5

$$E_f = E_x - [(3.5-x)/2 \times E_{Na_{1.5}VMg(PO_4)_3}] - [(x-1.5)/2 \times E_{Na_{3.5}VMg(PO_4)_3}](1.5 < x < 3.5) \quad (4.2)$$

Composition at charged states	VO_6 distortion index
$Na_{3.5}V_{1.5}Mg_{0.5}(PO_4)_3$	0.001
$Na_{2.25}V_{1.5}Mg_{0.5}(PO_4)_3$	0.079
$Na_2V_{1.5}Mg_{0.5}(PO_4)_3$	0.098
$Na_4VMg(PO_4)_3$	0.007
$Na_3VMg(PO_4)_3$	0.017
$Na_{2.25}VMg(PO_4)_3$	0.088

Table 4.3: Compositions at charged states with VO_6 octahedral distortion index.

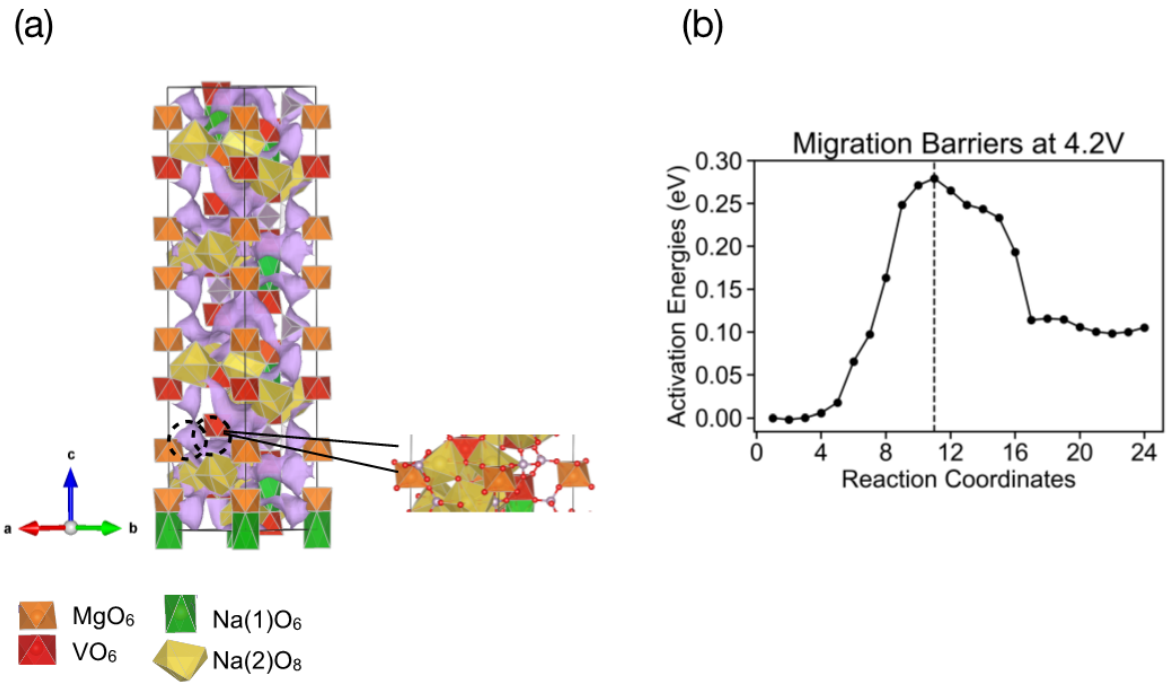

Figure 4.16: (a) Bond valence sum map for the composition $Na_2V_{1.5}Mg_{0.5}(PO_4)_3$ obtained on charge to 4.2 V. Dashed regions indicate vacated Na(2) sites. Insets compare regions in the sodiated structures for reference. Isosurfaces (in purple) denote possible sites/pathways for Mg migration within the lattice (isosurface threshold used: 0.1). (b) Migration energy barrier from MgO_6 sites into a nearby vacant Na(2) site in the lattice obtained from CI-NEB.

Atom	Wyckoff Site	x	y	z	B_{iso}	Occ.
3.8 V Charge Phase 01 ($R\bar{3}c$)						
Na1	6b	0	0	0	0.0002(6)	0.839(1)
Na2	18e	0.6355(8)	0	0.25	0.69(9)	0.389(6)
V	12c	0	0	0.1461(1)	0.0001(5)	0.75
Mg	12c	0	0	0.1461(1)	0.0001(5)	0.25
P	18e	0.2890(3)	0	0.25	0.0002(5)	1.0
O1	36f	0.0228(7)	0.1953(5)	0.1924(2)	0.0001(3)	1.0
O2	36f	0.1852(4)	0.1630(5)	0.0883(3)	0.0001(3)	1.0
Phase 02 ($R\bar{3}c$)						
Na1	6b	0	0	0	0.0001(8)	0.804(18)
Na2	18e	0.6570(2)	0	0.25	0.005(3)	0.399(6)
V	12c	0	0	0.1470(2)	0.0001(9)	0.75
Mg	12c	0	0	0.1470(2)	0.0001(9)	0.25
P	18e	0.2909(7)	0	0.25	0.0002(4)	1.0
O1	36f	0.0179(1)	0.2097(1)	0.1961(4)	0.0002(4)	1.0
O2	36f	0.1940(1)	0.1807(9)	0.0904(6)	0.0002(3)	1.0
3.8 – 2.75 V Discharge ($R\bar{3}c$)						
Na1	6b	0	0	0	0.12(2)	0.92(2)
Na2	18e	0.6424(5)	0	0.25	0.016(1)	0.836(1)
V	12c	0	0	0.1472(2)	0.004(2)	0.75
Mg	12c	0	0	0.1472(2)	0.004(2)	0.25
P	18e	0.2998(1)	0	0.25	0.056(7)	1.0
O1	18e	0.0235(8)	0.2006(8)	0.1961(5)	0.060(8)	1.0
O2	36f	0.1890(9)	0.1719(6)	0.09227(2)	0.011(2)	1.0

Table 4.4: Atomic coordinates obtained by Rietveld refinement for the y = 0.5 samples cycled in the 3.8−2.75 V window.

Atom	Wyckoff Site	x	y	z	B_{iso}	Occ.
4.2 V Charge Phase 01 ($R\bar{3}c$)						
Na1	6b	0	0	0	0.017(8)	0.77(2)
Na2	18e	0.620(4)	0	0.25	0.56(1)	0.26(2)
V	12c	0	0	0.14375(1)	0.0025(1)	0.75
Mg	12c	0	0	0.14375(1)	0.0025(1)	0.25
P	18e	0.2875(5)	0	0.25	0.014(2)	1.0
O1	36f	0.0237(8)	0.1918(7)	0.1950(3)	0.015(3)	1.0
O2	36f	0.1868(6)	0.1575(7)	0.0934(3)	0.014(2)	1.0
Phase 02 ($R\bar{3}c$)						
Na1	6b	0	0	0	0.01(3)	0.67(5)
Na2	18e	0.624(1)	0	0.25	0.63(1)	0.28(5)
V	12c	0	0	0.1430(4)	0.001(4)	0.75
Mg	12c	0	0	0.1430(4)	0.001(4)	0.25
P	18e	0.291(2)	0	0.25	0.000(6)	1.0
O1	18e	0.017(2)	0.202(2)	0.2015(8)	0.001(1)	1.0
O2	36f	0.195(2)	0.157(2)	0.0965(8)	0.016(6)	1.0
4.2 − 2.75 V Discharge ($R\bar{3}c$)						
Na1	6b	0	0	0	0.019(1)	0.901(1)
Na2	18e	0.6379(6)	0	0.25	0.018(4)	0.707(7)
V	12c	0	0	0.1465(8)	0.011(1)	0.75
Mg	12c	0	0	0.1465(8)	0.011(1)	0.25
P	18e	0.2975(5)	0	0.25	0.051(4)	1.0
O1	18e	0.0337(5)	0.2118(5)	0.1949(2)	0.014(3)	1.0
O2	36f	0.1976(5)	0.1623(5)	0.0938(2)	0.013(8)	1.0

Table 4.5: Atomic coordinates obtained by Rietveld refinement for the y = 0.5 samples cycled in the 4.2−2.75 V window.

Atom	Wyckoff Site	x	y	z	B_{iso}	Occ.
3.8 V Charge ($R\bar{3}c$)						
Na1	6b	0	0	0	0.11(4)	0.907(1)
Na2	18e	0.6359(6)	0	0.25	0.07(1)	0.668(3)
V	12c	0	0	0.14791(1)	0.007(7)	0.50
Mg	12c	0	0	0.14791(1)	0.007(7)	0.50
P	18e	0.2880(3)	0	0.25	0.050(3)	1.0
O1	36f	0.0329(6)	0.2049(5)	0.19162(1)	0.06(6)	1.0
O2	36f	0.1976(4)	0.1787(5)	0.0894(2)	0.0006(8)	1.0
3.8 – 2.75 V Discharge ($R\bar{3}c$)						
Na1	6b	0	0	0	0.043(2)	1.0
Na2	18e	0.641	0	0.25	0.03(4)	0.97(4)
V	12c	0	0	0.149	0.004(4)	0.50
Mg	12c	0	0	0.1431(3)	0.00(4)	0.50
P	18e	0.2917(1)	0	0.25	0.01(2)	1.0
O1	36f	0.0184(7)	0.2057(3)	0.1912(4)	0.01(1)	1.0
O2	36f	0.1854(7)	0.1703(9)	0.0868(3)	0.003(2)	1.0

Table 4.6: Atomic coordinates obtained by Rietveld refinement for the y = 1.0 samples cycled in the 3.8−2.75 V window.

Atom	Wyckoff Site	x	y	z	B_{iso}	Occ.
4.2 V Charge (C2/c)						
Na1	4c	0.25	0.25	0	0.27(2)	0.62(8)
Na2	4e	0	0.89(4)	0.25	0.41(8)	0.63(1)
Na3	8f	0.6666(2)	0.924(1)	0.628(1)	0.21(5)	0.51(6)
V	8f	0.600(5)	0.252(6)	0.646(5)	0.13(4)	0.5
Mg	8f	0.600(5)	0.252(6)	0.646(5)	0.13(4)	0.5
P1	8f	0.851(1)	0.103(5)	0.963(1)	0.28(4)	1.0
P2	4e	0	0.537(1)	0.25	0.20(6)	1.0
O1	8f	0.135(4)	0.140(1)	0.35(2)	0.23(4)	1.0
O2	8f	0.077(1)	0.459(1)	0.223(1)	0.51(7)	1.0
O3	8f	0.454(1)	0.671(1)	0.97(2)	0.47(7)	1.0
O4	8f	0.155(1)	0.06(2)	0.053(2)	0.60(9)	1.0
O5	8f	0.763(1)	0.834(1)	0.273(9)	0.13(3)	1.0
O6	8f	0.071(5)	0.349(1)	0.928(9)	0.31(7)	1.0
4.2 – 2.75 V Discharge (C2/c)						
Na1	4c	0.25	0.25	0	0.030(1)	0.90(3)
Na2	4e	0	0.900(1)	0.25	0.03(2)	0.84(5)
Na3	8f	0.6653(1)	0.933(2)	0.629(3)	0.052(1)	0.77(4)
V	8f	0.5997(1)	0.2500(1)	0.650(2)	0.12(1)	0.5
Mg	8f	0.5997(1)	0.2500(1)	0.650(2)	0.12(1)	0.5
P1	8f	0.855(2)	0.106(3)	0.956(3)	0.19(5)	1.0
P2	4e	0	0.541(4)	0.25	0.08(2)	1.0
O1	8f	0.151(3)	0.153(5)	0.375(6)	0.38(3)	1.0
O2	8f	0.079(4)	0.460(2)	0.227(3)	0.1(6)	1.0
O3	8f	0.460(5)	0.696(4)	0.976(5)	0.20(1)	1.0
O4	8f	0.157(3)	0.074(3)	0.056(6)	0.007(1)	1.0
O5	8f	0.782(8)	0.855(1)	0.314(1)	1.4(1)	1.0
O6	8f	0.074(2)	0.354(2)	0.928(5)	0.013(1)	1.0

Table 4.7: Atomic coordinates obtained by Rietveld refinement for the y = 1.0 samples cycled in the 4.2−2.75 V window.

	Pristine				3.8 V				3.8-2.75 V		
δ_{iso} / ppm	48.8	-3.4	0.0	δ_{iso} / ppm	177.3	46.0	-15.0	δ_{iso} / ppm	48.2	-6.0	0.0
δ_{obs} / ppm	25.1	-10.1	0.0	δ_{obs} / ppm	137.1	25.1	-15.1	δ_{obs} / ppm	24.9	-10.9	-5.7
η_Q	0.606	0.0	0.0	η_Q	0.00	0.399	0.0	η_Q	0.399	0.015	0.0
C_Q / MHz	2.29	1.79	1.35	C_Q / MHz	3.30	2.20	1.44	C_Q / MHz	2.29	0.662	1.70
LB / kHz	2.53	3.97	0.72	LB / kHz	3.77	7.49	3.24	LB / kHz	3.18	4.15	4.2
Intensity	48.9	16.3	1	Intensity	1.0	7.24	2.04	Intensity	7.76	2.62	1

		4.2 V				4.2-2.75 V		
δ_{iso} / ppm	200.7	95.7	-8.4	11.4	δ_{iso} / ppm	44.8	-3.8	0.0
δ_{obs} / ppm	137.1	47.0	-18.8	-37.2	δ_{obs} / ppm	32.4	-10.6	-28.4
η_Q	0.503	0.58	0.00	0.08	η_Q	0.00	0.04	0.0
C_Q / MHz	4.05	3.48	1.69	3.51	C_Q / MHz	1.81	1.49	2.91
LB / kHz	3.33	2.31	2.66	4.18	LB / kHz	4.10	4.67	5.63
Intensity	1.0	0.80	1.41	1.43	Intensity	3.06	0.85	1.0

Table 4.8: ^{23}Na ssNMR parameters obtained from fits of the data obtained on ex situ y = 0.5 cathode samples at 7.05 T and 30 kHz MAS

	Pristine				3.8 V				3.8-2.75 V		
δ_{iso} / ppm	62.7	16.1	10.6	δ_{iso} / ppm	1.6	36.3	-71.0	δ_{iso} / ppm	61.8	15.3	10.6
δ_{obs} / ppm	58.5	24.5	5.0	δ_{obs} / ppm	-2.3	-36.3	-71.0	δ_{obs} / ppm	58.1	25.1	5.4
η_Q	0.23	0.0	0.0	η_Q	0.0	0.0	0.0	η_Q	0.18	0.0	0.0
C_Q / MHz	2.07	1.78	3.04	C_Q / MHz	2.42	0.0	0.0	C_Q / MHz	2.62	1.34	2.92
LB / kHz	12.7	8.23	3.28	LB / kHz	4.98	15.3	8.0	LB / kHz	9.07	7.64	3.18
Intensity	1.0	5.45	7.02	Intensity	18.3	7.1	1.0	Intensity	1.0	7.08	12.1

	4.2 V				4.2-2.75 V			
δ_{iso} / ppm	54.8	-4.9	-12.9	-71.6	δ_{iso} / ppm	47.7	4.8	2.0	-52.8
δ_{obs} / ppm	51.8	-7.0	-14.6	-71.1	δ_{obs} / ppm	47.7	4.8	-2.3	-52.8
η_Q	0.10	0.10	0.11	0.1	η_Q	0.0	0.0	0.0	0.0
C_Q / MHz	0.10	0.12	0.09	0.09	C_Q / MHz	0.0	0.0	2.75	0.0
LB / kHz	18.7	3.61	2.22	6.37	LB / kHz	12.7	9.59	5.15	10.1
Intensity	5.58	40.2	10.94	1.0	Intensity	2.4	4.4	3.39	1.0

Table 4.9: ^{23}Na ssNMR parameters obtained from fits of the data obtained on ex situ y = 1.0 cathode samples at 18.8 T and 20 kHz MAS

Chapter 5

Impact of isovalent Al substitution on the Na (de)intercalation processes in $Na_3V_{2-y}Al_y(PO_4)_3$ cathodes

The sodium superionic conductor (NASICON) $Na_3V_2(PO_4)_3$ cathode is a particularly attractive material for Na-ion batteries. It has recently been reported that the widely believed two-phase reaction in NVP between the $Na_3V_2(PO_4)_3$ – $NaV_2(PO_4)_3$ compositional end-members actually produces an intermediate $Na_2V_2(PO_4)_3$ phase during non-equilibrium cycling. Further, as was shown in Chapters 3 and 4, transition metal dopant choice, such as Mg substitution for V, changes the intercalation mechanism from two-phase to a solid solution reaction mechanism. Here, we show the ability of aluminum substitution into the $Na_3V_2(PO_4)_3$ framework to enhance the propensity of intermediate phase formation when cycling even at low C-rates, namely C/10 and C/20, leading to successive biphasic reactions between $Na_3V_{1.5}Al_{0.5}(PO_4)_3$ – $Na_{2.24}V_{1.5}Al_{0.5}(PO_4)_3$ –

$NaV_{1.5}Al_{0.5}(PO_4)_3$. We highlight the ability of the intermediate phase to preserve the $R\bar{3}c$ structure through ex situ X-ray diffraction (XRD), ^{23}Na solid-state NMR, and differential capacity analysis. Additionally, we also demonstrate the ability of Al incorporation into the NVP framework to reduce the propensity for particle cracking through scanning electron microscopy (SEM), a finding further supported by galvanostatic intermittent titration (GITT) cycling. *Ex-situ* synchrotron diffraction data was collected by Hayden Evans of the National Institute of Scientific Standards (NIST) and neutron diffraction data were collected by Hector C. Mandujano of the Department of Chemistry and Biochemistry, Univeristy of Maryland, College Park. Rietveld refinements of the neutron diffraction data were performed by Dr. Tianyu Li of the Clément group. Scanning electron microscopy images were collected in collaboration with Dr. Ravit Silverstein.

5.1 Introduction

Sodium-ion batteries have emerged as promising alternatives to traditional lithium-ion batteries owing to the greater natural abundance of sodium resources and their potential for large-scale energy storage applications [151, 152, 153]. Among the various sodium-ion cathode materials, $Na_3V_2(PO_4)_3$ (NVP) has garnered significant attention from the research community owing to its high theoretical capacity, excellent thermal & structural stability, rate capability, and cyclability [154, 155, 156]. The Na-ion transport and (de)insertion properties of NVP are intricately linked to its complex phase stability landscape characterized by a large number of Na/vacancy ordered structures. For example, it has been established that NVP undergoes a phase transition near room temperature (25−26°C) from the ordered monoclinic (C2/c) $\alpha-Na_3V_2(PO_4)_3$ structure to two intermediate $\beta-$ and $\beta'-Na_3V_2(PO_4)_3$ incommensurate modulated structures, and eventually an order-disorder transition takes place at around 177° C to the $\gamma-Na_3V_2(PO_4)_3$

with R$\bar{3}$c symmetry [34]. The crystal structure of NVP is composed of two VO_6 octahedra corner shared with three PO_4 tetrahedra termed "lantern units" stacked along the c-direction. Within the open three-dimensional framework created by these lantern units, two crystallographic sodium sites in the R$\bar{3}$c structure, labeled Na(1) and Na(2) are usually reported for simplicity (those sites further split in the lower symmetry structures). Upon electrochemical desodiation, a two-phase reaction between the $Na_3V_2(PO_4)_3$ and $NaV_2(PO_4)_3$ end members has been widely reported at relatively slow charge-discharge rates [157]. Prior work has indicated that, in $NaV_2(PO_4)_3$, the majority of Na is believed to be extracted from the eight-coordinate Na(2) sites [97], while the remaining Na in the six-coordinate Na(1) sites is believed to be crucial for the structural integrity of the NASICON structure. A recent study by Chotard et al., has demonstrated the existence of an intermediate $Na_2V_2(PO_4)_3$ phase when cycling this cathode at moderate C-rates (e.g., 0.77C). The authors have argued that the formation of an intermediate $Na_2V_2(PO_4)_3$ phase concurrently with the disappearance of the $Na_3V_2(PO_4)_3$ phase and formation of $NaV_2(PO_4)_3$ facilitates the overall phase transition by reducing the lattice mismatch between the end member phases [37]. Because $Na_2V_2(PO_4)_3$ always coexists with both $Na_3V_2(PO_4)_3$ and $NaV_2(PO_4)_3$ and does not lead to any noticeable feature in the differential capacity (dQ/dV vs. V) curve, it is extremely difficult to isolate electrochemically, complicating the determination of its crystal structure.

Interestingly, one of our previous studies, and as discussed in Chapter 3 which covered Mg substitution for V in the NVP framework showed that Mg incorporation leads to a solid-solution (de)intercalation mechanism from a two-phase mechanism when the concentration of Mg is increased beyond y = 0.5 in $Na_{3+y}V_{2-y}Mg_y(PO_4)_3$ cathodes [32]. In this work, we use partial Al^{3+} substitution for V^{3+} in $Na_3V_2(PO_4)_3$ to exacerbate the formation of an intermediate phase during electrochemical cycling of NVP, determine its structure, and understand its role in mitigating strain build-up and particle crack-

ing during long-term cycling. Previous reports on Al-substituted NVP cathodes have shown that these cathodes form an intermediate phase when cycled at a current rate of 1 Na^+/ 20 hours (i.e. C/40) deduced from differential capacity analysis [82]. Nevertheless, to the best of our knowledge, no structural information on the intermediate phase in $Na_3V_{2-y}Al_y(PO_4)_3$ cathodes has been provided to date. The influence of transition metal dopant choice on (de)intercalation mechanics highlights the importance of understanding their effect on electrochemical performance.

Here, we study the formation and structure intermediate phase via ex situ synchrotron X-ray diffraction, ^{23}Na solid-state nuclear magnetic resonance (NMR) spectroscopy, scanning electron microscopy (SEM), and relate it to the electrochemical performance. Unlike NVP, the intermediate phase forms at any C-rate tested here (i.e. even low C/10 and C/20 rates), suggesting a greater lattice mismatch between the two end-member phases obtained on charge and discharge. We find that Al incorporation into the NVP framework lowers the overpotentials associated with Na (de)intercalation by forming a stable intermediary $Na_{2.24}V_{1.5}Al_{0.5}(PO_4)_3$ phase and preserves the NASICON structure during electrochemical cycling in contrast to the primitive $P2_1/c$ intermediate phase formed during cycling of the undoped $Na_3V_2(PO_4)_3$ cathode. The formation of the intermediate phase in the Al-doped sample provides a transitional state between the $Na_3V_{1.5}Al_{0.5}(PO_4)_3$ and $NaV_{1.5}Al_{0.5}(PO_4)_3$ compositional endmembers that reduces the propensity of particle cracking during electrochemical cycling. This study is relevant to improving our understanding of NVP and other electrode materials that display a miscibility gap at low cycling rates and intermediate phases at high cycling rates with, in the extreme case, $LiFePO_4$ which goes from a two-phase reaction to a non-equilibrium solid solution that spans the entire composition between two thermodynamic phases, $LiFePO_4$ and $FePO_4$, at high current rates [158].

5.2 Results and Discussion

5.2.1 Crystal and electronic structures of as-synthesized $Na_3V_{2-y}Al_y(PO_4)_3$ (y = 0, 0.5) cathodes

NASICON $Na_3V_{2-y}Al_y(PO_4)_3$ (y = 0, 0.5) cathodes were prepared via a solution-assisted solid-state method [159]. Inductively coupled plasma−optical emission spectroscopy (ICP−OES) analysis of the composition of the synthesis products revealed a Na content of 2.94 for the y = 0.5 compound, hinting at a slight sodium deficiency in this material. The total elemental composition was normalized assuming full V occupation in both the unsubstituted (y = 0) and Al-substituted (y = 0.5) samples. For the y = 0.5 sample, the Na:V:Al:P ratio was found to be 2.94: 1.5:0.48:3.17, respectively. In the undoped sample, no aluminum precursors were used, albeit trace amounts of Al were found with a resulting Na:V:Al:P ratio of 2.90:2.0:0.04:3.18, the tabulated values are shown in Table 5.1 in Appendix C. The crystal structure of the pristine y = 0 and y = 0.5 cathodes was determined using synchrotron X-ray diffraction (sXRD) and neutron diffraction for the Al-substitued cathode. $Na_3V_2(PO_4)_3$ has been reported to undergo a phase transition to a Na/vacancy ordered monoclinic C2/c phase near room temperature, while the higher symmetry, disordered R$\bar{3}$c structure is observed above 177°C [34]. The monoclinic structure comprises three crystallographic sites for Na (Na(1), Na(2), and Na(3)) as opposed to two sites in the rhombohedral structure (Na(1) and Na(2)). The sXRD diffraction pattern of the y = 0 system was best refined using the C2/c space group as shown in Figure 5.1a, resulting in Na(1), Na(2) and Na(3) site occupancies of 0.83, 0.73, and 0.69, respectively. The computed Na content from Rietveld refinements (Figure 5.1b) of the sXRD pattern for the y = 0.5 sample results in 2.98, approximately 0.04 higher than what was observed via ICP-OES. For the Al-substituted cathode, neutron

diffraction experiments were performed at low (10 K) and room (300 K) temperature, and Rietveld refinements of the data were carried out using both a $R\bar{3}c$ and C2/c space group. The results, shown in Figures 5.7, 5.8, and Table 5.3 in Appendix C, indicate that the monoclinic (C2/c) structural model better fits the data at both temperatures. The Rietveld refinement of the room temperature data results in Na(1), Na(2), and Na(3) site occupancies of 0.86, 0.77, and 0.58, respectively in good agreement with the sXRD data. At 10 K, the increased propensity for Na ordering causes both the Na(1) and Na(3) sites to fill as the Na(2) occupancy decreases, resulting in Na occupancies for Na(1), Na(2), and Na(3) of 0.96, 0.60, and 0.84, respectively. The room temperature y = 0.5 cathode structure was also investigated using sXRD, and a Rietveld refinement of the pattern using the same C2/c structure model leads to Na(1), Na(2), and Na(3) site occupancies of 0.86, 0.76, and 0.6, respectively, in good agreement with the neutron results. As expected, as Al^{3+} is substituted into the NVP cathode, the sXRD Bragg peaks shift to higher 2θ values due to unit cell contraction resulting from the smaller radius of Al^{3+} (r (6 C.N.) = 0.535 Å) compared to V^{3+} (r (6 C.N.) = 0.64 Å) [160].

Next, V K-edge X-ray absorption spectroscopy (XAS) experiments were performed on the as-synthesized Al-NVP samples to determine the nominal oxidation state of V, and identify potential differences in the local structure around V in the two compounds. The normalized X-ray absorption near edge (XANES) spectra are shown in Figure 5.1c The position of the absorption edge is similar in the spectra obtained on the y = 0 and 0.5 compounds, confirming that the average V oxidation state is +3 in both samples.

^{23}Na solid-state NMR experiments were also conducted to compare the distribution of Na local environments in the y = 0 and y = 0.5 compounds. The spin echo spectra collected at a high magnetic field of 18.8 T and at a magic angle spinning (MAS) speed of 30 kHz are shown in Figure 5.1d. The presence of open-shell V^{3+} species in these materials results in hyperfine (or paramagnetic) interactions between unpaired electron

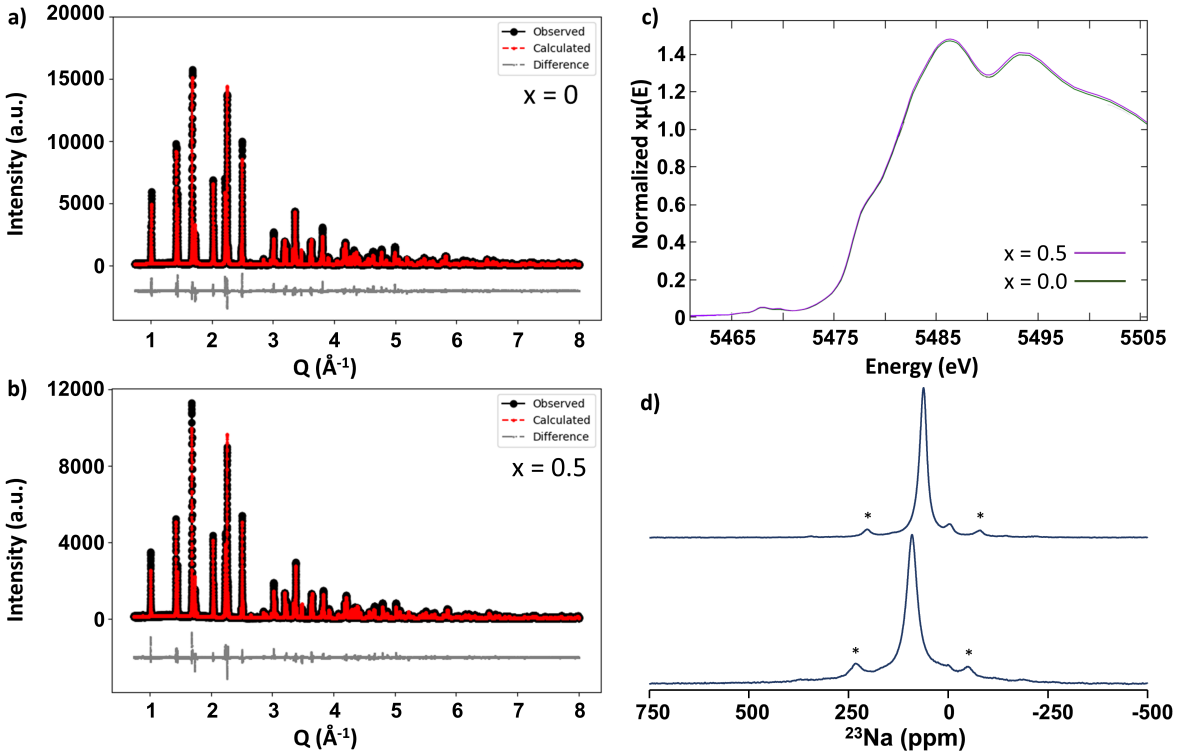

Figure 5.1: a,b) refined diffraction patterns of the y = 0 and 0.5 samples. c) ^{23}Na solid-state NMR spectra collected on the as-synthesized samples at 18.8 T and 30 kHz MAS. d) Normalized absorption spectra.

spins originating from the V 3d orbitals and the ^{23}Na nuclei under investigation. These strong hyperfine interactions lead to significant ^{23}Na NMR line broadening that cannot be fully removed by MAS. They also lead to an isotropic Fermi contact shift (δ_{iso}) of the ^{23}Na resonant frequency due to delocalization of unpaired electron spin density from the V 3d orbitals to the Na s orbitals via bridging O 2p orbitals. For quadrupolar nuclei (spin $> \frac{1}{2}$), such as ^{23}Na, the interaction between the nuclear quadrupole moment and the electric field gradient (EFG) generated by surrounding ions/charges at the nuclear position also broadens the NMR lines and leads to a second-order quadrupolar shift (δ_Q) of the ^{23}Na resonant frequency. δ_Q is significantly reduced at high fields (here, 18.8 T), such that the observed chemical shift can be approximated to the Fermi contact

contribution: $\delta_{obs} = \delta_{iso} + \delta_Q \approx \delta_{iso}$. In the two spectra shown in Figure 5.1d, the sharp signal centered around 0 ppm results from (a) minor diamagnetic impurity(ies), possibly sodium phosphate and/or pyrophosphate [161], in the as-synthesized y = 0 and y = 0.5 samples. All other resonances correspond to Na species in the paramagnetic cathodes, and a general shift of the ^{23}Na resonances towards 0 ppm is observed upon partial substitution of the paramagnetic V^{3+} species by diamagnetic Al^{3+} ions (from y = 0 to y = 0.5) due to the reduced paramagnetic interactions. The presence of multiple Na environments in the cathode structures, particularly in the Al-substituted system, leads to multiple broad and overlapping signals that complicate their assignment. In addition, rapid Na chemical exchange between the various Na sites in the NASICON structure on the NMR timescale results in partial averaging of the resonances [32], further complicating the assignment. A deconvolution of the spectrum obtained on NVP (y = 0), shown in Figure 5.9, Appendix B, indicates the presence of at least 2 resonances, one relatively sharp and one broad signal near δ_{obs} = 91 and 102 ppm. We previously assigned the resonances to Na in Na(1) and Na(2) sites in the NVP structure, with the assistance of first principles calculations of paramagnetic NMR shifts. The as-synthesized y = 0 powder crystallizes in the monoclinic C2/c structure where more than two Na sites are present. The fact that we only see two average NASICON resonances, from fitting with least amount of sites needed to achieve a reasonable fit, implies fast Na exchange on the NMR timescale between the Na(1), Na(2), and Na(3) sites in good agreement with what was observed in a previous study (and in Chapter 3) exploring Mg substitution into the NVP framework [32]. The spectrum obtained on the Al-substituted cathode can be fit with two resonances at δ_{obs} = 60 and 64 ppm, corresponding to Na species in Na(1) and Na(2) sites in the NASICON structure, along with the diamagnetic impurity resonance near 0 ppm. Once again, the observation of only two paramagnetic resonances in this spectrum, despite the large number of Na environments expected in this material due

to the large number of possible arrangements of Al and V species around the Na(1) and Na(2) sites, indicates fast Na exchange between those sites on the NMR timescale.

5.2.2 Impact of Al substitution on the Na (de)intercalation properties of the NVP cathode

Having demonstrated how Al^{3+} incorporation into the NVP framework affects the long-range, local crystal, and electronic structures, the focus was then placed on assessing its impact on Na (de)intercalation properties via galvanostatic cycling over two voltage windows: 4.2−2.4 V and 3.8−2.4 V vs. Na^+/Na^0. The voltage-capacity profiles of the y = 0 and y = 0.5 cathodes over the 3.8−2.4 V cycling window and at a rate of C/10 are shown in Figures 5.2a and 5.2b, along with their differential capacity (dQ/dV vs. V) plots as insets.

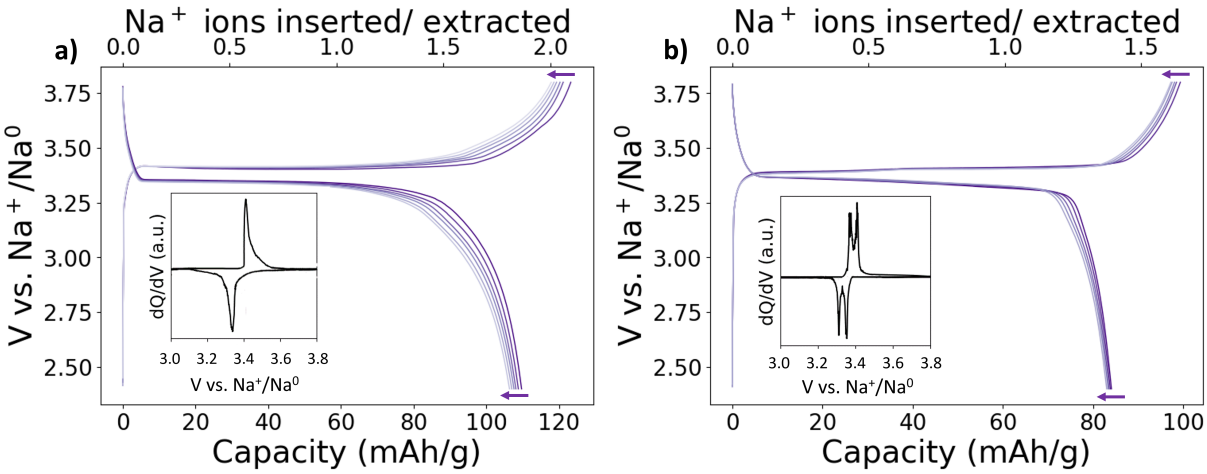

Figure 5.2: Voltage vs. capacity profiles and differential capacity (dQ/dV vs. V as inset) plots in the 3.8−2.4 V cycling window for $Na_3V_{2-y}Al_y(PO_4)_3$ cathodes in Na half-cells at a rate of 0.1 V: a) y = 0 and b) y = 0.5 Note: The first 6 cycles are shown for each composition

The voltage profile and differential capacity plot obtained for NVP at a relatively low rate feature a single plateau or redox peak at 3.41 V on charge and 3.35 V on discharge, in

good agreement with previous reports [82]. The voltage profile and differential capacity plot obtained for the y = 0.5 cathode exhibit two consecutive plateaus or redox peaks at 3.38 and 3.41 V on charge, and at 3.37 and 3.34 V on discharge. Those results suggest the presence of a well-defined intermediate phase at approximately 3.39 V on charge and 3.35 V on discharge, or two successive biphasic reactions on Na (de)intercalation, in good agreement with previous reports [82]. This behavior is notably different from that reported for unsubstituted NVP cycled at fast C rates where no additional redox features could be observed in the voltage profile or differential capacity plot despite the appearance of an intermediate $Na_2V_2(PO_4)_3$ phase in the cathode, and suggests that the intermediate phase in the Al-substituted cathode could be easier to isolate. To determine the impact of the voltage window on the redox properties of the y = 0.5 compound, the cathode was also cycled over a larger 4.2−2.4 V window, with the corresponding voltage profile and differential capacity plot shown in Figure 5.3a and 5.3b, respectively. While minor changes are observed over the 3.8−2.4 V range, as compared to the electrochemical test performed over a smaller voltage window, an additional voltage/redox feature is observed at 3.95 V on charge, and 3.91 on discharge, which has been ascribed to the V^{4+}/V^{5+} redox couple when cycled in the 4.2−2.4 V (CITE) window for the Al-doped system (CITE) .

5.2.3 *Ex-situ* analysis of structural changes during electrochemical cycling over the 4.2−2.4 V window

To gain further insight into the structural processes underlying the two successive biphasic reactions in the Al-substituted compound, ex situ y = 0.5 cathode samples stopped at various states of (dis)charge during the second cycle were analyzed using sXRD. When comparing the sXRD pattern collected on a cathode sample discharged to 2.4 V after an initial charge to 4.2 V to the pattern obtained on the pristine powder, we

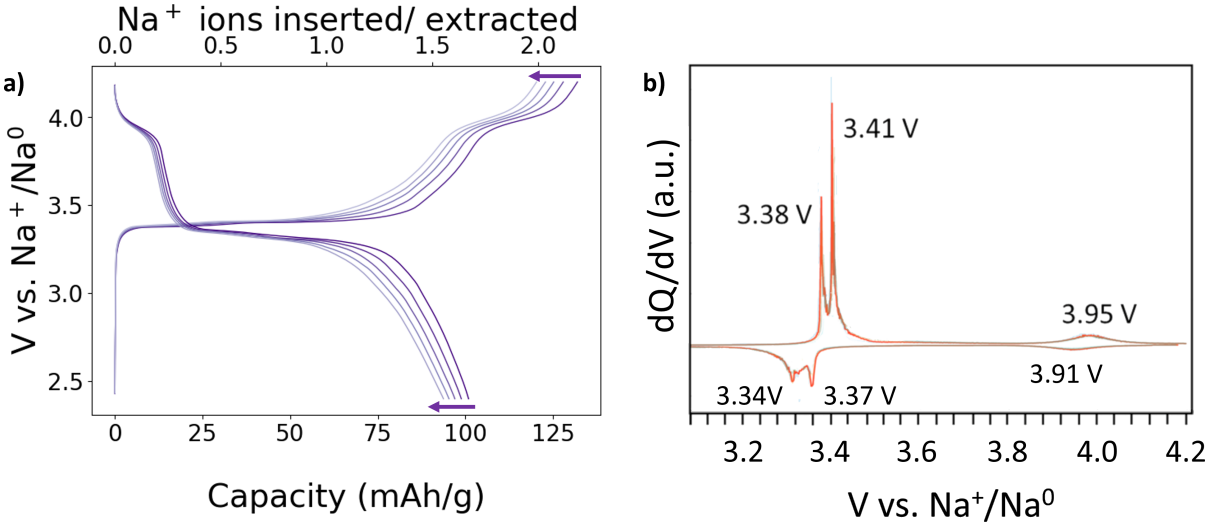

Figure 5.3: a) Voltage vs. capacity profile and b) differential capacity (dQ/dV vs. V) plot in the 4.2−2.4 V cycling window for the $Na_3V_{2-y}Al_y(PO_4)_3$ (y = 0.5) cathode in a Na half-cell at a rate of 0.1 C. Note: cycles 2−6 are shown in a) with the dQ/dV plot of the second cycle in b).

notice an irreversible change from the pristine monoclinic (C2/c) structure to a rhombohedral ($R\bar{3}c$) structure. While the initial Na stoichiometry in the y = 0.5 cathode is approximately 2.98 as evidenced by Rietveld refinement (Table 5.3, Appendix C), as mentioned earlier, the sXRD results on the discharged sample suggest an irreversible loss of ≈ 0.26 Na ions per formula unit during the first charge-discharge cycle, resulting in a cathode composition of $Na_{2.65}V_{1.5}Al_{0.5}(PO_4)_3$ with refined Na(1) and Na(2) occupancies of 0.67 and 0.66, respectively. When the y = 0.5 sample is subsequently charged to 3.39 V to isolate the intermediate phase (minimum in the dQ/dV plot on charge in Figure 5.3b), roughly 0.33 Na ions per formula unit are extracted based on the observed capacity, suggesting an intermediate composition of $Na_{2.31}V_{1.5}Al_{0.5}(PO_4)_3$. The Rietveld refinement of the sXRD pattern collected on the 3.39 V charged sample requires a two phase model, with one phase being the $Na_{2.65}V_{1.5}Al_{0.5}(PO_4)_3$ rhombohedral phase observed in the discharged state and accounting for roughly 13.6% of the phase fraction of

the total diffraction pattern. The second, intermediate phase accounts for 86.4% of the phase fraction of the total diffraction pattern and can be refined using the R$\bar{3}$c space group and Na occupancies for the Na(1) and Na(2) sites of 0.71 and 0.51, respectively, resulting in a composition of $Na_{2.24}V_{1.5}Al_{0.5}(PO_4)_3$. Based on those fractions and compositions, the overall sample composition is $Na_{2.30}V_{1.5}Al_{0.5}(PO_4)_3$, which is very close to that obtained from the observed capacity. The presence of both the discharged phase and the intermediate phase in this sample is likely caused by structural relaxation during ex situ cathode sample preparation. Notably, the results presented here indicate a clear miscibility gap between the $Na_{2.65}V_{1.5}Al_{0.5}(PO_4)_3$ phase that predominates in the discharged state, and the $Na_{2.24}V_{1.5}Al_{0.5}(PO_4)_3$ phase stabilized at intermediate potentials. The reduced Na(2) site occupancy, and increased Na(1) site occupancy in the intermediate structure, as compared to the discharged structure, highlights the presence of a new stable Na/vacancy ordering at 3.39 V. Rietveld refinement of the sXRD pattern collected on the top of charge (4.2 V) sample can be achieved using a single phase with R$\bar{3}$c symmetry, and indicates that Na is extracted from the Na(2) sites (the occupancy decreases to 0.16), as the Na(1) sites fill (occupancy increases to 0.96) over the second voltage plateau. Similar findings have been made for related NVP-type cathodes [97]. The overall composition of the phase stabilized at high states of charge is $Na_{1.41}V_{1.5}Al_{0.5}(PO_4)_3$, suggesting that 1.56 Na per formula unit can be cycled reversibly over the 4.2−2.4 V window at a rate of C/10. Details of the refinements are provided in Table 5.3 in Appendix C.

Ex situ x= 0.5 cathode samples stopped at similar states of charge were investigated using ^{23}Na solid-state NMR to monitor the evolution of the local structure around Na during cycling over the 4.2−2.4 V window. In the uncycled y = 0.5 cathode film, composed of the active cathode material mixed with carbon and PTFE binder in a weight ratio of 70:20:10, respectively, three resonances are observed at δ_{obs} = 0, 51, and 70 ppm, with relative intensities for the 51 and 70 ppm signals of 1 and 0.94, respectively. The

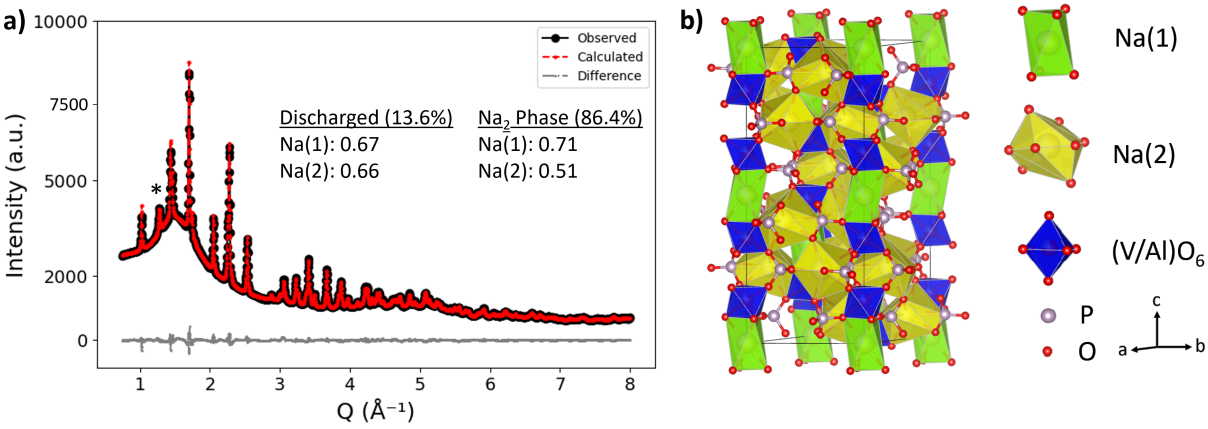

Figure 5.4: a) Refinement of the synchrotron XRD pattern collected on an ex situ x=0.5 cathode sample stopped at 3.39 V during the second charge process, in the potential range where the intermediate phase predominates. The sample contains two rhombohedral phases with compositions $Na_{2.65}V_{1.5}Al_{0.5}(PO_4)_3$ and $Na_{2.24}V_{1.5}Al_{0.5}(PO_4)_3$. b) Structural model of the intermediate $Na_{2.24}V_{1.5}Al_{0.5}(PO_4)_3$ phase.

resonance at 0 ppm is the diamagnetic impurity mentioned earlier and the other two resonances are assigned to ^{23}Na paramagnetic environments present in the NASICON structure, fits of the ^{23}Na spectrum are shown in Figure 5.11a, Appendix C. The difference in ^{23}Na chemical shifts between the pristine (as-synthesized) powder (Figure 5.1d) and the uncycled cathode film may arise from a change of the electronic environment surrounding Na ions in the cathode film leading to a (de)shielding effect created by the incorporation of conductive carbon. When the y = 0.5 sample is charged to 4.2 V then discharged to 2.4 V, three resonances are observed at $\delta_{obs} = -7$, 43, and 68 ppm. The two resonances attributed to the NASICON cathode are shifted upfield (to lower ppm values) by a few ppm compared to those observed in the spectrum collected on the pristine cathode film, in good agreement with the sXRD results. The signal at -7 ppm may arise due in part to electrolyte decomposition products with potential signal overlap of the impurity peak at 0 ppm. The ^{23}Na spectrum collected on a cathode sample stopped on subsequent charge to 3.39 V comprises six ^{23}Na resonances at $\delta_{obs} = -4$, 43, 68, 93,

175, and 220 ppm (a deconvolution of this spectrum is shown in Figure 5.12a, Appendix C). Further, all three ^{23}Na resonances at $-4/-7$ ppm, 43 ppm, and 68 ppm observed in the spectrum collected on the discharged sample are still present in the spectrum obtained on mid-charge, albeit less intense, and three new resonances appear at 93, 175, and 220 ppm. Those findings are consistent with the two-phase reaction identified electrochemically and with sXRD, and the three new resonances are assigned to Na sites in the intermediate NASICON structure. Those three resonances are shifted downfield (to higher ppm values). Finally, the ^{23}Na spectrum collected on a sample is discharged to 3.35 V, exhibits the same three resonances at 93, 175, and 220 ppm (fits are shown in Figure 5.12b) observed in the 3.39V charged spectrum, which indicates that a similar intermediate phase is formed on charge and on discharge.

At the top of charge, we see the emergence of new sites not previously observed in the spectra collected on the pristine and 3.39 V charged samples. As already established earlier, from the Rietveld refinements we see that the Na(1) site fills at 4.2 V and becomes relatively immobile in the NASICON structure and assume distinct sites with various possible V/Al coordinations. Thus, the emergence of various new resonances is unsurprising as fast Na exchange among these sites no longer leads to signal averaging.

5.2.4 Discussion

In the case of the NVP cathode material, there are no electrochemical features distinctly marking the formation of the $Na_2V_2(PO_4)_3$ intermediate phase, which only occurs at high cycling rates and is best observed in situ or operando. Further, such measurements fail to isolate this intermediate phase, which always coexists with the $Na_3V_2(PO_4)_3$ and $NaV_2(PO_4)_3$ end-member phases, complicating the elucidation of its crystal structure. Conversely, the formation of an intermediate phase upon electrochem-

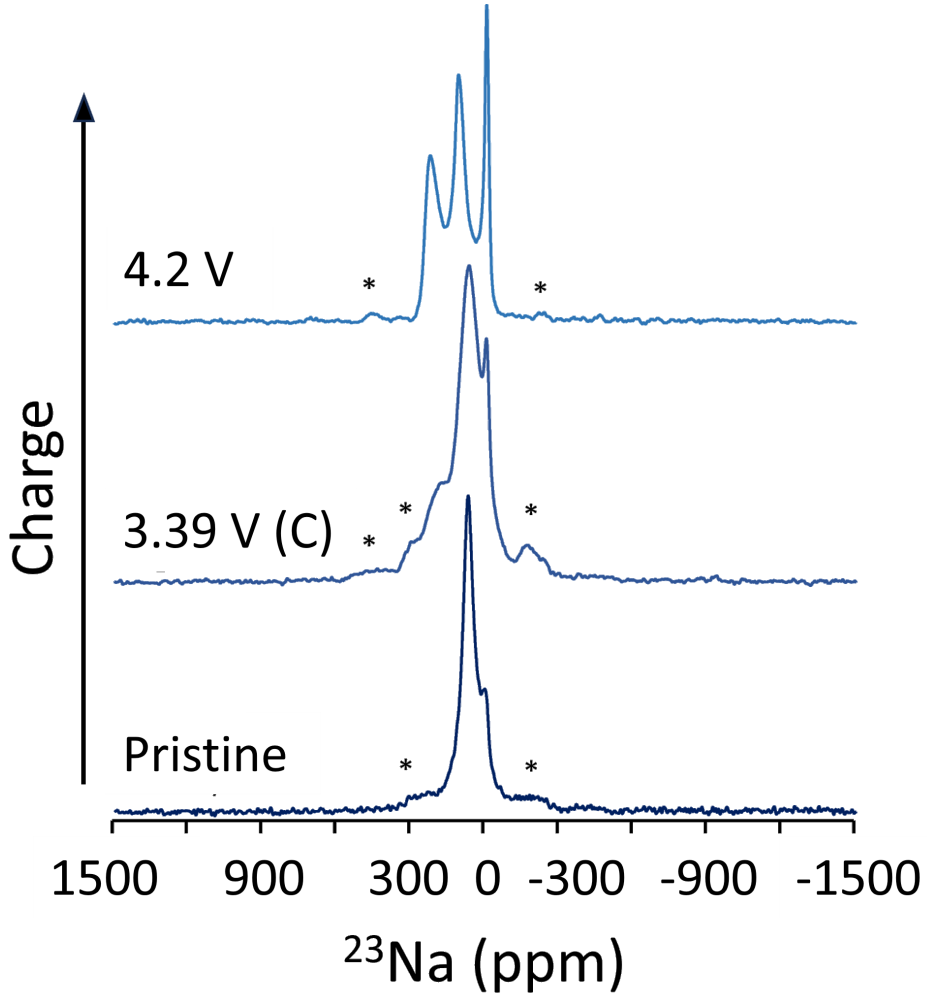

Figure 5.5: ^{23}Na solid-state NMR spectra collected on ex situ y = 0.5 samples stopped at various states of charge during the 2nd cycle in the 4.2−2.4 V window at 18.8 T and 50 kHz MAS.

ical Na (de)intercalation from the Al-substituted y = 0.5 cathode results in a clear step in the voltage profile, and a clear double redox peak in the differential capacity (dQ/dV) curve at 3.38 and 3.41 V, as shown in Figure 5.2b and 5.3b. This indicates the formation of a stable Na/vacancy ordered composition between these specific potentials, establishing the intermediate phase as a true intermediary with miscibility seen in both the charged and discharged phases. As a result, the electrochemistry proceeds as two sequential biphasic reactions taking place on charge and on discharge. It should be noted that

in the NVP system (i.e. $Na_3V_2(PO_4)_3$), the intermediate $Na_2V_2(PO_4)_3$ model appeared as a primitive space group with $P2_1/c$ as the most likely structure. However, Al incorporation allows for the intermediary $Na_2V_2(PO_4)_3$ phase to appear as the rhombohedral $R\bar{3}c$ space group further hinting at the ability of Al to better preserve the NASICON structure during electrochemical cycling. A potential driving force for the formation of an intermediate phase could be the volume changes (ΔV) between the $Na_3V_2(PO_4)_3$ and $NaV_2(PO_4)_3$ compositional end-members during cycling. It is known that the formation of an intermediate phase in a two-phase reaction can help reduce the build up of strain upon Na (de)intercalation, as well as particle cracking, by providing a buffer or pathway for accommodating volume changes associated with Na (de)intercalation during (dis)charge cycles. For the Al-substituted cathode, the change in the unit cell volume from the pristine state to the end of charge state, as obtained from Rietveld analysis of ex situ sXRD data (Table 5.2, Appendix C) is 30 $Å^3$ greater than that observed for the undoped $Na_3V_2(PO_4)_3$ system, which is consistent with the observation that an intermediate (buffer) phase form more readily during cycling in the latter system. To investigate whether the formation of an intermediate phase reduces particle cracking in the Al-substituted cathode, as compared to the unsubstituted cathode (with no intermediate phase forming at low cycling rates), scanning electron microscopy (SEM) images (shown in Figure 5.6) were obtained on y = 0 and 0.5 cathode samples before cycling (the pristine cathode films were exposed to the electrolyte for 24 hours to eliminate the potential impact of electrolyte wetting on particle cracking, SEM images shown in Figure 5.13, Appendix C) and after 40 cycles over the 3.8−2.4 V voltage window. The smaller, reversible, voltage window was chosen to deconvolute potential particle cracking from high voltage degradation processes observed at high voltage. Both uncycled y = 0 and 0.5 samples show no particle cracking after being in contact with the 1M NaPF6 electrolyte overnight as shown in Figure 5.13, Appendix C. After 40 cycles, the y = 0

sample shows a substantial amount of particle cracking with a complete cleavage of select particles (Figure 5.6a,b) when compared to the y = 0.5 sample (Figure 5.6c,d), which may imply that the reason we see a more pronounced intermediate phase in the Al-doped sample could be to reduce the stress and strain associated with greater amount of volume change occurring between the $Na_3V_{1.5}Al_{0.5}(PO_4)_3$ and $NaV_{1.5}Al_{0.5}(PO_4)_3$ compositional end-members.

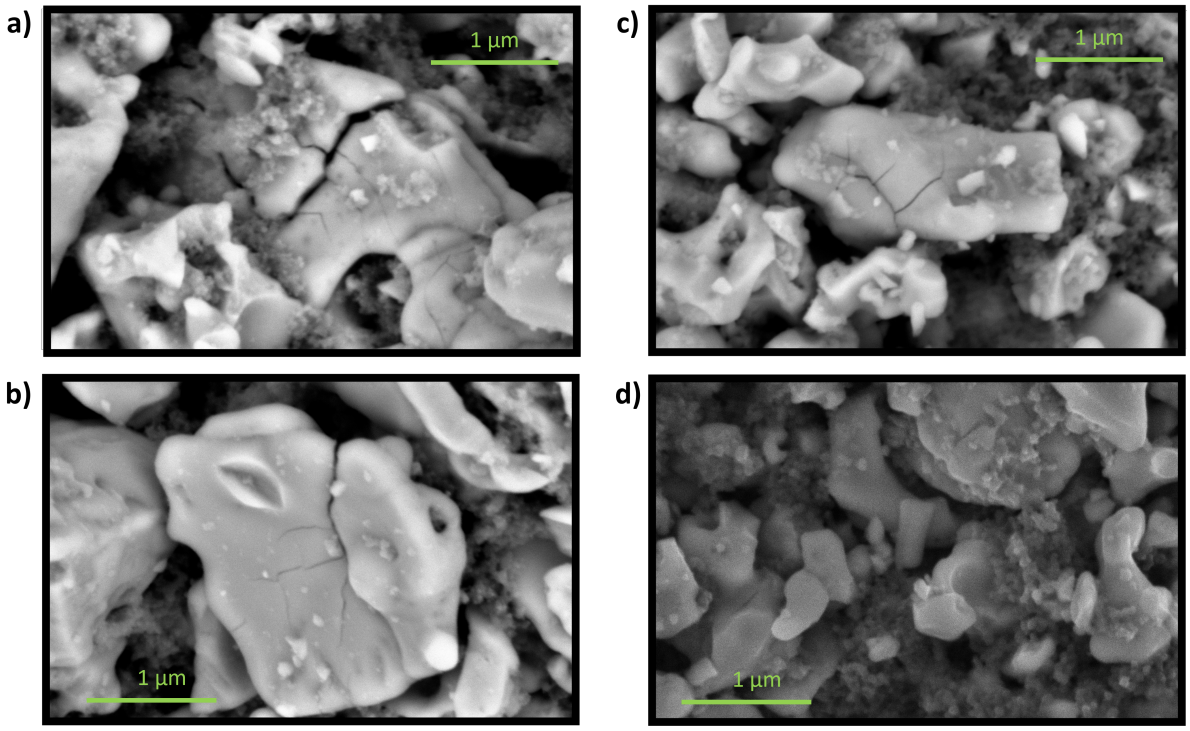

Figure 5.6: Scanning electron microscopy (SEM) images of ex-situ samples after 40 cycles in the 3.8−2.4 V window for a,b) y = 0 and b,d) y = 0.5 samples

We also suspect that the formation of an intermediate phase might improve Na insertion / extraction kinetics during cycling at relatively slow rates (to prevent the formation of an intermediate phase in the unsubstituted NVP system). To test this hypothesis, galvanostatic intermittent titration technique (GITT) experiments were performed, with results shown in Figure 5.14, Appendix C. The undoped (y = 0) sample shows larger

overpotentials throughout the entire cycling window when compared to the y = 0.5 sample and when the amount of Na extracted per formula unit exceeds two, as expected due to the necessity of the Na(1) site for structural integrity [97]. On the other hand, the y = 0.5 sample shows smaller overpotentials during Na^+ extraction suggesting the improved Na^+ kinetics provided by the formation of the intermediate phase during cycling.

5.3 Conclusions

This study focused on the investigation of $Na_3V_{2-y}Al_y(PO_4)_3$ (y = 0, and 0.5) cathodes to better understand the influence of Al incorporation into the NVP framework and its subsequent effects on electrochemical performance. Synchrotron and neutron XRD confirm that Al incorporation leads to a monoclinic C2/c structure at room temperature similar to $Na_3V_2(PO_4)_3$ along with unit cell contraction due to the smaller ionic radii of Al when compared to V in this structure. Al incorporation also promotes the formation of an intermediary phase to a greater extent than pure NVP. When the $Na_3V_{1.5}Al_{0.5}(PO_4)_3$ sample is charged and then discharged, an irreversible change from the monoclinic C2/c structure to a rhombohedral $R\bar{3}c$ structure occurs. While the investigation of successive biphasic (de)intercalation mechanics is still underway, it is already apparent that the formation of an intermediate phase in the y = 0.5 sample reduces the strain associated with the greater volume changes occurring in the Al-doped system during electrochemical cycling. Rietveld refinements of the intermediary phase illustrate the difficulty of completely isolating the intermediate phase electrochemically given the narrow 30 mV window in which it exists exacerbated by sample relaxation after the current is no longer applied. For these two reasons, it will always make complete isolation of the intermediate phase difficult, at least electrochemically. However, it does show that the intermediate phase remains rhombohedral ($R\bar{3}c$) in contrast to the primitive ($P2_1/c$) structure found

for the undoped $Na_3V_2(PO_4)_3$ system [37]. The presence of multiple phases is also seen in the ex-situ ^{23}Na solid-state NMR data and is observed both on charge and discharge. The ability of the intermediate phase to remain rhombohedral during electrochemical cycling highlights the improvement in efficiency when Al is incorporated into the NVP framework and is further corroborated by the lower overpotentials observed in the GITT data presented here. Additionally, SEM of the y = 0 and 0.5 electrodes after 40 cycles also shows the ability of the intermediary phase to reduce the propensity for particle cracking. The results here may help guide the choice of transition metal species for NVP to improve efficiency and reduce the stress and strain associated with two-phase (de)intercalation mechanics. Future directions of work could include exploring transitions metals with multiple oxidation states to reduce particle cracking and simultaneously improve performance metrics such as specific capacity.

5.4 Experimental section

5.4.1 Synthesis

The synthesis of NASICON $Na_3V_{2-x}Al_x(PO_4)_3$ (y = 0, 0.5) cathodes were prepared via a solution-assisted solid-state method [159]. NH_4VO_3, NaH_2PO_4, $Al[OC(CH_3)_3]_3$, and oxalic acid (reducing agent) were used as the starting precursors in stoichiometric proportions. NH_4VO_3 and NaH_2PO_4 were initially dissolved in warm deionized water, and oxalic acid was added to provide 10 wt% of carbon to the target compound, also acting as a reducing agent to lower the vanadium oxidation state from V^{5+} to V^{3+}. Aluminum-tert butoxide ($Al[OC(CH_3)_3]_3$) previously dissolved in 200 proof ethanol was then added dropwise while stirring until all of the liquid had evaporated. The resulting gel was dried at 120°C overnight, ground in an agate mortar & pestle, then dried at 450°C

for 4 hours under Ar gas flow to evolve gases and control volumetric expansion. After the preheating step, the powder was ground again, pelletized, and calcined at 750°C for 12 hours under Ar flow.

5.4.2 Inductively Coupled Plasma Optical Emission

Bulk chemical compositions were determined via ICP (Agilent 5800 ICP-OES). Samples were dissolved in a solution consisting of a 10:1 (v/v) ratio of 70% HNO_3 (Sigma-Aldrich) and concentrated HCl (Sigma-Aldrich).

5.4.3 Diffraction

Pristine Al-NVP samples were packed in Kapton capillaries and high-resolution synchrotron XRD patterns were collected on Beamline 11-BM at the Advanced Photon Source (APS) at Argonne National Laboratory using an average wavelength of 0.46 Å. All patterns were collected in the Debye-Scherrer geometry from 0.5° to 50° 2θ at room temperature with data points at a nominal 2θ step of 0.001 degrees with a time per step of 0.1 s. Ex situ cycled (y = 0.5) samples were collected on Beamline 17-BM at the Advanced Photon Source at Argonne National Laboratory. All samples were measured at room temperature (approximately 303 K). The average wavelength for measurements was 0.24 Å. Time-of-flight neutron diffraction data were obtained at the POWGEN beamline at the SNS. Data were collected at 10 and 300 K. Approximately 2 grams of the y = 0.5 powder sample (as synthesized) were used for the measurements with each scan lasting roughly 2 hours.

The TOPAS software suite was used for Rietveld refinements [162] using Pseudo-Voigt peak shapes set by the 11- and 17-BM instrument resolution file. For all refinements, an initial Pawley fit was first performed to refine the background with Chebyshev polynomial

(9 terms), crystallite size, zero shift, lattice parameters, microstrain, and absorption. The values for these parameters obtained from the Pawley fit were then fixed and used in the following Rietveld refinement to obtain atomic coordinates and Na site occupancies. In the Rietveld refinements, the total V content was constrained to the as-synthesized values of 2 for undoped NVP, and 1.5 for the Al doped sample (y = 0.5). The total Na occupancy was allowed to refine.

5.4.4 Solid-state Nuclear Magnetic Resonance

Room temperature ^{23}Na solid-state nuclear magnetic resonance (NMR) spectra were collected on the as-synthesized powder and ex situ cathode film Al-NVP ($y = 0, 0.5$) samples using an 18.8 T (800 MHz for ^{1}H) Bruker standard bore spectrometer equipped with a Bruker Avance III console and operating at a Larmor frequency of 211.65 MHz for ^{23}Na. The ^{23}Na spectra obtained on the pristine (as-synthesized) samples were collected at a magic angle spinning (MAS) rate of 30 kHz using a 2.5 mm double-resonance HX probe, while the spectra obtained on ex situ cathode samples were collected under 50 kHz MAS using a 1.3 mm double-resonance HX probe. A smaller rotor size was used for the ex situ samples to increase the filling factor due to the limited sample size. All ^{23}Na spectra were referenced against a 1 M NaCl solution ($\delta(^{23}\text{Na}) = 0$ ppm). Lineshape analysis was carried out within the Bruker TopSpin software using the SOLA lineshape simulation package and a QUAD + CSA model. The ^{23}Na spectra were obtained using a rotor-synchronized spin-echo sequence (90°–τ_r–180°–τ_r–acq). Pristine ^{23}Na spin echo spectra were obtained using a 90° RF pulse of 0.75 μs and a 180° pulse of 1.5 μs at 300 W, with a recycle delay of 50 ms and averaged over 16,000 transients. Ex situ ^{23}Na spectra were collected at various states of charge when cycled over the wider voltage window of 4.2–2.4 V vs Na^+/Na^0. The ex situ spectra used a 90° RF pulse of 0.85 μs and a 180°

pulse of 1.70 μs, with a recycle delay of 50 ms optimized to selectively enhance the signal intensity of the paramagnetic component(s).

5.4.5 Electrochemical Characterization

Electrochemical tests of the Al-NVP cathodes were performed in two-electrode Swagelok cells. The cathode active materials were mixed with carbon (C65 TIMCAL) and polytetrafluoroethylene (PTFE) binder in a weight ratio of 70:20:10, respectively. The resulting mixture was prepared into free-standing films and punched into 6 mm electrodes with a mass loading of active material between 2.0 – 3.0 mg/cm^2. Sodium metal (Sigma, $>$ 99%) was used as the counter electrode and a 1 M $NaPF_6$ in a weight ratio of 98:2 of propylene carbonate (PC) and fluoroethylene carbonate (FEC) was used as the electrolyte. The cells were assembled in an Ar-filled glovebox (O2 $<$ 0.5 ppm, H2O $<$ 0.5 ppm) and evaluated in a battery cycler (Arbin BT2000) over two voltage ranges of 4.2−2.4 V and 3.8−2.4 V versus Na^+/Na^0 and at a C-rate of C/10. For GITT experiments, a current equivalent to a C/20 rate was applied with a 30-minute relaxation period. Prior to the GITT experiments, the cells were cycled at C/20 for one formation cycle.

5.4.6 X-ray absorption spectroscopy

X-ray absorption spectroscopy (XAS) studies of the as-synthesized NASICON samples were performed at beamline 20-BM at Argonne National Laboratory equipped with a double-crystal Si(111) monochromator. Powder samples were diluted with h-BN and adhered to kapton tape then mounted to slotted aluminum sample holders. The data was collected at the V K-edge in transmission geometry with a vertical beam size of 1 mm. The sweeps started at 5460 eV and ended at 5560 eV, repeated four times per

sample. A V foil was measured simultaneously to reference correct the data. The data was processed using Athena (Demeter package) [104].

5.5 Appendix C

Sample	Na	V	Al	P
$\mathbf{Na_3V_2(PO_4)_3}$	2.90	2.0	0.04	3.18
$\mathbf{Na_3V_{2-y}Al_y(PO_4)_3}$	2.94	1.50	0.48	3.17

Table 5.1: Na:V:Al:P ratios of the as-synthesized powder samples obtained via ICP-OES analysis normalized to assume full V content

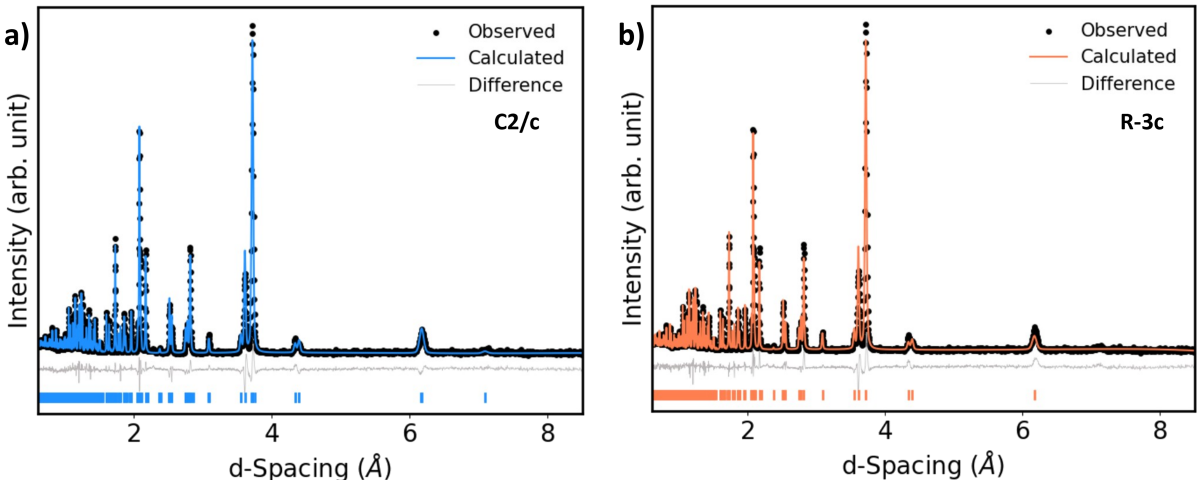

Figure 5.7: Room temperature neutron diffraction data collected on the as-synthesized y = 0.5 cathode powder and Rietveld refinement using a) monoclinic C2/c and b) rhombohedral R$\bar{3}$c space groups. The R$\bar{3}$c space group does not account for the low intensity peak near 7Å

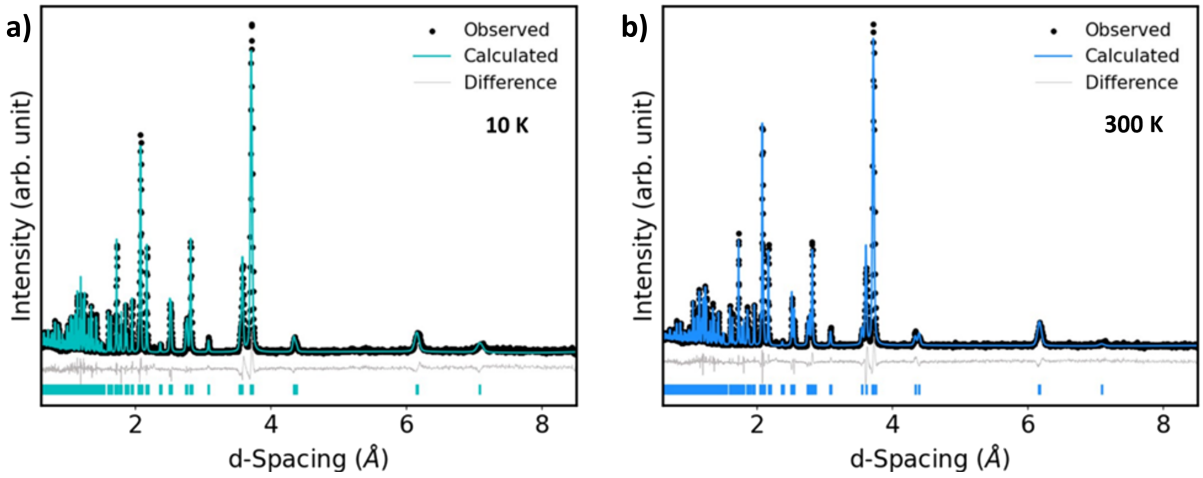

Figure 5.8: Neutron diffraction data collected at 10 K and 300 K on the as-synthesized y = 0.5 sample. Rietveld refinements were performed using a monoclinic C2/c space group. The refinement parameters are shown in Table 5.3.

Sample	Vol. (Å^3)	a(Å)	b(Å)	c(Å)	**Sample**	Vol. (Å^3)	a(Å)	b(Å)	c(Å)
y = 0.5 (pristine)	941.4	15.28	8.67	8.79	y = 0.0 (pristine)	959.8	15.38	8.72	8.85
y = 0.5 (4.2 V)	1406.8	8.45	8.45	21.50	y = 0.0 (4.2 V)	1320.0	8.42	8.42	21.48
Diff.(Δ)	390.6	−6.8	−0.2	12.7	Diff.(Δ)	360.2	−6.9	−0.3	12.6

Table 5.2: Changes in lattice parameters and unit cell volumes on initial charge for the y = 0 and y = 0.5 cathodes. Differences in lattice parameters and volume are given in the last row.

	$Na_3V_{1.5}Al_{0.5}(PO_4)_3$									
S.O.C.	**S.G.**	**a (Å)**	**b (Å)**	**c (Å)**	**Volume (Å^3)**	**Na(1)**	**Na(2)**	**Na(3)**	**R_{wp}**	**Phase fraction (%)**
Pristine sXRD	C2/c	15.27	8.67	8.79	941.2	0.86	0.76	0.590	10.9	100
Pristine Neutron (300K)	C2/c	15.25	8.66	8.79	939.1	0.88	0.770	0.580	7.58	100
Pristine Neutron (10K)	C2/c	15.15	8.66	8.75	932.8	0.96	0.60	0.840	8.59	100
2.4 V	R-3c	8.65	8.65	21.66	1406.1	0.673	0.666	---	1.54	100
3.39 V	R-3c	8.65	8.65	21.66	1406.1	0.673	0.666	---	1.54	13.6
	R-3c	8.58	8.58	21.58	1376.3	0.713	0.510	---	1.79	86.4
4.2 V	R-3c	8.45	8.45	21.52	1332.4	0.975	0.12	---	4.52	100

Table 5.3: Refined phase fractions, cell parameters, and Na occupancies based on synchrotron XRD data collected on y = 0.5 samples stopped at various states of charge. The refined phase fractions, cell parameters, and Na occupancies based on neutron XRD data are also listed

	Pristine				**4.2−2.4 V**		
δ_{iso} **(ppm)**	0.0	51.0	70.4	δ_{iso} **(ppm)**	−4.1	43.0	68.0
δ_{obs} **(ppm)**	4.6	51.0	69.4	δ_{obs} **(ppm)**	−5.7	43.0	68.7
η_Q	0.02	0.03	0.06	η_Q	0.08	0.23	0.00
C_Q **(MHz)**	0.16	0.00	3.50	C_Q **(MHz)**	2.17	0.00	0.08
LB (kHz)	5.01	19.6	9.36	**LB (kHz)**	5.19	24.7	11.6
Intensity	1.0	4.96	4.65	**Intensity**	1.0	4.51	3.89

Table 5.4: ^{23}Na NMR paramaters obtained from fits of the a) pristine cathode film and b) 2.4 V discharged spectra collected on y = 0.5 cathode samples as shown in Figure 5.11

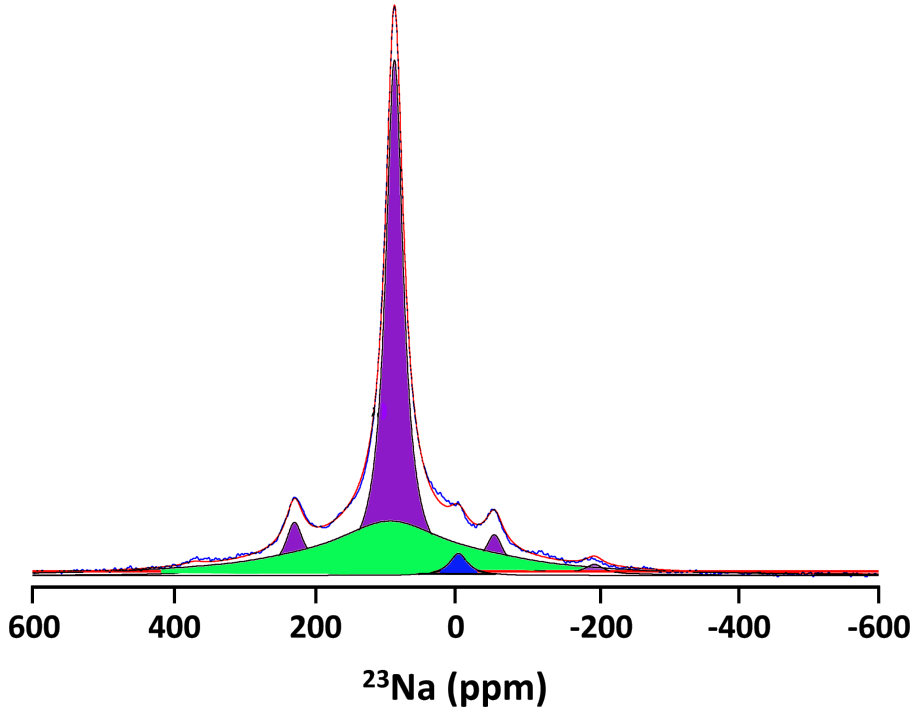

Figure 5.9: Fit of the y = 0 as-synthesized powdered sample ^{23}Na ssNMR spectrum acquired at 18.8T and 30kHz MAS using a 2.5mm rotor. Sample spectrum was acquired prior to mixing with carbon and PTFE binder for electrochemical measurements.

3.39 V (Intermediate phase on charge)						
δ_{iso} **(ppm)**	−5.2	45.6	69.0	94.6	179.5	216.6
δ_{obs} **(ppm)**	−4.5	43.8	70.0	95.5	177.9	218.0
η_Q	0.08	0.08	0.14	0.06	0.03	0.11
C_Q **(MHz)**	0.10	0.0	0.05	0.12	0.15	0.10
LB (kHz)	7.01	15.7	10.6	14.5	17.3	14.7
Intensity	1.0	2.62	1.25	1.31	0.75	0.42
3.35 V (Intermediate phase on discharge)						
δ_{iso} **(ppm)**	−4.9	43.7	69.0	93.8	179.0	218.9
δ_{obs} **(ppm)**	−4.5	43.9	69.3	94.7	178.1	220.0
η_Q	0.11	0.08	0.13	0.07	0.03	0.11
C_Q **(MHz)**	0.12	0.18	0.05	0.14	0.07	0.10
LB (kHz)	6.1	14.7	12.3	17.7	14.0	12.0
Intensity	1.0	2.53	1.28	2.13	0.62	0.77

Table 5.5: NMR paramaters obtained from fits of the ex situ ^{23}Na solid-state NMR spectra collected on the 2nd cycle of y = 0.5 cathode samples stopped at a) 3.39 V on charge and b) 3.35 V on discharge as shown in Figure 5.12

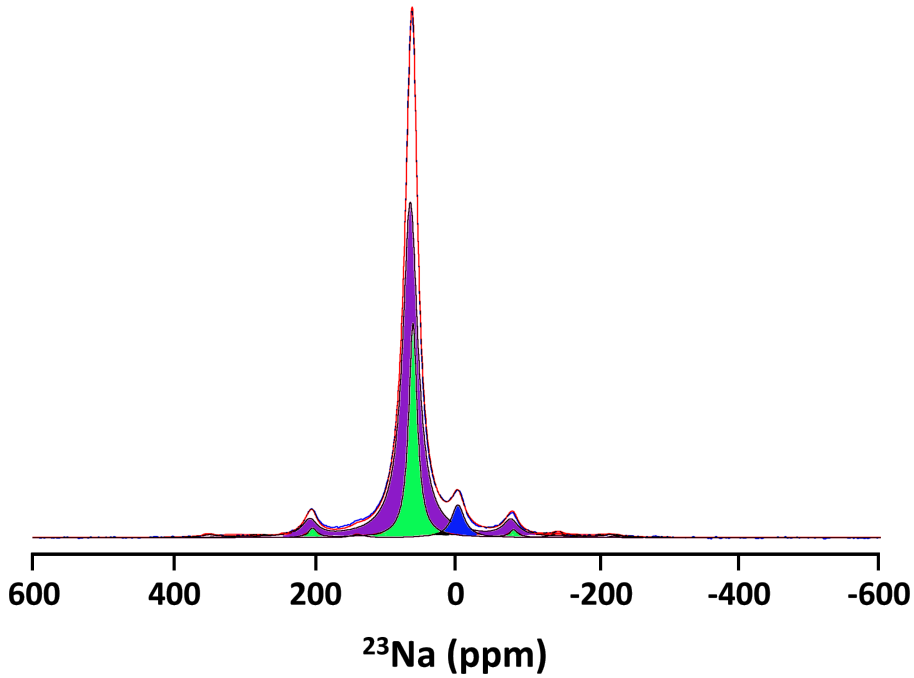

Figure 5.10: Fit of the Al-doped y = 0.5 as-synthesized powdered sample ^{23}Na ssNMR spectrum acquired at 18.8T and 30kHz MAS using a 2.5mm rotor. Sample spectrum was acquired prior to mixing with carbon and PTFE binder for electrochemical measurements.

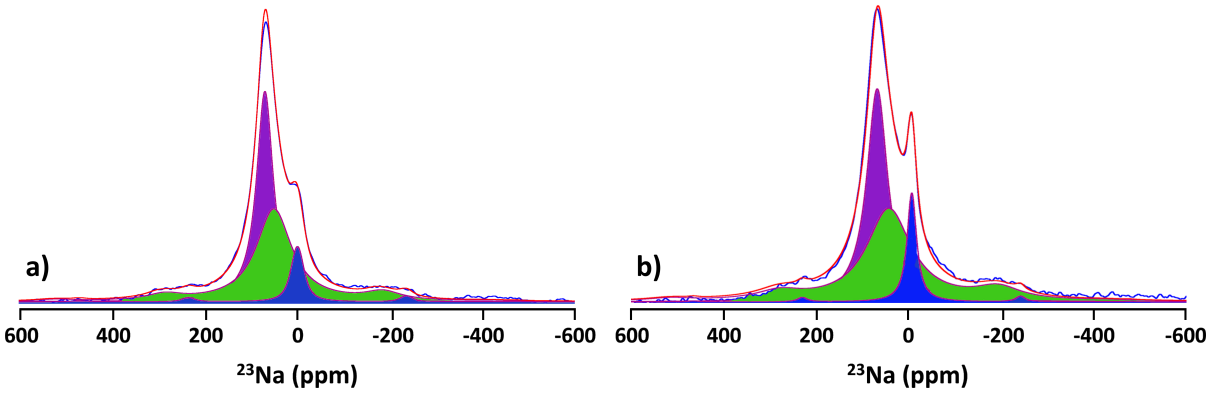

Figure 5.11: Fits of the ^{23}Na solid-state NMR spectra acquired at 18.8 T and 50 kHz MAS a) on the pristine y = 0.5 cathode film (active material mixed with carbon and PTFE binder), and b) on the y = 0.5 ex situ cathode sample stopped on discharge to 2.4 V after an initial charge to 4.2 V.

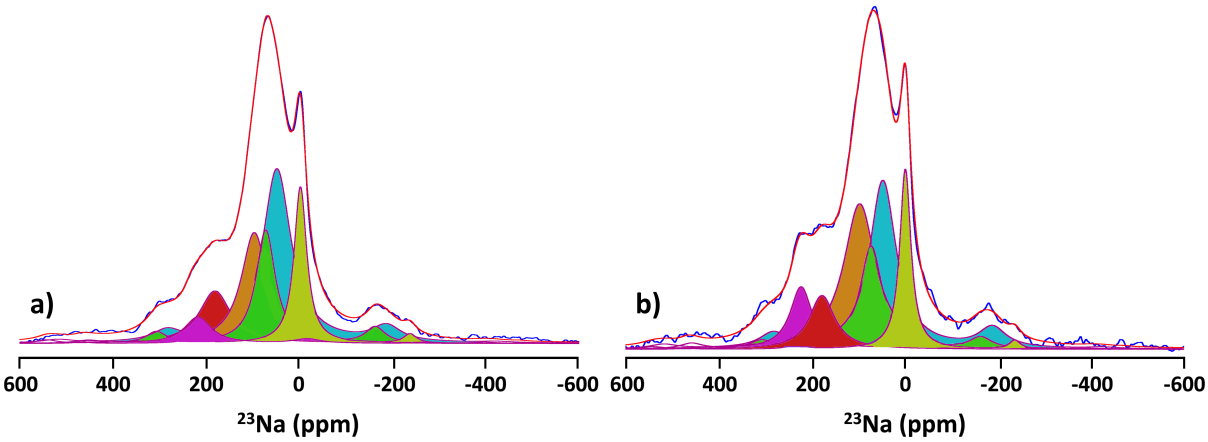

Figure 5.12: Fits of the ^{23}Na solid-state NMR spectra acquired at 18.8 T and 50 kHz MAS on samples collected at a) 3.39 V on charge collected on the 2nd charge cycle, and b) 3.35 V collected on the 2nd discharge cycle. Both samples completed one full cycle in the voltage window of 4.2−2.4 V.

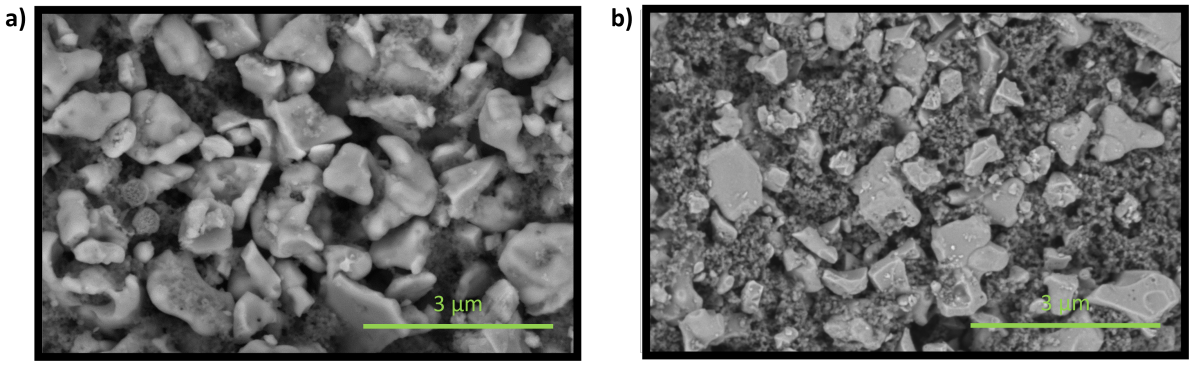

Figure 5.13: Scanning electron microscopy images of uncycled a) y = 0 and b) y = 0.5 samples after being left in contact with 1M $NaPF_6$ electrolyte overnight to deconvolute the effect of potential particle cracking due to reactions occurring between the active material and electrolyte and those occurring during cycling.

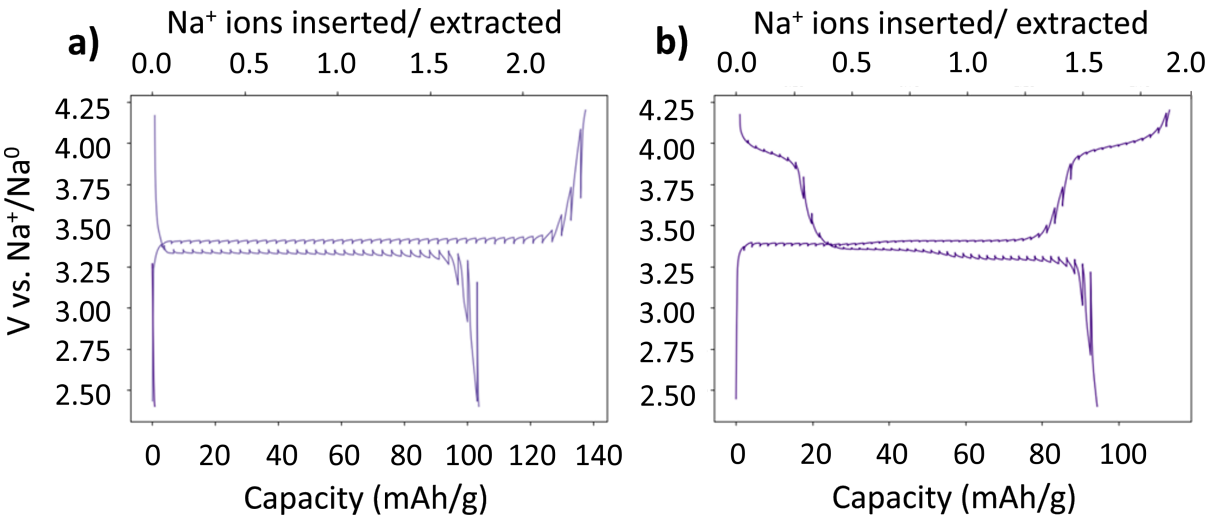

Figure 5.14: GITT profiles of the 2nd cycle for a) y = 0 and b) y = 0.5 samples.

Chapter 6

Conclusions

This dissertation has explored the nuanced details related to Na^+ (de)intercalation mechanics of the $Na_3V_2(PO_4)_3$ NASICON structured cathode material when aliovalent (Mg^{2+}) and isovalent (Al^{3+}) transition metal dopants are substituted for V^{3+} in the NVP framework. Through comprehensive experimental and theoretical techniques, we've unveiled the propensity for dopant choice to exacerbate or mitigate the formation of intermediary phases by modifying the intercalation mechanism. Specifically, for (Mg^{2+}), the (de)intercalation mechanism transitions from two-phase reaction to a solid solution mechanism at Mg concentrations above y = 0.5 in $Na_{3+y}V_{2-y}Mg_y(PO_4)_3$. Conversely, ($Al^{3+}$) incorporation into the same NVP framework has the opposite effect and leads to clear successive biphasic reactions during electrochemical cycling as evidenced ex situ diffraction and ssNMR analysis.

In Chapter 3, we explored the long-range and local structural changes occurring in $Na_{3+y}V_{2-y}Mg_y(PO_4)_3$ (y = 0, 0.25, 0.5, 0.75, and 1.0) via XRD, XAS, ^{23}Na, and ^{31}P ssNMR along with first principles CRYSTAL 17 calculations to compare theoretical NMR parameters to those observed by experiment. These combined techniques revealed a complex evolution of the local structure upon progressive replacement of V^{3+} by Mg^{2+}

in conjunction with a greater amount of Na ions into the Na(1) and Na(2) sites resulting in a change of the Na^+ diffusion properties further supported by operando XRD analysis. Excellent reversible capacity is observed when Mg-NVP is cycled in a low voltage cycling window (3.8−2.75 V), and the voltage-capacity profiles show an increase in the average intercalation voltage attributed to more ionic V−O bonds, as determined from pDOS and Bader charge analysis [32].

We then proceeded to investigate the $Na_{3+y}V_{2-y}Mg_y(PO_4)_3$ compositional series when cycled at high voltage (4.2−2.75 V) in Chapter 4 to determine the limiting factors associated with Na extraction/ reinsertion. Ex situ ^{23}Na and ^{31}P ssNMR results indicate that, while the local structure is reversible upon cycling over the 3.8−2.75 V range, it irreversibly disorders when the upper cutoff voltage is increased to 4.2 V. At an Mg concentration of y = 1.0 (i.e. $Na_4VMg(PO_4)_3$), and when cycled up to 4.2 V, a change in symmetry from $R\bar{3}c$ to monoclinic C2/c occurs significantly hindering Na reinsertion upon discharge. The cause for this symmetry reduction was not caused by V migration as seen in a similar $Na_3VCr(PO_4)_3$ system [87], rather, it was evidenced by ^{51}V ssNMR that ^{51}V resonances do not change significantly during (dis)charge implying similar local environments during electrochemical cycling at high voltage. If V cation migration was indeed occurring, significant changes in the ^{51}V ssNMR resonances would be observed, however, this is not the case. Rather, our DFT calculations suggest that the source of this structural degradation could potentially arise Mg^{2+} migration into the Na(2) sites during electrochemical cycling.

In Chapter 5 we turn our attention from aliovalent to isovalent transition metal doping by substituting Al^{3+} for V^{3+} in the NVP framework. While earlier studies have hinted at the formation of an intermediary phase between the $Na_3V_2(PO_4)_3$ and $NaV_2(PO_4)_3$ compositional endmembers during electrochemical cycling [82], to the best of our knowledge no rigorous description of this intermediate phase was provided. While the investigation

of successive biphasic (de)intercalation mechanics is still ongoing, it is already apparent that the formation of an intermediate phase in the $Na_3V_{1.5}Al_{0.5}(PO_4)_3$ sample reduces the strain associated with greater volume changes during electrochemical cycling when compared to its undoped counterpart as evidenced by the reduction in propensity for particle cracking during long term cycling (40 cycles) seen in ex situ SEM. A complete isolation and characterization of the intermediate phase was complicated by the narrow (30 mV) window in which it exists, a problem further exacerbated by sample relaxation after current is no longer applied to the cell during electrochemical cycling.

Regardless of this fact, our ex situ XRD and ssNMR study of the Al-doped system highlights the ability of Al incorporation into the NVP framework to retain the rhombohedral ($R\bar{3}c$) phase in contrast to the primitive ($P2_1/c$) structured found in the undoped system [37]. The ability of Al incorporation to preserve the rhombohedral structure during electrochemical cycling highlighths the improvement in efficiency when Al is incorporated into the NVP framework, corroborated by the lowering of overpotentials associated with Na extraction as evidenced by the GITT data presented in Chapter 5, Appendix C.

The work presented here has highlighted the signifcant role of transition metal dopants to modify the structure-(electrochemical) property relationships of cathode materials and their subsequent effect on electrochemical performance. These results may help guide the choice of transition metal species for $Na_3V_2(PO_4)_3$ (or other Na-ion battery compounds) to improve efficiency and reduce the stress and strain associated with two-phase (de)intercalation mechanics. Future directions of work could include exploring transition metal species with multiple oxidation states to improve performance metrics such as specific capacity and reliability while avoiding bulk structural degradation associated with Na insertion/ extraction into the framework of cathode materials.

Bibliography

[1] M. Z. Jacobson, M. A. Delucchi, Z. A. Bauer, S. C. Goodman, W. E. Chapman, M. A. Cameron, C. Bozonnat, L. Chobadi, H. A. Clonts, P. Enevoldsen, J. R. Erwin, S. N. Fobi, O. K. Goldstrom, E. M. Hennessy, J. Liu, J. Lo, C. B. Meyer, S. B. Morris, K. R. Moy, P. L. O'Neill, I. Petkov, S. Redfern, R. Schucker, M. A. Sontag, J. Wang, E. Weiner, and A. S. Yachanin, *100% clean and renewable wind, water, and sunlight all-sector energy roadmaps for 139 countries of the world*, *Joule* **1** (2017), no. 1 108–121, [https://www.sciencedirect.com/science/article/pii/S2542435117300120].

[2] E. A. Olivetti, G. Ceder, G. G. Gaustad, and X. Fu, *Lithium-ion battery supply chain considerations: analysis of potential bottlenecks in critical metals*, *Joule* **1** (2017), no. 2 229–243.

[3] X. Fu, D. N. Beatty, G. G. Gaustad, G. Ceder, R. Roth, R. E. Kirchain, M. Bustamante, C. Babbitt, and E. A. Olivetti, *Perspectives on cobalt supply through 2030 in the face of changing demand*, *Environmental science & technology* **54** (2020), no. 5 2985–2993.

[4] M. S. Whittingham and A. Yoshino, *Lithium-ion batteries*, *The Royal Swedish Academy of Sciences* (2019).

[5] K. Mizushima, P. Jones, P. Wiseman, and J. B. Goodenough, *Lixcoo2 (0¡ x¡-1): A new cathode material for batteries of high energy density*, *Materials Research Bulletin* **15** (1980), no. 6 783–789.

[6] F. Baakes, D. Witt, and U. Krewer, *Impact of electrolyte impurities and sei composition on battery safety*, *Chemical Science* **14** (2023), no. 47 13783–13798.

[7] J. S. Edge, S. O'Kane, R. Prosser, N. D. Kirkaldy, A. N. Patel, A. Hales, A. Ghosh, W. Ai, J. Chen, J. Yang, *et. al.*, *Lithium ion battery degradation: what you need to know*, *Physical Chemistry Chemical Physics* **23** (2021), no. 14 8200–8221.

[8] G. G. Eshetu, S. Grugeon, H. Kim, S. Jeong, L. Wu, G. Gachot, S. Laruelle, M. Armand, and S. Passerini, *Comprehensive insights into the reactivity of electrolytes based on sodium ions*, *ChemSusChem* **9** (2016), no. 5 462–471.

[9] R. Zhang, B. Xia, B. Li, Y. Lai, W. Zheng, H. Wang, W. Wang, and M. Wang, *Study on the characteristics of a high capacity nickel manganese cobalt oxide (nmc) lithium-ion battery—an experimental investigation*, *Energies* **11** (2018), no. 9 2275.

[10] H. Yoshizawa and T. Ohzuku, *An application of lithium cobalt nickel manganese oxide to high-power and high-energy density lithium-ion batteries*, *Journal of Power Sources* **174** (2007), no. 2 813–817.

[11] R. J. Clément, P. G. Bruce, and C. P. Grey, *manganese-based p2-type transition metal oxides as sodium-ion battery cathode materials*, *Journal of The Electrochemical Society* **162** (2015), no. 14 A2589.

[12] V. Ahuja, B. Senthilkumar, and P. Senguttuvan, *Synthesis, structural and electrochemical properties of sodium transition metal fluorosulfate cathodes for na-ion batteries*, in *Electrochemical Society Meeting Abstracts 242*, no. 64, pp. 2307–2307, The Electrochemical Society, Inc., 2022.

[13] Z. Hao, X. Shi, Z. Yang, X. Zhou, L. Li, C.-Q. Ma, and S. Chou, *The distance between phosphate-based polyanionic compounds and their practical application for sodium-ion batteries*, *Advanced Materials* (2023) 2305135.

[14] L. Coleby, *A history of prussian blue*, *Annals of Science* **4** (1939), no. 2 206–211.

[15] L. Hartmann, J. Deshmukh, L. Zhang, S. Buchele, and M. Metzger, *Processability of prussian white cathode active materials for sodium ion batteries-towards a green electrode preparation*, in *Electrochemical Society Meeting Abstracts 242*, no. 4, pp. 459–459, The Electrochemical Society, Inc., 2022.

[16] F. Maddar, A. Menon, K. Gonos, J. Compton, D. Atkinson, L. F. Piper, M. Copley, and I. Hasa, *Enabling aqueous processing of prussian white cathodes for sodium ion cells by understanding the effect of structural water*, in *Electrochemical Society Meeting Abstracts 242*, no. 4, pp. 500–500, The Electrochemical Society, Inc., 2022.

[17] J. Hu, H. Tao, M. Chen, Z. Zhang, S. Cao, Y. Shen, K. Jiang, and M. Zhou, *Interstitial water improves structural stability of iron hexacyanoferrate for high-performance sodium-ion batteries*, *ACS Applied Materials & Interfaces* **14** (2022), no. 10 12234–12242.

[18] W. Wang, Y. Gang, J. Peng, Z. Hu, Z. Yan, W. Lai, Y. Zhu, D. Appadoo, M. Ye, Y. Cao, *et. al.*, *Effect of eliminating water in prussian blue cathode for sodium-ion batteries*, *Advanced Functional Materials* **32** (2022), no. 25 2111727.

[19] X. Zhang, X. Rui, D. Chen, H. Tan, D. Yang, S. Huang, and Y. Yu, *Na 3 v 2 (po 4) 3: an advanced cathode for sodium-ion batteries*, *Nanoscale* **11** (2019), no. 6 2556–2576.

[20] K. Kim, J. Mundy, and W. Chen, *Diffusion and ionic conductivity in sodium beta alumina*, *Journal of Physics and Chemistry of Solids* **40** (1979), no. 10 743–755.

[21] J. Briant and G. Farrington, *Ionic conductivity in na+, k+, and ag+ β-alumina*, *Journal of Solid State Chemistry* **33** (1980), no. 3 385–390.

[22] N. a. Anantharamulu, K. Koteswara Rao, G. Rambabu, B. Vijaya Kumar, V. Radha, and M. Vithal, *A wide-ranging review on nasicon type materials*, *Journal of materials science* **46** (2011) 2821–2837.

[23] Z. Dai, U. Mani, H. T. Tan, and Q. Yan, *Advanced cathode materials for sodium-ion batteries: what determines our choices?*, *Small Methods* **1** (2017), no. 5 1700098.

[24] H.-P. Hong, *Crystal structures and crystal chemistry in the system na1+ xzr2sixp3- xo12*, *Materials Research Bulletin* **11** (1976), no. 2 173–182.

[25] J. B. Goodenough, H.-P. Hong, and J. Kafalas, *Fast na+-ion transport in skeleton structures*, *Materials Research Bulletin* **11** (1976), no. 2 203–220.

[26] F. Lalère, J.-B. Leriche, M. Courty, S. Boulineau, V. Viallet, C. Masquelier, and V. Seznec, *An all-solid state nasicon sodium battery operating at 200 c*, *Journal of Power Sources* **247** (2014) 975–980.

[27] A. J. K. Tieu, E. Mahayoni, Y. Li, Z. Deng, F. Fauth, J.-N. Chotard, V. Seznec, S. Adams, C. Masquelier, and P. Canepa, *Zirconia-free nasicon solid electrolyte materials for sodium all-solid-state batteries*, *Journal of Materials Chemistry A* **11** (2023), no. 43 23233–23242.

[28] Q. Zheng, H. Yi, X. Li, and H. Zhang, *Progress and prospect for nasicon-type na3v2 (po4) 3 for electrochemical energy storage*, *Journal of energy chemistry* **27** (2018), no. 6 1597–1617.

[29] W. Duan, Z. Zhu, H. Li, Z. Hu, K. Zhang, F. Cheng, and J. Chen, *Na 3 v 2 (po 4) 3@ c core–shell nanocomposites for rechargeable sodium-ion batteries*, *Journal of Materials Chemistry A* **2** (2014), no. 23 8668–8675.

[30] J. Liu, K. Tang, K. Song, P. A. van Aken, Y. Yu, and J. Maier, *Electrospun na 3 v 2 (po 4) 3/c nanofibers as stable cathode materials for sodium-ion batteries*, *Nanoscale* **6** (2014), no. 10 5081–5086.

[31] G. Li, D. Jiang, H. Wang, X. Lan, H. Zhong, and Y. Jiang, *Glucose-assisted synthesis of na3v2 (po4) 3/c composite as an electrode material for high-performance sodium-ion batteries*, *Journal of Power Sources* **265** (2014) 325–334.

[32] S. Ghosh, N. Barman, E. Gonzalez-Correa, M. Mazumder, A. Zaveri, R. Giovine, A. Manche, S. K. Pati, R. J. Clément, and P. Senguttuvan, *Elucidating the impact of mg substitution on the properties of nasicon-na3+ yv2- ymgy (po4) 3 cathodes*, *Advanced Functional Materials* **31** (2021), no. 48 2105463.

[33] F. Chen, V. M. Kovrugin, R. David, O. Mentré, F. Fauth, J.-N. Chotard, and C. Masquelier, *A nasicon-type positive electrode for na batteries with high energy density: Na4mnv(po4)3*, *Small Methods* **3** (2019), no. 4 1800218, [https://onlinelibrary.wiley.com/doi/pdf/10.1002/smtd.201800218].

[34] J.-N. Chotard, G. Rousse, R. David, O. Mentré, M. Courty, and C. Masquelier, *Discovery of a sodium-ordered form of na3v2(po4)3 below ambient temperature*, *Chemistry of Materials* **27** (2015), no. 17 5982–5987, [https://doi.org/10.1021/acs.chemmater.5b02092].

[35] C. Delmas, R. Olazcuaga, F. Cherkaoui, R. Brochu, and G. Le Flem, *Sur une nouvelle famille de phosphates de formule na3m2 (po4) 3 (m= ti, v, cr, fe)*, *Comptes rendus hebdomadaires des séances de l'Académie des sciences. Série C, Sciences chimiques* **287** (1978) 169–171.

[36] Z. Wang, T. P. Mishra, W. Xie, Z. Deng, G. S. Gautam, A. K. Cheetham, and P. Canepa, *Kinetic monte carlo simulations of sodium ion transport in nasicon electrodes*, *ACS Materials Letters* **5** (2023), no. 9 2499–2507.

[37] S. Park, Z. Wang, Z. Deng, I. Moog, P. Canepa, F. Fauth, D. Carlier, L. Croguennec, C. Masquelier, and J.-N. Chotard, *Crystal structure of na2v2 (po4) 3, an intriguing phase spotted in the na3v2 (po4) 3–na1v2 (po4) 3 system*, *Chemistry of Materials* **34** (2021), no. 1 451–462.

[38] C. Hammond, *The Basics of Crystallography and Diffraction*. No. 12 in International Union of Crsytallography Texts. Oxford University Press, Oxford, New York, 3rd ed., 2009.

[39] M. Ladd and R. Palmer, *Structure Determination by X-ray Crystallography: Analysis by X-rays and Neutrons*. Springer US, Boston, MA, 2013.

[40] G. S. Pawley, *Unit-cell refinement from powder diffraction scans*, *Journal of Applied Crystallography* **14** (Dec, 1981) 357–361.

[41] H. M. Rietveld, *A profile refinement method for nuclear and magnetic structures*, *Journal of Applied Crystallography* **2** (1969), no. 2 65–71, [https://onlinelibrary.wiley.com/doi/pdf/10.1107/S0021889869006558].

[42] M. H. Levitt, *Spin dynamics: basics of nuclear magnetic resonance*. John Wiley & Sons, 2013.

[43] N. Stone, *Table of nuclear electric quadrupole moments*, *Atomic Data and Nuclear Data Tables* **111** (2016) 1–28.

[44] E. Andrew, A. Bradbury, and R. Eades, *Nuclear magnetic resonance spectra from a crystal rotated at high speed*, *Nature* **182** (1958), no. 4650 1659–1659.

[45] M. J. Duer, *Solid state NMR spectroscopy: principles and applications*. John Wiley & Sons, 2008.

[46] R. Dovesi, V. Saunders, C. Roetti, R. Orlando, C. Zicovich-Wilson, F. Pascale, B. Civalleri, K. Doll, N. Harrison, I. Bush, *et. al.*, *Crystal17*, .

[47] R. E. Wasylishen, S. E. Ashbrook, and S. Wimperis, *NMR of quadrupolar nuclei in solid materials*, vol. 3. John Wiley & Sons, 2012.

[48] J. Kim, D. S. Middlemiss, N. A. Chernova, B. Y. Zhu, C. Masquelier, and C. P. Grey, *Linking local environments and hyperfine shifts: A combined experimental and theoretical 31p and 7li solid-state nmr study of paramagnetic fe (iii) phosphates*, *Journal of the American Chemical Society* **132** (2010), no. 47 16825–16840.

[49] C. P. Grey, C. M. Dobson, A. K. Cheetham, and R. J. Jakeman, *Studies of rare-earth stannates by trin-119 mas nmr. the use of paramagnetic shift probes in the solid state*, *Journal of the American Chemical Society* **111** (1989), no. 2 505–511.

[50] Y. J. Lee, F. Wang, and C. P. Grey, *6li and 7li mas nmr studies of lithium manganate cathode materials*, *Journal of the American Chemical Society* **120** (1998), no. 48 12601–12613.

[51] N. C. Nielsen, H. Bildsøe, and H. J. Jakobsen, *Multiple-quantum mas nutation nmr spectroscopy of quadrupolar nuclei*, *Journal of Magnetic Resonance (1969)* **97** (1992), no. 1 149–161.

[52] P. B. Kingsley, *Methods of measuring spin-lattice (t1) relaxation times: an annotated bibliography*, *Concepts in Magnetic Resonance* **11** (1999), no. 4 243–276.

[53] H. Z. Wang, S. J. Riederer, and J. N. Lee, *Optimizing the precision in t1 relaxation estimation using limited flip angles*, *Magnetic resonance in medicine* **5** (1987), no. 5 399–416.

[54] R. Dovesi, A. Erba, R. Orlando, C. M. Zicovich-Wilson, B. Civalleri, L. Maschio, M. Rérat, S. Casassa, J. Baima, S. Salustro, *et. al.*, *Quantum-mechanical condensed matter simulations with crystal*, *Wiley Interdisciplinary Reviews: Computational Molecular Science* **8** (2018), no. 4 e1360.

[55] A. Becke, *Density-functional thermochemistry. iii. the role of exact exchange. j. chem. phys., 98: 5648-5652*, 1993.

[56] C. Lee, W. Yang, and R. G. Parr, *Development of the colle-salvetti correlation-energy formula into a functional of the electron density*, *Physical review B* **37** (1988), no. 2 785.

[57] S. H. Vosko, L. Wilk, and M. Nusair, *Accurate spin-dependent electron liquid correlation energies for local spin density calculations: a critical analysis*, *Canadian Journal of physics* **58** (1980), no. 8 1200–1211.

[58] P. J. Stephens, F. J. Devlin, C. F. Chabalowski, and M. J. Frisch, *Ab initio calculation of vibrational absorption and circular dichroism spectra using density functional force fields*, *The Journal of physical chemistry* **98** (1994), no. 45 11623–11627.

[59] N. Kaltsoyannis, J. McGrady, F. Corà, M. Alfredsson, G. Mallia, D. S. Middlemiss, W. C. Mackrodt, R. Dovesi, and R. Orlando, *The performance of hybrid density functionals in solid state chemistry*, *Principles and Applications of Density Functional Theory in Inorganic Chemistry II* (2004) 171–232.

[60] J. Muscat, A. Wander, and N. Harrison, *On the prediction of band gaps from hybrid functional theory*, *Chemical Physics Letters* **342** (2001), no. 3-4 397–401.

[61] X. Feng and N. Harrison, *Magnetic coupling constants from a hybrid density functional with 35% hartree-fock exchange*, *Physical Review B* **70** (2004), no. 9 092402.

[62] D. S. Middlemiss, L. M. Lawton, and C. C. Wilson, *A solid-state hybrid density functional theory study of prussian blue analogues and related chlorides at pressure*, *Journal of Physics: Condensed Matter* **20** (2008), no. 33 335231.

[63] I. de PR Moreira, F. Illas, and R. L. Martin, *Effect of fock exchange on the electronic structure and magnetic coupling in nio*, *Physical Review B* **65** (2002), no. 15 155102.

[64] D. S. Middlemiss, A. J. Ilott, R. J. Clement, F. C. Strobridge, and C. P. Grey, *Density functional theory-based bond pathway decompositions of hyperfine shifts: equipping solid-state nmr to characterize atomic environments in paramagnetic materials*, *Chemistry of Materials* **25** (2013), no. 9 1723–1734.

[65] R. J. Clément, A. J. Pell, D. S. Middlemiss, F. C. Strobridge, J. K. Miller, M. S. Whittingham, L. Emsley, C. P. Grey, and G. Pintacuda, *Spin-transfer pathways in paramagnetic lithium transition-metal phosphates from combined broadband isotropic solid-state mas nmr spectroscopy and dft calculations*, *Journal of the American Chemical Society* **134** (2012), no. 41 17178–17185.

[66] A. Schäfer, H. Horn, and R. Ahlrichs, *Fully optimized contracted gaussian basis sets for atoms li to kr*, *The Journal of chemical physics* **97** (1992), no. 4 2571–2577.

[67] H. J. Monkhorst and J. D. Pack, *Special points for brillouin-zone integrations*, *Physical review B* **13** (1976), no. 12 5188.

[68] D. Carlier, M. Ménétrier, C. Grey, C. Delmas, and G. Ceder, *Understanding the nmr shifts in paramagnetic transition metal oxides using density functional theory calculations*, *Physical Review B* **67** (2003), no. 17 174103.

[69] R. Dugas, J. D. Forero-Saboya, and A. Ponrouch, *Methods and protocols for reliable electrochemical testing in post-li batteries (na, k, mg, and ca)*, *Chemistry of Materials* **31** (2019), no. 21 8613–8628.

[70] G. Yan, D. Alves-Dalla-Corte, W. Yin, N. Madern, G. Gachot, and J.-M. Tarascon, *Assessment of the electrochemical stability of carbonate-based electrolytes in na-ion batteries*, *Journal of The Electrochemical Society* **165** (2018), no. 7 A1222.

[71] Y. Zhu and C. Wang, *Galvanostatic intermittent titration technique for phase-transformation electrodes*, *The Journal of Physical Chemistry C* **114** (2010), no. 6 2830–2841, [https://doi.org/10.1021/jp9113333].

[72] S. Chen, C. Wu, L. Shen, C. Zhu, Y. Huang, K. Xi, J. Maier, and Y. Yu, *Challenges and perspectives for nasicon-type electrode materials for advanced sodium-ion batteries*, *Advanced Materials* **29** (2017), no. 48 1700431, [https://onlinelibrary.wiley.com/doi/pdf/10.1002/adma.201700431].

[73] C. Delmas, F. Cherkaoui, A. Nadiri, and P. Hagenmuller, *A nasicon-type phase as intercalation electrode: Nati2(po4)3*, *Materials Research Bulletin* **22** (1987), no. 5 631–639.

[74] K. Kawai, W. Zhao, S.-i. Nishimura, and A. Yamada, *High-voltage cr4+/cr3+ redox couple in polyanion compounds*, *ACS Applied Energy Materials* **1** (2018), no. 3 928–931, [https://doi.org/10.1021/acsaem.7b00105].

[75] S. Qiu, X. Wu, M. Wang, M. Lucero, Y. Wang, J. Wang, Z. Yang, W. Xu, Q. Wang, M. Gu, J. Wen, Y. Huang, Z. J. Xu, and Z. Feng, *Nasicon-type*

na3fe2(po4)3 as a low-cost and high-rate anode material for aqueous sodium-ion batteries, *Nano Energy* **64** (2019) 103941.

[76] H. Kim, R. A. Shakoor, C. Park, S. Y. Lim, J.-S. Kim, Y. N. Jo, W. Cho, K. Miyasaka, R. Kahraman, Y. Jung, and J. W. Choi, *Na2fep2o7 as a promising iron-based pyrophosphate cathode for sodium rechargeable batteries: A combined experimental and theoretical study*, *Advanced Functional Materials* **23** (2013), no. 9 1147–1155, [https://onlinelibrary.wiley.com/doi/pdf/10.1002/adfm.201201589].

[77] W. Song, X. Ji, Z. Wu, Y. Zhu, Y. Yang, J. Chen, M. Jing, F. Li, and C. E. Banks, *First exploration of na-ion migration pathways in the nasicon structure na3v2(po4)3*, *J. Mater. Chem. A* **2** (2014) 5358–5362.

[78] M. J. Aragón, P. Lavela, R. Alcántara, and J. L. Tirado, *Effect of aluminum doping on carbon loaded na3v2(po4)3 as cathode material for sodium-ion batteries*, *Electrochimica Acta* **180** (2015) 824–830.

[79] A. Inoishi, Y. Yoshioka, L. Zhao, A. Kitajou, and S. Okada, *Improvement in the energy density of na3v2(po4)3 by mg substitution*, *ChemElectroChem* **4** (2017), no. 11 2755–2759, [https://chemistry-europe.onlinelibrary.wiley.com/doi/pdf/10.1002/celc.201700540].

[80] F. Hu and X. Jiang, *A stable and superior performance of na3v2(po4)3/c nanocomposites as cathode for sodium-ion batteries*, *Inorganic Chemistry Communications* **115** (2020) 107860.

[81] W. Shen, H. Li, Z. Guo, Z. Li, Q. Xu, H. Liu, and Y. Wang, *Improvement on the high-rate performance of mn-doped na3v2(po4)3/c as a cathode material for sodium ion batteries*, *RSC Adv.* **6** (2016) 71581–71588.

[82] F. Lalère, V. Seznec, M. Courty, R. David, J. N. Chotard, and C. Masquelier, *Improving the energy density of na3v2(po4)3-based positive electrodes through v/al substitution*, *J. Mater. Chem. A* **3** (2015) 16198–16205.

[83] R. Liu, G. Xu, Q. Li, S. Zheng, G. Zheng, Z. Gong, Y. Li, E. Kruskop, R. Fu, Z. Chen, K. Amine, and Y. Yang, *Exploring highly reversible 1.5-electron reactions (v3+/v4+/v5+) in na3vcr(po4)3 cathode for sodium-ion batteries*, *ACS Applied Materials & Interfaces* **9** (2017), no. 50 43632–43639, [https://doi.org/10.1021/acsami.7b13018]. PMID: 29164850.

[84] Y. Zhao, X. Gao, H. Gao, H. Jin, and J. B. Goodenough, *Three electron reversible redox reaction in sodium vanadium chromium phosphate as a high-energy-density cathode for sodium-ion batteries*, *Advanced Functional Materials* **30** (2020), no. 10 1908680, [https://onlinelibrary.wiley.com/doi/pdf/10.1002/adfm.201908680].

[85] W. Zhou, L. Xue, X. Lü, H. Gao, Y. Li, S. Xin, G. Fu, Z. Cui, Y. Zhu, and J. B. Goodenough, *Naxmv(po4)3 (m = mn, fe, ni) structure and properties for sodium extraction*, *Nano Letters* **16** (2016), no. 12 7836–7841, [https://doi.org/10.1021/acs.nanolett.6b04044]. PMID: 27960482.

[86] M. V. Zakharkin, O. A. Drozhzhin, I. V. Tereshchenko, D. Chernyshov, A. M. Abakumov, E. V. Antipov, and K. J. Stevenson, *Enhancing na+ extraction limit through high voltage activation of the nasicon-type na4mnv(po4)3 cathode*, *ACS Applied Energy Materials* (2018).

[87] R. Liu, S. Zheng, Y. Yuan, P. Yu, Z. Liang, W. Zhao, R. Shahbazian-Yassar, J. Ding, J. Lu, and Y. Yang, *Counter-intuitive structural instability aroused by transition metal migration in polyanionic sodium ion host*, *Advanced Energy Materials* **11** (2021), no. 3 2003256, [https://onlinelibrary.wiley.com/doi/pdf/10.1002/aenm.202003256].

[88] S. Ghosh, N. Barman, M. Mazumder, S. K. Pati, G. Rousse, and P. Senguttuvan, *High capacity and high-rate nasicon-na3.75v1.25mn0.75(po4)3 cathode for na-ion batteries via modulating electronic and crystal structures*, *Advanced Energy Materials* **10** (2020), no. 6 1902918, [https://onlinelibrary.wiley.com/doi/pdf/10.1002/aenm.201902918].

[89] D. V. Anishchenko, M. V. Zakharkin, V. A. Nikitina, K. J. Stevenson, E. V. Antipov, K. J. Stevenson, and E. V. Antipov, *Phase boundary propagation kinetics predominately limit the rate capability of nasicon-type* $na_{3+x}mn_xv_{2-x}(po_4)_3$ *(0≤x≤1) materials*, *Electrochimica Acta* **354** (sep, 2020) 136761.

[90] R. Shulman, *Nmr and hyperfine interactions in paramagnetic solutions*, *The Journal of Chemical Physics* **29** (1958), no. 4 945–947.

[91] K. H. Lim and C. P. Grey, *Analysis of the anisotropic dimension in the riact (ii) multiple quantum mas nmr experiment for i= 3/2 nuclei*, *Solid State Nuclear Magnetic Resonance* **13** (1998), no. 1-2 101–112.

[92] D. Liu, X. Li, L. Wei, T. Zhang, A. Wang, C. Liu, and R. Prins, *Disproportionation of hypophosphite and phosphite*, *Dalton Trans.* **46** (2017) 6366–6378.

[93] P. Conte, A. Piccolo, and R. Spaccini, *Evaluation of the factors affecting direct polarization solid state 31p-nmr spectroscopy of bulk soils*, *European Journal of Soil Science* **59** (2008).

[94] S. Y. Lim, H. Kim, R. Shakoor, Y. Jung, and J. W. Choi, *Electrochemical and thermal properties of nasicon structured na3v2 (po4) 3 as a sodium rechargeable battery cathode: a combined experimental and theoretical study*, *Journal of The Electrochemical Society* **159** (2012), no. 9 A1393.

[95] B. C. Melot, D. O. Scanlon, M. Reynaud, G. Rousse, J.-N. Chotard, M. Henry, and J.-M. Tarascon, *Chemical and structural indicators for large redox potentials in fe-based positive electrode materials*, *ACS Applied Materials & Interfaces* **6** (2014), no. 14 10832–10839.

[96] Z. Jian, W. Han, X. Lu, H. Yang, Y.-S. Hu, J. Zhou, Z. Zhou, J. Li, W. Chen, D. Chen, *et. al.*, *Superior electrochemical performance and storage mechanism of na3v2 (po4) 3 cathode for room-temperature sodium-ion batteries*, *Advanced Energy Materials* **3** (2013), no. 2 156–160.

[97] Z. Jian, C. Yuan, W. Han, X. Lu, L. Gu, X. Xi, Y.-S. Hu, H. Li, W. Chen, D. Chen, *et. al.*, *Atomic structure and kinetics of nasicon naxv2 (po4) 3 cathode for sodium-ion batteries*, *Advanced Functional Materials* **24** (2014), no. 27 4265–4272.

[98] M. V. Zakharkin, O. A. Drozhzhin, S. V. Ryazantsev, D. Chernyshov, M. A. Kirsanova, I. V. Mikheev, E. M. Pazhetnov, E. V. Antipov, and K. J. Stevenson, *Electrochemical properties and evolution of the phase transformation behavior in the nasicon-type na3+ xmnxv2-x (po4) 3 (0≤ x≤ 1) cathodes for na-ion batteries*, *Journal of Power Sources* **470** (2020) 228231.

[99] F. Omenya, N. A. Chernova, Q. Wang, R. Zhang, and M. S. Whittingham, *The structural and electrochemical impact of li and fe site substitution in lifepo4*, *Chemistry of Materials* **25** (2013), no. 13 2691–2699.

[100] G. Chen, A. K. Shukla, X. Song, and T. J. Richardson, *Improved kinetics and stabilities in mg-substituted limnpo 4*, *Journal of Materials Chemistry* **21** (2011), no. 27 10126–10133.

[101] F. Omenya, B. Wen, J. Fang, R. Zhang, Q. Wang, N. A. Chernova, J. Schneider-Haefner, F. Cosandey, and M. S. Whittingham, *Mg substitution clarifies the reaction mechanism of olivine lifepo4*, *Advanced Energy Materials* **5** (2015), no. 7 1401204.

[102] F. Omenya, B. Wen, J. Fang, R. Zhang, Q. Wang, N. A. Chernova, J. Schneider-Haefner, F. Cosandey, and M. S. Whittingham, *Mg substitution clarifies the reaction mechanism of olivine lifepo4*, *Advanced Energy Materials* **5** (2015), no. 7 1401204.

[103] M. Newville, *IFEFFIT: interactive XAFS analysis and FEFF fitting*, *Journal of Synchrotron Radiation* **8** (Mar, 2001) 322–324.

[104] B. Ravel and M. Newville, *Athena, artemis, hephaestus: data analysis for x-ray absorption spectroscopy using ifeffit*, *Journal of synchrotron radiation* **12** (2005), no. 4 537–541.

[105] G. Kresse and D. Joubert, *From ultrasoft pseudopotentials to the projector augmented-wave method*, *Physical review b* **59** (1999), no. 3 1758.

[106] G. Kresse and J. Hafner, *Ab initio molecular dynamics for liquid metals*, *Physical review B* **47** (1993), no. 1 558.

[107] G. Kresse and J. Furthmüller, *Efficiency of ab-initio total energy calculations for metals and semiconductors using a plane-wave basis set*, *Computational materials science* **6** (1996), no. 1 15–50.

[108] G. Kresse and J. Furthmüller, *Efficient iterative schemes for ab initio total-energy calculations using a plane-wave basis set*, *Physical review B* **54** (1996), no. 16 11169.

[109] J. P. Perdew, K. Burke, and M. Ernzerhof, *Generalized gradient approximation made simple*, *Physical review letters* **77** (1996), no. 18 3865.

[110] K. Okhotnikov, T. Charpentier, and S. Cadars, *Supercell program: a combinatorial structure-generation approach for the local-level modeling of atomic substitutions and partial occupancies in crystals*, *Journal of cheminformatics* **8** (2016) 1–15.

[111] W. Tang, E. Sanville, and G. Henkelman, *A grid-based bader analysis algorithm without lattice bias*, *Journal of Physics: Condensed Matter* **21** (2009), no. 8 084204.

[112] G. Henkelman, B. P. Uberuaga, and H. Jónsson, *A climbing image nudged elastic band method for finding saddle points and minimum energy paths*, *The Journal of chemical physics* **113** (2000), no. 22 9901–9904.

[113] R. Dovesi, V. Saunders, C. Roetti, R. Orlando, C. Zicovich-Wilson, F. Pascale, B. Civalleri, K. Doll, N. Harrison, I. Bush, *et. al.*, *Crystal17*, .

[114] R. Dovesi, A. Erba, R. Orlando, C. M. Zicovich-Wilson, B. Civalleri, L. Maschio, M. Rérat, S. Casassa, J. Baima, S. Salustro, *et. al.*, *Quantum-mechanical condensed matter simulations with crystal*, *Wiley Interdisciplinary Reviews: Computational Molecular Science* **8** (2018), no. 4 e1360.

[115] A. D. Becke, *A new mixing of hartree–fock and local density-functional theories*, *The Journal of chemical physics* **98** (1993), no. 2 1372–1377.

[116] Y. Liu, J. Li, Q. Shen, J. Zhang, P. He, X. Qu, and Y. Liu, *Advanced characterizations and measurements for sodium-ion batteries with nasicon-type cathode materials*, *EScience* **2** (2022), no. 1 10–31.

[117] M. Hou, F. Liang, K. Chen, Y. Dai, and D. Xue, *Challenges and perspectives of nasicon-type solid electrolytes for all-solid-state lithium batteries*, *Nanotechnology* **31** (2020), no. 13 132003.

[118] C. Masquelier and L. Croguennec, *Polyanionic (phosphates, silicates, sulfates) frameworks as electrode materials for rechargeable li (or na) batteries*, *Chemical Reviews* **113** (2013), no. 8 6552–6591.

[119] B. Ouyang, J. Wang, T. He, C. J. Bartel, H. Huo, Y. Wang, V. Lacivita, H. Kim, and G. Ceder, *Synthetic accessibility and stability rules of nasicons*, *Nature communications* **12** (2021), no. 1 5752.

[120] V. Soundharrajan, S. Nithiananth, K. Sakthiabirami, J. H. Kim, C.-Y. Su, and J.-K. Chang, *The advent of manganese-substituted sodium vanadium phosphate-based cathodes for sodium-ion batteries and their current progress: a focused review*, *Journal of Materials Chemistry A* **10** (2022), no. 3 1022–1046.

[121] S. Ghosh, N. Jose, B. Senthilkumar, P. Amonpattaratkit, and P. Senguttuvan, *Multi-redox (v5+/v4+/v3+/v2+) driven asymmetric sodium (de) intercalation reactions in nasicon-na3vin (po4) 3 cathode*, *Journal of The Electrochemical Society* **168** (2021), no. 5 050534.

[122] C. Xu, J. Zhao, E. Wang, X. Liu, X. Shen, X. Rong, Q. Zheng, G. Ren, N. Zhang, X. Liu, *et. al.*, *A novel nasicon-typed na4vmn0. 5fe0. 5 (po4) 3 cathode for high-performance na-ion batteries*, *Advanced Energy Materials* **11** (2021), no. 22 2100729.

[123] P. Lavela, R. Klee, M. Hidalgo, and J. Tirado, *Iron substitution in na4vmn (po4) 3 as a strategy for improving the electrochemical performance of sodium-ion batteries*, *Journal of Electroanalytical Chemistry* **895** (2021) 115533.

[124] S. Bag, H. Murarka, C. Zhou, A. Bhattacharya, D. Jokhakar, V. G. Pol, and V. Thangadurai, *Understanding the na-ion storage mechanism in na3+ x v2–x m x (po4) 3 (m= ni2+, co2+, mg2+; x= 0.1–0.5) cathodes*, *ACS Applied Energy Materials* **3** (2020), no. 9 8475–8486.

[125] S. Park, J.-N. Chotard, D. Carlier, I. Moog, M. Duttine, F. Fauth, A. Iadecola, L. Croguennec, and C. Masquelier, *An asymmetric sodium extraction/insertion mechanism for the fe/v-mixed nasicon na4fev (po4) 3*, *Chemistry of Materials* **34** (2022), no. 9 4142–4152.

[126] H. Stokes, D. Hatch, and B. Campbell, *Isotropy software suite, iso. byu. edu, 2007*, .

[127] B. J. Campbell, H. T. Stokes, D. E. Tanner, and D. M. Hatch, *Isodisplace: a web-based tool for exploring structural distortions*, *Journal of Applied Crystallography* **39** (2006), no. 4 607–614.

[128] A. R. Jones, R. Winter, G. N. Greaves, and I. H. Smith, *23na, 29si, and 13c mas nmr investigation of glass-forming reactions between na2co3 and sio2*, *The Journal of Physical Chemistry B* **109** (2005), no. 49 23154–23161, [https://doi.org/10.1021/jp053953y]. PMID: 16375277.

[129] P. J. Dirken, J. B. H. Jansen, and R. D. Schuiling, *Influence of octahedral polymerization on 23Na and 27Al MAS NMR in alkali fluoroaluminates*, *American Mineralogist* **77** (08, 1992) 718–724, [https://pubs.geoscienceworld.org/msa/ammin/article-pdf/77/7-8/718/4208861/am77_718.pdf].

[130] Y. Lee, J. Lee, J. Lee, K. Kim, A. Cha, S. Kang, T. Wi, S. J. Kang, H.-W. Lee, and N.-S. Choi, *Fluoroethylene carbonate-based electrolyte with 1 m sodium bis(fluorosulfonyl)imide enables high-performance sodium metal electrodes*, *ACS Applied Materials & Interfaces* **10** (2018), no. 17 15270–15280, [https://doi.org/10.1021/acsami.8b02446]. PMID: 29648435.

[131] A. R. Iarchuk, D. V. Sheptyakov, and A. M. Abakumov, *Hydrothermal microwave-assisted synthesis of na3+ x v2–y mn y (po4) 2f3 solid solutions as potential positive electrodes for na-ion batteries*, *ACS Applied Energy Materials* **4** (2021), no. 5 5007–5014.

[132] R. Siegel, N. Dupré, M. Quarton, and J. Hirschinger, *51v magic angle spinning nmr in vopo4 phases*, *Magnetic Resonance in Chemistry* **42** (2004), no. 12 1022–1026.

[133] S. Ennaciri, C. R'kha, P. Barboux, J. Livage, and J. Maquet, *31 p and 51 v mas-nmr characterisation of mixed vanadium and titanium phosphates prepared from molecular precursors*, *Journal of sol-gel science and technology* **34** (2005) 197–203.

[134] A. A. Shubin, D. F. Khabibulin, and O. B. Lapina, *Solid-state 51v nmr and its potentiality in investigation of vanadia systems with paramagnetic centres*, *Catalysis Today* **142** (2009), no. 3-4 220–226.

[135] K. J. MacKenzie and M. E. Smith, *Multinuclear solid-state nuclear magnetic resonance of inorganic materials*. Elsevier, 2002.

[136] C. Szczuka, R.-A. Eichel, and J. Granwehr, *Exploring the solvation sphere and spatial accumulation of dissolved transition-metal ions in batteries: a case study of vanadyl ions released from v2o5 cathodes*, *ACS Applied Energy Materials* **5** (2021), no. 1 449–460.

[137] R. Liu, S. Zheng, Y. Yuan, P. Yu, Z. Liang, W. Zhao, R. Shahbazian-Yassar, J. Ding, J. Lu, and Y. Yang, *Counter-intuitive structural instability aroused by transition metal migration in polyanionic sodium ion host*, *Advanced Energy Materials* **11** (2021), no. 3 2003256.

[138] E. N. Bassey, P. J. Reeves, M. A. Jones, J. Lee, I. D. Seymour, G. Cibin, and C. P. Grey, *Structural origins of voltage hysteresis in the na-ion cathode p2–na0. 67 [mg0. 28mn0. 72] o2: a combined spectroscopic and density functional theory study*, *Chemistry of Materials* **33** (2021), no. 13 4890–4906.

[139] J. Rodríguez-Carvajal, *Recent advances in magnetic structure determination by neutron powder diffraction*, *Physica B: Condensed Matter* **192** (1993), no. 1-2 55–69.

[140] A. Zunger, S.-H. Wei, L. Ferreira, and J. E. Bernard, *Special quasirandom structures*, *Physical review letters* **65** (1990), no. 3 353.

[141] M. J. Buerger, *Derivative crystal structures*, *The Journal of Chemical Physics* **15** (1947), no. 1 1–16.

[142] G. Kresse and J. Hafner, *Ab initio molecular dynamics for liquid metals*, *Physical review B* **47** (1993), no. 1 558.

[143] G. Kresse and J. Furthmüller, *Efficiency of ab-initio total energy calculations for metals and semiconductors using a plane-wave basis set*, *Computational materials science* **6** (1996), no. 1 15–50.

[144] G. Kresse and J. Hafner, *Norm-conserving and ultrasoft pseudopotentials for first-row and transition elements*, *Journal of Physics: Condensed Matter* **6** (1994), no. 40 8245.

[145] P. E. Blöchl, *Projector augmented-wave method*, *Physical review B* **50** (1994), no. 24 17953.

[146] J. P. Perdew, K. Burke, and M. Ernzerhof, *Perdew, burke, and ernzerhof reply*, *Physical Review Letters* **80** (1998), no. 4 891.

[147] W. Press, S. Teukolsky, W. Vetterling, and B. Flannery, *Numerical recipes in fortran 77 (section 10.4)*, 1986.

[148] G. Henkelman, B. P. Uberuaga, and H. Jónsson, *A climbing image nudged elastic band method for finding saddle points and minimum energy paths*, *The Journal of chemical physics* **113** (2000), no. 22 9901–9904.

[149] K. Momma and F. Izumi, *Vesta 3 for three-dimensional visualization of crystal, volumetric and morphology data*, *Journal of applied crystallography* **44** (2011), no. 6 1272–1276.

[150] W. Baur, *The geometry of polyhedral distortions. predictive relationships for the phosphate group*, *Acta Crystallographica Section B: Structural Crystallography and Crystal Chemistry* **30** (1974), no. 5 1195–1215.

[151] H. S. Hirsh, Y. Li, D. H. Tan, M. Zhang, E. Zhao, and Y. S. Meng, *Sodium-ion batteries paving the way for grid energy storage*, *Advanced Energy Materials* **10** (2020), no. 32 2001274.

[152] Y. Li, Y. Lu, C. Zhao, Y.-S. Hu, M.-M. Titirici, H. Li, X. Huang, and L. Chen, *Recent advances of electrode materials for low-cost sodium-ion batteries towards practical application for grid energy storage*, *Energy Storage Materials* **7** (2017) 130–151.

[153] M. D. Slater, D. Kim, E. Lee, and C. S. Johnson, *Sodium-ion batteries*, *Advanced Functional Materials* **23** (2013), no. 8 947–958.

[154] S. Y. Lim, H. Kim, R. Shakoor, Y. Jung, and J. W. Choi, *Electrochemical and thermal properties of nasicon structured na3v2 (po4) 3 as a sodium rechargeable battery cathode: a combined experimental and theoretical study*, *Journal of The Electrochemical Society* **159** (2012), no. 9 A1393.

[155] K. Saravanan, C. W. Mason, A. Rudola, K. H. Wong, and P. Balaya, *The first report on excellent cycling stability and superior rate capability of na3v2 (po4) 3 for sodium ion batteries*, *Advanced Energy Materials* **3** (2013), no. 4 444–450.

[156] R. Ling, S. Cai, D. Xie, X. Li, M. Wang, Y. Lin, S. Jiang, K. Shen, K. Xiong, and X. Sun, *Three-dimensional hierarchical porous na3v2 (po4) 3/c structure with high rate capability and cycling stability for sodium-ion batteries*, *Chemical Engineering Journal* **353** (2018) 264–272.

[157] Z. Jian, W. Han, X. Lu, H. Yang, Y.-S. Hu, J. Zhou, Z. Zhou, J. Li, W. Chen, D. Chen, *et. al.*, *Superior electrochemical performance and storage mechanism of na3v2 (po4) 3 cathode for room-temperature sodium-ion batteries*, *Advanced Energy Materials* **3** (2013), no. 2 156–160.

[158] H. Liu, F. C. Strobridge, O. J. Borkiewicz, K. M. Wiaderek, K. W. Chapman, P. J. Chupas, and C. P. Grey, *Capturing metastable structures during high-rate cycling of lifepo¡sub¿4¡/sub¿ nanoparticle electrodes*, *Science* **344** (2014), no. 6191 1252817, [https://www.science.org/doi/pdf/10.1126/science.1252817].

[159] V. C. Wu, R. Giovine, E. E. Foley, J. Finzel, M. Balasubramanian, E. Sebti, E. M. Mozur, A. H. Kwon, and R. J. Clément, *Unlocking new redox activity in alluaudite cathodes through compositional design*, *Chemistry of Materials* **34** (2022), no. 9 4088–4103, [https://doi.org/10.1021/acs.chemmater.2c00324].

[160] R. D. Shannon and C. T. Prewitt, *Revised values of effective ionic radii*, *Acta Crystallographica Section B* **26** (Jul, 1970) 1046–1048.

[161] P. M. Doan, N. Ange, and S. Patrick, *Production of sodium dihydrogen phosphate using sodium chloride and orthophosphoric acid*, *Industrial & Engineering Chemistry Research* **54** (2015), no. 50 12467–12473, [https://doi.org/10.1021/acs.iecr.5b02892].

[162] A. A. Coelho, *Topas and topas-academic: an optimization program integrating computer algebra and crystallographic objects written in c++*, *Journal of Applied Crystallography* **51** (2018), no. 1 210–218.